Chapter 3

Thermochemistry of Fluorocarbons

3.1 Introduction

With the recent international restrictions on the production and deployment of chloro- and bromo-fluorocarbons (CFC, BFC), much effort is currently devoted to the search for suitable ozone-friendly replacements. An important use of halons, such as trifluorobromomethane (CF_3Br), has been as fire suppressants. Unfortunately, the bromine atoms that are so efficient in extinguishing flames, by removing hydrogen radicals, are also efficient catalysts of the ozone reduction process. Indeed, the ozone depletion potential of CF_3Br is an order of magnitude greater than that of most CFC's.[1] Fluorocarbons and hydro-fluorocarbons have been identified as promising candidates for fire-suppressants[2] and considerable effort is being devoted to their study. This has resulted in the generation of extensive thermochemical and kinetic databases.[3,4] Unlike CFC's and BFC's, fluorinated hydrocarbons have zero ozone depleting potential, although they are potential greenhouse gases. Fluorocarbons are also widely used as lubricants, blowing and sterilising agents, anaesthetics, propellants, refrigerants, and in the preparation of semiconductors.

There is considerable current interest in 2-H-heptafluoropropane (CF_3CHFCF_3, FM-200) as a potential fire retardant.[5,6] Unlike bromine, fluorine forms much stronger bonds and thus fluorine atoms are not recycled in the flame, as one fluorine radical will terminate just one hydrogen radical. Hence, with 7 fluorines per molecule, it is not surprising that flame tests have shown CF_3CHFCF_3 to be a very effective fire retardant[7]. The pyrolysis kinetics of CF_3CHFCF_3 at 1200-1500 K has been the subject of a recent shock tube and kinetic modelling study by Hynes et al.[8] The dominant initiation pathways were identified as HF elimination and CC bond fission:

$$CF_3CHFCF_3 \rightarrow C_3F_6 + HF \qquad (3.1)$$

and

$$CF_3CHFCF_3 \rightarrow CF_3CHF + CF_3 \qquad (3.2)$$

The most important subsequent reactions are

(1) the decomposition of the CF_3CHF radical

$$CF_3CHF \rightarrow CF_2{=}CHF + F \qquad (3.3)$$

(2) the abstraction of H from the parent molecule

$$CF_3CHFCF_3 + F \rightarrow CF_3CFCF_3 + HF$$

followed by the decomposition reactions

$$CF_3CFCF_3 \rightarrow CF_3CF{:} + CF_3 \qquad (3.4)$$

$$CF_3CF{:} \rightarrow CF_2{=}CF_2 \rightarrow CF_2 + CF_2 \qquad (3.5)$$

and the secondary reaction

$$CF_2{=}CF_2 + CF_2 \rightarrow \text{cyclo-}C_3F_6 \qquad (3.6)$$

and

(3) the radical recombination reactions

$$CF_3CHF + CHF_2 \rightarrow CF_3CHFCHF_2 \qquad (3.7)$$

and

$$CF_3 + CF_3 \rightarrow CF_3CF_3 \qquad (3.8)$$

As the thermochemistry of a number of species participating in the above reactions had been poorly characterised at the time, ab initio quantum chemical calculations were carried out concurrently with the modelling studies, generating heats of formation for most of the

intermediates in reactions (3.1) to (3.8). These calculations constitute the major part of this chapter.

In subsequent work Hynes et al.[9] studied the kinetics of high-temperature oxidation of C_3F_6 by $O(^3P)$, where the initial step is the addition of an oxygen atom across the double bond of C_3F_6:

$$CF_3CF{=}CF_2 + O \rightarrow CF_3CFCF_2O \qquad (3.9)$$

The resulting triplet biradical could:

(1) simply decompose to the triplet CF_3CF: and CF_2O,

(2) undergo a 1,2 F-atom shift and decompose to form CF_3CF_2 + CFO and

(3) lose fluorine, to yield $CF_3CFCF{=}O$ + F.

Some of these reactions were also studied using ab initio techniques and the thermochemical information generated was subsequently used in the kinetic modelling studies of Hynes et al.[9]

The most recent work in this area has been the shock tube kinetic study[10] of the high temperature reaction of H atoms with hexafluoropropene (C_3F_6) over the temperature range of 1250-1550 K, in an effort to understand the role C_3F_6 plays in a flame (given that it is a pyrolysis product of 2-H-heptafluoropropane). Addition of H across the double bond yields CF_3CHFCF_2 or CF_3CFCHF_2 which can then decompose by CC bond scissions to yield CF_3 + $CHFCF_2$, CF_3CHF + CF_2, etc., or after F loss, CF_2CHF + CF_2. Again, ab initio calculations were carried out to compute, in particular, the heat of formation of the hexafluoropropyl radicals.

The work presented in this chapter, including the computation of heats of formation of C1, C2 and C3 halons (closed shell singlets, radicals and carbenes), therefore complements and extends the thermochemical database representing ~ 30 years of experimental work by numerous scientists as well as ab initio theoretical work principally by Westmoreland, Zachariah and co-workers[2,3,11-13] and by Francisco and co-workers[14-17] over the last 7 years. Of

particular significance is the work of Smith[18] who computed the heats of formation of all the halons of importance in the kinetic modelling studies using the approximate Gaussian-2 technique: G2(MP2)[19].

An important advance in the computation of thermochemistry, particularly of fluorine containing molecules, was made with the introduction of Gaussian-3 (G3) theory[20]. G3 has been demonstrated to be significantly more accurate than Gaussian-2 (G2)[21] as well as being computationally cheaper. This work, therefore, comprises of the recalculation, using G3, of the heats of formation previously obtained by Smith, as well as a number of other C_1 and C_2 halons of general interest, in particular those included in the set of molecules studied by Zachariah et al.[3] by the bond additivity corrected MP4 (BAC-MP4) method[22-24].

The accuracy of these computations was maximised, where possible, by calculating the heats of formation of the species of interest via suitable isodesmic reactions, that is, utilising G3 heats of reaction in conjunction with accepted literature values for all other species in the reactions. While this approach is generally more accurate than using computed atomisation energies, its accuracy is also limited by the reliability of the available literature data. Two approximate schemes that derive from G3 are also presented which reduce the computational cost of G3 and therefore allow heats of formation for larger molecules (i.e., those with more than 6 heavy atoms) to be obtained on modest workstations.

3.2 Theory and Computational Methods

Recent advances in computational quantum chemistry have made the ab initio calculation of heats of formation via the computation of atomisation energies a realistic endeavour. As noted in **Section 2.7.2**, the Gaussian methods, G2[21] and more recently G3[20], developed by Pople and co-workers, achieve this via accurate estimates of the atomic and molecular energies in a near-complete one-particle basis (and by incorporating an empirical "higher level" correction term). This is done by correcting the energy obtained in a quadratic configuration interaction (QCISD(T)) calculation in a small split valence + polarisation functions basis (6-311G(*d*,*p*) or 6-31G(*d*)) by MP4 and MP2 estimates of the changes in the energy with systematic

enlargement of the basis sets. Alternatively, as pioneered by Martin[25,26], Dixon and Feller[27,28] as well as others[29,30], the same high level of theory (most commonly the coupled cluster (CCSD(T)) method) is employed in successively larger correlation consistent basis computations, such that the computed energies can be confidently extrapolated to an effectively complete basis limit (see **Section 2.7.3**). Using computed atomisation energies at 0 K in conjunction with experimental heats of formation of the elements in their atomic states, the heats of formation of the molecules at 0 K and hence at 298 K are readily obtained, as discussed in detail by Curtiss et al.[31], by calculating also the appropriate thermal contributions to the atomic and molecular enthalpies.

Direct use of atomisation energies for the computation of heats of formation of chemical accuracy (usually understood to be ~ 1 kcal mol^{-1}) requires, of course, that level of accuracy in the computed atomisation energies. For small molecules this is achievable. For example, for the Gaussian data set of 299 molecules, on average, the G2 and G3 atomisation energies have been found to be within 1.48 and 1.02 kcal mol^{-1} of experiment respectively.[20] More recently, Martin and Oliveira[25], using a range of extrapolation schemes for CCSD(T) energies, demonstrated an even higher level of accuracy of ± 0.24 kcal mol^{-1} in the computation of heats of formation of some 30 small first and second row molecules.

The major part of the work reported in this chapter was carried out using the G3 level of theory. Unfortunately, given the current limitations of our computing resources, it was not practicable to carry out G3 calculations for molecules with more than 6 heavy atoms. To treat larger molecules two approximations to G3 are proposed in the spirit of the G3(MP2)[32] and G2(MP2)[19]; these, in our view, retain the major advantages of G3 while offering considerable reductions in computational cost. To develop and justify the proposed approximations we write the (vibrationless) equilibrium G3 energy (at the MP2/6-31G(*d*) geometry), $E_0(\mathrm{G3})$, as

$$E_0(\mathrm{G3}) = E\left[\mathrm{QCISD(T)/6-31G}(d)\right] + \Delta E(+) + \Delta E(2df,p) + \Delta E(\mathrm{G3Large}) + \Delta E(\mathrm{hlc}) + \Delta E(\mathrm{SO}) \tag{3.10}$$

where $\Delta E(+)$, $\Delta E(2df,p)$, $\Delta E(\mathrm{G3Large})$, $\Delta E(\mathrm{SO})$ and $\Delta E(\mathrm{hlc})$ are corrections for diffuse,

higher polarisation and larger basis set effects (along with core-valence correlation and non-additivity in the latter), spin-orbit coupling effects and the so-called "higher level" corrections respectively, as defined by Curtiss et al.[20] In G3, $\Delta E(+)$ and $\Delta E(2df,p)$ are evaluated at the MP4(SDTQ) level, while $\Delta E(\mathrm{G3Large})$ consists of MP2 energies, including MP2(Full)/ G3large. As the most expensive step in a G3 calculation is the MP4(SDTQ)/6-31G($2df,p$) computation of the energy in $\Delta E(2df,p)$, which is dominated by the evaluation of the triple excitations' contribution, an obvious and reasonable approximation to G3 is to calculate the contributions to $\Delta E(2df,p)$ or even both $\Delta E(+)$ and $\Delta E(2df,p)$ at a lower level, such as MP4(SDQ), MP3 or even MP2. Thus we define the G3(MP4SDQ) approximation as

$$\begin{aligned} E_0\left(\mathrm{G3(MP4SDQ)}\right) = {} & E\left[\mathrm{QCISD(T)/6-31G}(d)\right] + \Delta E(+)_{\mathrm{MP4SDQ}} \\ & + \Delta E(2df,p)_{\mathrm{MP4SDQ}} + \Delta E(\mathrm{G3Large}) \\ & + \Delta E(\mathrm{hlc}) + \Delta E(\mathrm{SO}) \end{aligned} \tag{3.11}$$

The MP2 alternative then trivially results in the G3[MP2(Full)] approximation

$$\begin{aligned} E_0\left(\mathrm{G3}\left[\mathrm{MP2(Full)}\right]\right) = {} & E\left[\mathrm{QCISD(T)/6-31G}(d)\right] \\ & + E\left[\mathrm{MP2(Full)/G3Large}\right] - E\left[\mathrm{MP2(Full)/6-31G}(d)\right] \\ & + \Delta E(\mathrm{hlc}) + \Delta E(\mathrm{SO}) \end{aligned} \tag{3.12}$$

The G3[MP2(Full)] method is, of course, closely related to the G3(MP2)[32] method. In the latter the MP2 correction does not include core-valence correlation and thus the G3large basis is reduced to the smaller G3MP2large set.

The proposed G3[MP2(Full)] and G3(MP4SDQ) methods can be further improved by optimisation of the hlc terms, as done for G3(MP2). As discussed in the following section, in order to minimise the deviation between the G3 and G3(MP4SDQ) or G3[MP2(Full)] heats of formation for the molecules studied in this work, we propose an adjustment to the hlc terms of the atoms only, namely to *C* and *D*, in the expression

$$\Delta E\left(\mathrm{hlc}_{\mathrm{atoms}}\right) = -Cn_\beta - D\left(n_\alpha - n_\beta\right) \tag{3.13}$$

For G3(MP4SDQ) these are (in mE_h) $C = 5.708$, $D = 0.922$, while for G3[MP2(Full)] $C = 6.461$, $D = 0.979$. The equilibrium geometries and vibrational frequencies in all these approximate G3 schemes are identical to those defined by G3.

In order to complement the G3 (and approximate G3) calculations described above, Dr George Bacskay completed a more extensive computational study on a group of small molecules (namely the closed shell HCCH, HCCF and FCCF acetylenes and the HCC, FCC and formyloxyl (HCOO) radicals), in which their heats of formation were computed by a complete basis set extrapolation technique, as recommended by Dixon and Feller[27]. This work is an integral part of our collaborative project, and as such it is included here for completeness. It is particularly relevant as it demonstrates the reliability of G3 results in cases where they differ significantly from experimentally determined values.

In this work the equilibrium geometries were optimised at the CCSD(T)/cc-pVTZ level. The zero point vibrational energies of these molecules (with the exception of HCOO) were calculated at the MP2/cc-pVTZ level and scaled by a factor of 0.96, as in previous work by this group[33]. (A very similar factor, 0.9646, was proposed by Pople et al.[34] for the scaling of zero point energies obtained at the MP2(Full)/6-31G(*d*) level.) The open shell coupled cluster and MP2 calculations were carried out using the restricted formalisms, viz. RCCSD(T) and ROMP2. As discussed in a subsequent section, the HCOO frequencies were taken from the published work of Rauk et al.[35]

The electronic energies of the molecules and their constituent atoms were computed at the valence (R)CCSD(T) level using the sequence of (diffuse function) augmented correlation consistent basis sets aug-cc-pV*x*Z, $x = 2$ (D), 3 (T), 4 (Q)[36-38]. The resulting energies $E(x)$ were then fitted to a mixed exponential/Gaussian function

$$E(x) = A + B\exp(1-x) + C\exp\left(-(1-x)^2\right) \tag{3.14}$$

and to the asymptotic formula

$$E(x) = A + B(l_{\max} + 1/2)^{-4} \tag{3.15}$$

where A, B and C are (fitted) constants and $l_{\max}$ is the highest angular momentum quantum number in the basis set. The constant A thus represents the complete basis set (CBS) limit to the valence (R)CCSD(T) energy ($x \to \infty$). Using the notation of Dixon and Feller[27], the resulting extrapolated energies are denoted CBS(aDTQ/mix) and CBS(aTQ/$l_{\max}$), indicating the extrapolation technique and the sequence of basis sets used. (Note that the $l_{\max}$ type fit utilises only the (augmented) triple and quadruple zeta basis sets.) The extrapolated energies were then corrected for core-valence correlation (CV corr), using the cc-pCVQZ basis[39,40], by computing the difference between the all-electron (R)CCSD(T)/cc-pCVQZ and valence (R)CCSD(T)/cc-pVQZ energies. The energies were further corrected for scalar relativistic effects, by computing, using first order perturbation theory, the Darwin and mass-velocity contributions[41,42]. As in previous work by this group on the heats of formation of halocarbenes[33], these relativistic corrections were computed at the complete active space 2nd order perturbation theory (CASPT2) level of theory[43,44] with full valence complete active space self-consistent field (CASSCF)[45,46] reference states, using the G3large basis.

After combining the molecular electronic and zero point vibrational energies and correcting the computed atomic energies for spin-orbit coupling, the atomisation energies at 0 K, ΣD_0, and hence the heats of formation at 0 K were computed. By adding to $\Delta_f H_0^0$ the appropriate enthalpy differences ($H_{298}^0 - H_0^0$), for which accurate experimental values are available in the case of the elements and which can be readily calculated for the molecule of interest from the rotational constants and vibrational frequencies (as described in **Section 2.8**), the heats of formation at 298 K are obtained, as discussed in detail by Curtiss et al.[31]

All Gaussian-3 and related calculations were carried out using the Gaussian98 programs[47]. The (R)CCSD(T) and ROMP2 computations of the CBS studies were performed using the MOLPRO[48-50] , CADPAC6[51] and ACES2[52] programs, while MOLCAS4[53] was used to carry out the CASPT2 relativistic correction calculations. All computations were performed on DEC alpha 600/5/333 and COMPAQ XP1000/500 workstations of the Theoretical Chemistry group at the University of Sydney.

3.3 Results and Discussion

3.3.1 Heats of Formation from G3 and Related Atomisation Energies

The G3 energies (including zero point vibrational contributions) for the C_1 and C_2 halons are listed in **Table 3.1** and **Table 3.2** respectively along with the heats of formation at 298 K obtained from atomisation energies computed at the G3, G3[MP2(Full)] and G3(MP4SDQ) levels of theory; the G2 results of Berry[12,54] and Curtiss[21] and the G2(MP2) results of Smith[18] are also included for comparison. The appropriate atomic data used in the computation of the molecular atomisation energies and heats of formation are given in **Appendix 1.1**.

As the geometries of the majority of these molecules, calculated at the SCF/6-31G(*d*) level, were published by Zachariah et al.[3], the MP2(Full)/6-31G(*d*) geometries obtained in this work are not included in this thesis. However, as all rotational constants and vibrational frequencies are given in **Appendices 1.2 – 1.4**, any additional thermochemical data could be readily generated.

Table 3.1 and **Table 3.2** also contain current literature data, that is, experimental values and/or the results of accurate, high level ab initio computations. In the majority of cases the G3 heats of formation agree with the literature values to within ~ 1 kcal mol^{-1}, once allowance is made for the quoted uncertainties in the latter. In some instances, however, larger discrepancies (in excess of 2 kcal mol^{-1}) are noted, e.g. for CF_2O, CFO, CF_2CF_2, CF_3O and HCOO. The first three of these molecules were recently the subject of an extensive theoretical study by Dixon, Feller and Sandrone[27,28] who concluded that the heats of formation of these molecules at 0 K are −145.2 ± 0.8, −44.1 ± 0.5 and −159.8 ± 1.5 kcal mol^{-1}. These differ from the accepted experimental estimates by up to 6 kcal mol^{-1}, but are consistent with the G3 predictions. The theoretical value for tetrafluoroethylene has been recently confirmed by the high level computations of Bauschlicher and Ricca[55], who obtained $\Delta_f H^0_{298}$ = −160.5 ± 1.5 kcal mol^{-1}. The remaining problem cases, including CF_3O, will be discussed in the next section on isodesmic calculations. For a number of systems no errors are reported in the literature cited. For these the estimated errors of Zachariah et al.[3] have therefore been quoted.

Table 3.1 C_1 fluoro hydrocarbons: G3 energies and computed and literature heats of formation (in kcal mol^{-1} unless indicated otherwise).

Molecule	E_0(G3)/E_h	$\Delta_f H^0_{298}$ G3	$\Delta_f H^0_{298}$ G3[MP2(Full)]	$\Delta_f H^0_{298}$ G3(MP4SDQ)	$\Delta_f H^0_{298}$ G2[a]	$\Delta_f H^0_{298}$ G2(MP2)	$\Delta_f H^0_{298}$ Literature[b]	Diff G3–Lit
CH_4	–40.45762	–18.1	–17.5	–18.7	–18.6	–18.1	–17.90±0.08 [c]	–0.2
CH_3F	–139.64964	–56.9	–56.3	–57.3	–58.3	–58.6	–55.6±2.0 [d]	–1.3
CH_2F_2	–238.86227	–108.4	–107.9	–108.8	–110.8	–111.6	–108.1±0.4 [d]	–0.3
CHF_3	–338.08656	–167.1	–166.9	–167.6	–170.9	–171.8	–166.7±0.6 [d]	–0.4
CF_4	–437.30780	–223.9	–223.7	–224.7	–228.6	–230.1	–223.0±0.4 [d]	–0.9
							–223.1±1.1 [e]	–0.8
CH_3	–39.79329	34.0	34.5	33.4	35.1	35.6	35.1±0.1 [f]	–1.1
CH_2F	–138.98968	–7.7	–7.4	–8.3		–7.9	–7.8±2.0 [g]	0.1
CHF_2	–238.20132	–58.6	–58.6	–59.2		–60.6	–59.2±2.0 [g]	0.6
CF_3	–337.41737	–112.2	–112.3	–112.9	–114.7	–115.8	–112.8 [h]	–0.6
							–112.5±1.0 [i]	–0.5
CH_2 ($^1A_1$)	–39.10301	101.9	102.2	101.2	101.4	101.7	101.7±0.7 [j]	0.2
							102.6±1.0 [k]	–0.7
CHF	–138.34011	34.8	34.7	34.4	31.7	32.6	34.2±3.0 [l]	0.6
							35.1±1.0 [k]	–0.3
CF_2	–237.60041	–46.6	–47.2	–47.0	–48.2	–50.7	–44.6 [m]	–2.0
							–44.0 [l]	–2.6
							–45.9±0.3 [i]	–0.7

Table 3.1 continued

Molecule	E_0(G3)/E_h	$\Delta_f H^0_{298}$ G3	$\Delta_f H^0_{298}$ G3[MP2(Full)]	$\Delta_f H^0_{298}$ G3(MP4SDQ)	$\Delta_f H^0_{298}$ G2[a]	$\Delta_f H^0_{298}$ G2(MP2)	$\Delta_f H^0_{298}$ Literature[b]	Diff G3–Lit
CH	–38.45831	141.1	141.3	140.4	141.9	142.2	142.0±0.1 [c]	–0.9
CF	–137.72111	58.0	57.6	57.4		57.0	59.4±0.3 [i]	–1.4
CH_2O	–114.43106	–26.6	–26.5	–26.3	–27.9	–26.5	–26.0±1.5 [n,o]	–0.6
CHFO	–213.66577	–92.0	–92.0	–91.7		–93.0	–90.0±3.6 [c,o]	–2.0
							–91.6±1.7 [p]	0.4
CF_2O	–312.88194	–145.7	–145.7	–145.5	–148.6	–147.8	–152.7±0.4 [c]	7.0
							–145.9±0.8 [q]	0.2
CHO	–113.79156	9.7	9.4	10.0	9.3	10.8	9.96±0.20 [f]	–0.3
CFO	–213.00549	–42.7	–43.0	–42.4		–43.0	–38.5±1.7 [r]	–4.9
							–44.0±0.5 [q]	1.3
CH_3OH	–115.62921	–48.1	–47.3	–47.8	–49.4	–47.8	–48.1±0.1 [s,o]	0.0
CH_2FOH	–214.84531	–101.9	–101.1	–101.4		–102.9		
CHF_2OH	–314.07127	–161.6	–161.0	–161.2		–163.9		
CF_3OH	–413.29243	–218.3	–217.7	–218.1		–222.1	–217.7±2.0 [p]	–4.8
CH_3OF	–214.71751	–21.5	–20.1	–21.1		–21.9	–17.3±3.0 [t,o]	–4.2
CH_2FOF	–313.92729	–71.2	–69.9	–70.7		–73.1		
CHF_2OF	–413.14211	–123.9	–122.7	–123.6		–126.4		
CF_3OF	–512.35912	–178.0	–176.8	–177.8		–183.0	–173.0±2.0 [p]	4.8

Table 3.1 continued

Molecule	E_0(G3)/E_h	$\Delta_f H^0_{298}$ G3	$\Delta_f H^0_{298}$ G3[MP2(Full)]	$\Delta_f H^0_{298}$ G3(MP4SDQ)	$\Delta_f H^0_{298}$ G2[a]	$\Delta_f H^0_{298}$ G2(MP2)	$\Delta_f H^0_{298}$ Literature[b]	Diff G3–Lit
CH_3O	–114.96272	4.9	5.6	4.3		7.0	4.1±0.2 [u]	0.8
CH_2FO	–214.17891	–48.9	–48.4	–49.3		–48.3		
CHF_2O	–313.38786	–98.0	–97.6	–98.6		–99.0		
CF_3O	–412.60361	–151.2	–150.9	–151.9		–153.8	–149.2±2.0 [p]	5.5
CH_2OH	–114.97710	–3.9	–3.4	–3.7	–3.8	–2.1	–4.08±0.8 [f]	0.2
CHFOH	–214.18595	–53.0	–52.6	–52.7		–54.9		
CF_2OH	–313.40523	–108.7	–108.3	–108.4		–110.0		
CH_2OF	–214.05996	26.1	27.3	26.5		27.2		
CHFOF	–313.25679	–15.3	–14.2	–15.3		–18.0		
CH_3OOH	–190.72485	–30.1	–28.7	–29.0		–28.9	–33.2 [v]	3.1
							–31.3±2.0 [n,o]	1.2
CF_3OOH	–488.37663	–193.1	–191.8	–192.2		–194.9		
CH_3OO	–190.09001	2.9	4.1	3.0		5.7	2.2 [v]	0.7
CF_3OO	–487.73047	–152.9	–151.9	–153.0		–154.7	–144.0±3.0 [t,o]	–8.9
HCOOH	–189.65671	–90.6	–90.2	–89.4	–92.5	–85.6	–90.5±0.1 [n,o]	–0.1
FCOOH	–288.87711	–146.9	–146.6	–145.8		–145.4		

Table 3.1 continued

Molecule	E_0(G3)/E_h	$\Delta_f H^0_{298}$ G3	$\Delta_f H^0_{298}$ G3[MP2(Full)]	$\Delta_f H^0_{298}$ G3(MP4SDQ)	$\Delta_f H^0_{298}$ G2[a]	$\Delta_f H^0_{298}$ G2(MP2)	$\Delta_f H^0_{298}$ Literature[b]	Diff G3–Lit
HCOO ($^2A_1$)	–188.98028	–31.1	–30.3	–29.7		–26.8	–37.7±3.0 [w]	5.6
							–29.3±1.0 [x]	–2.8
FCOO ($^2B_2$)	–288.19901	–86.5	–86.1	–85.5		–85.5		
CH_2OHOH	–190.82596	–93.9	–92.8	–92.6		–92.7	–93.5±2.0 [y]	–0.4
CF_2OHOH	–389.27646	–212.3	–211.3	–211.1		–213.7		
OCH_2OH	–190.15797	–39.9	–39.0	–39.5		–37.0		
OCF_2OH	–388.59024	–146.9	–146.2	–146.7		–139.3		

[a] G2 results from Refs 12, 21 and 54.

[b] Experimental value unless otherwise indicated by italics and footnotes.

[c] Ref. 56.

[d] Ref. 57.

[e] CCSD(T)/CBS computations, Ref. 55.

[f] Ref. 58.

[g] Ref. 59.

[h] Ref. 60.

[i] CCSD(T)/CBS computations, Ref. 28, with thermal corrections from this work.

[j] Ref. 61.

[k] CCSD(T)/CBS computations, Ref. 33.

[l] Ref. 62.

[m] Ref. 63.

[n] Ref. 64.

[o] Error as given in Ref. 3.

[p] Ref. 65.

[q] CCSD(T)/CBS computations, Ref. 27, with thermal corrections from this work.

[r] Ref. 66.

[s] Ref. 67.

[t] Ref. 68.

[u] Ref. 69.

[v] Ref. 70.

[w] Ref. 71.

[x] Ref. 72.

[y] Ref. 73.

Table 3.2 C_2 fluoro hydrocarbons: G3 energies and computed and literature heats of formation (in kcal mol^{-1} unless indicated otherwise).

Molecule	E_0(G3)/E_h	$\Delta_f H^0_{298}$ G3	$\Delta_f H^0_{298}$ G3[MP2(Full)]	$\Delta_f H^0_{298}$ G3(MP4SDQ)	$\Delta_f H^0_{298}$ G2[a]	$\Delta_f H^0_{298}$ G2MP2	$\Delta_f H^0_{298}$ Literature[b]	Diff G3–Lit
CH_3CH_3	–79.72340	–20.4	–19.9	–20.9	–20.6	–19.9	–20.1±1.0 [c,d]	–0.3
CH_3CH_2F	–178.92623	–65.7	–65.2	–66.1	–71.2	–66.8	–66.1±1.0 [e]	0.4
CH_2FCH_2F	–278.12348	–107.3	–106.9	–107.6	–109.9	–110.9	*–103.7±2.8* [f]	–3.6
CH_3CHF_2	–278.14559	–121.3	–120.9	–121.6	–123.9	–123.9	–119.7±1.5 [g]	–1.6
CHF_2CH_2F	–377.33990	–161.1	–160.7	–161.3	–164.2	–165.3	–158.9±1.0 [h]	–2.2
CH_3CF_3	–377.37214	–181.3	–181.0	–181.7	–184.5	–185.3	–178.2±0.4 [g]	–3.1
CHF_2CHF_2	–476.55281	–212.5	–212.2	–212.7	–216.7	–216.9	–209.8±4.2 [f]	–2.7
CH_2FCF_3	–476.56312	–219.0	–218.7	–219.3	–223.3	–224.7	–214.1±2.0 [g]	–4.9
CHF_2CF_3			–268.2	–268.8	–273.9		–264.0±1.1 [g]	
CF_3CF_3			–323.8	–324.5	–330.7		–320.9±1.5 [g]	
CH_3CH_2	–79.06400	28.7	29.0	28.0	29.9	30.7	28.3±1.0 [c,d]	0.4
CH_2FCH_2	–178.26370	–14.7	–14.4	–15.2		–14.4	–14.2±2.0 [i]	–0.5
CH_3CHF	–178.26902	–18.2	–18.0	–18.7		–18.0	–16.8±2.0 [i]	1.4
CH_2FCHF	–277.46342	–58.1	–58.0	–58.6		–59.6	*–57.0±3.0* [f]	–1.1
CHF_2CH_2	–277.47984	–68.3	–68.0	–68.7		–69.5	*–68.3±3.6* [f]	0.0
CH_3CF_2	–277.48538	–71.9	–71.9	–72.5		–73.5	–72.3±2.0 [j]	0.4
CH_2FCF_2	–376.67696	–110.0	–110.0	–110.5		–113.3	*–107.5±3.6* [f]	–2.5
CHF_2CHF	–376.67800	–110.6	–110.6	–111.1		–113.6	*–109.0±3.6* [f]	–1.6
CF_3CH_2	–376.70469	–127.3	–127.1	–127.7		–129.8	–123.6±1.0 [j]	–3.7
CF_3CHF	–475.90075	–168.3	–168.3	–168.8		–172.7	–162.7±2.3 [k]	–5.6
CHF_2CF_2	–475.88795	–160.3	–160.4	–160.7		–165.0	*–158.9±4.5* [f]	–1.4
CF_3CF_2			–216.5	–216.9			–213.0±1.0 [j]	

Table 3.2 continued

Molecule	E_0(G3)/E_h	$\Delta_f H^0_{298}$ G3	$\Delta_f H^0_{298}$ G3[MP2(Full)]	$\Delta_f H^0_{298}$ G3(MP4SDQ)	$\Delta_f H^0_{298}$ G2[a]	$\Delta_f H^0_{298}$ G2MP2	$\Delta_f H^0_{298}$ Literature[b]	Diff G3–Lit
CH_2CH_2	–78.50742	12.3	11.7	12.1	12.8	13.2	12.54±0.07 [l]	–0.3
CH_2CHF	–177.71256	–34.4	–35.1	–34.5	–34.9	–35.0	–33.5±0.6 [m]	–0.9
CHFCHF–*Z*	–276.90631	–73.8	–74.6	–73.9		–76.0	–71.0±2.4 [n]	–2.8
CHFCHF–*E*	–276.90730	–74.5	–75.3	–74.7		–76.9	–70.0±2.4 [n]	–4.5
CH_2CF_2	–276.92299	–84.5	–85.2	–84.6		–86.4	–80.4±1.0 [m]	–4.1
$CHFCF_2$	–376.11080	–120.1	–120.9	–120.2		–123.7	–117.4±2.2 [m]	–2.7
CF_2CF_2	–475.30917	–162.3	–163.2	–162.6	–165.6	–167.5	–157.4±0.7 [l]	–4.9
							–160.6±1.5 [o]	–1.7
							–160.5±1.5 [p]	–1.8
CH_3CH	–78.38810	87.5	87.4	87.0		87.7		
CH_2FCH	–177.59324	40.7	40.6	40.5		39.6		
CHF_2CH	–276.79333 [q]	–12.1 [q]						
CF_3CH	–376.01256	–58.2	–58.2	–58.5		–63.4		
CH_3CF	–177.62985	17.9	17.5	17.6		16.2		
CH_2FCF	–276.82347	–21.7	–22.1	–21.9		–25.2		
CHF_2CF	–376.02767	–67.7	–68.1	–67.9		–73.0		
CF_3CF	–475.24834	–124.0	–124.4	–124.2		–131.0		
CH_2CH	–77.83307	70.5	70.0	70.2	72.7	73.4	71.6±0.8 [r]	–1.1
CHFCH–*Z*	–177.03040	28.7	28.1	28.4		29.8		
CHFCH–*E*	–177.03102	28.3	27.7	27.9		29.4		
CH_2CF	–177.03465	26.0	25.3	25.6		26.9		
CHFCF–*Z*	–276.22409	–10.8	–11.6	–11.2		–11.7		
CHFCF–*E*	–276.22357	–10.4	–11.1	–10.8		–11.2		

Table 3.2 continued

Molecule	E_0(G3)/E_h	$\Delta_f H^0_{298}$ G3	$\Delta_f H^0_{298}$ G3[MP2(Full)]	$\Delta_f H^0_{298}$ G3(MP4SDQ)	$\Delta_f H^0_{298}$ G2[a]	$\Delta_f H^0_{298}$ G2MP2	$\Delta_f H^0_{298}$ Literature[b]	Diff G3–Lit
CF_2CH	–276.23666	–18.7	–19.4	–19.1		–19.2		
CF_2CF	–375.42392	–54.0	–54.8	–54.4		–56.4	–45.9±2.0 [s]	–8.1
CH_3C	–77.75331	120.6	120.4	120.0		122.0		
CH_2FC	–176.95053	78.8	78.6	78.4		78.6		
CHF_2C	–276.14927	36.1	35.8	35.6		34.8		
CF_3C	–375.36705	–18.4	–18.7	–18.9		–22.0		
HCCH	–77.27596	54.9	53.6	55.3	55.8	56.3	54.2±0.2 [c,d]	0.7
HCCF	–176.45463	24.8	23.4	25.0		24.9	30.0±5.3 [l]	–5.2
FCCF	–275.62524	0.0	–1.6	–0.1		–1.1	5.0±5.0 [l]	–5.0
CH_2C	–77.20691	98.5	97.4	98.3		99.3		
CHFC	–176.38031	71.5	70.4	71.3		70.4		
CF_2C	–275.57646	30.4	29.2	30.2		27.5		
CCH	–76.56469	136.3	135.1	136.1	138.7	139.4	135.0±1.0 [t]	1.3
CCF	–175.73867	109.3	107.8	108.9		110.5	110.0±5.3 [f]	–0.7
CH_2CO	–152.50687	–12.1	–13.2	–11.5	–12.1	–10.4	–11.4±0.4 [u]	–0.7
CHFCO	–251.68018	–38.8	–39.9	–38.2		–38.9		
CF_2CO	–350.86874	–75.0	–76.0	–74.4		–76.5		
CHCO	–151.84066	40.9	39.8	41.2		43.4	41.9±2.0 [r]	–1.0
CFCO	–251.00583	19.3	18.1	19.6		24.1		
CH_3CHO	–153.71480	–39.8	–39.8	–39.4	–41.0	–39.1	–39.7±0.1 [v,d]	–0.1
CH_2FCHO	–252.90987	–80.2	–80.2	–79.7		–80.1		
CHF_2CHO	–352.12071	–130.4	–130.4	–129.8		–132.8		
CF_3CHO	–451.34093	–186.5	–186.5	–186.0		–190.3		

Table 3.2 continued

Molecule	E_0(G3)/E_h	$\Delta_f H^0_{298}$ G3	$\Delta_f H^0_{298}$ G3[MP2(Full)]	$\Delta_f H^0_{298}$ G3(MP4SDQ)	$\Delta_f H^0_{298}$ G2[a]	$\Delta_f H^0_{298}$ G2MP2	$\Delta_f H^0_{298}$ Literature[b]	Diff G3–Lit
CH_3CFO	–252.95069	–105.8	–105.8	–105.4	–107.7	–106.2		
CH_2FCFO	–352.14170	–143.6	–143.7	–143.1		–144.7		
CHF_2CFO	–451.34766	–190.7	–190.8	–190.2		–194.6		
CF_3CFO	–550.56716	–246.3	–246.3	–245.8		–251.4		
CH_3CO	–153.07373	–2.5	–2.7	–2.1	–2.8	–0.9	–2.4±0.3 [r]	–0.1
CH_2FCO	–252.26707	–41.9	–42.1	–41.5		–41.7		
CHF_2CO	–351.47501	–90.3	–90.5	–89.8		–92.1		
CF_3CO	–450.69399	–145.6	–145.9	–145.2		–148.9		

[a] G2 results from Refs 12, 21 and 54.

[b] Experimental value unless otherwise indicated by italics and footnotes.

[c] Ref. 74.

[d] Error as given in Ref. 3.

[e] Ref. 75.

[f] BACMP4, Ref. 3.

[g] Ref. 76.

[h] Ref. 77.

[i] Ref. 78.

[j] Ref. 63.

[k] Ref. 79.

[l] Ref. 56.

[m] Ref. 60.

[n] Ref. 80.

[o] CCSD(T)/CBS computations, Ref. 28, with thermal corrections from Ref. 55.

[p] CCSD(T)/CBS computations, Ref. 55.

[q] Computed at HF/6-31G(*d*) geometry, see text.

[r] Ref. 58.

[s] Ref. 81.

[t] Ref. 59.

[u] Ref. 82.

[v] Ref. 64.

On the whole the G3[MP2(Full)] and G3(MP4SDQ) results are in reasonable agreement with those obtained by the application of G3. The average absolute deviations of G3[MP2(Full)] and G3(MP4SDQ) from G3 are ~ 0.5 and 0.4 kcal mol^{-1} respectively, the largest deviation being 1.6 kcal mol^{-1} in the case of FCCF. The deviations are significantly larger when the G2(MP2) and G3 results are compared, up to 6 kcal mol^{-1}. However, as discussed in the next section, the consistency between the computed heats of formation is much improved once isodesmic reaction schemes are used.

It is noted that no equilibrium structure was found at the MP2(Full)/6-31G(*d*) level for the CHF_2CH carbene. The MP2 as well as B3LYP/6-31G(*d*) density functional optimisations converge to difluoro ethylene, CF_2CH_2. These results suggest that CHF_2CH may not exist as a distinct molecule. Nevertheless, to give an estimate of the energy of this probably metastable carbene, its G3 heat of formation was computed at the HF/6-31G(*d*) geometry, as at that level of theory there is a local minimum on the potential surface for CHF_2CH.

Comparison of the G3 heats of formation with the BAC-MP4 values for the C_1 and C_2 halons studied by Zachariah et al.[3] suggests remarkably good agreement on the average, the mean absolute deviation between the two sets being just 1.6 kcal mol^{-1}. While the agreement is mostly excellent (~ 1 kcal mol^{-1} or better), for a number of molecules, e.g. FCCF, CCH, CH and CH_2FOF, substantial disagreement (~ 5 kcal mol^{-1}) has been noted.

3.3.2 Heats of Formation from G3 and related Isodesmic Reaction Enthalpies

The calculation of accurate atomisation energies and hence heats of formation is a stringent and demanding test of the quantum chemical methodology since the molecules of interest and their constituent atoms need to be described in an accurate and balanced manner. It has long been recognised, however, that the computation of isodesmic reaction energies, where the number of bond types is conserved, is much less demanding with respect to the resolution of electron correlation. Therefore reasonably accurate predictions of heats of formation are possible by utilising isodesmic schemes, even at relatively low levels of theory. The success of such an

approach, however, crucially depends on the availability of accurate thermochemical data for molecules that are chemically similar to those under study, that is, molecules with the same type of bonds. Given the demonstrated accuracy of G3 theory in the calculation of atomisation energies, major improvements are not expected in the heats of formation when these are recalculated from suitable isodesmic reaction energies. It is expected, however, that there will be a higher level of consistency between the three methods used, viz. G3, G3[MP2(Full)] and G3(MP4SDQ) (and with the G2(MP2)-*ID* values of Smith), than observed in the data in **Table 3.1** and **3.2**. The application of isodesmic schemes to the heats of formation obtained from atomisation energies can therefore also be regarded as a test of the consistency of the calculations and their results.

There are relatively few bond types among the molecules in this study (C-H, C-F, C-C, C=C, C-O, C=O, etc.) but, as may be noted on inspection of the data in **Table 3.1** and **3.2**, the number of molecules with accurate (≤ 1 kcal mol^{-1}) experimental or computed heats of formation is quite small; this means that not all bond types are represented by the selected set: CH_4, CF_4, CH_3, CH_2, CF_2, CF_2O, CFO, CH_3OH, CH_3O, C_2H_6, C_2H_4 and C_2H_2. Nevertheless, using these 12 molecules it is possible to construct isodesmic reactions for the majority of the molecules studied in this work, as demonstrated by the results summarised in **Table 3.3**. For example, the heats of formation of all hydrofluoroethanes can be obtained from the computed heats of the reactions

$$C_2H_6 + \frac{x}{4}CF_4 \rightarrow C_2H_{6-x}F_x + \frac{x}{4}CH_4 \tag{3.16}$$

and experimental enthalpies of formation of C_2H_6, CH_4 and CF_4. As discussed by Berry et al.[12], such use of isodesmic reactions is equivalent to applying a bond additivity correction to the heat of formation of the molecule of interest, $C_2H_{6-x}F_x$ in the current example. Such a bond additivity corrected enthalpy of formation is then written

$$\Delta_f H^0_{298}(\text{BAC}) = \Delta_f H^0_{298}(\text{calc}) - \Delta_{CC} - (6-x)\Delta_{CH} - x\Delta_{CF} \tag{3.17}$$

where $\Delta_f H^0_{298}(\text{calc})$ is the enthalpy of formation of $C_2H_{6-x}F_x$ calculated from its atomisation energy. The bond correction parameters Δ_{CC}, Δ_{CH} and Δ_{CF} are obtained by comparison of

$\Delta_f H^0_{298}(\text{calc})$ and $\Delta_f H^0_{298}(\text{expt})$ of the reference molecules C_2H_6, CH_4 and CF_4, for example:

$$\Delta_{CH} = \tfrac{1}{4}\left[\Delta_f H^0_{298}(CH_4,\text{calc}) - \Delta_f H^0_{298}(CH_4,\text{expt})\right] \qquad (3.18)$$

As expected, the G3, G3[MP2(Full)], G3(MP4SDQ) and G2(MP2) heats of formation obtained from the corresponding isodesmic reaction enthalpies, as listed in **Table 3.3**, are in much closer agreement than those obtained from atomisation energies. The differences are generally no greater than 0.3 kcal mol^{-1}. Clearly, considerable error cancellation occurs when we compute the heats of isodesmic reactions. It is worth noting also that all empirical hlc contributions to the Gaussian-2, -3, etc. energies completely cancel when one computes isogyric or isodesmic reaction energies. Nevertheless, the differences between the G3 heats of formation when obtained from atomisation energies and isodesmic reaction enthalpies are moderately small: ~ 0.9 kcal mol^{-1} on the average and no larger than 1.6 kcal mol^{-1}. This is of course expected, given that the heats of formation of the above 12 reference molecules are quite accurately predicted from the G3 atomisation energies. On the other hand, in the case of certain heats of formation, such as CF_3O, CH_2FCF_3 and CF_3CHF, where initially large discrepancies (~ 5 kcal mol^{-1}) between the G3 and literature values of were noted (see **Tables 3.1** and **3.2**), the application of isodesmic (viz. bond additivity) corrections, does not significantly improve the situation. We believe that in the case of such molecules the precision in the literature values is considerably less than implied by the quoted errors.

Table 3.4 summarises the heats of formation for the C_3 systems that were of direct interest in the kinetic modelling studies of Hynes et al.[10] The various schemes yield very consistent results in that the isodesmic heats of formation are, with one exception, within 0.2 kcal mol^{-1} of each other and up to ~ 3 kcal mol^{-1} higher than when obtained from atomisation energies. The variations are largest for hexafluoropropene and the hexafluoropropyl radical. Utilising the isodesmic results, it is estimated that the heats of formation of these two species as –276.2 ± 2 and –266.4 ± 3 kcal mol^{-1} respectively, on the basis of the spread of computed values and the expected intrinsic accuracy of the G3 method. Given the good agreement between the computed (isodesmic) and experimental heats of formation for propene, n-propyl and hexafluoropropene, the computed value for hexafluoropropyl, –266.4 ± 3 kcal mol^{-1}, is expected to be similarly reliable.

Table 3.3 C_1 and C_2 fluoro hydrocarbons: Computed heats of formation via isodesmic (*ID*) reactions of selected species (in kcal mol^{-1}).

Molecule	Eq[n]	G3	Diff[b]	G3[MP2(Full)]	G3(MP4SDQ)	G2(MP2)	Literature[c]	Diff
		ID	*ID – AE*	*ID*	*ID*	*ID*		G3(*ID*) – Lit
CH_3F	1	–56.5	0.4	–56.4	–56.3	–56.7	–55.6±2.0	–0.9
CH_2F_2	1	–107.8	0.6	–107.7	–107.5	–108.0	–108.1±0.4	0.2
CHF_3	1	–166.4	0.7	–166.5	–166.1	–166.5	–166.7±0.6	0.4
CH_2F	2	–6.5	1.2	–6.7	–6.3	–6.8	–7.8±2.0	1.3
CHF_2	2	–57.2	1.4	–57.5	–57.0	–57.7	–59.2±2.0	2.0
CF_3	2	–110.7	1.5	–111.0	–110.6	–111.3	–112.5±1.0 [d]	1.8
CHF	3	35.7	0.9	35.4	36.0	35.2	35.1±1.0 [e]	0.6
CF_2	3	–45.5	0.9	–46.2	–45.1	–46.3	–45.9±0.3 [d]	1.2
CHF	4	35.1	0.3	35.5	35.6	35.7	35.1±1.0 [e]	0.0
CH_2O	5	–27.2	–0.6	–27.3	–27.2	–28.0	–26.0	–1.2
CHFO	5	–92.4	–0.4	–92.5	–92.3	–92.8	–90.0	–2.4
CHO	6	8.0	–1.7	7.9	8.0	7.9	10.4±2.0	–0.9
CH_2FOH	7	–101.7	0.2	–101.6	–101.5	–101.5		
CHF_2OH	7	–161.2	0.4	–161.2	–161.0	–160.8		
CF_3OH	7	–217.8	0.5	–217.7	–217.7	–217.2	–213.5	–4.3
CH_2FO	8	–49.6	–0.7	–49.7	–49.4	–49.6		
CHF_2O	8	–98.6	–0.6	–98.7	–98.5	–98.6		
CF_3O	8	–151.6	–0.4	–151.7	–151.5	–151.7		

Table 3.3 continued

Molecule	Eq[n]	G3	Diff[b]	G3[MP2(Full)]	G3(MP4SDQ)	G2(MP2)	Literature[c]	Diff
		ID	*ID* – *AE*	*ID*	*ID*	*ID*		G3(*ID*) – Lit
CH_3CH_2F	9	–65.2	0.5	–65.1	–65.1	–65.3	–62.9±0.4	–2.3
CH_2FCH_2F	9	–106.6	0.7	–106.5	–106.3	–107.7	–103.7±2.8	–2.9
CH_3CHF_2	9	–120.6	0.7	–120.5	–120.3	–120.7	–119.7±1.5	–1.0
CHF_2CH_2F	9	–160.2	0.9	–160.1	–159.8	–160.4	–158.9±1.0	–1.4
CH_3CF_3	9	–180.5	0.8	–180.4	–180.2	–180.4	–178.2±0.4	–2.3
CHF_2CHF_2	9	–211.5	1.0	–211.3	–211.0	–210.2	–209.8±4.2	–1.7
CH_2FCF_3	9	–218.0	1.0	–217.8	–217.6	–218.0	–214.1±1.0	–3.9
CHF_2CF_3	9			–267.0	–266.9		–264.0±1.1	1.3
CF_3CF_3	9			–322.3	–322.3		–320.9±1.5	–2.1
CH_3CH_2	10	29.8	1.1	29.7	29.8	29.7	28.3	1.5
CH_2FCH_2	10	–13.4	1.3	–13.5	–13.2	–13.6	–11.40±0.24	–2.0
CH_3CHF	10	–16.9	1.3	–17.1	–16.7	–17.3	–18.2±1.4	1.3
CH_2FCHF	10	–56.6	1.5	–56.7	–56.3	–57.1	–57.0±3.0	0.4
CHF_2CH_2	10	–67.0	1.3	–66.9	–66.8	–67.2	–68.3±3.6	1.3
CH_3CF_2	10	–70.6	1.3	–70.8	–70.6	–71.0	–72.3±2.0	1.8
CH_2FCF_2	10	–108.5	1.5	–108.6	–108.4	–109.1	–107.5±3.6	–1.0
CHF_2CHF	10	–109.1	1.5	–109.2	–109.0	–109.4	–109.0±3.6	–0.1
CF_3CH_2	10	–125.8	1.5	–125.7	–125.6	–125.8	–123.6±1.0	–2.3
CF_3CHF	10	–166.7	1.6	–166.7	–166.5	–167.0	–162.7±2.3	–4.0
CHF_2CF_2	10	–158.7	1.6	–158.8	–158.4	–159.3	–158.9±4.5	0.2
CF_3CF_2	10			–214.6	–214.3		–213.0±1.0	

Table 3.3 continued

Molecule	Eq[n]	G3	Diff[b]	G3[MP2(Full)]	G3(MP4SDQ)	G2(MP2)	Literature[c]	Diff
		ID	*ID* – *AE*	*ID*	*ID*	*ID*		G3(*ID*) – Lit
CH_2CHF	11	–34.0	0.4	–34.0	–33.8	–34.0	–33.5±0.6	–0.5
CHFCHF–*Z*	11	–73.2	0.6	–73.2	–73.0	–73.3	–71.0±2.4	–2.2
CHFCHF–*E*	11	–73.9	0.6	–73.9	–73.8	–74.1	–70.0±2.4	–3.9
CH_2CF_2	11	–83.9	0.6	–83.8	–83.7	–83.7	–80.4±1.0	–3.5
$CHFCF_2$	11	–119.3	0.8	–119.2	–119.1	–119.3	–117.4±2.2	–2.0
CF_2CF_2	11	–161.3	1.0	–161.2	–161.2	–160.6	–160.5	–0.8
CH_2CH	12	71.4	0.9	71.6	71.3	71.7	71.6±0.8	–0.2
CHFCH–*Z*	12	29.8	1.1	30.0	29.7	30.0		
CHFCH–*E*	12	29.4	1.1	29.6	29.2	29.6		
CH_2CF	12	27.1	1.1	27.2	26.9	26.9		
CHFCF–*Z*	12	–9.6	1.2	–9.5	–9.7	–9.9		
CHFCF–*E*	12	–9.2	1.2	–9.0	–9.3	–9.4		
CF_2CH	12	–17.5	1.2	–17.3	–17.6	–17.4		
CF_2CF	12	–52.6	1.4	–52.4	–52.6	–52.9	–45.9±2.0	–6.7
CH_3CH	13	88.3	0.8	88.0	88.4	88.2		
CH_2FCH	13	41.7	1.0	41.5	42.1	41.9		
CHF_2CH	13	–10.9	1.2					
CF_3CH	13	–56.9	1.3	–56.8	–56.4	–57.7		
CH_3CF	14	18.5	0.6	18.7	18.5	18.8		
CH_2FCF	14	–20.9	0.8	–20.6	–20.8	–20.9		
CHF_2CF	14	–66.7	1.0	–66.3	–66.6	–66.9		
CF_3CF	14	–122.8	1.2	–122.3	–122.6	–123.9		

Table 3.3 continued

Molecule	Eq[n]	G3 *ID*	Diff[b] *ID* – *AE*	G3[MP2(Full)] *ID*	G3(MP4SDQ) *ID*	G2(MP2) *ID*	Literature[c]	Diff G3(*ID*) – Lit
HCCF	15	24.3	–0.5	24.3	24.1	24.6	30.0±5.3	–5.7
FCCF	15	–0.4	–0.4	–0.5	–0.8	0.3	5.0±5.0	–5.4
CCH	16	136.2	–0.1	135.6	136.2	136.3	135.0±1.0	1.2
CCF	16	109.4	0.1	108.6	109.4	109.2	110.0±5.3	–0.6

[a] Isodesmic Reactions:

(1) $\left(1-\frac{x}{4}\right)CH_4 + \frac{x}{4}CF_4 \rightarrow CH_{4x}F_x$

(2) $CH_3 + \frac{x}{4}CF_4 \rightarrow \frac{x}{4}CH_4 + CH_{3x}F_x$

(3) $CH_2 + \frac{x}{4}CF_4 \rightarrow CH_{2x}F_x + \frac{x}{4}CH_4$

(4) $\frac{1}{2}CH_2 + \frac{1}{2}CF_2 \rightarrow CHF$

(5) $CF_2O + \frac{x}{4}CH_4 \rightarrow CH_xF_{2x}O + \frac{x}{4}CF_4$

(6) $CFO + \frac{1}{4}CH_4 \rightarrow CHO + \frac{1}{4}CF_4$

(7) $CH_3OH + \frac{x}{4}CF_4 \rightarrow \frac{x}{4}CH_4 + CH_{3x}F_xOH$

(8) $CH_3O + \frac{x}{4}CF_4 \rightarrow \frac{x}{4}CH_4 + CH_{3x}F_xO$

(9) $C_2H_6 + \frac{x}{4}CF_4 \rightarrow \frac{x}{4}CH_4 + C_2H_{6x}F_x$

(10) $C_2H_6 + CH_3 + \frac{x}{4}CF_4 \rightarrow \left(1+\frac{x}{4}\right)CH_4 + C_2H_{5x}F_x$

(11) $C_2H_4 + \frac{x}{4}CF_4 \rightarrow \frac{x}{4}CH_4 + C_2H_{4x}F_x$

(12) $C_2H_4 + CH_3 + \frac{x}{4}CF_4 \rightarrow \left(1+\frac{x}{4}\right)CH_4 + C_2H_{3x}F_x$

(13) $C_2H_6 + CH_2 + \frac{x}{4}CF_4 \rightarrow \left(1+\frac{x}{4}\right)CH_4 + CH_{3x}F_xCH$

(14) $C_2H_6 + CF_2 + \frac{x-1}{4}CF_4 \rightarrow \left(\frac{x+3}{4}\right)CH_4 + CH_{3x}F_xCF$

(15) $C_2H_2 + \frac{x}{4}CF_4 \rightarrow \frac{x}{4}CH_4 + C_2H_{2x}F_x$

(16) $C_2H_2 + CH_3 + \frac{x}{4}CF_4 \rightarrow \left(1+\frac{x}{4}\right)CH_4 + C_2H_{1x}F_x$

[b] Difference between G3 heats of formation obtained via isodesmic (*ID*) reactions and atomisation energies (*AE*).

[c] Experimental value as in **Tables 3.1** and **3.2**, unless otherwise indicated.

[d] CCSD(T)/CBS computations, Ref. 28, with thermal corrections from this work.

[e] CCSD(T)/CBS computations, Ref. 33.

Table 3.4 C_3 fluoro hydrocarbons: G3 energies and computed values of heats of formation from atomisation energies (*AE*) and isodesmic reactions (*ID*) as specified (in kcal mol^{-1} unless indicated otherwise).

Molecule	E_0(G3)/E_h	$\Delta_f H^0_{298}$ G3		$\Delta_f H^0_{298}$ G3[(MP2(Full)]		$\Delta_f H^0_{298}$ G3(MP4SDQ)		$\Delta_f H^0_{298}$ Experiment
		AE	*ID*	*AE*	*ID*	*AE*	*ID*	
CH_3CHCH_2	–117.78219	4.7	5.0	3.8	4.8	4.6	5.0	4.88[b]
$CH_3CH_2CH_2$	–118.33332	24.5	25.7	24.6	25.5	23.8	25.4	23.9 ± 0.5[c]
CF_3CFCF_2	–713.01767	–277.6	–276.2	–278.3	–275.6	–277.5	–275.7	–275.3 ± 1.1[d]
CF_3CHFCF_2				–269.1	–266.5	–269.3	–266.3	

[a] Isodesmic Reactions:

$CH_3CH_3 + CH_2CH_2 \rightarrow CH_3CHCH_2 + CH_4$

$2CH_3CH_3 + CH_3 \rightarrow CH_3CH_2CH_2 + 2CH_4$

$CH_3CH_3 + CH_2CH_2 + \frac{3}{2}CF_4 \rightarrow CF_3CFCF_2 + \frac{5}{2}CH_4$

$2CH_3CH_3 + CH_3 + \frac{3}{2}CF_4 \rightarrow CF_3CHFCF_2 + \frac{7}{2}CH_4$

[b] Ref. 83.

[c] Ref. 84.

[d] Ref. 85.

3.3.3 Comparison of G2 and G3 Methods: Analysis of Atomisation Energies of Fluoromethanes

As the results of the previous sections clearly indicate, the G3 method is superior to G2 and G2(MP2) in the prediction of heats of formation of fluoro hydrocarbons from the computed atomisation energies. In an effort to gain some understanding of the reasons for this an analysis of the G2 and G3 energetics for the fluoromethanes CH_4, CH_3F, CH_2F_2, CHF_3 and CF_4 was carried out, where the individual contributions to the composite G2 and G3 atomisation energies were compared.

Using the decomposition scheme of Equation (3.10), **Table 3.5** lists the G2 and G3 atomisation energies (*AE*) obtained by the appropriate QCISD(T) calculations, followed by the MP4 and MP2 corrections (for basis incompleteness) and the zero point corrections. Up to this point the differences between G2 and G3 are due to the different "parent" bases: 6-311G(*d*,*p*) for G2 and 6-31G(*d*) for G3, and the different "large" bases: 6-311+G(3*df*,2*p*) for G2 and the G3large set for G3. Note that thus far all correlated energies, including the MP2/(G3large), are valence only and thus the sum of these contributions is denoted *AE*(valence). The core valence correlation (CV) corrections to the G3 energies are listed separately, along with the empirical hlc terms and the spin-orbit coupling corrections that are implicit in G3 and, finally, the resulting total atomisation energies at 0 K.

The trends displayed by the data in **Table 3.5** are interesting and informative. The largest corrections to the QCI values of the atomisation energies (apart from ZPE) are the MP4/(2*df*,*p*) terms. While these are relatively constant in the G3 calculations, ranging from 23.3 to 26.5 kcal mol^{-1}, in the case of G2 they vary from 5.7 to 30.1 kcal mol^{-1}. In contrast with these, the MP4/(+) corrections are more significant for G3, especially in CHF_3 and CF_4. These trends point to some basic differences between G2 and G3 in the quality of the respective QCI energies and the relative importance of the MP4/(+) and MP4/(2*df*,*p*) corrections in the two schemes. As a further illustration of this point, **Figure 3.1** shows a plot of the QCI atomisation energies, corrected by the MP4/(+) and zero-point contributions, against the G3 total atomisation energies. The resulting QCISD(T) + MP4/(+) + ZPE energies, as obtained in the G2 and G3 calculations, correlate linearly with the benchmark G3 (total) atomisation energies but the two slopes are very

Table 3.5 Comparison of G2 and G3 methods: Analysis of atomisation energies (kcal mol^{-1}) of CH_4, CH_3F, CH_2F_2, CHF_3 and CF_4.

	CH_4			CH_3F			CH_2F_2		
	G2	G3	G3 – G2	G2	G3	G3 – G2	G2	G3	G3 – G2
AE [QCISD(T)]	401.6	382.9	–18.6	397.9	385.4	–12.5	408.2	402.9	–5.3
Δ*AE* [MP4/(+)]	–0.4	–1.3	–0.9	1.9	1.3	–0.6	1.6	–0.1	–1.7
Δ*AE* [MP4/(2*df*,*p*)]	5.7	26.5	20.7	10.9	24.9	14.0	16.7	23.8	7.1
Δ*AE* [MP2/(G3large)]	4.3	2.7	–1.6	4.2	1.7	–2.5	4.2	1.5	–2.7
Δ*AE* [ZPE]	–26.8	–26.8	0.0	–23.8	–23.8	0.0	–20.2	–20.2	0.0
AE (valence)[a]	384.5	384.0	–0.5	391.1	389.5	–1.5	410.5	407.9	–2.6
Δ*AE* [CV]	0.0	1.1	1.1	0.0	1.2	1.2	0.0	1.4	1.4
Δ*AE* [hlc]	8.7	7.7	–1.0	8.7	8.0	–0.7	8.7	8.3	–0.4
Δ*AE* [Spin Orbit]	0.0	–0.1	–0.1	0.0	–0.5	–0.5	0.0	–0.9	–0.9
AE (total)[b]	393.2	392.8	–0.4	399.8	398.3	–1.5	419.2	416.7	–2.5

Table 3.5 continued

	CHF_3			CF_4		
	G2	G3	G3 – G2	G2	G3	G3 – G2
AE [QCISD(T)]	425.8	429.5	3.7	441.4	454.5	13.1
Δ*AE* [MP4/(+)]	–0.2	–5.1	–5.0	–2.8	–12.3	–9.5
Δ*AE* [MP4/(2*df*,*p*)]	23.2	23.3	0.1	30.1	23.5	–6.6
Δ*AE* [MP2/(G3large)]	4.2	1.6	–2.6	4.3	2.1	–2.2
Δ*AE* [ZPE]	–15.8	–15.8	0.0	–10.7	–10.7	0.0
AE (valence)[a]	437.4	433.5	–3.8	462.4	457.2	–5.2
Δ*AE* [CV]	0.0	1.7	1.7	0.0	1.9	1.9
Δ*AE* [hlc]	8.7	8.6	–0.1	8.7	8.9	0.2
Δ*AE* [Spin Orbit]	0.0	–1.2	–1.2	0.0	–1.6	–1.6
AE (total)[b]	446.1	442.5	–3.5	471.1	466.4	–4.7

[a] *AE* (valence) = *AE* [QCISD(T)] + Δ*AE* [MP4/(+) + MP4/(2*df*,*p*) + MP2/(G3large) + ZPE]

[b] *AE* (total) = *AE* (valence) + Δ*AE* [CV + hlc + Spin Orbit]

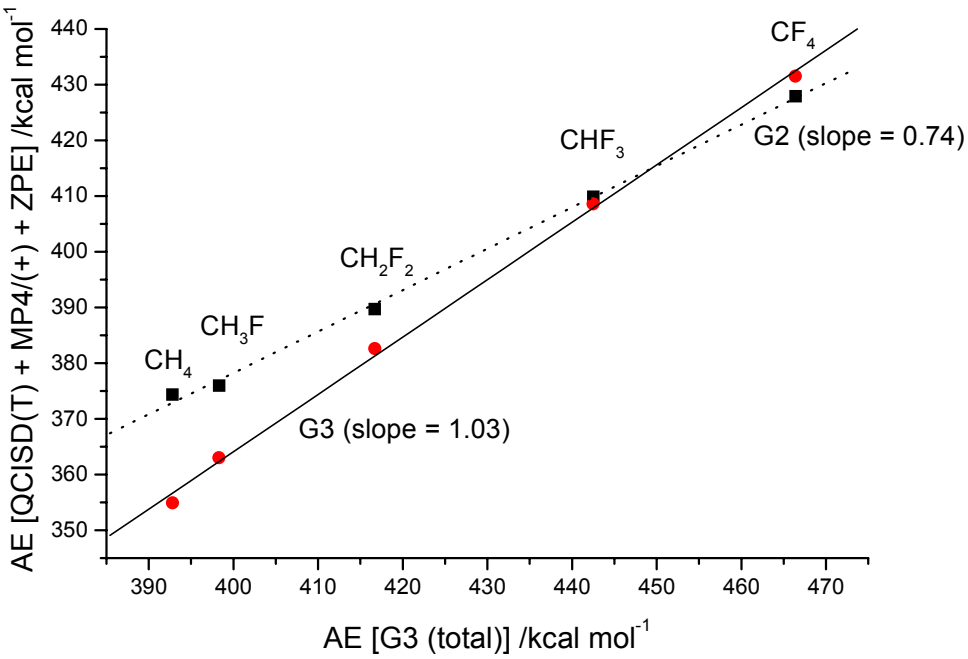

Figure 3.1 Comparison of G2 and G3 atomisation energies of fluoromethanes: Correlation of the QCISD(T) + MP4/(+) + ZPE components with the G3 total atomisation energies.

different: 1.03 for G3 and 0.74 for G2. Thus, even at this base level of theory, viz. QCISD(T) + MP4/(+), the G3 values of these scale significantly better with the number of fluorines than the corresponding G2 values. This, of course, is also reflected in the large variation in the MP4/(2*df*,*p*) corrections in the case of G2, as remarked above. This behaviour points to some imbalance in the QCI component of the G2 atomisation energies due to inadequacies of the 6-311G(*d*,*p*) basis.

Core-valence correlation increases the G3 atomisation energies by 1.1 to 1.9 kcal mol^{-1}, while spin-orbit coupling corrections change them by –0.1 to –1.6 kcal mol^{-1}, resulting in net changes of 0.3 to 1.0 kcal mol^{-1}. The G2 and G3 hlc contributions to the atomisation energies differ by 1.0 kcal mol^{-1} at most, but such that they reduce the differences due to core-valence correlation and spin-orbit coupling. Thus, effectively, the differences between the total G2 and G3 atomisation energies are almost fully reproduced by the valence calculations alone.

In summary, the shortcomings of G2 when applied to the above molecules are traced to inadequacies in the 6-311G(*d*,*p*) basis. These problems were briefly discussed by Curtiss et al. in their first paper on G3[20], although not actually quantified or analysed as in our work.

3.3.4 Heats of Formation by Complete Basis Set Coupled Cluster Calculations

HCCH, HCCF, FCCF, CCH, CCF and HCOO were selected for further study, carried out by Dr George Bacskay, whereby their heats of formation were calculated using the coupled cluster RCCSD(T) method and large basis sets, allowing the sequences of atomic and molecular energies to be extrapolated to the hypothetical complete basis set (CBS) limit. These small molecules were chosen for further study partly because the experimental heats of formation of several of these (HCCF, FCCF, CCF) are poorly characterised, with estimated errors of ~ 5 kcal mol^{-1} in the literature values. The BAC-MP4 heats of formation for HCCF, FCCF and CCH are also at significant variance with the G3 values. The formyloxyl (HCOO) radical is an unusual system in that it has several low-lying electronic states. An excellent summary of the theoretical literature on this interesting molecule is provided in a relatively recent paper by Rauk et al.[35], who also report the results of an extensive CASPT2 and multi-reference CI (MRCI) study of formyloxyl. Rauk et al. were unable to conclude unequivocally whether the ground state is $^2A_1$ or $^2B_2$, since the order of the two states (separated by no more than 2.2 kcal mol^{-1}) was found to be dependent on the method of calculation, although the broken symmetry $^2A'$ state consistently appeared to be an excited state. According to G3 the ground state is $^2A_1$, but the G3 prediction of $\Delta_f H^0_{298}$= −32.1 kcal mol^{-1} could be regarded as being equally consistent with the two conflicting literature values −37.7 ± 3.0 and −29.3 ± 1.0 kcal mol^{-1}. Consequently, formyloxyl represents an interesting and challenging application for a coupled cluster CBS study.

As indicated in **Section 3.2**, the CBS energies of the above molecules and their constituent atoms were obtained by extrapolating the sequence of valence correlated (R)CCSD(T) energies computed using the aug-cc-pV*x*Z (*x* = D, T, Q) basis sets, followed by corrections for core-valence correlation, scalar relativistic effects and zero point vibrational contributions. The latter were computed at the (RO)MP2/cc-pVTZ level of theory, except in the case of HCOO, for which the CASPT2 harmonic frequencies of Rauk et al.[35], all scaled by 0.96, were utilised. **Table 3.6** contains a representative part of the raw data, namely the total valence CCSD(T) energies of the molecules obtained in the aug-cc-pVQZ basis, along with the

Table 3.6 Computed and extrapolated CCSD(T) energies, core-valence correlation corrections, zero point vibrational energies, thermal corrections to enthalpies at 298 K and relativistic corrections (in E_h unless otherwise indicated).

	CCSD(T) aug-cc-pVQZ	CCSD(T) CBS(*mix*)	CCSD(T) CBS(l_{max})	CV corr[a]	ZPE /kcal mol^{-1}	H_{298} /kcal mol^{-1}	E_{rel}[b]
C_2H_2	–77.21098	–77.22119	–77.22182	–0.11010	16.08	18.50	–0.02956
CFCH	–176.35179	–176.37717	–176.37800	–0.17499	12.21	14.93	–0.11622
C_2F_2	–275.48392	–275.52446	–275.52548	–0.23992	8.09	11.34	–0.20291
C_2H - $^2\Sigma$	–76.48915	–76.49876	–76.49922	–0.10949	8.61	10.94	–0.02957
C_2F - $^2\Sigma$	–175.62574	–175.65050	–175.65120	–0.17442	5.12	8.04	–0.11722
HCOO - $^2A_1$	–188.87336	–188.90056	–188.90120	–0.17690	10.07	12.70	–0.11897
HCOO - $^2B_2$	–188.87499	–188.90196	–188.90261	–0.17673	11.75	14.27	–0.11885
HCOO - $^2A'$	–188.87209	–188.89898	–188.89963	–0.17679	12.03	14.60	–0.11888
H	–0.49995	–0.50000	–0.50000	0.00000		1.48	0.00000
C	–37.78660	–37.78940	–37.78950	–0.05317		1.48	–0.01501
O	–74.99484	–75.00401	–75.00424	–0.06065		1.48	–0.05230
F	–99.65266	–99.66690	–99.66710	–0.06463		1.48	–0.08699

[a] Core-valence correlation from cc-pCVQZ calculations.

[b] Scalar relativistic correction from CASPT2/G3large calculations.

corresponding extrapolated values and the core-valence correlation corrections, zero point vibrational energies, thermal corrections to the enthalpies and scalar relativistic corrections. The resulting atomisation energies at 0 K are given in **Table 3.7**. Although the effect of the extrapolation on the total molecular energies is ~ 10 - 25 kcal mol^{-1} in comparison with those obtained at the CCSD(T)/aug-cc-pVQZ level of theory, the effect on the atomisation energies is a modest 3 - 4 kcal mol^{-1}. The *mix* and l_{max} methods yield comparable results, so the CBS atomisation energies were defined as the average of the two sets of extrapolated values. Core-valence correlation further increases the atomisation energies by ~ 2 kcal mol^{-1}. The scalar relativistic corrections to the atomisation energies are generally quite small, the largest correction being just –0.7 kcal mol^{-1} (for FCCF).

The heats of formation at 0 and 298 K, that were computed from the atomisation energies are summarised in **Table 3.8** along with the corresponding G3 as well as G2 values. The agreement between the CBS and G3 results is excellent for all molecules, except HCOO, where the deviation is 2 kcal mol^{-1}. The agreement between the G2 and CBS heats of formation is generally less good, the maximum difference being 2.8 kcal mol^{-1}. In line with previous work of this quality, the CBS heats of formation are expected to be accurate to within 1 kcal mol^{-1}, although this may prove to be a conservative estimate. In the case of acetylene, where the heat of formation is known accurately, the CBS prediction is in excellent agreement with experiment. For CCH the theoretical results agree well with the experimental value of McMillen and Golden[59]. Given the high level of disagreement when the former are compared with the current JANAF value[56] of 114.0 ± 6.9 kcal mol^{-1}, we must conclude that the JANAF value is seriously in error. For CFCH, C_2F_2 and C_2F the theoretical predictions, while consistent with the available experimental estimates, are expected to be more reliable than the latter. The overall agreement between the CBS and G3 results further supports the reliability of G3 in predicting heats of formation.

For formyloxyl the $^2A_1$ state is found to be the ground state, with the $^2B_2$ and $^2A'$ states being just 1.0 and 3.1 kcal mol^{-1} higher in energy at 0 K. This ordering is largely the result of the zero point energies, since in the absence of zero point correction the $^2B_2$ would be predicted to be the ground state. The resulting heat of formation of HCOO ($^2A_1$) at 0 K, viz. –29.4 kcal mol^{-1}, is in excellent agreement with the experimental value of –28.6 ± 0.7 kcal mol^{-1}

Table 3.7 Atomisation energies[a] ΣD_0 at 0 K computed at various levels of theory (kcal mol^{-1}).

	CCSD(T) aug-cc-pVQZ	CCSD(T) CBS(*mix*)	CCSD(T) CBS(l_{max})	CCSD(T) CBS[b] + CV corr	CCSD(T) CBS[b] + CV corr + E_{rel} [c]
C_2H_2	384.02	386.85	387.12	389.34	389.04
CFCH	380.03	383.48	383.75	386.13	385.63
C_2F_2	370.85	374.91	375.18	377.75	377.06
C_2H	252.25	254.74	254.91	256.79	256.50
C_2F	245.25	248.35	248.53	250.60	250.72
HCOO - $^2A_1$	364.63	367.87	367.92	369.41	369.01
HCOO - $^2B_2$	363.98	367.07	367.12	368.51	368.02
HCOO - $^2A'$	361.34	364.92	364.97	366.40	365.94

[a] Using atomic energies corrected for spin-orbit contributions (from Ref. 20).

[b] Average of CBS(aDTQ/*mix*) and CBS(aTQ/l_{max}) results.

[c] Scalar relativistic corrections from CASPT2/G3large calculations.

Table 3.8 Computed heats of formation at 0 and 298 K (kcal mol^{-1}).

	$\Delta_f H_0^0$			$\Delta_f H_{298}^0$			
	CBS[a]	G2	G3	CBS[a]	G2	G3	Experiment
C_2H_2 - $^1\Sigma_g$	54.2	56.0	55.1	54.0	55.8	54.9	54.2±0.2 [b]
CFCH - $^1\Sigma$	24.4	25.0	24.8	24.6	25.0	24.8	30.3±5.3 [c]
C_2F_2 - $^1\Sigma_g$	–0.2	–0.7	–0.5	0.5	–0.2	0.0	–5.5±5.0 [c]
C_2H - $^2\Sigma$	135.1	137.8	135.4	135.9	138.7	136.3	135.0±1.0 [d]
							114.0±6.9 [c]
C_2F - $^2\Sigma$	107.7	109.4	108.0	109.1	110.7	109.3	110.0±5.3 [e]
HCOO - $^2A_1$	–29.4	–31.2	–30.4	–30.1	–31.9	–31.1	–29.3±0.7 [f]
							–37.7±3.0 [g]
HCOO - $^2B_2$	–28.4	–29.9	–28.6	–29.3	–30.7	–29.4	
HCOO - $^2A'$	–26.3	–27.9	–27.0	–27.1	–28.7	–27.8	

[a] Average of CBS(aDTQ/*mix*) and CBS(aTQ/l_{max}) results and including scalar relativistic corrections.

[b] Ref. 74.

[c] Ref. 56.

[d] Ref. 59.

[e] Estimated from bond dissociation energies, Ref. 3.

[f] Based on $\Delta_f H_0^0$ = 28.6 ± 0.7 kcal mol^{-1} from Ref. 72 with thermal corrections from this work.

[g] Ref. 71.

reported by Langford et al.[72], who used H (Rydberg) atom photofragment translational spectroscopy to deduce the OH bond dissociation energy of formic acid and hence heat of formation of formyloxyl. It is worth noting that using G2(MP2) in conjunction with several isodesmic reactions Yu et al.[86] deduced a value of -30.3 ± 0.7 kcal mol^{-1} for $\Delta_f H^0_{298}$ which is clearly in very good agreement with the current CBS prediction as well as experiment.

3.4 Conclusion

Using the G3 and related methodologies the heats of formation of ~ 120 C_1 and C_2 hydrofluorocarbons and oxidised hydrofluorocarbons, including a number of C_2 carbenes, were computed. For most molecules studied in this work the G3 heats of formation are in good agreement with the available experimental data, attesting to the capability and reliability of G3. Indeed, there is growing evidence, in the form of accurate ab initio values, that where the discrepancy between G3 and experiment is in excess of 2 kcal mol^{-1}, it may well signal inaccuracies in the latter. While for most molecules the G3 predictions agree well with those of the BAC-MP4 method, there are also sizeable discrepancies. Given the apparent robustness of G3 and its relative ease of application as displayed in this chapter, it is highly recommended for use in the computation of thermochemical data. The application of suitable isodesmic reaction schemes, as expected, has the potential to improve the accuracy and consistency of the predictions, especially when using approximate forms of G3, such as G3[MP2(Full)] and G3(MP4SDQ). Using this approach, the heat of formation of the hexafluoropropyl radical, an important intermediate in the high temperature reaction of H atoms with hexafluoropropene, was computed and subsequently used in the kinetic model describing the pyrolysis of 2-H-heptafluoropropane.[10] In addition to the G3 and related applications, the heats of formation of the fluoroacetylenes (HCCF and C_2F_2 as well as C_2H_2) and the C_2H, C_2F and formyloxyl radicals were computed using the coupled cluster method, with extrapolations to the CBS limit. The computed heats of formation are believed to be accurate to within 1 kcal mol^{-1}, providing useful and reliable data for HCCF, C_2F_2 and C_2F, while in the case of formyloxyl it strongly supports the experimental value of 29.3 ± 0.7 kcal mol^{-1} of Langford et al.[72] These results provide additional support for our confidence in the reliability of the G3 method.

3.5 References

1. A. Miziolek and W. Tsang, Eds., *Halon Replacements: Technology and Science*; ACS Symposium Series; Vol. 611; American Chemical Society: Washington, D.C., **1995**.
2. M. D. Nyden, G. T. Linteris, D. R. Burgess, Jr., P. R. Westmoreland, W. Tsang and M. R. Zachariah, *Flame Inhibition Chemistry and the Search for Additional Fire Fighting Chemicals* in *Evaluation of Alternative In-Flight Fire Suppressants for Full-Scale Testing in Simulated Aircraft Engine Nacelles and Dry Bays*, W. Grosshandler, R. Gann, and W. Pitts, Eds.; NIST Special Publication 861; National Institute of Standards and Technology: Washington, D.C., **1994**. p. 467.
3. M. R. Zachariah, P. R. Westmoreland, D. R. Burgess, Jr., W. Tsang and C. F. Melius, *J. Phys. Chem.*, **1996**, *100*, 8737.
4. D. R. Burgess, Jr., M. R. Zachariah, W. Tsang and P. R. Westmoreland, *Prog. Ener. Comb. Sci.*, **1995**, *21*, 453.
5. O. Sanogo, J.-L. Delfau, R. Akrich and C. Vovelle, *Combust. Sci. Technol.*, **1997**, *122*, 33.
6. R. G. Hynes, J. C. Mackie and A. R. Masri, *Combust. Flame*, **1998**, *113*, 554.
7. G. T. Linteris, D. R. Burgess, Jr., V. Babushok, M. Zachariah, W. Tsang and P. Westmoreland, *Combust. Flame*, **1998**, *113*, 164.
8. R. G. Hynes, J. C. Mackie and A. R. Masri, *J. Phys. Chem. A*, **1999**, *103*, 54.
9. R. G. Hynes, J. C. Mackie and A. R. Masri, *J. Phys. Chem. A*, **1999**, *103*, 5967.
10. R. G. Hynes, J. C. Mackie and A. R. Masri, *Proc. Combust. Inst.*, **2000**, *28*, 1557.
11. D. R. F. Burgess, Jr., M. R. Zachariah, W. Tsang and P. R. Westmoreland, *Thermochemical and Kinetic Data for Fluorocarbons*; NIST Technical Note 1412; National Institute of Standards and Technology: Washington, D.C., **1995**
12. R. J. Berry, D. R. F. Burgess, Jr., M. R. Nyden, M. R. Zachariah and M. Schwartz, *J. Phys. Chem.*, **1995**, *99*, 17145.
13. M. R. Zachariah, W. Tsang, P. R. Westmoreland and D. R. F. Burgess, Jr., *J. Phys. Chem.*, **1995**, *99*, 12512.
14. J. S. Francisco, *Chem. Phys.*, **1992**, *163*, 27.
15. J. S. Francisco, *Chem. Phys.*, **1997**, *214*, 217.

16. J. A. Montgomery, H. H. Michels and J. S. Francisco, *Chem. Phys. Lett.*, **1994**, *220*, 391.
17. J. S. Francisco, Z. Li, A. Bradley and A. E. W. Knight, *Chem. Phys. Lett.*, **1993**, *214*, 77.
18. M. H. Smith, *Honours Thesis*, School of Chemistry, University of Sydney, **1998**.
19. L. A. Curtiss, K. Raghavachari and J. A. Pople, *J. Chem. Phys.*, **1993**, *98*, 1293.
20. L. A. Curtiss, K. Raghavachari, P. C. Redfern, V. Rassolov and J. A. Pople, *J. Chem. Phys.*, **1998**, *109*, 7764.
21. L. A. Curtiss, K. Raghavachari, G. W. Trucks and J. A. Pople, *J. Chem. Phys.*, **1991**, *94*, 7221.
22. P. Ho and C. F. Melius, *J. Phys. Chem.*, **1995**, *99*, 2166.
23. C. F. Melius, *Thermochemistry of Hydrocarbon Intermediates in Combustion: Application of the BAC-MP4 Method.* in *Chemistry and Physics of Energetic Materials*, S. N. Bulusu, Ed.; Vol. 309; Kluwer Academic Publishers: Dordrecht, Germany, **1990**, p. 21.
24. C. F. Melius and J. S. Binkley, in *Twenty-First Symp. (Int.) on Combustion*; The Combustion Institiute: Pittsburgh, Pennysylvania, **1986**, p. 1953.
25. J. M. L. Martin and G. de Oliveira, *J. Chem. Phys.*, **1999**, *111*, 1843.
26. J. M. L. Martin and P. R. Taylor, *J. Chem. Phys.*, **1997**, *106*, 8620.
27. D. A. Dixon and D. Feller, *J. Phys. Chem. A*, **1998**, *102*, 8209.
28. D. A. Dixon, D. Feller and G. Sandrone, *J. Phys. Chem. A*, **1999**, *103*, 4744.
29. T. Helgaker, W. Klopper, H. Koch and J. Noga, *J. Chem. Phys.*, **1997**, *106*, 9639.
30. C. W. Bauschlicher, Jr. and A. Ricca, *J. Phys. Chem. A*, **1998**, *102*, 8044.
31. L. A. Curtiss, K. Raghavachari, P. C. Redfern and J. A. Pople, *J. Chem. Phys.*, **1997**, *106*, 1063.
32. L. A. Curtiss, P. C. Redfern, K. Raghavachari, V. Rassolov and J. A. Pople, *J. Chem. Phys.*, **1999**, *110*, 4703.
33. K. Sendt and G. B. Bacskay, *J. Chem. Phys.*, **2000**, *112*, 2227.
34. J. A. Pople, A. P. Scott, M. W. Wong and L. Radom, *Isr. J. Chem.*, **1993**, *33*, 345.
35. A. Rauk, D. Yu, P. Borowski and B. Roos, *Chem. Phys.*, **1995**, *197*, 73.
36. T. H. Dunning, Jr., *J. Chem. Phys.*, **1989**, *90*, 1007.
37. R. A. Kendall, T. H. Dunning, Jr. and R. J. Harrison, *J. Chem. Phys.*, **1992**, *96*, 6796.

38. D. E. Woon and T. H. Dunning, Jr., *J. Chem. Phys.*, **1993**, *98*, 1358.

39. D. E. Woon and T. H. Dunning, Jr., *J. Chem. Phys.*, **1995**, *103*, 4572.

40. Basis sets were obtained from the Extensible Computational Chemistry Environment Basis Set Database, Version 1.0, as developed and distributed by the Molecular Science Computing Facility, Environmental and Molecular Sciences Laboratory which is part of the Pacific Northwest Laboratory, P.O. Box 999, Richland, Washington 99352, USA, and funded by the U.S. Department of Energy. The Pacific Northwest Laboratory is a multi-program laboratory operated by Battelle Memorial Institue for the U.S. Department of Energy under contract DE-AC06-76RLO 1830. Contact David Feller or Karen Schuchardt for further information.

41. R. D. Cowan and D. C. Griffin, *J. Opt. Soc. Am.*, **1976**, *66*, 1010.

42. R. L. Martin, *J. Phys. Chem.*, **1983**, *87*, 750.

43. K. Andersson, P.-Å. Malmqvist, B. O. Roos, A. J. Sadlej and K. Wolinski, *J. Phys. Chem.*, **1990**, *94*, 5483.

44. K. Andersson, P.-Å. Malmqvist and B. O. Roos, *J. Chem. Phys.*, **1992**, *96*, 1218.

45. B. O. Roos, P. R. Taylor and P. E. M. Siegbahn, *Chem. Phys.*, **1980**, *48*, 157.

46. B. O. Roos, in *Ab initio Methods in Quantum Chemistry II*, K. P. Lawley, Ed.; *Advances in Chemical Physics*, I. Prigogine and S. A. Rice, Eds.; Vol. LXIX; J. Wiley & Sons Ltd.: Chichester, UK, **1987**, p. 399.

47. M. J. Frisch, G. W. Trucks, H. B. Schlegel, G. E. Scuseria, M. A. Robb, J. R. Cheeseman, V. G. Zakrzewski, J. A. Montgomery, R. E. Stratmann, J. C. Burant, S. Dapprich, J. M. Millam, A. D. Daniels, K. N. Kudin, M. C. Strain, O. Farkas, J. Tomasi, V. Barone, M. Cossi, R. Cammi, B. Mennucci, C. Pomelli, C. Adamo, S. Clifford, J. Ochterski, G. A. Petersson, P. Y. Ayala, Q. Cui, K. Morokuma, D. K. Malik, A. D. Rabuk, K. Raghavachari, J. B. Foresman, J. Cioslowski, J. V. Ortiz, B. B. Stefanov, G. Lui, A. Liashenko, P. Piskorz, I. Komaromi, R. Gomperts, R. L. Martin, D. J. Fox, T. Keith, M. A. Al-Laham, C. Y. Peng, A. Nanayakkara, C. Gonzalez, M. Challacombe, P. M. W. Gill, B. G. Johnson, W. Chen, M. W. Wong, J. L. Andres, M. Head-Gordon, E. S. Replogle and J. A. Pople, Gaussian 98 Revision A.7, Gaussian, Inc.: Pittsburgh, PA, **1998**,

48. C. Hampel, K. A. Peterson and H.-J. Werner, *Chem. Phys. Lett.*, **1992**, *190*, 1.

49. P. J. Knowles, C. Hampel and H.-J. Werner, *J. Chem. Phys.*, **1993**, *99*, 5219.

50. MOLPRO 96.3 is a package of ab initio programs written by H.-J. Werner and P. J. Knowles with contributions from J. Almlöf, R. D. Amos, M. J. O. Degan, S. T. Elbert, C. Hampel, W. Meyer, K. Peterson, R. Pitzer, A. J. Stone, P. R. Taylor, R. Lindh, M. E. Mura, T. Thorsteinsson.

51. CADPAC 6.0: The Cambridge Analytical Derivatives Package Issue 6, Cambridge, 1995. A suite of quantum chemistry programs developed by R. D. Amos, with contributions from I. L. Alberts, J. S. Andrews, S. M. Colwell, N. C. Handy, D. Jayatilaka, P. J. Knowles, R. Kobayashi, K. E. Laidig, G. Laming, A. M. Lee, P. E. Maslen, C. W. Murray, J. E. Rice, E. D. Simandiras, A. J. Stone, M.-D. Su, D. J. Tozer.

52. ACES II is a program product of the Quantum Theory Project, University of Florida. Authors: J. F. Stanton, J. Gauss, J. D. Watts, M. Nooijen, N. Oliphant, S. A. Perera, P. G. Szalay, W. J. Lauderdale, S. R. Gwaltney, S. Beck, A. Balková, D. E. Bernholdt, K.-K. Baeck, P. Rozyczko, H. Sekino, C. Hober, R. J. Bartlett. Integral packages included are VMOL (J. Almlöf, P. R. Taylor); VPROPS (P. Taylor); ABACUS (T. Helgekar, H. J. Aa. Jensen, P. Jørgensen, J. Olsen, P. R. Taylor).

53. K. Andersson, M. R. A. Blomberg, M. P. Fülscher, G. Karlström, R. Lindh, P.-Å. Malmqvist, P. Neogrády, J. Olsen, B. O. Roos, A. J. Sadlej, M. Schültz, L. Seijo, L. Serrano-Andrés, P. E. M. Siegbahn and P.-O. Widmark, MOLCAS Version 4, Lund University: Lund, Sweden, **1997**,

54. R. J. Berry, C. J. Ehlers, D. R. Burgess, Jr., M. R. Zachariah, M. R. Nyden and M. Schwartz, *J. Mol. Struct. (Theochem)*, **1998**, *422*, 89.

55. C. W. Bauschlicher, Jr. and A. Ricca, *Chem. Phys. Lett.*, **1999**, *315*, 449.

56. D. R. Stull and H. Prophet, JANAF Thermochemical Tables, *Natl. Stand. Ref. Data Ser. (U.S. Natl. Bur. Stand.)*, **1971**, *37*, 1.

57. V. P. Kolesov, *Russ. Chem. Rev.*, **1978**, *47*, 599.

58. J. Berkowitz, G. B. Ellison and D. Gutman, *J. Phys. Chem.*, **1994**, *98*, 2744.

59. D. F. McMillen and D. M. Golden, *Annu. Rev. Phys. Chem.*, **1982**, *33*, 493.

60. L. Gurvich, I. V. Veyts and C. B. Alcock, Eds., *Thermodynamic Properties of Individual Substances*; Hemisphere Publishing Corp.: Bristol, PA, **1991**.

61. R. K. Lengel and R. N. Zare, *J. Am. Chem. Soc.*, **1978**, *100*, 7495.

62. J. C. Poutsma, J. A. Paulino and R. R. Squires, *J. Phys. Chem.*, **1997**, *101*, 5327.

63. A. S. Rodgers, *ACS Symp. Ser.*, **1978**, *66*, 296.

64. D. L. Baulch, R. A. Cox, R. F. Hampson, Jr., J. A. Kerr, J. Troe and R. T. Watson, *J. Phys. Chem. Ref. Data*, **1984**, *13*, 1259.
65. W. F. Schneider and T. J. Wallington, *J. Phys. Chem.*, **1994**, *98*, 7448.
66. V. D. Knyazev, Á. Bencsura and I. R. Slagle, *J. Phys. Chem.*, **1997**, *101*, 849.
67. S. S. Chen, R. C. Wilhoit and B. J. Zwolinski, *J. Phys. Chem. Ref. Data*, **1977**, *6*, 105.
68. L. Batt and R. Walsh, *Int. J. Chem. Kinet.*, **1982**, *14*, 933.
69. L. Batt, J. P. Burrows and G. N. Robinson, *Chem. Phys. Lett.*, **1981**, *78*, 467.
70. V. D. Knyazev and I. R. Slagle, *J. Phys. Chem.*, **1998**, *102*, 1770.
71. J. L. Holmes, F. P. Lossing and P. M. Mayer, *J. Am. Chem. Soc.*, **1991**, *113*, 9723.
72. S. R. Langford, A. D. Batten, M. Kono and M. N. R. Ashfold, *J. Chem. Soc., Faraday Trans.*, **1997**, 3757.
73. S. W. Benson, *Thermochemical Kinetics*; John Wiley: New York, NY, **1976**.
74. W. Tsang and R. F. Hampson, *J. Phys. Chem. Ref. Data*, **1986**, *15*, 1087.
75. Y.-R. Luo and S. W. Benson, *J. Phys. Chem. A*, **1997**, *101*, 3042.
76. S. S. Chen, A. S. Rodgers, J. Chao, R. C. Wilhoit and B. J. Zwolinski, *J. Phys. Chem. Ref. Data*, **1975**, *4*, 441.
77. J. R. Lacher and H. A. Skinner, *J. Chem. Soc. A*, **1968**, 1034.
78. K. Miyokawa, S. Ozaki and T. Yano, *Bull. Chem. Soc. Japan*, **1996**, *69*, 869.
79. J. P. Martin and G. Paraskevopoulos, *Can. J. Chem.*, **1983**, *61*, 861.
80. J. P. Stadelmann and J. Vogt, *Int. J. Mass Spectrom. Ion Phys.*, **1980**, *35*, 83.
81. W. M. D. Bryant, *J. Polym. Sci.*, **1962**, *56*, 277.
82. R. L. Nuttall, A. H. Laufer and M. V. Kilday, *J. Chem. Thermodyn.*, **1971**, *3*, 167.
83. S. Furuyama, D. M. Golden and S. W. Benson, *J. Chem. Thermodyn.*, **1969**, *1*, 363.
84. W. Tsang, *Heats of Formation of Organic Radicals by Kinetic Methods*. in *Energetics of Free Radicals*, A. Greenberg and J. F. Liebman, Eds.; Chapman and Hall: New York, **1996**.
85. T. S. Papina, V. P. Kolesov and Y. G. Golovanova, *Russ. J. Phys. Chem.*, **1987**, *61*, 1168.
86. D. Yu, A. Rauk and D. A. Armstrong, *J. Chem. Soc. Perkin Trans. 2*, **1994**, 2207.

Chapter 4

The Role of Phosphorus Compounds in the H + OH Recombination Reaction

4.1 Introduction

The recombination reaction of H and OH radicals to form water is a key exothermic reaction in a range of combustion processes, particularly in flames and in the combustion of hydrogen fuel in the presence of oxygen. As pointed out by Twarowski,[1-4] this last reaction is of special importance in supersonic aircraft engines, where recombination must be as fast as possible in order to maximise engine efficiency. Twarowski carried out a number of experimental studies of the H + OH recombination reaction in the presence of phosphine and concluded the reaction is catalysed by the oxidation products of PH_3, namely PO_2, HOPO and $HOPO_2$. Two possible reaction sequences were proposed to account for this catalysis:

$$H + PO_2 \ (+ M) \rightarrow HOPO \ (+ M) \qquad (4.1.a)$$

$$H + HOPO \rightarrow H_2 + PO_2 \qquad (4.1.b)$$

$$OH + H_2 \rightarrow H_2O + H \qquad (4.1.c)$$

and

$$OH + PO_2 \ (+ M) \rightarrow HOPO_2 \ (+ M) \qquad (4.2.a)$$

$$H + HOPO_2 \rightarrow H_2O + PO_2 \qquad (4.2.b)$$

The net result of both proposed catalytic cycles is the recombination reaction of interest:

$$H + OH \rightarrow H_2O \qquad (4.3)$$

The full reaction model put forward by Twarowski[3] consists of 175 reactions involving 24 species, 17 of which contain P atoms. A serious limitation of the model has been the lack of reliable rate and thermochemical data; the rate coefficients of 162 of these reactions were estimated by Benson's rules.[5]

This chapter describes the resolution of this problem through the computation of accurate theoretical heats of formation for the phosphorus containing molecular species in Twarowski's model[3] and the subsequent re-evaluation of the rate coefficients for the critical reactions that make up the proposed catalytic cycles (4.1) and (4.2) given above. The

thermochemical calculations were performed using Gaussian-2 (G2)[6], Gaussian-3 (G3)[7], and Gaussian-3X (G3X)[8] theories as well as other ab initio quantum chemical methods. The applicability and reliability of the Gaussian methods to phosphorus containing molecules such as PO_2, HOPO and $HOPO_2$ are tested by comparing the results obtained with those from other studies using alternative methods such as the coupled cluster method.

Given the documented catalytic properties of these simple phosphorus containing molecules it is highly likely that these, as well as various organic derivatives, would be efficient fire retardants. The work reported here was motivated to a large extent by this idea and represents the initial steps of a study that focuses on the investigation of the flame suppression mechanisms by organophosphorus compounds, using both computational and experimental techniques. Achieving an improved level of understanding of the mechanisms of flame suppression by these species has the potential to provide guidance for the development of efficient and environmentally friendly fire retardants. Indeed, it has been shown recently that dimethyl methylphosphonate (DMMP) or trimethylphosphate (TMP) when added to flames retard the flame velocity with an efficiency comparable with that of CF_3Br.[9] This agent, prior to the Montreal protocol, was in widespread use as a fire suppressant especially for aircraft engines and in military applications. A further potential bonus of phosphorus compounds is that they can be added to polymer blends whereby they can act as condensed phase inhibitors promoting the formation of chars to inhibit the burning of plastics; upon vaporisation they also act as vapour phase inhibitors.[10]

A further recent interest in phosphorus flame chemistry has arisen from the need to destroy toxic chemical waste and chemical warfare agents such as sarin.[11] Recent investigations[12,13] of incineration of these agents have involved a study of the combustion of organophosphorus compounds, including DMMP and TMP as models for sarin. Korobeinichev et al.[12] measured the concentrations of PO, PO_2, HOPO and $HOPO_2$ in the burnt gases of premixed low pressure flames of H_2 / O_2 / Ar doped with DMMP. Using kinetic modelling, they optimised rate coefficients for key phosphorus flame gas reactions to their measured profiles. They concluded that organophosphorus additives can actually promote low pressure H_2 / O_2 / Ar flames. In a subsequent study[13] they found, however, that TMP inhibits atmospheric CH_4 / O_2 / Ar and H_2 / O_2 / Ar flames. Macdonald et al.[14] found that the inhibiting ability of DMMP in non-premixed CH_4 / O_2 / Ar flames diminishes with increasing adiabatic flame temperature. The ability to model these inhibition and promotion characteristics of organophosphorus

additives to flames is very dependent on the availability of reliable rate coefficients for key phosphorus flame reactions over a wide range of pressures and temperatures.

4.2 Theory and Computational Methods

The heats of formations of approximately 30 molecules were obtained by quantum chemical computations of energies and enthalpies, utilising the Gaussian-*n* methods (G2, G3 and G3X) of Pople and co-workers[6-8]. In these approaches, as described in **Section 2.7.2**, the energies of the atomic and molecular species of interest are obtained via quadratic configuration interaction (QCISD(T)) calculations in small valence triple and double zeta + polarisation functions bases (6-311G(*d*,*p*) and 6-31G(*d*)) respectively, which are then corrected by MP4, MP2 and SCF estimates of the energy changes with systematic enlargement of the basis sets and by empirical higher level corrections. Open shell systems are treated by the unrestricted versions of the above approaches. The heats of formation at 298 K are obtained from the computed G2, G3 and G3X values of the atomisation energies (at 0 K) in conjunction with experimental heats of formation of the elements in their atomic states and thermal corrections, as discussed in detail by Curtiss et al.[15] For some radical species (particularly PO), a variant of the G3(RAD) approach of Radom and co-workers[16-18] was also used, where the unrestricted Hartree-Fock (UHF) and Møller-Plesset (UMP) computations are replaced by their restricted open shell ROHF and ROMP analogues, while the (unrestricted) quadratic CI (QCISD(T)) method[19] implicit in G2 and G3 is replaced by the restricted singles and doubles coupled cluster method with perturbative correction for triples (RCCSD(T))[20,21].

The rates of the reactions in Twarowski's reaction sequence were determined using transition state theory (TST)[22] (**Section 2.9.1**). In the case of reactions with well defined transition states (that is, first order saddle points) the G3 method was used, whereby the saddle points were located at the appropriate SCF and MP2 levels of theory. Using the appropriate energies and partition functions, the limiting high pressure rate coefficient k_∞ at any given temperature T is then obtained from:

$$k_\infty(T) = \frac{k_B T}{h} \frac{q^\ddagger}{\prod_i q_i} \exp\left(\frac{-\Delta E^\ddagger}{k_B T}\right) \tag{4.4}$$

where $\Delta E^{\ddagger}$ is the critical energy of reaction, k_B is the Boltzmann constant, h is Planck's constant, $q^{\ddagger}$ is the partition function of the transition state and $\{q_i\}$ are the partition functions of the reactants. The latter are obtained readily from the computed rotational constants and vibrational frequencies, using the standard formulas of statistical mechanics, with the rigid rotor and harmonic vibrations approximations as described in **Section 2.8.1**.[23]

The computed rate coefficients, over a range of temperatures, could then be fitted to the standard Arrhenius form

$$k_{\infty}(T) = A\exp\left(-\frac{E_a}{k_B T}\right) \tag{4.5}$$

(where E_a is the activation energy and A is the Arrhenius pre-exponential factor). Rate coefficients were generated at 1000, 1250, 1500, 1750 and 2000 K. These temperatures gave a sensible range over which rate coefficients could be fitted and spans the temperatures studied by Twarowski[1-4] and Korobeinichev[13]. Alternatively, the rate coefficients could be fitted to a modified Arrhenius equation:

$$k_{\infty}(T) = AT^{n}\exp\left(-\frac{E_a}{k_B T}\right) \tag{4.6}$$

As a number of the reactions studied are barrierless recombinations, with no saddle-point to define the transition state, variational transition state theory (VTST, **Section 2.9.2**)[24-26] was used to calculate the appropriate rate coefficients. These calculations were carried out by evaluating the rate coefficients k_{dis} of the (reverse) dissociation reactions along the intrinsic reaction coordinate and thus locating the geometry (at a given temperature) where the rate coefficient is a minimum[27,28]. As such transition states generally correspond to molecules near a bond dissociation limit, the VTST geometries were located via complete active space SCF (CASSCF) calculations[29,30], using Dunning's correlation consistent cc-pVDZ basis sets[31,32]. The active spaces in these CASSCF calculations (on H + PO_2 and OH + PO_2 transition states) typically correspond to 8 - 18 active electrons in 6 - 13 active orbitals. The critical energy of the dissociation reaction is then obtained by correcting the dissociation energy obtained by G3 or other high level theory, by the computed energy difference between the dissociated system

and the transition state that had been determined at the CASSCF/cc-pVDZ level of theory. In the case of reaction (4.2.a) the energy difference was recalculated using complete active space second order perturbation (CASPT2)[33,34] theory in conjunction with Dunning's cc-pVTZ basis. (Use of a higher level of theory and larger basis set, as exemplified by the CASPT2/cc-pVTZ approach, is expected to yield more reliable energies than the lower level CASSCF/cc-pVDZ method that was employed for the determination of geometries and frequencies.) The rate coefficient k_{ass} for the association reaction is then obtained from

$$\frac{k_{\text{ass}}}{k_{\text{dis}}} = K_c \tag{4.7}$$

where K_c is the equilibrium constant for the association (recombination) reaction; it is readily calculated at any temperature from the appropriate Gibbs free energy of reaction, $\Delta_r G^0$.

The pressure dependence of the dissociation rate coefficients in a bath gas of N_2 was determined via the RRKM model (**Section 2.9.3**) in the weak collision approximation, using an average collisional energy transfer parameter, α, of 400 cm^{-1}, at pressures ranging from 1 to 10^4 torr and temperatures 1000 - 2000 K. In order to obtain the rate coefficients in a convenient form for use by combustion modellers the RRKM rate coefficients were then expressed in terms of a Troe fit[35], as defined by the equations

$$\frac{k}{k_\infty} = \left(\frac{k_0/k_\infty}{1+k_0/k_\infty} \right) F\left(k_0/k_\infty\right) \tag{4.8}$$

$$\log F\left(k_0/k_\infty\right) = \frac{\log F_{cent}}{1+\left[\frac{\log\left(k_0/k_\infty\right)+c}{N-d\left(\log\left(k_0/k_\infty\right)+c\right)} \right]^2} \tag{4.9}$$

where

$$c = -0.4 - 0.67\log\left(F_{cent}\right) \tag{4.10}$$

$$N = 0.75 - 1.27\log\left(F_{cent}\right) \tag{4.11}$$

$$d = 0.14 \tag{4.12}$$

and

$$F_{cent} = (1-a)\exp\left(-\frac{T}{T^{***}}\right) + a\exp\left(-\frac{T}{T^{*}}\right) + \exp\left(-\frac{T^{**}}{T}\right) \qquad (4.13)$$

k_0 is the pseudo-first order limiting low pressure rate coefficient, that is, equal to the bimolecular rate coefficient multiplied by the bath gas concentration. k_∞ is the high pressure rate coefficient calculated by transition state theory. a, T^*, T^{**}, T^{***} are fitted parameters expressing the variation with temperature of the pressure-dependant rate coefficients.

All G2, G3 and G3X calculations were carried out using the Gaussian98 programs[36]. The ROMP and RCCSD(T) computations were performed using ACESII[37], while DALTON[38] and MOLCAS4[39] were used for the CASSCF geometry optimisations and CASPT2 energy calculations respectively. The CHEMRATE[40] programs were employed for the RRKM calculations. All computations were performed on DEC alpha 600/5/333 and COMPAQ XP1000/500 workstations of the Theoretical Chemistry group at the University of Sydney.

4.3 Results and Discussion

4.3.1 G2, G3, and G3X Thermochemistry

The energies and heats of formation of the 24 species involved in Twarowski's reaction schemes[1-4], calculated using the G2, G3 and G3X methods, are reported in **Table 4.1**. As will be discussed later, the standard G3 and G3X results for PO (based on spin unrestricted calculations) are regarded as unreliable. We recommend instead the G3(RAD) and G3X(RAD) values, which are also listed in **Table 4.1**. Where available, experimental and/or other theoretical heats of formation[41-45] are also listed for comparison. The computed equilibrium geometries, rotational constants and vibrational frequencies are listed in **Appendix 2.1**. A number of species, such as P_2O_2, have several geometric isomers as well as low lying excited electronic states, giving rise to potential uncertainties as to the nature of the ground electronic state. In such cases all possible isomers as well as a range of electronic

Table 4.1 Total energies and heats of formation computed at the G2, G3 and G3X levels of theory.

Species	E_0(0 K) /E_h			$\Delta_f H^0_{298}$/kcal mol^{-1}			
	G2	G3	G3X	G2	G3	G3X	Literature [a]
H	–0.50000	–0.49959	–0.50097				52.1030 ± 0.0014 [b]
O	–74.98203	–75.02957	–75.03224				59.553 ± 0.024 [b]
P	–340.81821	–341.11502	–341.11699				75.62 ± 0.24 [b]
H_2 - $^1\Sigma_g$ ($D_{\infty h}$)	–1.16636	–1.16738	–1.16721	–1.1	–0.5	–0.4	0.0
O_2 - $^3\Sigma_g$ ($D_{\infty h}$)	–150.14821	–150.24821	–150.25248	2.4	1.1	0.0	0.0
P_2 - $^1\Sigma_g$ ($D_{\infty h}$)	–681.81931	–682.41600	–682.41907	35.6	35.5	34.3	34.3 ± 0.5 [b]
P_4 - $^1A_1$ (T_d)	–1363.71963	–1364.91465	–1364.92008	19.6	18.2	16.2	14.1 ± 0.05 [b]
OH - $^2\Pi$ ($C_{\infty v}$)	–75.64391	–75.69490	–75.69607	9.1	8.4	8.4	9.32 ± 0.29 [b]
							8.83 ± 0.09 [c]
H_2O - $^1A_1$ (C_{2v})	–76.33205	–76.38204	–76.38323	–58.1	–57.5	–57.5	–57.798 ± 0.010 [b]
HO_2 - $^2A'$ (C_s)	–150.72792	–150.82689	–150.82950	3.3	3.3	3.2	0.5 ± 2.0 [b]
PH - $^3\Sigma$ ($C_{\infty v}$)	–341.42844	–341.73033	–341.73131	57.7	56.0	55.7	*60.6 ± 8.0* [d]
PH_2 - $^2B_1$ (C_{2v})	–342.04913	–342.34974	–342.35096	32.9	32.6	32.2	*26 ± 23* [e]
PH_3 - $^1A'$ (C_s)	–342.67900	–342.97851	–342.98004	2.0	3.1	2.4	1.3 ± 0.4 [b]
PO - $^2\Sigma$ ($C_{\infty v}$)	–416.02430	–416.37332	–416.38022	–6.4	–7.6	–10.8	–5.6 ± 1.0 [b]
					–7.1 [f]	–7.7 [f]	–6.8 ± 1.9 [g]
							–7.8 [h]
PO_2 - $^2A_1$ (C_{2v})	–491.19500	–491.59301	–491.59877	–66.4	–67.5	–69.2	–66.6 ± 2.6 [g]
					–69.1 [f]	–70.2 [f]	*–70.3* [h]
PO_3 - $^2A_2''$ (D_{3h})	–566.32361	–566.77130	–566.78381	–100.1	–101.7	–106.3	*–107.5* [h]
PO_3 - $^2B_2$ (C_{2v})		–566.77102			–101.4		
PPO - $^1\Sigma$ ($C_{\infty v}$)	–756.94248	–757.58837	–757.59417	5.8	5.5	3.3	
P_2O - $^1A_1$ (C_{2v})	–756.93141	–757.57613		12.7	13.1		

Table 4.1 continued

Species	E_0(0 K) /E_h	$\Delta_f H^0_{298}$/kcal mol^{-1}					
	G2	G3	G3X	G2	G3	G3X	Literature [a]
P_2O_2 - planar - ^1A_g (D_{2h})	–832.12205	–832.81642	–832.82515	–59.8	–59.8	–63.4	
P_2O_2 - butterfly – ^1A (C_1)	–832.10890	–832.80295		–51.8	–51.6		
P_2O_2 - *cis* - $^3A''$ (C_s)	–832.10775	–832.80583		–50.7	–53.0		
P_2O_2 - *trans* - $^3A''$ (C_s)	–832.10457	–832.80259		–48.5	–50.8		
P_2O_3 - gauche - ^1A (C_2)	–907.34228	–908.08682	–908.09849	–150.3	–151.1	–155.3	
HPO - $^1A'$ (C_s)	–416.62879	–416.97614	–416.98030	–21.1	–20.5	–22.0	*–22.6* [h]
POH - $^3A''$ (C_s)	–416.59568	–416.95018		–0.2	–4.2		
HPOH - *trans* - $^2A''$ (C_s)	–417.21175	–417.56145	–417.56447	–22.2	–22.5	–23.4	
HPOH - *cis* - $^2A''$ (C_s)	–417.21070	–417.56045		–21.4	–21.7		
H_3PO - $^1A_1$ (C_{3v})	–417.83301	–418.18166	–418.18604	–47.9	–46.9	–48.6	
H_2POH - *trans* - $^1A'$ (C_s)	–417.83334	–418.18206	–418.18558	–47.8	–46.8	–48.0	
H_2POH - *cis* - $^1A'$ (C_s)	–417.83292	–418.18168		–47.6	–46.7		
HOPO - *cis* - $^1A'$ (C_s)	–491.84249	–492.23992	–492.24608	–108.1	–108.3	–110.3	–110.6 ± 3 [i] *–112.4* [h]
HOPO - *trans* - $^1A'$ (C_s)	–491.83848	–492.23577		–105.6	–105.7		
HPO_2 - $^1A_1$ (C_{2v})	–491.82318	–492.22032		–96.1	–96.1		
$HOPO_2$ - planar - $^1A'$ (C_s)	–567.00756	–567.45385	–567.46232	–164.7	–164.8	–167.4	–168.8 ± 4 [i] *–171.4* [h]

[a] Experimental values unless otherwise indicated by italics and footnotes.

[b] Ref. 41.

[c] Ref. 42.

[d] Semiempirical estimate, Ref. 41.

[e] Estimate, Ref. 41.

[f] Computed by G3(RAD) and G3X(RAD) type procedures.

[g] Ref. 43.

[h] RCCSD(T)/CBS computations, Ref. 44.

[i] Ref. 45.

states were explicitly considered in the calculations. The results in **Table 4.1** and **Appendix 2.1** pertain to the electronic ground states thus located for the lowest energy isomers.

Comparison with the available experimental data suggests that for most systems the difference between theory and experiment is ~ 2 kcal mol^{-1} or less. For some molecules, however, notably P_4 and $HOPO_2$, the difference between the G3 result and experiment can be up to ~ 4 kcal mol^{-1}. The G3X results, as expected, are generally superior to those obtained by G3. However, quite large discrepancies are noted when G3 and G3X heats of formations are compared with those calculated by Bauschlicher.[44] The latter were obtained by extrapolation of (R)CCSD(T) energies, obtained with the cc-pV*x*Z (for P and H) and aug-cc-pV*x*Z (for O) basis sets (*x* = T, Q, 5), to the complete basis set (CBS) limit, and include core-valence correlation, scalar relativistic and spin-orbit corrections. Given the discrepancies between the G3X and Bauschlicher's CBS heats of formation, Bauschlicher's recommended values for PO_2, HOPO and $HOPO_2$ have been used in the computation of rate coefficients and reaction enthalpies. The demonstrated weakness of the Gaussian-*n* approach for some of these systems is further analysed in the next section.

HOPO and $HOPO_2$, which are particularly important species in Twarowski's reaction scheme[1-4], possess low frequency torsional modes. Treating these as harmonic oscillators in the calculation of partition functions might be expected to affect the accuracy of the computed thermal contributions. The reliability of the harmonic model for these cases was checked by computing full (360°) torsional potentials by a series of MP2/6-31G(*d*) calculations (at 5 - 10 degree intervals) and hence the corresponding energy eigenvalue spectra and partition functions. For HOPO the torsional partition function was found to be 5.05 at 2000 K (the highest temperature of interest), indicating that effectively only the fifth torsional energy level was available to the molecule. The energy of this level was 6.08 kcal mol^{-1} above the minimum in the potential, which corresponds to being 4.42 kcal mol^{-1} below the height of the barrier to rotation. Consequently, no rotation would be expected to occur in this molecule. Similarly, for $HOPO_2$ the torsional partition function at 2000 K was computed to be 7.74 indicating occupancy of the seventh torsional level, which has an energy of 4.45 kcal mol^{-1}, and which is again significantly lower than the rotational barrier of 7.68 kcal mol^{-1}. The hindered rotor correction therefore would result in insignificant changes in the molecular partition functions. Thus use of the all-vibration model for the computation of thermal corrections has been validated.

The reaction enthalpies for the 175 reactions that make up Twarowski's scheme[1-4], as obtained from the G3 and G3X heats of formation, are listed in **Appendix 2.2**.

4.3.2 Reliability of G3, G3X and Related Methods

As noted above, our G3 heats of formation for a number of phosphorus containing molecules, especially P_4, PO_2, PO_3 and $HOPO_2$, differ by up to ~ 6 kcal mol^{-1} from experiment or the computed values of Bauschlicher[44]. Errors of this magnitude were found for several other non-hydrogen systems such as SF_6 and PF_5,[46] although these problems appear to have been overcome by the recent introduction of G3X[8]. Consequently, testing G3X on some of the problem molecules encountered in this work is particularly relevant.

G3X differs from G3 in three major respects: in the calculations of geometries and vibrational frequencies (at B3LYP/6-31G(2*df*,*p*) level in G3X) and in the inclusion of an SCF energy correction for basis set expansion (to G3XLarge in the G3X method). In addition the higher-level correction parameters have been revised.[8] As a small modification to G3X, it is proposed that the G3XLarge basis set expansion correction be applied at the MP2(Full) level, (equivalently the MP2(Full)/G3Large computation in G3 theory is replaced with MP2(Full)/G3Xlarge). This modified G3X technique is denoted G3X2.

The computed G3X and G3X2 heats of formation are given in **Table 4.2**, where they are also compared with the G3 values and Bauschlicher's CBS results[44]. As the latter contain scalar relativistic corrections, the same corrections are applied to the G3, G3X and G3X2 results, so as to make the comparisons more meaningful. As discussed below, in the case of PO the G3(RAD), G3X(RAD) and G3X2(RAD) results are preferred over their standard (unrestricted) counterparts. With that proviso, it is noted that going from G3 to G3X and to G3X2 does yield significant improvements. In the case of PO_3 much of the improvement can be traced to the lower zero point energies at the B3LYP level in comparison with the SCF values which are used in G3. The (scaled) UB3LYP/6-31G(2*df*, *p*) and UHF/6-31G(*d*) zero point energies of PO_3 are 5.65 and 8.20 kcal mol^{-1} respectively; the 2.6 kcal mol^{-1} difference is thus responsible for 55% of the improvement in the heat of formation of PO_3 that occurs

Table 4.2 Phosphorus oxides and acids: Comparison of computed heats of formation ($\Delta_f H^0_{298}$ /kcal mol^{-1})[a].

	G3	G3X	G3X2	RCCSD(T)/CBS[b]
PO	–7.3 (–6.8)[c]	–10.5 (–7.4)[c]	–11.9 (–8.8)[c]	–7.8
PO_2	–66.7 (–69.1)[c]	–68.4 (–70.2)[c]	–70.6 (–72.2)[c]	–70.3
PO_3	–100.5	–105.2	–108.3	–107.5
HPO	–19.9	–21.6	–23.6	–22.6
HOPO	–107.5	–109.5	–111.6	–112.4
$HOPO_2$	–163.2	–165.8	–168.8	–171.4

[a] All heats of formation corrected for scalar relativistic effects, as in Ref. 44.

[b] Ref. 44.

[c] Computed by G3(RAD), G3X(RAD) and G3X2(RAD) type procedures.

when G3 is replaced by G3X. (In the other systems the differences between the G3X and G3 zero point energies are less than 0.2 kcal mol^{-1}.) Significant further improvements are obtained, however, with the introduction of the G3X2 method. The heats of formation for PO_2, PO_3, HPO and HOPO are lowered by a further 2 - 3 kcal mol^{-1} so that the G3X2 values are generally within 1 kcal mol^{-1} of Bauschlicher's CBS results[44]. In the case of $HOPO_2$, where Bauschlicher judges the reliability of the CBS heat of formation as ± 2 kcal mol^{-1}, the discrepancy between the G3X2 and the CBS values at 2.6 kcal mol^{-1} can still be regarded as acceptable.

4.3.2.1 PO and G3(RAD) Procedures

The problem with PO, where the improvements in the level of theory appear to destroy the initial agreement between G3 and CBS, was traced to the presence of spin contamination in the UHF based calculations that leads to a quite bizarre bond distance dependence. **Figure 4.1** shows the distance dependence of the UHF, UMP2, UMP4 and UQCISD(T) energies, all computed with the 6-31G(*d*) basis, along with the UMP2/G3Large energy. In the region of about 1.47 - 1.53 Å the UHF energy appears to flatten out, remaining too low, due to a noticeable increase in spin contamination, as indicated by the expectation value of the total

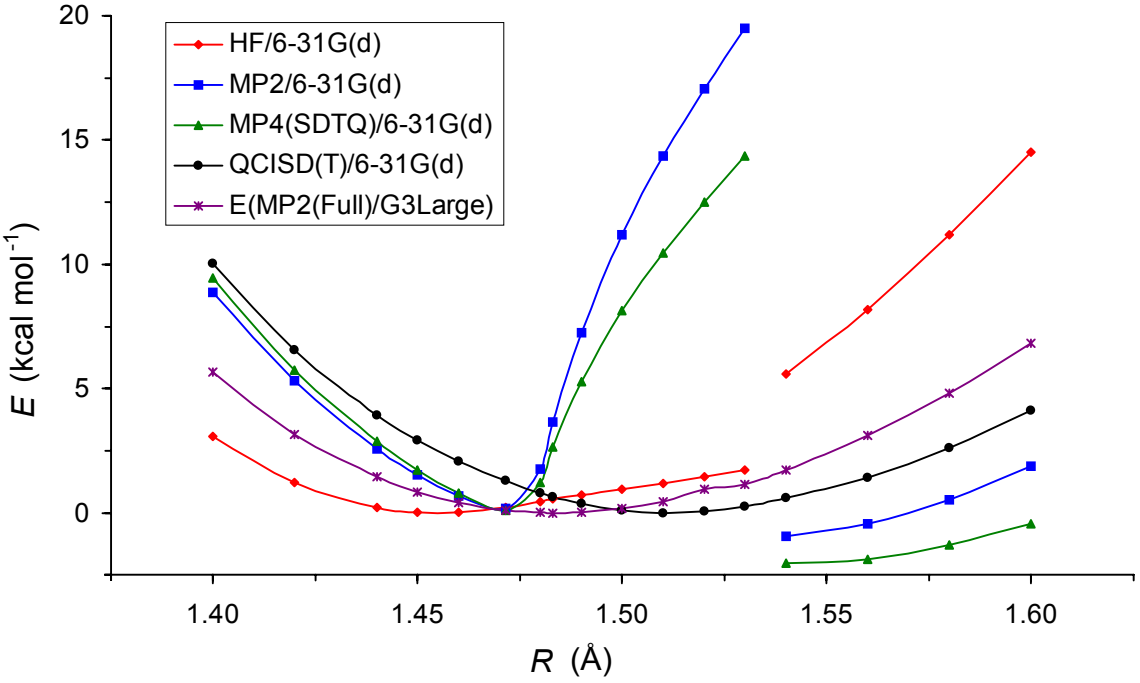

Figure 4.1 Potential energy curves of PO obtained at unrestricted Hartree-Fock, MP2, MP4 and QCISD(T) levels of theory (relative to respective equilibrium values).

spin operator $\hat{S}^2$ which increases from 0.76 to 1.16 over the above range of distances. There appears to be a discontinuity at a distance slightly greater than 1.53 Å, so that at 1.54 Å the value of $\langle \hat{S}^2 \rangle$ has fallen to 0.77 with a corresponding jump in the energy. The UMP2 and UMP4 energies, with much larger discontinuities, further amplify the un-physical behaviour of the UHF wave function and energy. The UQCISD(T) energy shows normal behaviour, demonstrating the robustness of the underlying coupled cluster expansion of the wave function to spin contamination in the reference state. Interestingly, when larger, extended basis sets are used, for example G3Large, there is only a small blip in the MP2 energy instead of the ~ 20 kcal mol^{-1} jump shown by the MP2/6-31G(*d*) energies.

The UHF and UMP2 energies are contrasted with the restricted open shell ROHF and ROMP2 energies in **Figure 4.2**. The latter behave in a perfectly sensible manner, with the ROHF energies being near-identical to the UHF energies outside the 1.47 - 1.53 Å region, but the former smoothly bridge the gap where UHF is discontinuous. In **Figure 4.3** the behaviour

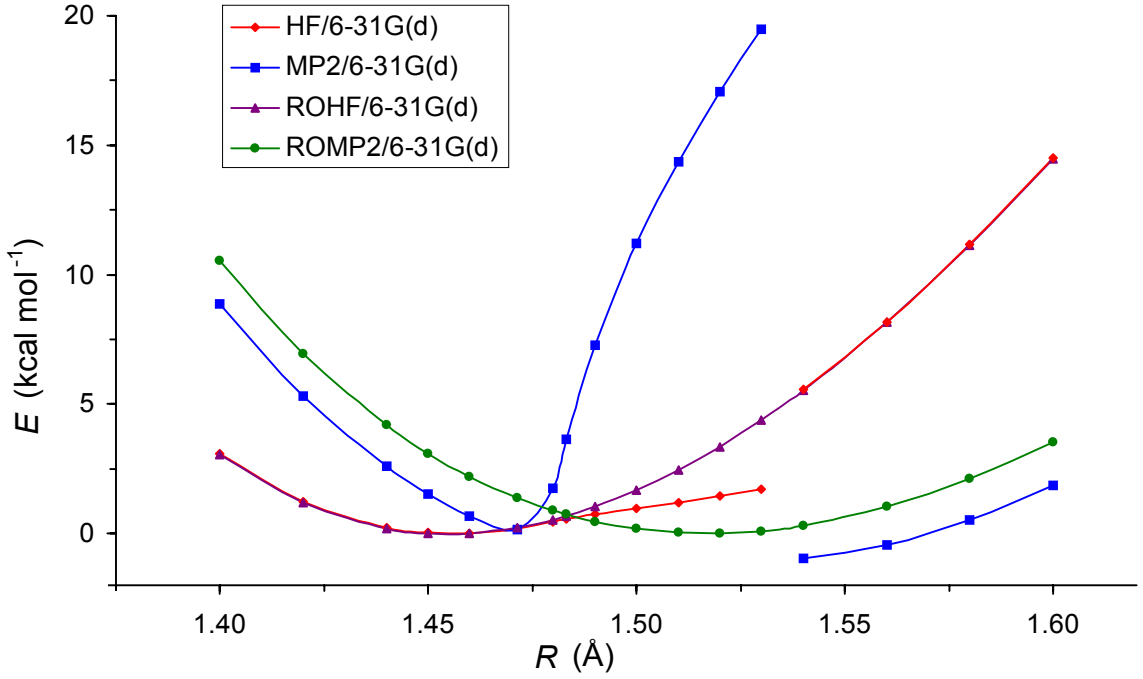

Figure 4.2 Potential energy curves of PO obtained at restricted and unrestricted Hartree-Fock and MP2 levels of theory (relative to respective minimum values).

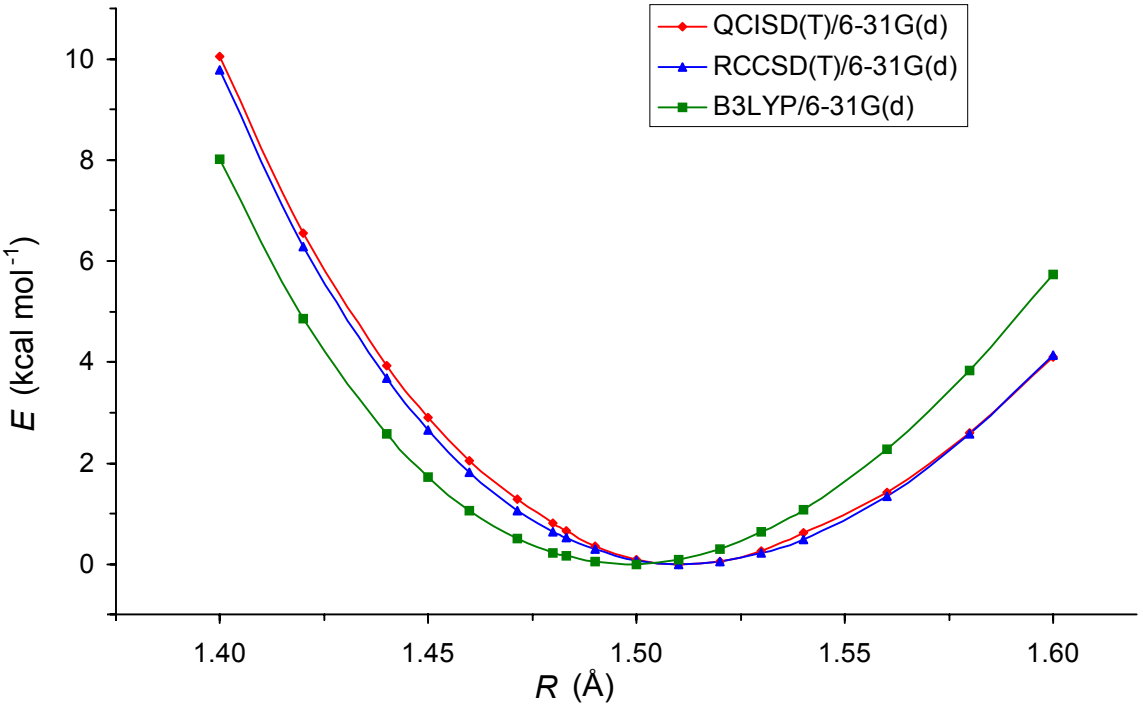

Figure 4.3 Potential energy curves of PO obtained at unrestricted QCISD(T), B3LYP and restricted CCSD(T) levels of theory (relative to respective minimum values).

of the high level theories RCCSD(T), UQCISD(T) and B3LYP are compared. Overall, the UQCISD(T) energies closely match the RCCSD(T) values, although a small blip in the former can now be clearly seen at 1.54 Å. The behaviour of the UB3LYP energies is completely sensible and predicts an equilibrium PO distance of ~ 1.50 Å, which is ~ 0.015 Å lower than the RCCSD(T) value.

In light of the above findings the unusual behaviour of the G3 and G3X results is easy to rationalise. The G3 energies were obtained at the UMP2/6-31G(*d*) bond distance of 1.4715 Å, that is, just outside the problem region identified above, and thus a seemingly sensible value for the heat of formation was obtained. The G3X and G3X2 calculations, at the UB3LYP/6-31G(2*df*,*p*) bond distance of 1.4988 Å, are affected by spin contamination. Note, however, that the UMP2/6-31G(*d*) value for the bond distance cannot be accepted as reliable, as the corresponding minimum is largely an artefact of the non physical behaviour of the UMP2 energy. In contrast with other (well-behaved) P and O containing molecules, where the MP2 PO distances are typically ~ 0.02 Å *longer* than the B3LYP values, in PO the UMP2 distance is actually ~ 0.03 Å shorter than the UB3LYP value. Therefore, the seemingly sensible heat of formation of PO at the G3 level is fortuitous.

4.3.2.2 Comparison with QCISD(T,Full)

As a further test of the G3, G3X and G3X2 methods, the atomisation energies of PO, PO_2, PO_3, HPO, HOPO and $HOPO_2$, obtained at the above levels of theory are summarised in **Table 4.3**, along with the atomisation energies computed at the QCISD(T,Full) level of theory using both the G3Large and G3XLarge basis sets, with the higher level correction terms implicit in the G3 techniques included. Such a comparison of G3 and QCI results is relevant since the Gaussian methods aim to produce reliable estimates of the QCISD(T,Full) energies in the largest basis sets used, viz. G3Large and G3XLarge, by applying a series of lower level quantum chemical methods in conjunction with a range of basis sets. In the case of the PO and PO_2 radicals the standard UHF based results are compared with those obtained by the appropriate ROHF based techniques. The latter are analogous to Radom's G3(RAD) and related methods[16-18]. Finally, comparisons are also made with Bauschlicher's (R)CCSD(T) results[44]. In all cases G3 reproduces the QCISD(T,Full)/G3Large atomisation energies to within ~ 1 kcal mol^{-1}, but mostly better. Similarly, G3X2 reproduces the QCISD(T,Full)/

Table 4.3 Phosphorus oxides and acids: Comparison of computed atomisation energies (in kcal mol^{-1}).

	Atomisation Energy [a]							
	PO		PO_2		PO_3	HPO	HOPO	$HOPO_2$
Method/Reference State	UHF	ROHF [b]	UHF	ROHF [b]	UHF			
G3	143.54	143.05	264.15	263.06	360.79	211.92	362.60	480.76
UQCISD(T,Full)/G3large[c]	143.69	142.36	265.00	263.11	361.69	211.87	362.37	480.84
G3X	146.72	143.66	265.79	264.13	363.39	213.23	364.64	483.51
G3X2	148.10	144.98	268.07	266.15	366.52	215.20	366.71	486.56
UQCISD(T,Full)/G3Xlarge[d]	145.86	144.49	269.43	266.81	368.00	215.50	366.87	487.37
RCCSD(T)/TZ+CV[e]	135.16		253.10		346.14	204.35	352.11	466.70
RCCSD(T)/QZ+CV[e]	140.27		261.72		357.74	210.37	361.39	479.97
RCCSD(T)/5Z+CV[e]	142.12		264.83		361.89	212.39	364.43	na
RCCSD(T)/CBS+CV[e]	144.05		268.09		366.25	214.51	367.61	489.65

[a] Not including zero point energy.

[b] All ROHF based calculations performed at UB3LYP/6-31G(2*df*,*p*) geometries and use RCCSD(T) in place of QCISD(T) where appropriate.

[c] Including G3 higher level correction.

[d] Including G3X higher level correction.

[e] Including core-valence correlation corrections, Ref. 44.

G3XLarge atomisation energies to within ~ 1.5 kcal mol^{-1}, except in the case of PO, where the discrepancy is ~ 2.3 kcal mol^{-1}, for the UHF based calculations. The consistency of the ROHF based results is significantly better. Comparison with Bauschlicher's results demonstrates that the G3X2 method is capable of yielding chemically accurate atomisation energies and hence heats of formation for this class of difficult molecules. The worst discrepancy between G3X2 and the CBS results occurs for $HOPO_2$, where the difference is 3.1 kcal mol^{-1}, although at the QCISD(T,Full)/G3XLarge level it is reduced to 2.3 kcal mol^{-1}.

In light of the encouraging performance of the G3X2 method for the above six molecules a larger systematic evaluation of G3X2 has been undertaken, applying it to a larger number of phosphorus containing molecules, including all those in **Table 4.1**. These results are reported in **Chapter 5**.

4.4 Kinetic Parameters

A primary aim of this chapter is the calculation of rate coefficients for the PO_2 + H and PO_2 + OH recombination reactions (4.1.a) and (4.2.a), and for the subsequent abstraction reactions, (4.1.b), (4.1.c) and (4.2.b). The rates of these reactions that make up the catalytic cycles are compared with the (experimental) rates of the (uncatalysed) H + OH recombination reaction (4.3). The computed geometries of the transition states of these reactions are shown in **Figure 4.4**. The corresponding heats of formation at 298 K, rotational constants and vibrational frequencies are summarised in **Table 4.4**. The geometries of the transition states of reactions (4.1.b), (4.1.c) and (4.2.b) correspond to well-defined first order saddle points. However, the recombination reactions (4.1.a) and (4.2.a) are barrierless and thus require a VTST treatment to locate the geometries of the appropriate transition states at a given temperature, as outlined in the **Sections 2.9.2** and **4.2**. The variational transition states were determined at five temperatures in the range 1000 - 2000 K. The parameters in **Figure 4.4** and **Table 4.4** pertaining to the transition states of reactions (4.1.a) and (4.2.a) were obtained at 1000 K. The full set of geometries, rotational constants and vibrational frequencies are given in **Appendices 2.3** and **2.4**.

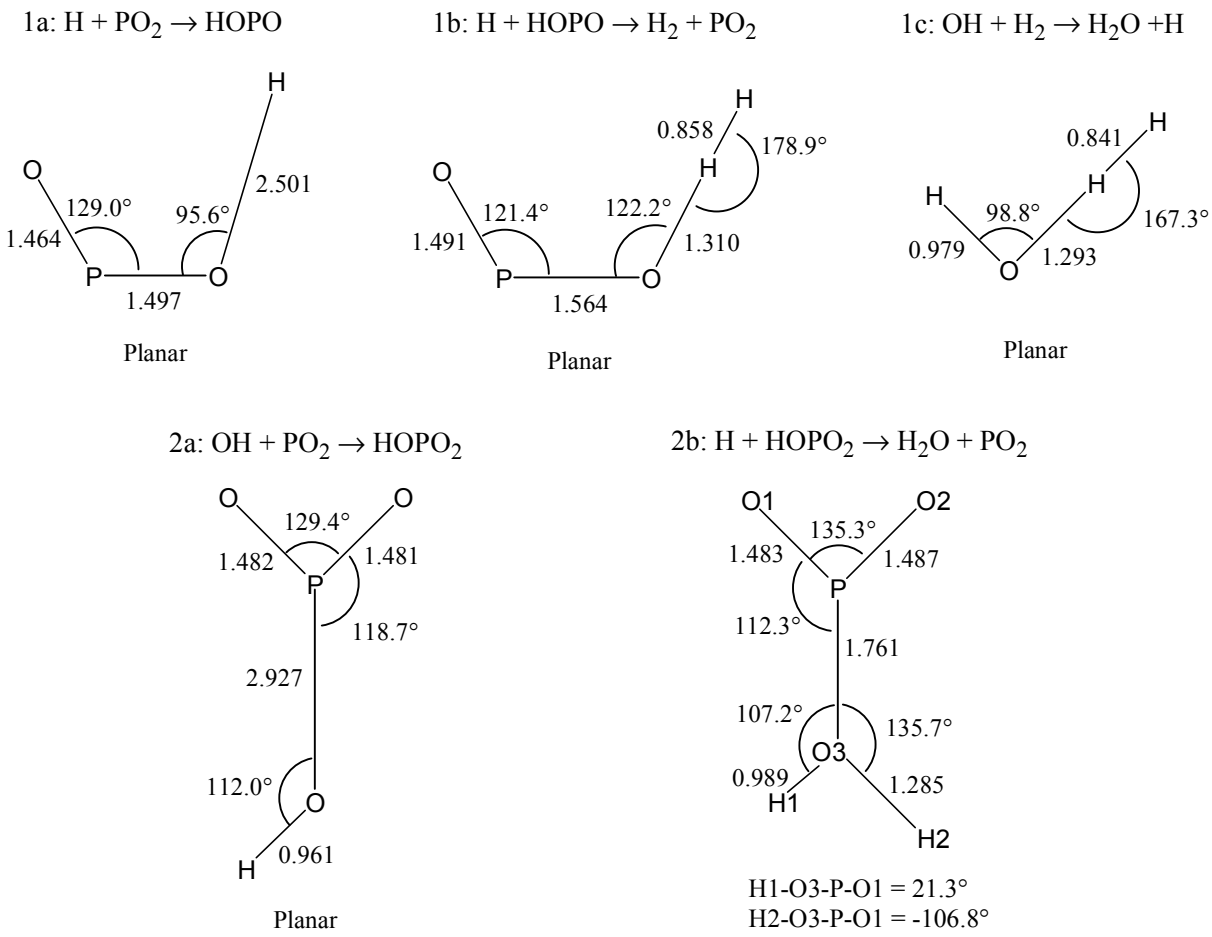

Figure 4.4 Geometries of transition states: Variational transition state geometries at 1000 K for reactions (4.1.a) and (4.2.a) obtained at CASSCF/cc-pVDZ level of theory. All others are saddle points computed at MP2/6-31G(*d*) level.

Given the barrierless nature of the recombination reactions (4.1.a) and (4.2.a), the dissociation rates of HOPO and $HOPO_2$ were initially computed using RRKM at a number of temperatures in the range 1000 - 2000 K, at pressures 1 - 10^4 Torr, for a bath gas of N_2. The heats of reactions involving phosphorus containing species were computed using Bauschlicher's CBS heats of formation[44] (at 298 K) for PO_2, HOPO and $HOPO_2$ and experimental literature values for all other species[41-43,45], with the appropriate thermal corrections also taken from JANAF tabulations[41] or computed on the basis of the B3LYP geometries and frequencies[44]. The rate coefficients were then fitted to the Troe equations (4.8) - (4.13)[35]. **Figure 4.5 – 4.8** display the individual rate coefficients and the resulting Troe fits of these. Clearly, the quality of the fits is generally very good.

Table 4.4 Computed heats of formation, vibrational frequencies and rotational constants of transition states.[a]

Reaction	$\Delta_f H^0_{298}$ /kcal mol^{-1}	Rotational Constants /cm^{-1}			Vibrational Frequencies /cm^{-1}					
1a: H + PO_2 → HOPO	–20.3	1.2566	0.2936	0.2380	340*i*	82	152	406	1022	1329
1b: HOPO + H → PO_2 + H_2	–45.1	1.0019	0.2722	0.2140	2668*i*	224	270	469	774	787
					899	1276	1477			
1c: H_2 + OH → H_2O + H	12.9	18.5846	2.9867	2.5732	2813*i*	628	675	1283	1443	3602
2a: PO_2 +OH → $HOPO_2$	–66.9	0.2919	0.1124	0.0812	200*i*	86	126	164	426	470
					1087	1212	3982			
2b: $HOPO_2$ + H → PO_2 + H_2O	–90.2	0.2708	0.2481	0.1321	3665*i*	244	279	327	438	530
					632	738	1115	1238	1405	3530

[a] Computed at 1000 K for variational transition states (4.1.a) and (4.2.a).

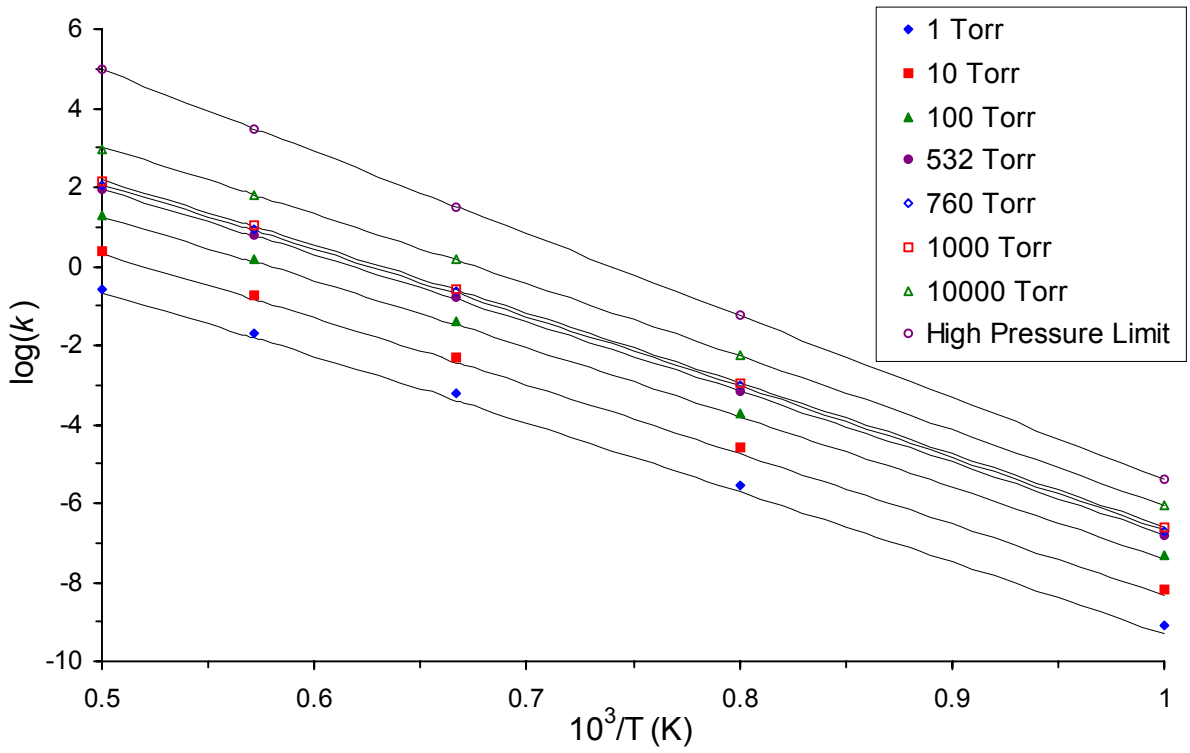

Figure 4.5 Arrhenius plots of RRKM rate constants for HOPO → PO_2 + H reaction at a range of pressures. (Symbols = computed rate constants, Lines = Troe fits.)

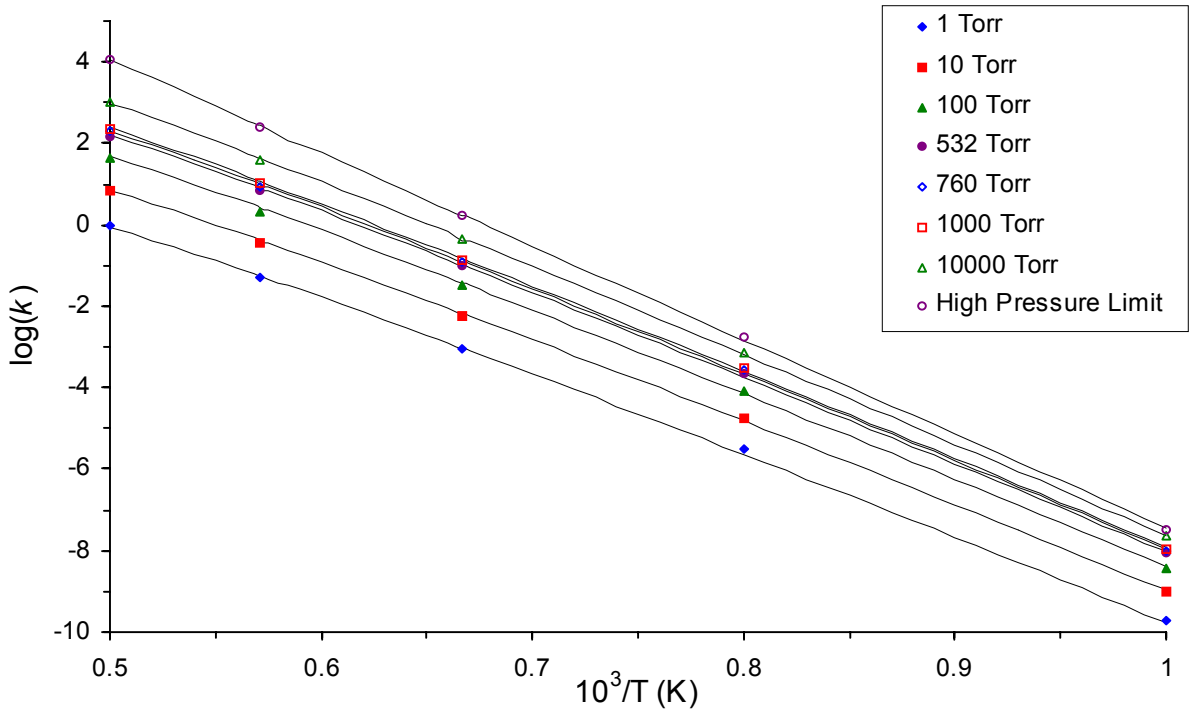

Figure 4.6 Arrhenius plots of RRKM rate constants for $HOPO_2$ → PO_2 + OH reaction at a range of pressures. (Symbols = computed rate constants, Lines = Troe fits.)

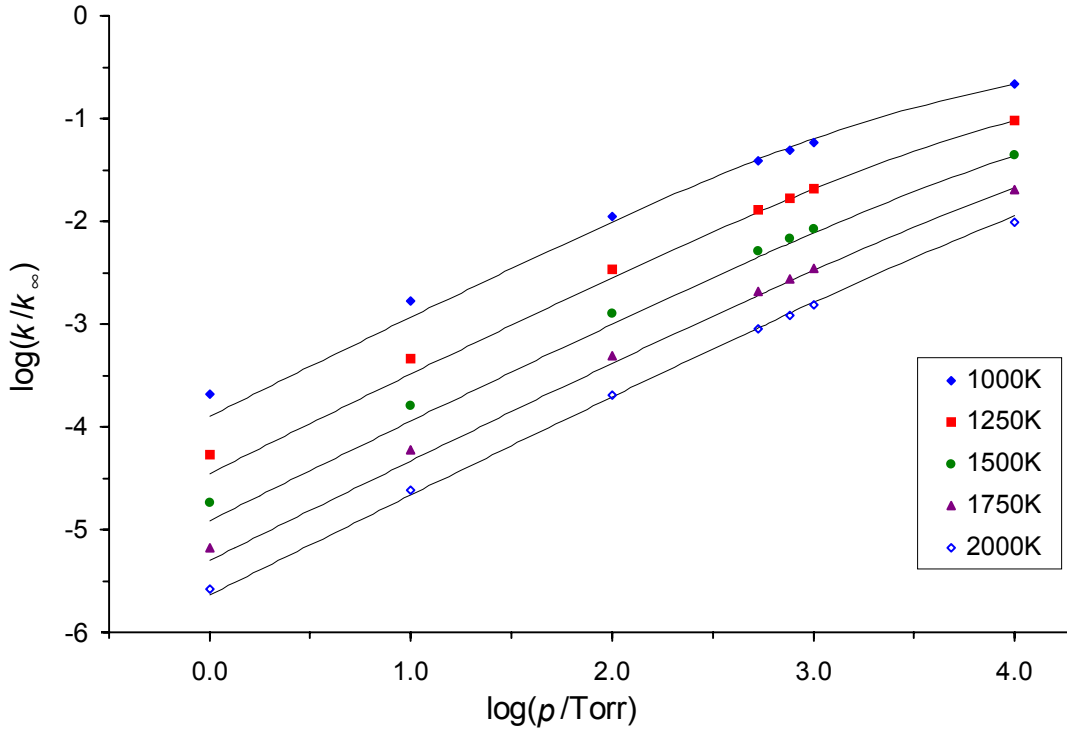

Figure 4.7 Pressure dependence of RRKM rate constants for HOPO → PO_2 + H reaction at a range of temperatures. (Symbols = computed rate constants, Lines = Troe fits.)

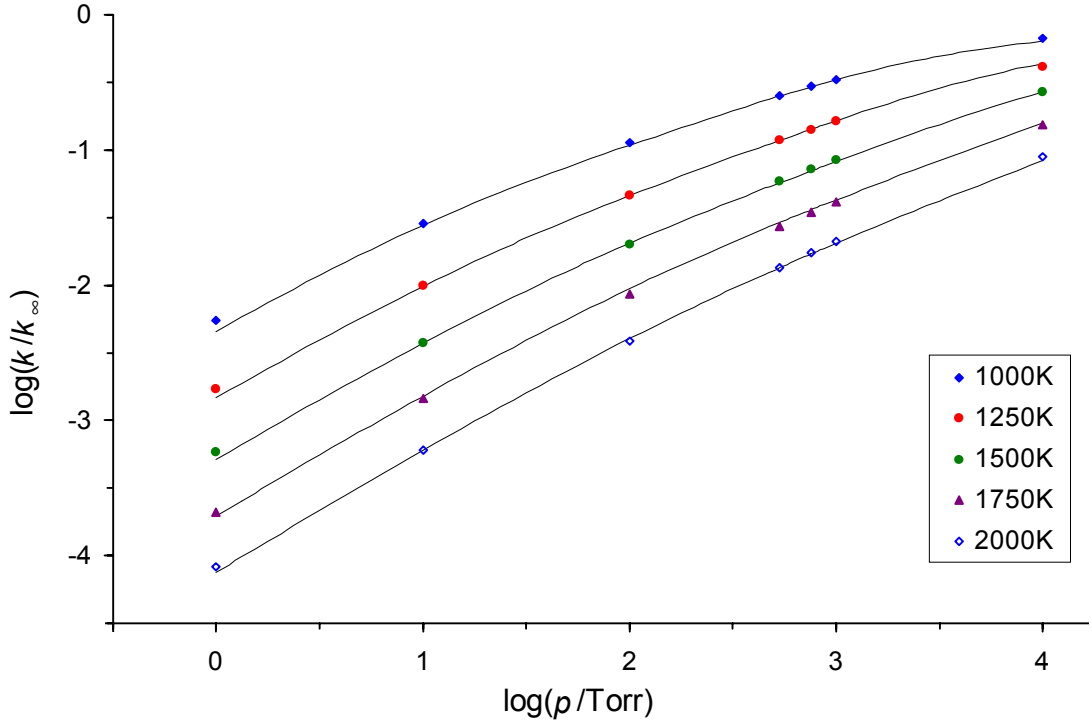

Figure 4.8 Pressure dependence of RRKM rate constants for $HOPO_2$ → PO_2 + OH reaction at a range of temperatures. (Symbols = computed rate constants, Lines = Troe fits.)

The calculated rate coefficients of all the reactions studied in this chapter, in the form of Troe, Arrhenius or modified Arrhenius fits, are summarised in **Table 4.5**, in the temperature range 1000 - 2000 K. Further, pertinent computational details of the individual reactions are discussed below. The rate coefficients of the association (that is, recombination) reactions were calculated by utilising the appropriate equilibrium constants, as given by Equation (4.7). The calculated Gibbs free energies of reactions and reaction enthalpies at a number of temperatures are given in **Table 4.6**.

HOPO → H + PO_2. Initially, the potential energy surfaces of both the *cis* and *trans* isomers were studied in the region of dissociation at the CASSCF/cc-pVDZ level of theory. In the case of the *trans* isomer a saddle point was found at an O···H distance of 2.54 Å. This transition state was ~ 7 kcal mol^{-1} higher in energy than the dissociation products H + PO_2. In contrast with such a 7 kcal mol^{-1} barrier to the recombination reaction to give the *trans* isomer, no barrier could be found for the dissociation of the lower energy *cis* isomer. This indicates that the latter mechanism represents the preferred reaction channel. The geometries and frequencies of the variational transition states were located at CASSCF/cc-pVDZ level of theory. As the potential energy surface is very flat in the critical region, the transition state geometries at the various temperatures show little variation, as the data in **Appendices 2.3** and **2.4** indicate. The energies of the transition states relative to the dissociated products were obtained from CASSCF/cc-pVDZ calculations.

H + HOPO → H_2 + PO_2 and OH + H_2 → H_2O + H. The transition state geometries (corresponding to first order saddle points) and critical energies were computed at the G3 level of theory.

$HOPO_2$ → OH + PO_2. The geometries of the variational transition states were located at the CASSCF/cc-pVDZ level of theory. The energies of the transition states relative to the dissociated products were calculated at the CASPT2/cc-pVTZ level. As before, the enthalpy of dissociation was determined using Bauschlicher's CBS heats of formation (at 298 K) for PO_2 and $HOPO_2$ and experimental values for OH.

Table 4.5 Computed rate coefficients: Troe[a], Arrhenius[b] and modified Arrhenius[b] fit parameters.

	High pressure limit					Low pressure limit				
	Arrhenius		*Modified Arrhenius*			*Arrhenius*		*Modified Arrhenius*		
	log *A*	E_a	log *A*	*n*	E_a	log *A*	E_a	log *A*	*n*	E_a
$HOPO \rightarrow PO_2 + H$	15.34	94.9	13.57	0.50	93.6	16.57	82.1	34.97	–5.13	96.1
$PO_2 + H \rightarrow HOPO$			10.06	1.29	–1.5			31.46	–4.33	1.02
$HOPO + H \rightarrow H_2 + PO_2$ [c]	14.28	16.1	7.33	1.94	10.8					
$H_2 + OH \rightarrow H_2O + H$ [c]	14.33	9.9	5.92	2.34	3.5					
$HOPO_2 \rightarrow HO + PO_2$	15.56	105.2	24.44	–2.48	112.0	18.41	91.5	57.26	–10.83	121.0
$HO + PO_2 \rightarrow HOPO_2$			14.19	–0.24	0.0			47.01	–8.59	9.0
$HOPO_2 + H \rightarrow PO_2 + H_2O$ [c]	14.10	26.7	8.74	1.49	22.6					

	Troe Fit				
	a	1–*a*	*T**	*T***	*T****
$HOPO \rightarrow PO_2 + H$	1.00	0.00	950.72	4797.20	–115.31
$PO_2 + H \rightarrow HOPO$					
$HOPO + H \rightarrow H_2 + PO_2$ [c]					
$H_2 + OH \rightarrow H_2O + H$ [c]					
$HOPO_2 \rightarrow HO + PO_2$	1.00	-2.22×10^{-6}	640.64	3973.10	–202.75
$HO + PO_2 \rightarrow HOPO_2$					
$HOPO_2 + H \rightarrow PO_2 + H_2O$ [c]					

[a] See equations (8) - (13); *T**, *T***, *T**** in K.

[b] See equations (5) and (6); E_a in kcal mol^{-1}, *A* in s^{-1} or $cm^3\,mol^{-1}\,s^{-1}$.

[c] These reactions are not pressure dependent.

Table 4.6 Computed enthalpies and Gibbs free energies of reaction (in kcal mol^{-1}) at a range of temperatures.

	$H + PO_2 \rightarrow HOPO$		$OH + PO_2 \rightarrow HOPO_2$	
T /K	$\Delta_r H_T^0$	$\Delta_r G_T^0$	$\Delta_r H_T^0$	$\Delta_r G_T^0$
298.15	–94.2	–86.6	–110.4	–99.1
1000	–95.4	–67.4	–110.0	–72.4
1250	–95.6	–60.4	–109.5	–63.1
1500	–95.7	–53.4	–108.9	–53.9
1750	–95.7	–46.3	–108.3	–44.7
2000	–95.7	–39.3	–107.6	–35.7

$H + HOPO_2 \rightarrow H_2O + PO_2$. The search for a transition state for this reaction initially yielded a minimum corresponding to a weakly bound $PO_2 \cdots H_2O$ dimer. This dimer had a binding energy of 4.8 kcal mol^{-1} after applying the counterpoise correction for basis set superposition effects. However, from the point of view of this work the existence of such a dimer is of academic interest only as it would not be expected to be stable at ~ 2000 K. The transition state for OH abstraction by H is characterised by a long OH bond and a slightly elongated PO bond. The geometry and barrier height were located at the G3 level of theory.

Finally, the calculated rate coefficients at the temperatures of 1000 and 2000 K and a pressure of 532 torr are summarised in **Table 4.7** where they are compared with Twarowski's estimated values (which were obtained by the application of Benson's rules), the modelling values of Korobeinichev et al.[13] and experiment.[47]

At 2000 K the rate coefficients in the two reaction schemes considered are comparable in magnitude, suggesting that both routes are important, in qualitative agreement with Twarowski's conclusions. However, in an absolute sense, the rate coefficients obtained in this work are significantly lower than Twarowski's, especially at 1000 K, although order of magnitude differences can exist even at the higher temperature. Our values agree somewhat better with the modelled values of Korobeinichev et al.,[13] but there remain significant differences. Under the conditions studied by Twarowski (0.7 atm pressure and 1970 K) the rate coefficient for (4.1.a) is substantially into falloff (approximately 1,000 fold lower than the high pressure limit), whereas the coefficient for (4.2.a) is significantly less so (only ~ 60 fold

Table 4.7 Comparison of computed and experimental rate coefficients at 532 Torr pressure at 1000 and 2000 K (in $cm^3mol^{-1}s^{-1}$).

Reaction	T (K)	k (This work)	k (Twarowski[a])	k (Korobeinichev et al.[b])	k (expt.)
1a: $PO_2 + H \rightarrow HOPO$	1000	7.03×10^{12}	4.42×10^{12} [c]	4.55×10^{13} [c]	
	2000	2.78×10^{11}	2.87×10^{11} [c]	6.51×10^{12} [c]	
1b: $HOPO + H \rightarrow H_2 + PO_2$	1000	6.08×10^{10}	3.15×10^{13}	7.7×10^{11}	
	2000	3.53×10^{12}	3.16×10^{13}	7.8×10^{11}	
1c: $H_2 + OH \rightarrow H_2O + H$	1000	1.52×10^{12}	6.28×10^{13}		1.26×10^{12} [d]
	2000	1.88×10^{13}	6.30×10^{13}		8.33×10^{12} [d]
2a: $HO + PO_2 \rightarrow HOPO_2$	1000	7.40×10^{12}	1.74×10^{14} [c]	1.71×10^{13} [c]	
	2000	3.68×10^{11}	5.62×10^{12} [c]	1.89×10^{12} [c]	
2b: $HOPO_2 + H \rightarrow PO_2 + H_2O$	1000	1.93×10^{8}	3.16×10^{13}	1.55×10^{9}	
	2000	1.60×10^{11}	3.16×10^{13}	3.13×10^{10}	
3: $H + OH \rightarrow H_2O$	1000		3.56×10^{9} [c]		7.12×10^{12} [c,e]
	2000		1.17×10^{9} [c]		8.91×10^{9} [c,e]

[a] Ref. 3.

[b] Ref. 13.

[c] Calculated as k[M].

[d] Fit to all NIST data, Ref. 48.

[e] Ref. 47.

lower than the high pressure limit). Thus, whilst it might be acceptable to use the termolecular rate coefficient for (4.1.a) in modelling, in light of its proximity to the limiting low pressure value, the appropriate falloff value of the rate coefficient should be used for (4.2.a). For the H_2 + OH abstraction reaction (4.1.c) the computed G3 rate coefficients agree with the observed values[48] to within a factor of approximately two or better, depending on the temperature.

4.5 Conclusion

Using ab initio quantum chemical and RRKM techniques, theoretical rate coefficients were obtained for the H + PO_2 (4.1.a) and OH + PO_2 (4.2.a) recombination reactions and for the subsequent H + HOPO (4.1.b) and H + $HOPO_2$ (4.2.b) abstraction reactions, which, along with the OH + H_2 abstraction reaction (4.1.c) constitute the catalytic pathway for the H + OH recombination reaction (4.3), as formulated by Twarowski[1-4] and also by Korobeinichev et al.[13] The computed rate coefficients for (4.1.c) agree well with experiment (within 20% at 1000 K and almost within a factor of 2 at 2000 K), while for the other reactions the rate coefficients are consistent with the modelled values of Korobeinichev et al.,[13] although for several key reactions ((4.1.b), (4.2.a), (4.2.b)) they are substantially lower than Twarowski's values. Whilst we utilised Bauschlicher's[44] recent thermochemical data in the derivation of our rate coefficients, we note that reasonable accuracy could be achieved by the application of the G3X and G3X2 methods to the computation of the heats of formation of the phosphorus containing species. Using the G2, G3 and G3X methods we also computed the thermochemistry of Twarowski's reaction model which includes 17 phosphorus containing molecules.

4.6 References

1. A. Twarowski, *Combustion and Flame*, **1993**, *94*, 91.
2. A. Twarowski, *Combustion and Flame*, **1993**, *94*, 341.
3. A. Twarowski, *Combustion and Flame*, **1995**, *102*, 41.
4. A. Twarowski, *Combustion and Flame*, **1996**, *105*, 407.
5. S. W. Benson, *Thermochemical Kinetics*; John Wiley: New York, NY, **1976**.
6. L. A. Curtiss, K. Raghavachari, G. W. Trucks and J. A. Pople, *J. Chem. Phys.*, **1991**, *94*, 7221.
7. L. A. Curtiss, K. Raghavachari, P. C. Redfern, V. Rassolov and J. A. Pople, *J. Chem. Phys.*, **1998**, *109*, 7764.
8. L. A. Curtiss, P. C. Redfern, K. Raghavachari and J. A. Pople, *J. Chem. Phys.*, **2001**, *114*, 108.
9. M. A. MacDonald, T. M. Jayaweera, E. M. Fisher and F. C. Gouldin, *Combustion and Flame*, **1999**, *116*, 166.
10. J. Green, *Fire Sciences*, **1996**, *14*, 426.
11. C. R. Dempsey and E. T. Oppelt, *Air and Waste*, **1993**, *43*, 25.
12. O. P. Korobeinichev, S. B. Ilyin, T. A. Bolshova, V. M. Shvartsberg and A. A. Chernov, *Combustion and Flame*, **2000**, *121*, 593.
13. O. P. Korobeinichev, T. A. Bolshova, V. M. Shvartsberg and A. A. Chernov, *Combustion and Flame*, **2001**, *125*, 744.
14. M. A. MacDonald, F. C. Gouldin and E. M. Fisher, *Combustion and Flame*, **2001**, *124*, 668.
15. L. A. Curtiss, K. Raghavachari, P. C. Redfern and J. A. Pople, *J. Chem. Phys.*, **1997**, *106*, 1063.
16. D. J. Henry and L. Radom, in *Theoretical Thermochemistry.* J. Cioslowski, Ed.; Kluwer: Dordrecht, **2001**.
17. P. M. Mayer, C. J. Parkinson, D. M. Smith and L. Radom, *J. Chem. Phys.*, **1998**, *108*, 604.
18. C. J. Parkinson, P. M. Mayer and L. Radom, *J. Chem. Soc., Perkin Trans. 2*, **1999**, *11*, 2305.
19. J. A. Pople, M. Head-Gordon and K. Raghavachari, *J. Chem. Phys.*, **1987**, *87*, 5968.

20. K. Raghavachari, G. W. Trucks, J. A. Pople and M. Head-Gordon, *Chem. Phys. Lett.*, **1989**, *157*, 479.
21. C. Hampel, K. A. Peterson and H.-J. Werner, *Chem. Phys. Lett.*, **1992**, *190*, 1.
22. J. I. Steinfeld, J. S. Francisco and W. L. Hase, *Chemical Kinetics and Dynamics*; Prentice Hall: Engelwood Cliffs, NJ, **1989**, 308.
23. D. A. McQuarrie, *Statistical Mechanics*; Harper & Row: New York, **1973**, 129.
24. E. Pollack, in *Theory of Chemical Reaction Dynamics.* M. Baer, Ed.; Vol. 3; CRC Press: Boca Raton, **1985**, p. 128.
25. D. G. Truhlar and B. C. Garrett, *Acc. Chem. Res.*, **1980**, *13*, 440.
26. W. L. Hase, S. L. Mondro, R. J. Duchovic and D. M. Hirst, *J. Am. Chem. Soc.*, **1987**, *109*, 2916.
27. G. B. Bacskay, M. Martoprawiro and J. C. Mackie, *Chem. Phys. Lett.*, **1999**, *300*, 321.
28. K. Sendt, G. B. Bacskay and J. C. Mackie, *J. Phys. Chem. A*, **2000**, *104*, 1861.
29. B. O. Roos, P. R. Taylor and P. E. M. Siegbahn, *Chem. Phys.*, **1980**, *48*, 157.
30. B. O. Roos, in *Ab initio Methods in Quantum Chemistry II.* K. P. Lawley, Ed.; J. Wiley & Sons Ltd.: Chichester, UK, **1987**, p. 399.
31. T. H. Dunning, Jr., *J. Chem. Phys.*, **1989**, *90*, 1007.
32. D. E. Woon and T. H. Dunning, Jr., *J. Chem. Phys.*, **1993**, *98*, 1358.
33. K. Andersson, P.-Å. Malmqvist, B. O. Roos, A. J. Sadlej and K. Wolinski, *J. Phys. Chem.*, **1990**, *94*, 5483.
34. K. Andersson, P.-Å. Malmqvist and B. O. Roos, *J. Chem. Phys.*, **1992**, *96*, 1218.
35. R. G. Gilbert, K. Luther and J. Troe, *Ber. Bunsenges. Phys. Chem.*, **1983**, *87*, 169.
36. M. J. Frisch, G. W. Trucks, H. B. Schlegel, G. E. Scuseria, M. A. Robb, J. R. Cheeseman, V. G. Zakrzewski, J. A. Montgomery, R. E. Stratmann, J. C. Burant, S. Dapprich, J. M. Millam, A. D. Daniels, K. N. Kudin, M. C. Strain, O. Farkas, J. Tomasi, V. Barone, M. Cossi, R. Cammi, B. Mennucci, C. Pomelli, C. Adamo, S. Clifford, J. Ochterski, G. A. Petersson, P. Y. Ayala, Q. Cui, K. Morokuma, D. K. Malick, A. D. Rabuck, K. Raghavachari, J. B. Foresman, J. Cioslowski, J. V. Ortiz, B. B. Stefanov, G. Lui, A. Liashenko, P. Piskorz, I. Komaromi, R. Gomperts, R. L. Martin, D. J. Fox, T. Keith, M. A. Al-Laham, C. Y. Peng, A. Nanayakkara, C. Gonzalez, M. Challacombe, P. M. W. Gill, B. G. Johnson, W. Chen, M. W. Wong, J. L. Andres, M. Head-Gordon, E. S. Replogle and J. A. Pople, Gaussian 98 (Revision A.7), Gaussian, Inc.: Pittsburgh, PA, **1998**.

37. ACES II is a program product of the Quantum Theory Project, University of Florida. Authors: J. F. Stanton, J. Gauss, J. D. Watts, M. Nooijen, N. Oliphant, S. A. Perera, P. G. Szalay, W. J. Lauderdale, S. R. Gwaltney, S. Beck, A. Balková, D. E. Bernholdt, K.-K. Baeck, P. Rozyczko, H. Sekino, C. Hober, R. J. Bartlett. Integral packages included are VMOL (J. Almlöf and P. R. Taylor); VPROPS (P. Taylor); ABACUS (T. Helgekar, H. J. Aa. Jensen, P. Jørgensen, J. Olsen and P. R. Taylor).

38. "DALTON, an ab initio electronic structure program, Release 1.0 (1997)" written by T. Helgaker, H. J. Aa. Jensen, P. Jørgensen, J. Olsen, K. Ruud, H. Ågren, T. Andersen, K. L. Bak, V. Bakken, O. Christiansen, P. Dahle, E. K. Dalskov, T. Enevoldsen, B. Fernandez, H. Heiberg, H. Hettema, D. Jonsson, S. Kirpekar, R. Kobayashi, H. Koch, K. V. Mikkelsen, P. Norman, M. J. Packer, T. Saue, P. R. Taylor and O. Vahtras.

39. K. Andersson, M. R. A. Blomberg, M. P. Fülscher, G. Karlström, R. Lindh, P.-Å. Malmqvist, P. Neogrády, J. Olsen, B. O. Roos, A. J. Sadlej, M. Schültz, L. Seijo, L. Serrano-Andrés, P. E. M. Siegbahn and P.-O. Widmark, MOLCAS (Version 4), Lund University: Lund, Sweden, **1997**.

40. V. Mokrushin, V. Bedanov, W. Tsang, M. Zachariah and V. Knyazev, Chemrate (1.10), National Institute of Standards and Technology: Gaithersburg, MD, USA, **1999**.

41. M. W. Chase, Jr., *J. Phys. Chem. Ref. Data*, **1998**, *Monograph 9*, 1.

42. B. Rusic, D. Feller, D. A. Dixon, K. A. Peterson, L. B. Harding, R. L. Asher and A. F. Wagner, *J. Phys. Chem. A*, **2001**, *105*, 1.

43. J. Drowart, C. E. Myers, R. Szwarc, A. Vander Auwera-Mahieu and O. M. Uy, *J. Chem. Soc., Faraday Trans. 2*, **1972**, *68*, 1749.

44. C. W. Bauschlicher, Jr., *J. Phys. Chem. A*, **1999**, *103*, 11126.

45. D. L. Hildenbrand and K. H. Lau, *J. Chem. Phys.*, **1994**, *100*, 8373.

46. L. A. Curtiss, K. Raghavachari, P. C. Redfern and J. A. Pople, *J. Chem. Phys.*, **2000**, *112*, 7374.

47. D. L. Baulch, C. J. Cobos, R. A. Cox, C. Esser, P. Frank, T. Just, J. A. Kerr, M. J. Pilling, J. Troe, R. W. Walker and J. Warnatz, *J. Phys. Chem. Ref. Data*, **1992**, *21*, 411.

48. W. G. Mallard, F. Westley, J. T. Herron, R. G. Hampson and D. H. Frizzell, *NIST Chemical Kinetic Database: Version 2Q98*. **1998**, National Institute of Standards and Technology, Gaithersburg, MD.

Chapter 5

Accurate Thermochemistry of Phosphorus Compounds

5.1 Introduction

During the last decade a considerable degree of interest has developed in phosphorus containing molecules as potential catalysts, with the ability to accelerate a range of radical recombination reactions.[1-7] Such catalytic activity has implications in a number of fields, such as flame suppression, engine fuel efficiency and nerve gas disposal. Unfortunately, the development of reliable kinetic models for these processes has been hampered by a lack of accurate thermochemical and kinetic data. The work reported in this chapter aims to aid in remedying this problem by undertaking the computation of accurate heats of formation for a number of small phosphorus-containing molecules using current techniques of computational quantum chemistry.

As in other work[8-17] concerned with the ab initio computation of thermochemistry, the approach here has been to compute the atomisation energies and hence heats of formation of the molecules of interest by the application of the CCSD(T) coupled cluster method in conjunction with correlation consistent basis sets (aug)-cc-pV*x*Z (*x* = T, Q, 5), followed by extrapolation to the complete basis set (CBS) limit, and inclusion of corrections for core-valence correlation, spin-orbit coupling and scalar relativistic effects. Such calculations have already been reported by Bauschlicher[15] for PO, PO_2, PO_3, HPO, HOPO and $HOPO_2$. In addition to these phosphorus oxides and acids, heats of formation for P_2, P_4, PH, PH_2, PH_3, P_2H_2, P_2H_4, P_2O, P_2O_2, HPOH, H_2POH, and H_3PO have been calculated and are reported here.

Regarding the computed CCSD(T)/CBS thermochemistry as a benchmark, the second aspect of this work is a critical test of Gaussian-3 type methods, in particular G3[18], G3X[19] and G3X2[20], when applied to the above set of molecules. As these techniques are considerably less computer resource intensive than the CCSD(T)/CBS approach, they would have a wider range of applicability, especially for larger systems. However, given that the original test set of molecules that was used to calibrate the G3 and G3X methods contains comparatively few phosphorus containing species (due largely to the lack of reliable experimental information), an assessment of the capability and reliability of these methods for a larger number of phosphorus containing molecules is clearly desirable.

The heats of formation of the above phosphorus compounds, as calculated by G3 and G3X, have been reported in the previous chapter (and also published[20]), although the main focus of that work was the computation of rate coefficients for the H + PO_2 and OH + PO_2 recombination reactions and for the H + HOPO → H_2 + PO_2, OH + H_2 → H + H_2O, and H + $HOPO_2$ → H_2 + PO_2 abstraction reactions, which constitute a catalytic pathway for the H + OH recombination reaction. Comparison of the G3 and G3X heats of formation with the CCSD(T)/CBS values of Bauschlicher for the six phosphorus oxides and acids PO, PO_2, … $HOPO_2$ revealed that the G3 and G3X heats of formation were in error by up to ~ 9 and 6 kcal mol^{-1} respectively, given that the CCSD(T)/CBS values are believed to be essentially chemically accurate, with estimated errors of ~ 1 kcal mol^{-1}. The performance of G3X2 was found to be superior to G3X, with the maximum deviation from the CCSD(T)/CBS values being ~ 3 kcal mol^{-1}.) Extending such comparisons to a larger set of molecules, as undertaken in this study, is seen as definitely warranted.

This work, therefore, has two primary aims: firstly to generate benchmark atomisation energies (*AE*) and heats of formation for a larger selection of small phosphorus containing molecules and secondly to use these results to assess the reliability of the G3 type methods for these systems.

5.2 Theory And Computational Methods

The application of coupled cluster theory in conjunction with correlation consistent basis sets and extrapolation to the CBS limit has become well established as a reliable approach for generating accurate heats of formation from atomisation energies.[8-17] This is the scheme that was employed by Bauschlicher[15] to calculate thermochemical data for the phosphorus oxides and acids. The approach here for the generation of benchmark heats of formation is effectively the same as Bauschlicher's.

The geometries and vibrational frequencies in this work were obtained using density functional theory, employing the B3LYP exchange-correlation functional[21-24] and the 6-31G(2*df*,*p*) basis set, as prescribed by G3X theory (with a scale factor of 0.9854 for the computation of zero point energies). This basis set is somewhat different from those used by

Bauschlicher, viz. 6-31+G(2*df*) for geometries and 6-31G(*d*) for frequencies. The single point energy calculations at the B3LYP optimised equilibrium geometries were performed using coupled cluster theory with single and double excitations, with the inclusion of triples by perturbation theory (CCSD(T))[25,26]. The open shell reference state orbitals and energies were generated by restricted Hartree-Fock (RHF) theory, while the subsequent coupled cluster energies were obtained by the restricted RCCSD(T) method.

The basis sets employed in the sequence of valence-correlated coupled cluster calculations (where the 1*s* electrons on O and 1*s*, 2*s*, 2*p* electrons on P are left uncorrelated) are the correlation consistent valence-polarised (cc-pV) triple-ζ (TZ), quadruple-ζ (QZ) and pentuple-ζ (5Z) basis sets developed by Dunning et al.[27-29] As recommended by Bauschlicher[15], an additional tight *d* function was added to each of the phosphorus basis sets with an exponent three times that of the largest *d* function in the original set (that is, 1.956, 3.11 and 8.00 for the TZ, QZ and 5Z sets respectively). Diffuse functions were also included in the oxygen basis sets; that is, for O atoms the aug-cc-pV*x*Z basis sets[27,28] are used. The resulting basis sets for molecules with P, O and H atoms are denoted (aug-)cc-pV*x*Z+*d*.

The three valence (R)CCSD(T) single point energies were then extrapolated to the CBS limit ({T,Q,5}). All four extrapolation schemes mentioned in **Section 2.7.3** were employed; that is, the mixed exponential/Gaussian extrapolation of Feller[30] ("*mix*", Equation (5.1)), the Schwartz type extrapolations[31] ("$l_{\max}$", Equation (5.2) and "$n^{-4}+n^{-6}$", Equation (5.3)) and the "x^{-3}" scheme of Helgaker et al.[16] (Equation (5.4)).

$$E(x) = A + B\exp(1-x) + C\exp\left(-(1-x)^2\right) \tag{5.1}$$

$$E(x) = A + B\left(l_{\max} + 1/2\right)^{-4} \tag{5.2}$$

$$E(x) = A + B\left(l_{\max} + 1/2\right)^{-4} + C\left(l_{\max} + 1/2\right)^{-6} \tag{5.3}$$

$$E(x) = A + Bx^{-3} \tag{5.4}$$

The core-valence (and core-core) correlation energies (CV) were computed via (R)CCSD(T) calculations using both the correlation consistent polarised core valence triple-ζ (cc-pCVTZ) basis sets of Dunning et al.[27,29,32] (aug-cc-pCVTZ for oxygen) as well as the core-valence basis sets proposed by Bauschlicher[15]. The CV contributions to the atomisation energies were corrected for basis set superposition effects (BSSE) by application of the counterpoise (CP) method of Boys and Bernardi[33]. The CP treatment was restricted to the phosphorus atoms of any given molecule; that is, CP corrections to the CV component of the energies, denoted CP(CV), were computed only for the P atoms.

The spin-orbit coupling energy corrections for the atomic species were taken from the tabulation of Curtiss et al.[18] The only molecule in the set which would be expected show appreciable spin-orbit coupling is PO; in this case the value calculated by Bauschlicher[15] was used. Scalar relativistic corrections, viz. the Darwin and mass-velocity contributions[34,35], were calculated using finite field perturbation theory, utilising the complete active space second order perturbation theory (CASPT2) method[36,37] with complete active space self-consistent field (CASSCF)[38,39] reference states, and the G3Large basis sets of Curtiss et al.[18]

The Gaussian methods, G1[40], G2[41], G3[18] and their variants[42-46], have been designed to approximate a molecular energy that would result from the application of a high level of quantum chemical theory in conjunction with a large basis set by a series of lower level calculations and/or smaller basis sets. This, of course, results in significant savings of computer resources. The G3 and G3X methods have already been described in detail in **Section 2.7.2**. In brief, in G3 the aim is to effectively reproduce the electronic energy of a QCISD(T, Full) calculation obtained with the G3Large basis set.

$$
\begin{aligned}
E_0[\mathrm{G3}] = {} & E[\mathrm{QCISD(T)/6\text{-}31G}(d)] \\
& + \{E[\mathrm{MP4/6\text{-}31+G}(d)] - E[\mathrm{MP4/6\text{-}31G}(d)]\} && (+\text{ correction}) \\
& + \{E[\mathrm{MP4/6\text{-}31G}(2df,p)] - E[\mathrm{MP4/6\text{-}31G}(d)]\} && (2df, p\text{ correction}) \\
& + \left\{ \begin{array}{l} E[\mathrm{MP2(Full)/G3Large}] - E[\mathrm{MP2/6\text{-}31G}(2df,p)] \\ \quad - E[\mathrm{MP2/6\text{-}31+G}(d)] + E[\mathrm{MP2/6\text{-}31G}(d)] \end{array} \right\} && (\mathrm{G3Large\ correction}) \\
& + \Delta E_{\mathrm{ZPE}} + \Delta E_{\mathrm{SO}} + \Delta E_{\mathrm{hlc}}
\end{aligned}
\qquad (5.5)
$$

G3X theory is a derivative of G3, designed primarily so as to improve agreement between theoretical and experimental heats of formation for molecules which contain second row atoms (Na-Ar). This is achieved by using improved geometries and vibrational frequencies and by the inclusion of a so-called G3XLarge correction at the SCF level using the G3XLarge basis set:

$$E_0\left[\mathrm{G3X}\right] = E_0\left[\mathrm{G3}\right] + \underbrace{\left\{E\left[\mathrm{HF/G3XLarge}\right] - E\left[\mathrm{HF/G3Large}\right]\right\}}_{\text{G3XLarge correction}} \tag{5.6}$$

(with the understanding that the equilibrium geometry and zero point vibrational correction are obtained by B3LYP/6-31G(2*df*,*p)* calculations).

The recently proposed G3X2 method (**Section 2.7.2.5**, **Chapter 4**) differs from G3X only in that the G3XLarge correction is now evaluated using MP2(Full):

$$E_0\left[\mathrm{G3X2}\right] = E_0\left[\mathrm{G3}\right] + \left\{E\left[\mathrm{MP2(Full)/G3XLarge}\right] - E\left[\mathrm{MP2(Full)/G3Large}\right]\right\} \tag{5.7}$$

The G3X2 approach can also be regarded as a G3 calculation (with the geometry and zero point energy correction determined at the B3LYP/6-31G(2*df*,*p*) level) where the G3Large basis has been replaced by the G3XLarge set:

$$\begin{aligned} E_0\left[\mathrm{G3X2}\right] = {} & E\left[\mathrm{QCISD(T)/6\text{-}31G}(d)\right] \\ & + \left\{E\left[\mathrm{MP4/6\text{-}31+G}(d)\right] - E\left[\mathrm{MP4/6\text{-}31G}(d)\right]\right\} && (+\text{ correction}) \\ & + \left\{E\left[\mathrm{MP4/6\text{-}31G}(2df,p)\right] - E\left[\mathrm{MP4/6\text{-}31G}(d)\right]\right\} && (2df,\,p\text{ correction}) \\ & + \left\{\begin{array}{l} E\left[\mathrm{MP2(Full)/G3XLarge}\right] - E\left[\mathrm{MP2/6\text{-}31G}(2df,p)\right] \\ \quad - E\left[\mathrm{MP2/6\text{-}31+G}(d)\right] + E\left[\mathrm{MP2/6\text{-}31G}(d)\right] \end{array}\right\} && (\mathrm{G3X2\ correction}) \\ & + \Delta E_{\mathrm{ZPE}} + \Delta E_{\mathrm{SO}} + \Delta E_{\mathrm{hlc}} \end{aligned} \tag{5.8}$$

G3X2 represents an approximation to a QCISD(T,Full)/G3XLarge computation and, as it accounts for a greater degree of electron correlation energy than G3X, it is reasonable to expect that it would be superior to G3X in an absolute sense, that is, yield closer agreement with experiment. Indeed, as remarked in the introduction to this chapter (**Section 5.1**), we

found that for the six phosphorus oxides and acids PO, PO_2, … $HOPO_2$ studied by Bauschlicher the G3X2 heats of formation were in significantly better agreement with Bauschlicher's CCSD(T)/CBS values than those obtained by G3X.

A further suggested refinement of G3X2 which is introduced in this work is to correct the CV component of the energy for BSSE, which can be quite large for phosphorus containing molecules. The analogous corrections for BSSE effects within the valence space are assumed to be taken care of by the higher level corrections. In G3X2 the latter are defined the same way as in G3X, that is, in terms of the valence electrons of a given molecules, according to Equations (2.7.12) and (2.7.13). While ultimately the parameters *A*, *B*, *C* and *D* would need to be reoptimised for G3X2, no such optimisation has been undertaken here, as there are too few molecules in our data set for such results to have wider applicability. Therefore, the hlc parameters of G3X, given in **Section 2.7.2.4**, have been adopted for the current implementation of G3X2.

The standard Gaussian theories treat open shell systems (atoms and molecules) by the unrestricted methods: UHF, UMP2, UMP4 and UQCISD(T). An alternative approach is the G*n*(RAD) type approach of Radom and co-workers[47-49], where the UHF and UMP computations are replaced by their restricted open shell ROHF and ROMP analogues and RCCSD(T) is used instead of the UQCISD(T) method implicit in G2 and G3. In this work both the standard (unrestricted) formulation of G3X2 as well as the (restricted) G3X2(RAD) procedure have been used for all atoms as well as several open shell molecules.

The B3LYP geometries and vibrational frequencies as well as the G3X2 energies were generated using the Gaussian98 suite of programs[50]. The (R)CCSD(T) and ROMP calculations were performed with MOLPRO[26,51,52] and ACESII[53] respectively. The CASSCF and CASPT2 calculations of the scalar relativistic corrections were carried out using MOLCAS[54]. The computations were performed on DEC alpha 600/5/333 and COMPAQ XP100/500 workstations of the Theoretical Chemistry group at the University of Sydney and on the COMPAQ AlphaServer SC system of the Australian Partnership for Advanced Computing National Facility at the National Supercomputing Centre, ANU, Canberra.

5.3 Results and Discussion

5.3.1 CCSD(T) Benchmark Calculations

The geometric parameters, rotational constants and vibrational frequencies of the species studied in this investigation can be found in **Appendix 2.1**.

Table 5.1 contains the absolute energies of the molecules of interest and their component atoms, as obtained at the highest level of (valence) correlated theory, namely (R)CCSD(T)/(aug-)cc-pV5Z+*d*, along with the {T,Q,5} x^{-3} extrapolated energies, CV correlation corrections, CP corrections for BSSE in the latter, zero point vibrational energies, thermal corrections to the enthalpies and the scalar relativistic energy corrections.

5.3.1.1 Testing the B3LYP Geometry

As a test of the reliability of the B3LYP functional for the computation of molecular geometries, P_4 was taken as test case and its equilibrium geometry re-computed using CCSD(T). The results are summarised in **Figure 5.1** which shows the computed molecular energy as a function of the P-P distance in tetrahedral P_4. The B3LYP and valence correlated CCSD(T) calculations yield effectively the same geometry, but a shorter bond length is obtained when the CCSD(T) calculations include CV correlation. (The force constants from these three calculations are comparable.) These findings are interesting, since the DFT calculations do include CV correlation. In the context of the current work, however, the discrepancy in the B3LYP geometry is negligible, as the resulting error in the molecular energy is only ~ 0.04 kcal mol^{-1}. As in this work P_4 is probably the most difficult molecule to describe accurately, it is expected that any inaccuracies in the molecular energies of other species, resulting from errors in the choice of equilibrium geometries will be similarly negligible.

Table 5.1 Total CCSD(T) energies, core-valence (CV) correlation corrections, counterpoise (CP) corrections to CV, zero point energies, thermal corrections to enthalpies and scalar relativistic corrections (in E_h unless otherwise indicated).

	CCSD(T) (aug-) cc-pV5Z+*d*	CCSD(T) CBS(x^{-3})	CV corr1 [a]	CV corr2 [b]	CP(CV corr2) [c] /kcal mol^{-1}	ZPE /kcal mol^{-1}	$H_{298}-H_0$ /kcal mol^{-1}	E_{rel}
P_2 - $^1\Sigma_g$ ($D_{\infty h}$)	–681.84172	–681.85074	–0.65340	–0.67441	0.20	1.13	2.12	–1.62549
P_2 - $^1\Sigma_g$ ($D_{\infty h}$) [d]	–681.84172	–681.85025	–0.65340	–0.67441	0.20	1.13	2.12	–1.62549
P_2 - $^1\Sigma_g$ ($D_{\infty h}$) [e]	–681.84189	–681.85080	–0.65340	–0.67441	0.20	1.13	2.12	–1.62549
P_4 - $^1A_1$ (T_d)	–1363.77256	–1363.79264	–1.30798	–1.34968	0.83	3.84	3.40	–3.25105
P_4 - $^1A_1$ (T_d) [d]	–1363.77256	–1363.79168	–1.30798	–1.34968	0.83	3.84	3.40	–3.25105
P_4 - $^1A_1$ (T_d) [e]	–1363.77274	–1363.79233	–1.30798	–1.34968	0.83	3.84	3.40	–3.25105
PH - $^3\Sigma$ ($C_{\infty v}$)	–341.44587	–341.44963	–0.32637	–0.33675	0.08	3.29	2.07	–0.81280
PH_2 - $^2B_1$ (C_{2v})	–342.07416	–342.07892	–0.32660	–0.33697	0.16	8.26	2.38	–0.81249
PH_3 - $^1A'$ (C_s)	–342.71361	–342.71915	–0.32685	–0.33721	0.26	14.79	2.42	–0.81222
P_2H_2 - ^1A_g (C_s)	–683.02997	–683.04004	–0.65348	–0.67431	0.35	10.90	2.63	–1.62437
P_2H_4 - ^1A_g (C_s)	–684.24539	–684.25625	–0.65369	–0.67442	0.51	21.52	3.30	–1.62460
PO - $^2\Sigma$ ($C_{\infty v}$)	–416.05555	–416.06728	–0.38065	–0.39187	0.23	1.77	2.08	–0.86497
PO_2 - $^2A_1$ (C_{2v})	–491.25104	–491.27104	–0.43455	–0.44653	0.46	3.94	2.60	–0.91602
PO_3 - $^2A_2''$ (D_{3h})	–566.40722	–566.43531	–0.48881	–0.50135	0.59	5.65	3.40	–0.96742
P_2O - $^1\Sigma$ ($C_{\infty v}$)	–756.99067	–757.00777	–0.70762	–0.72935	0.54	3.40	2.84	–1.67676
P_2O_2 - ^1A_g (D_{2h})	–832.19200	–832.21693	–0.76187	–0.78362	0.61	5.62	2.92	–1.72910

Table 5.1. continued

	CCSD(T) (aug-) cc-pV5Z+*d*	CCSD(T) CBS(x^{-3})	CV corr1 [a]	CV corr2 [b]	CP(CV corr2) [c] /kcal mol^{-1}	ZPE /kcal mol^{-1}	$H_{298} - H_0$ /kcal mol^{-1}	E_{rel}
HPO - ^{1}A′ (C_s)	–416.66743	–416.67983	–0.38068	–0.39180	0.29	6.09	2.40	–0.86449
HPOH - ^{2}A″ (C_s)	–417.26372	–417.27646	–0.38084	–0.39176	0.25	13.39	2.63	–0.86372
H_2POH - ^{1}A′ (C_s)	–417.89452	–417.90796	–0.38095	–0.39183	0.33	19.43	2.81	–0.86396
H_3PO - ^{1}A$_1$ (C_{3v})	–417.89612	–417.91002	–0.38055	–0.39161	0.45	19.07	2.51	–0.86326
HOPO - ^{1}A′ (C_s)	–491.90932	–491.92982	–0.43510	–0.44683	0.38	10.95	2.77	–0.91634
$HOPO_2$ - ^{1}A′ (C_s)		–567.13090	–0.48901	–0.50149	0.59	14.36	3.13	–0.96707
H	–0.49999	–0.50005	0.00000	0.00000			1.01	0.00000
O	–75.00041	–75.00653	–0.05354	–0.05414			1.04	–0.05230
P	–340.82973	–340.83229	–0.32617	–0.33656			1.28	–0.81296
P [d]	–340.82973	–340.83208	–0.32617	–0.33656			1.28	–0.81296
P [e]	–340.82980	–340.83235	–0.32617	–0.33656			1.28	–0.81296

[a] Calculated using Dunning's cc-pCV*n*Z basis sets, Refs 27, 29, 32.

[b] Calculated using Bauschlicher's core-valence basis sets, Ref. 15.

[c] Counterpoise correction for BSSE on P atoms in CV corr2.

[d] Extrapolation process includes the cc-pV6Z+*d* energy.

[e] Calculated using cc-pCV(*n*+*d*)Z basis sets, Ref. 56.

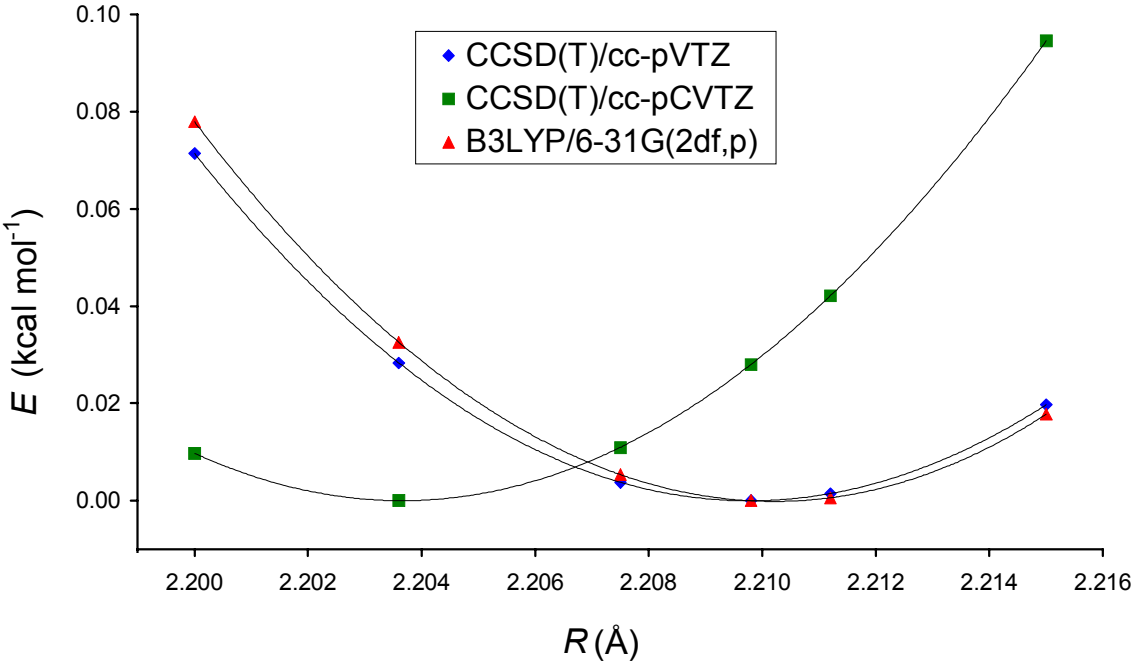

Figure 5.1 P_4: Comparison of computed equilibrium geometries and potential energy surfaces with respect to the symmetric stretch.

5.3.1.2 Atomisation Energies and Extrapolation Schemes

It is generally recognised that atomisation energies provide a far more convenient tool than absolute energies for investigating the merits of the various extrapolation schemes and the relative magnitudes of the corrections involved in the calculations of thermochemistry. Therefore a range of these, as obtained with all three basis sets used for valence correlated calculations (triple-, quadruple- and pentuple-ζ) and all four extrapolation methods, along with the CV and scalar relativistic corrections are listed in **Table 5.2**. We note here that in the case of $HOPO_2$ the RCCSD(T)/(aug-)cc-pV5Z+*d* calculation proved too demanding for our computing resources and for this molecule therefore, as in Bauschlicher's work, the extrapolations (for $HOPO_2$ and its atoms) are based on the triple- and quadruple-ζ energies alone ({T,Q}). (This necessarily means that only the l_{max} and x^{-3} extrapolation schemes could be implemented for $HOPO_2$.) Bauschlicher expressed some concern about this in his paper, stating that the two-point {T,Q} extrapolation is likely to result in an overestimation of the atomisation energy by 0.85 kcal mol^{-1}.

Table 5.2 Atomisation energies at 0K (including zero point energy and spin-orbit corrections; all energies in kcal mol^{-1}).

	CCSD(T) (aug-) cc-pVTZ+*d*	CCSD(T) (aug-) cc-pVQZ+*d*	CCSD(T) (aug-) cc-pV5Z+*d*	CCSD(T) CBS(*mix*)	CCSD(T) CBS($l_{\max}$)	CCSD(T) CBS ($n^{-4}+n^{-6}$)	CCSD(T) CBS(x^{-3})	CCSD(T) CBS(x^{-3}) + CV corr1 [a]	CCSD(T) CBS(x^{-3}) + CV corr2 [b]	CCSD(T) CBS(x^{-3}) + CV corr2 + CP(CV)	CCSD(T) CBS(x^{-3}) + CV corr2 + CP(CV) + E_{rel}
P_2	104.4	110.9	113.2	114.6	114.9	115.1	115.7	116.3	116.5	116.3	116.0
P_2 [c]	104.4	110.9	113.2	114.7	115.0	115.3	115.6	116.3	116.4	116.2	116.0
P_2 [d]	104.6	111.0	113.3	114.6	114.9	115.2	115.6	116.3	116.4	116.2	116.0
P_4	257.8	274.5	280.8	284.5	284.9	286.1	287.0	289.1	289.1	288.3	287.8
P_4 [c]	257.8	274.5	280.8	284.6	285.2	286.3	286.9	289.0	289.1	288.3	287.8
P_4 [d]	258.6	274.6	280.8	284.4	284.6	286.5	286.6	288.7	288.8	288.0	287.5
PH	67.2	69.1	69.6	69.9	70.1	70.0	70.3	70.4	70.4	70.3	70.2
PH_2	140.7	144.2	145.1	145.7	146.0	145.8	146.4	146.7	146.7	146.5	146.2
PH_3	220.2	224.8	226.1	226.9	227.3	227.0	227.9	228.3	228.3	228.0	227.6
P_2H_2	210.9	219.0	221.6	223.1	223.7	223.6	224.6	225.4	225.4	225.0	224.1
P_2H_4	334.1	343.3	346.2	347.8	348.5	348.3	349.6	350.5	350.5	349.9	349.1
PO	132.6	137.7	139.5	140.6	140.8	141.0	141.5	142.1	142.2	142.0	141.8
PO_2	247.5	256.3	259.5	261.4	261.6	262.1	262.7	263.5	263.8	263.3	262.4
PO_3	338.8	350.9	355.3	357.9	358.3	358.9	359.8	361.0	361.2	360.7	359.1
P_2O	190.7	200.5	204.0	206.0	206.4	206.7	207.6	208.7	208.9	208.4	207.5
P_2O_2	310.9	323.4	327.6	330.0	330.8	330.8	332.3	333.9	333.7	333.1	332.2

Table 5.2 continued

	CCSD(T) (aug-) cc-pVTZ+*d*	CCSD(T) (aug-) cc-pVQZ+*d*	CCSD(T) (aug-) cc-pV5Z+*d*	CCSD(T) CBS(*mix*)	CCSD(T) CBS($l_{\max}$)	CCSD(T) CBS ($n^{-4}+n^{-6}$)	CCSD(T) CBS(x^{-3})	CCSD(T) CBS(x^{-3}) + CV corr1 [a]	CCSD(T) CBS(x^{-3}) + CV corr2 [b]	CCSD(T) CBS(x^{-3}) + CV corr2 + CP(CV)	CCSD(T) CBS(x^{-3}) + CV corr2 + CP(CV) + E_{rel}
HPO	197.1	203.2	205.3	206.6	206.9	207.0	207.6	208.2	208.3	208.0	207.5
HPOH	250.1	256.6	258.5	259.6	260.2	259.8	261.0	261.7	261.6	261.4	260.4
H_2POH	324.7	332.3	334.5	335.8	336.5	336.1	337.4	338.2	338.1	337.8	337.0
H_3PO	324.6	333.1	335.9	337.5	338.0	338.0	339.1	339.6	339.6	339.2	337.9
HOPO	339.2	348.6	351.8	353.6	354.2	354.3	355.3	356.5	356.6	356.2	355.4
$HOPO_2$	449.8	463.2			470.6		473.0	474.4	474.6	474.0	472.4

[a] Calculated using Dunning's cc-pCVTZ basis sets, Refs 27, 29, 32.

[b] Calculated using Bauschlicher's core-valence basis sets, Ref. 15.

[c] Extrapolation includes the cc-pV6Z+*d* atomisation energy: $AE(P_2)$ = 114.2 kcal mol^{-1}, $AE(P_4)$ = 283.2 kcal mol^{-1}.

[d] Calculated using the cc-pV(*n*+*d*)Z basis sets, Ref. 56.

On inspection of the results in **Table 5.2** it can be seen that the atomisation energies increase by approximately 6 to 10 kcal mol^{-1} as the basis set is enlarged from triple- to quadruple-ζ and then by another 2 to 4 kcal mol^{-1} when going to the pentuple-ζ basis set. These corrections scale roughly with molecular size, viz. number of electrons, as expected, becoming as large as 16.7 kcal mol^{-1} (TZ to QZ) and 6.4 kcal mol^{-1} (QZ to 5Z) for the largest molecule in the set, P_4. Some degree of scatter is found among the atomisation energies given by the various extrapolation schemes. The x^{-3} scheme consistently yields the largest values, increasing the atomisation energy by roughly the same amount as the QZ to 5Z gap, while the mixed exponential/Gaussian extrapolation gave the lowest results, only increasing the *AE* by half of this amount. As a result, the scatter is also found to increase with molecular size; in general it is less than 2 kcal mol^{-1}, but it rises to ~ 2.4 kcal mol^{-1} for P_2O_2 and P_4. As the uncertainties in the computed *AE*'s are also expected to increase with the number of electrons, the observed scatter in the extrapolated results is expected to provide a reasonable measure of the expected errors in the *AE*'s. Based on this scatter, therefore, our estimated uncertainties are ± 1 kcal mol^{-1} for PH, PH_2, PH_3, P_2, PO and HPO, ± 1.5 kcal mol^{-1} for P_2H_2, PO_2, P_2O, HPOH, H_2POH, H_3PO and HOPO, ± 2 kcal mol^{-1} for P_2H_4 and PO_3 and ± 2.5 kcal mol^{-1} for P_4 and P_2O_2. While for $HOPO_2$ the uncertainty cannot be estimated this way, it is comparable in size to PO_3, and thus the same uncertainty is assigned to both.

As a test of the extrapolations, for P_2 and P_4 we computed the next energies in the sequence, that is, with the cc-pV6*Z*+*d* basis (the additional *d* exponent was 12.9024) and re-fitted these according to Equations (5.1) - (5.4). As can be seen from the results in **Table 5.2**, the 6*Z* calculations add 1.0 kcal mol^{-1} to the 5*Z* atomisation energy for P_2 and 2.4 kcal mol^{-1} for P_4. However, no appreciable difference can be discerned between the {T,Q,5} and {T,Q,5,6} extrapolated atomisation energies or the scatter among each set of energies.

The fits to the calculated atomisation energies of P_4 (including the 6*Z* result) are shown in graphical form in **Figure 5.2**. The plots nicely illustrate the asymptotic behaviour of the various equations utilised in the fits and extrapolations. The $l_{\max}$ and *mix* procedures suggest rapid convergence to the hypothetical CBS limit, while convergence (to a higher CBS limit) is slower for the x^{-3} and $n^{-4}+n^{-6}$ approaches. While the latter two procedures, along with *mix*, provide fits of comparable quality to the computed points, the $l_{\max}$ fit is found to be significantly poorer. Clearly, more energy points would be required before a definitive choice

between the *mix* and x^{-3} (or $n^{-4}+n^{-6}$) could be made on the basis of quality of fit. Nevertheless, in light of the accumulated compelling numerical evidence from other workers[16,17] concerning the accuracy and reliability of the x^{-3} procedure, we too have adopted it in this work as our preferred extrapolation technique.

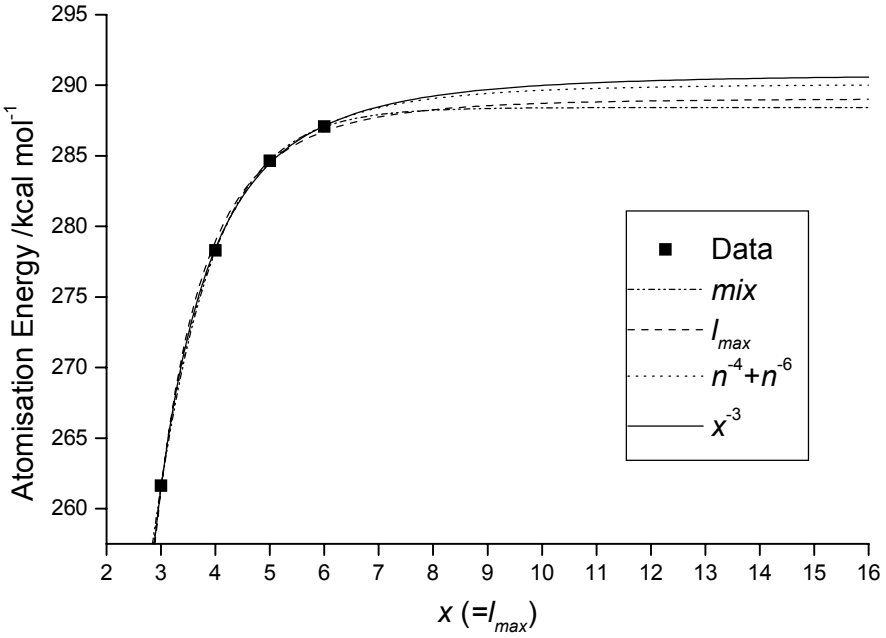

Figure 5.2 P_4: Comparison of fits to CCSD(T)/cc-pV*n*Z+*d* atomisation energies.

After the completion of this work it was suggested by Klopper and Radom[55] that, in the context of the x^{-3} extrapolation scheme, better quality results could be obtained by fitting only the final two energies in a given sequence, rather than by the inclusion of all $x \geq 3$ points, as has been done in this work. On testing this procedure for the current set of molecules it was found that the x^{-3} extrapolation of the QZ and 5Z energies ({Q,5}) yields atomisation energies which agree with those obtained by the three-point fits (as listed in **Table 5.2**) to within 0.3 kcal mol^{-1} for all systems except P_4, PH_3, P_2H_4, P_2O_2, HPOH, and H_2POH, where the differences between the two- and three-point fits are 0.5, –0.4, –0.5, –0.4, –0.5, and –0.6 kcal mol^{-1} respectively. In the case of P_4, however, the two-point fit of the 5Z and 6Z energies ({5,6}) yields an extrapolated atomisation energy which is 0.4 kcal mol^{-1} *lower* than obtained by the three-point {T,Q,5} and four-point {T,Q,5,6} fits. Such fluctuation may be interpreted as a measure of the degree of convergence and is thus indicative of the expected uncertainty in the atomisation energy of P_4. This uncertainty, we believe, is adequately accommodated by the proposed conservative error estimate of ± 2.5 kcal mol^{-1}. In light of these results, given

the relatively small differences between the two- and three-point fits relative to the proposed uncertainties, the heats of formation are calculated from the latter, that is, the atomisation energies in **Table 5.2**.

Recently, Dunning et al.[56] formulated a new set of (re-optimised) correlation consistent basis sets for second row atoms, denoted cc-pV(*x*+*d*)Z, which also include an additional tight *d* function in the basis. By way of comparison, we have carried out a set of calculations with this new set for P_2 and P_4. The resulting atomisation energies are given in **Table 5.2**. Clearly, there is very little difference (no more than 0.4 kcal mol^{-1}) between the extrapolated energies generated by this new cc-pV(*x*+*d*)Z and the "standard" cc-pV*x*Z+*d* basis sets. Since P_4 is effectively the largest of our systems of interest, such basis set effects are expected to be even less pronounced for the other molecules. This is clearly borne out for P_2.

5.3.1.3 Core-Valence Correlation, BSSE and Scalar Relativistic Effects

A legitimate question in the context of atomisation energy calculations concerns the presence and importance of basis set superposition error (BSSE). As the basis set is systematically expanded the magnitude of any BSSE will be reduced, so one may expect the extrapolated energy to be essentially free of superposition errors. As a test of this hypothesis, we applied the appropriate CP corrections to the energies of P_4 at the CCSD(T)/cc-pV*x*Z+*d* levels of theory (*x* = T, Q, 5) and extrapolated these to the CBS limit, as described above. The resulting CP corrections to the extrapolated atomisation energies are –0.46, –0.40, 0.19, and 0.0006, as obtained by the *mix*, $l_{\max}$, x^{-3} and $n^{-4}+n^{-6}$ procedures respectively. Thus, the $n^{-4}+n^{-6}$ extrapolation scheme can be seen to display near-ideal behaviour, as the "extrapolated" BSSE is effectively zero. Given that the actual CP correction at the CCSD(T)/cc-pV5Z+*d* levels of theory is only –0.67 kcal mol^{-1}, an extrapolated correction of ~ –0.5 kcal mol^{-1}, obtained by the *mix* and $l_{\max}$ methods is regarded as unrealistic. The positive correction of ~ 0.2 kcal mol^{-1}, corresponding to the x^{-3} approach, while non physical, is probably a reflection of the fact that the CP method itself is approximate. On the whole, in the light of these results, we believe that the x^{-3} and $n^{-4}+n^{-6}$ extrapolated atomisation energies can be accepted as being essentially free of BSSE artefacts.

The CV contributions to the *AE*'s are relatively small. Moreover, in the absence of CP corrections, both basis sets used to compute CV effects, namely Dunning's cc-pCVTZ (CV corr1) and Bauschlicher's core-valence sets (CV corr2), yield essentially identical results. The CP corrections are, however, significantly smaller when using Bauschlicher's basis, by up to 0.5 kcal mol^{-1} (in the case of P_4), suggesting that it is a better balanced basis in the context of CV calculations. Therefore, the heats of formation reported in the next section are based on *AE*'s generated via the x^{-3} extrapolation and CV corrections obtained via Bauschlicher's basis set, with the inclusion of CP corrections for BSSE.

The CV contribution to the *AE* is largest for P_4, as might be expected, where the CP corrected and uncorrected (CV corr2) values are 1.3 and 2.1 kcal mol^{-1} respectively. As indicated in the previous section, such corrections were applied only to the phosphorus atoms in each molecule, as corrections to the oxygen atoms are expected to be an order of magnitude smaller. This has been verified by computing the oxygen CP corrections in PO_3 and PPO, which resulted in BSSE estimates of 0.01 kcal mol^{-1} for each oxygen atom (in both molecules), compared with 0.59 kcal mol^{-1} for the phosphorus atom in PO_3 or with 0.54 and 0.28 kcal mol^{-1} for the two P atoms in PPO. Accepting the CP corrected CV values as the more reliable, we see that the CV contribution to *AE*'s is generally ~ 1 kcal mol^{-1} or less.

It is also clear from the data in **Table 5.2** that both CV and scalar relativistic corrections are relatively minor in comparison with the effects of extrapolation. In most cases the scalar relativistic corrections are less than ~ 1 kcal mol^{-1}. In addition, there is some cancellation between these two contributions, so that the net effects of CV and scalar relativistic corrections to the *AE*'s are often below ~ 0.5 kcal mol^{-1}.

The above observations concerning the relative importance of CV corrections in the computation of atomisation energies and heats of formation, however, are in disagreement with the findings of Persson et al.[57], who reported a value of ~ 6 kcal mol^{-1} as the CV correction to the energy of the $P_4 \rightarrow 2P_2$ reaction. This result was obtained by MP2 computations in a [6*s*,5*p*,4*d*,3*f*,2*g*,1*h*] atomic natural orbital (ANO) basis. Subsequent investigations, however, revealed that the exponent range of the polarisation functions used in the construction of the ANO's was not adequate to describe the 2*s*2*p* correlation reliably.[58] For a P atom this ANO basis resolves only ~ 60% of the CV correlation energy obtained with

the cc-pCVTZ basis, while with regard to the CV component of the energy of the $P_4 \rightarrow 2P_2$ reaction the results of subsequent counterpoise calculations are indicative of substantial superposition errors.

5.3.2 G3, G3X and G3X2 Calculations

The computed atomisation energies obtained by application of the G3, G3X, G3X2 and G3X2(RAD) methods are displayed in **Table 5.3**, along with the (R)CCSD(T)/CBS benchmark values for ready comparison. As discussed in **Section 5.2**, G3X2 represents an approximation to the QCISD(T,Full)/G3XLarge method (provided the latter also includes the G3X higher level correction). It is therefore instructive to compare the G3X2 atomisation energies with those obtained by QCISD(T,Full)/G3XLarge calculations. Such QCI results for P_4, PH, P_2H_2, P_2O, HPO and HOPO are thus also included in **Table 5.3**. These results are to be compared with the benchmark energies, both with and without the scalar relativistic corrections, since there seems to be some doubt as to whether G3 type results should be compared with benchmarks that include scalar relativistic corrections. The study by Kedziora et al.[59] concluded that in G3 such corrections are in fact compensated for by the higher level corrections and that their explicit inclusion in the G3 methodology leads to slightly worse agreement with experiment (even when the hlc is reoptimised).

In the previous chapter it was shown that it was necessary to employ restricted open shell methods when performing G3*n* type calculations for the PO radical since large spin contamination occurred in some of the UHF calculations. While no comparable spin contamination could be discerned for the other radical species studied here (atoms and molecules), we investigated whether the use of the G3*n*(RAD) procedure would be superior to the standard method. As the results in **Table 5.3** demonstrate, there is little difference between the standard G3X2 and G3X2(RAD) generated atomisation energies. Therefore, the routine use of G*n*(RAD) procedures for open shell atoms and molecules is unwarranted, unless the unrestricted formalism is unusable due to spin contamination. Note, however, that in the case of PO, where the UHF based formalisms are inapplicable, all the G*n* results quoted in **Table 5.3** are actually G*n*(RAD) values.

Table 5.3 Comparison of atomisation energies at 0K from CCSD(T)/CBS benchmark and G3*n* calculations (including zero point energy and spin-orbit corrections; all energies in kcal mol^{-1}).

	CCSD(T) CBS [a]	CCSD(T) CBS [b]	G3	G3X	G3X2	G3X2 + CP(CV)	G3X2 (RAD)[c]	QCI [d]
P_2	116.0	116.3	114.9	116.1	120.4	119.2	120.3	120.5
P_4	287.8	288.3	281.7	283.7	296.6	292.7	296.2	293.6
PH	70.2	70.3	70.8	71.1	71.9	71.8	72.6	73.0
PH_2	146.2	146.5	145.1	145.6	147.2	146.9	147.6	
PH_3	227.6	228.0	225.3	226.0	228.3	227.8	228.2	
P_2H_2	224.1	225.0	221.5	222.7	227.6	226.4		228.2
P_2H_4	349.1	349.9	344.3	345.8	351.0	349.7		
PO [c]	141.8	142.0	141.3	141.9	143.2	142.4	143.2	
PO_2	262.4	263.3	260.2	261.9	264.1	262.5	262.2	
PO_3	359.1	360.7	352.6	357.7	360.9	358.6	360.5	
P_2O	207.5	208.4	203.6	205.8	211.2	208.9	209.9	213.0
P_2O_2	332.2	333.1	327.3	330.5	334.8	332.6	334.5	
HPO	207.5	208.0	205.6	207.1	209.1	208.2	208.8	209.2
HPOH	260.4	261.4	258.5	259.3	261.1	260.3	260.7	
H_2POH	337.0	337.8	333.6	334.7	337.1	336.2	336.6	
H_3PO	337.9	339.2	333.4	335.0	337.8	336.7	337.0	
HOPO	355.4	356.2	351.7	353.7	355.8	354.4	355.2	355.5
$HOPO_2$	472.4	474.0	466.5	469.1	472.2	469.9	471.2	

[a] Including scalar relativistic corrections.

[b] Not including scalar relativistic corrections.

[c] Calculated by G3*n*(RAD) methods.

[d] QCISD(T,Full)/G3XLarge calculation including G3X higher level correction.

When compared with the benchmark atomisation energies, it is clear, as already noted by Curtiss et al., that G3 performs relatively poorly for molecules containing second row atoms. The G3 atomisation energies are found to be consistently too low, by over 6 kcal mol^{-1} in the worst case ($HOPO_2$). It should be noted, however, that in the case PO_3 much of the 6.5 kcal mol^{-1} difference between the G3 and benchmark results can be traced to the large difference between the respective zero point energies (computed at the UHF/6-31G(*d*) and UB3LYP/ 6-31G(2*df*,*p*) levels of theory respectively), as discussed in **Chapter 4**. For the molecules of this study, the root-mean-square (rms) deviation between the G3 and benchmark results is 3.8

kcal mol^{-1} when the latter include scalar relativistic correction. The deviation is 4.6 kcal mol^{-1} in the absence of such corrections.

In most cases the G3X atomisation energies are found to be appreciably closer to the benchmark results than those from G3 calculations. The superior performance of G3X is partly due to the introduction of the G3XLarge correction, which increases the atomisation energies by typically ~ 0.5 kcal mol^{-1}, as indicated by the data in **Table 5.4**. The use of DFT optimised geometries instead of MP2 is found to yield significantly lower total energies for all phosphorus oxides and acids (and P_4) and hence higher atomisation energies, by ~ 0.5 kcal mol^{-1} on the average. The differences in G3 and G3X zero point energies, with the exception of PO_3, are quite small at ~ 0.2 kcal mol^{-1}. However, as the data in **Table 5.4** shows, the hlc's contribution to the atomisation energies are quite large and the small differences between the G3X and G3 hlc parameters are responsible for an additional ~ 0.5 kcal mol^{-1} difference in the resulting atomisation energies. For the phosphorus compounds of this work the combined effect of the changes to G3, that define G3X, is that the rms deviations between the G3X and benchmark results (with and without scalar relativistic corrections) are significantly lower at 2.8 and 2.0 kcal mol^{-1} respectively. However, the atomisation energies are still underestimated by up to ~ 4 kcal mol^{-1}.

At first sight, the G3X2 calculations do not seem to represent a significant improvement over G3X. Whereas G3X generally underestimates the *AE*'s, G3X2 overestimates them by a comparable amount, due to much larger G3XLarge corrections (**Table 5.4**) which in G3X2 are evaluated at the MP2 level. However, with one exception (P_4), the G3X2 atomisation energies agree with the QCISD(T,Full)/G3XLarge values at least to within ± 2 kcal mol^{-1}. Four of the seven molecules (P_2, P_4, P_2H_2, P_2O) for which we carried out these large QCI calculations were chosen specifically because of the large deviations of their G3X2 atomisation energies from the benchmarks. The overall good agreement between the G3X2 and QCI results suggests that with the exception of "pathological" cases, such as P_4, the G3X2 approach is capable of providing a good approximation to a QCISD(T,Full)/G3XLarge calculation. Note that G3X represents a lower level of electron correlation treatment, since it is an approximation to QCISD(T,Full) with the smaller G3Large basis, where the energetic effects of basis set extension to G3XLarge is obtained at the SCF level. In spite of this, G3X2 actually appears to be inferior to G3X when comparing the rms deviations from the

Table 5.4 Various components of the G3X and G3X2 atomisation energies at 0K (in kcal mol^{-1}).

	SCF G3XLarge correction	MP2(Full) G3XLarge correction	CP(CV) correction of G3X2	G3X hlc
P_2	0.2	4.5	–1.1	8.3
P_4	0.8	13.7	–3.8	16.6
PH	0.0	0.9	–0.2	5.2
PH_2	0.1	1.7	–0.3	6.8
PH_3	0.1	2.4	–0.4	8.4
P_2H_2	0.3	5.2	–1.2	11.1
P_2H_4	0.3	5.5	–1.3	13.9
PO [a]	0.4	1.8	–0.8	6.7
PO_2	0.7	3.0	–1.6	9.3
PO_3	1.1	4.2	–2.3	12.0
P_2O	0.6	6.0	–2.2	11.0
P_2O_2	1.9	6.2	–2.2	13.7
HPO	0.4	2.4	–0.9	8.3
HPOH	0.5	2.2	–0.7	9.5
H_2POH	0.5	2.9	–0.9	11.1
H_3PO	0.5	3.3	–1.1	11.1
HOPO	0.8	2.8	–1.4	10.9
$HOPO_2$	1.1	4.2	–2.3	13.6

[a] Calculated by G3*n*(RAD) methods.

benchmark. In the case of G3X2 these are 2.9 and 2.6 kcal mol^{-1} respectively, when the benchmarks do and do not include scalar relativistic corrections. The apparent inferiority to G3X is, however, largely due to the inclusion of P_4, an extreme outlier, for which G3X2 predicts the atomisation energy to be up to ~ 9 kcal mol^{-1} higher than the benchmark. For this molecule the failure of the G3X2 procedure is partly due to a 3 kcal mol^{-1} overestimation of the QCISD(T,Full)/G3XLarge atomisation energy, which itself is a further 5 kcal mol^{-1} higher than the benchmark. For several other molecules, however, due to the fortuitous cancellation of errors, the G3X2 results agree slightly better with the benchmarks than those obtained by QCI. P_4 is clearly a special case, and as such, it will be the subject of a more

detailed discussion later in this chapter. At this point, however, it is reasonable to re-evaluate the rms errors when P_4 is removed from the test set. These are now 3.6 and 4.5 kcal mol^{-1} for G3; 1.8 and 2.7 kcal mol^{-1} for G3X and 2.1 and 1.7 kcal mol^{-1} for G3X2, the two sets of values corresponding to the inclusion and exclusion of scalar relativistic corrections in the benchmark results respectively. Thus, G3X2 represents a modest improvement upon G3X theory for this set of molecules, when compared with benchmark values without scalar relativistic corrections.

As remarked already, a legitimate modification of G3X and G3X2 would be to consider corrections to the CV component of the atomisation energies for BSSE. The computed corrections to the G3X2 energies, that is, at the MP2/G3XLarge level of theory, are given in **Table 5.4**. They range from −3.8 to −0.2 kcal mol^{-1} and reduce the rms deviation from the benchmark values (with and without scalar relativistic corrections) to 1.8 and 2.0 kcal mol^{-1} respectively. Omitting P_4 from the set results in further reductions in the above deviations to 1.5 and 1.8 kcal mol^{-1}. The analogous corrections to G3X are somewhat smaller but as they are negative their impact would be to degrade the agreement between the G3X and benchmark values. The introduction of these proposed modifications of course necessitates changes to the higher level corrections. As the current set of molecules is too small and not sufficiently representative, no modifications to the hlc are proposed at this stage. Further work is under way, however, to produce G3X2 atomisation energies for all the molecules in the G3/99 test set which contain second row atoms. This will allow re-optimisation of the hlc in the presence of BSSE corrections as well as a fuller investigation of the need (or otherwise) to correct the G3X2 energies for scalar relativistic effects. With the current (G3X) choice of hlc the fluctuation in the deviations of both G3X and G3X2 results is such that, in the rms sense, a comparable level of agreement is achieved with the two sets of benchmark values. It is possible, however, that re-optimisation of the hlc on the basis of G3X2 data will change this apparent insensitivity to relativistic corrections as well as the magnitude of the above rms deviations.

The deviations of the G3X, G3X2 and QCISD(T,Full)/G3XLarge atomisation energies from the benchmark results (including scalar relativistic corrections) are summarised graphically in **Figure 5.3**. It can be clearly seen that in most cases G3X2 is a good approximation to QCISD(T,Full)/G3XLarge. Where the difference between G3X2 and QCI is largest, both are

seen to show relatively poor agreement with the corresponding benchmark result, although corrections to the CV components for BSSE (in both G3X2 and QCI) do improve the agreement. This occurs for P_4, as noted above, and also for PPO. Both are somewhat unusual molecules. Tetrahedral P_4, with 60º bond angles, is a very "strained" molecule, while the bonding in PPO is best described in terms of a P-P^+ triple bond and a P^+-O^- semipolar bond, as suggested by the results of a Roby-Davidson population analysis[60-62]. Thus it should not be too surprising that such molecules would be difficult to describe accurately.

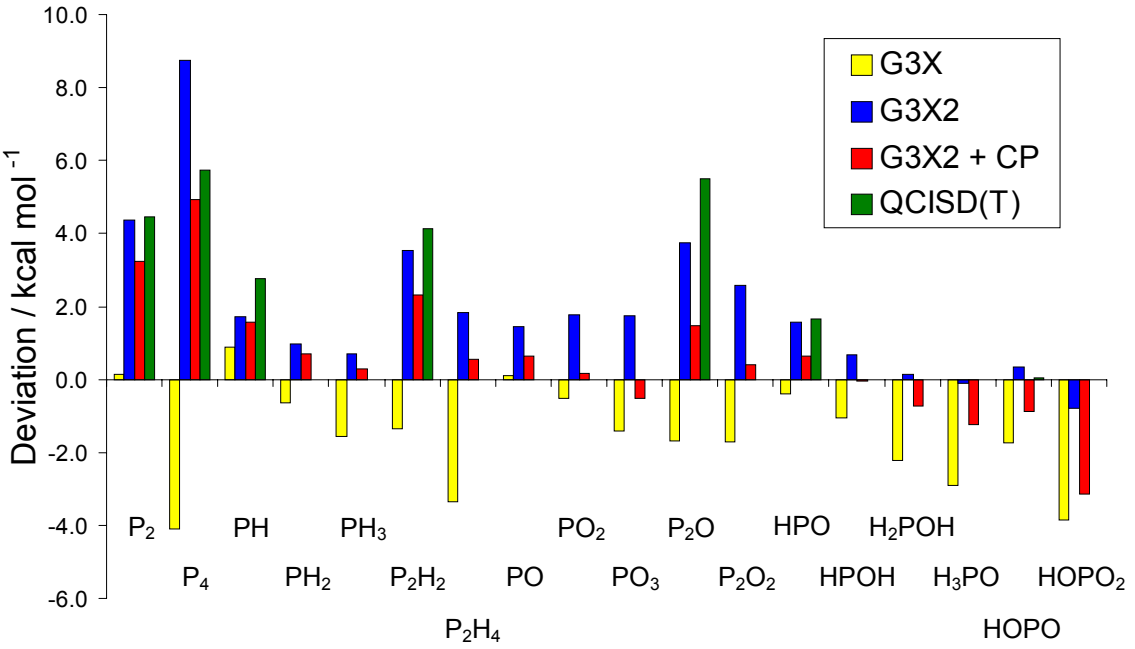

Figure 5.3 Deviations of G3X, G3X2 and QCISD(T,Full)/G3XLarge atomisation energies from CCSD(T)/CBS benchmark values (with scalar relativistic corrections).

As we expect that, in general, the G3X2 results would have an uncertainty of approximately ± 2 kcal mol^{-1}, it is noteworthy that all the molecules which fall outside this range (P_2, P_4, P_2H_2 and PPO) have multiple or strained P-P bonds. As P_2H_4 (with a P-P single bond) and P_2O_2 (with two phosphorus atoms but no P-P bond) are both described adequately by G3X2, it appears that this method could be expected to provide a satisfactory description of molecules with second row atoms but care should be taken when these atoms have formal multiple bonds with each other. As remarked earlier, G3X produces atomisation energies that are consistently lower than the benchmark values, while in most cases the G3X2 results are on the

high side. There is only one molecule, $HOPO_2$, for which the G3X2 atomisation energy is significantly below the benchmark result; however, as noted in the previous section, the latter may be 0.85 kcal mol^{-1} too high due to the absence of the CCSD(T)/(aug-)cc-pV5Z+*d* energy in extrapolations.

5.3.2.1 Analysis of Molecules for Which G3n Methods Perform Poorly

5.3.2.1.1 P_4

As noted above, in the case of P_4 there is significant deviation between the G3X2 atomisation energies and those resulting from QCISD(T,Full)/G3XLarge calculations. The discrepancy suggests at least a partial failure of the underlying assumption of G3 type theories for P_4; that is, that as the basis set is extended, the increased degree of correlation can be adequately approximated by lower levels of theory than QCISD(T). In order to identify the actual source of this problem, the individual G3X and G3X2 corrections, namely (+), (2*df*,*p*), G3Large, G3XLarge and G3X2, as defined in Equations (5.5) to (5.8), computed using MP4, MP2 (and SCF in the case of G3XLarge), are compared with the corresponding corrections evaluated by QCISD(T). The results for the phosphorus atom and P_4 are given in **Table 5.5**. In the case of P, the agreement between the corrections obtained by QCISD(T) and the relevant lower levels of theory is clearly very good, as may be expected. The largest discrepancy is 0.7 kcal mol^{-1} (in the MP2 determination of the G3Large correction) but in the case of G3X2 this is largely cancelled by the negative discrepancy in the G3XLarge term. Somewhat fortuitously, thus, G3X2 represents an excellent approximation to the QCI energy in the case of P. The situation is quite different for P_4, where MP4 overestimates the magnitude of the (2*df*,*p*) correction by 3.6 kcal mol^{-1}. The trends and deviations in the other corrections, specifically the G3Large and G3XLarge corrections, are similar to those observed for the phosphorus atom, provided we allow for the presence of four atoms in the molecule. Therefore, the major deviation between the G3X2 and QCI atomisation energies of P_4 results from the poor performance of MP4 in the prediction of the (2*df*,*p*) correction, as shown by the analysis of the atomisation energy in **Table 5.5**. The total error in the G3Large and G3XLarge terms as obtained by MP2 is −1.1 kcal mol^{-1}. Thus again there is some fortuitous error cancellation, resulting in a total discrepancy of 3.0 kcal mol^{-1} in the G3X2 atomisation energy of P_4.

Table 5.5 Basis set enlargement corrections to total G3X and G3X2 energies of P_4 and P and to the atomisation energy of P_4 at various levels of theory (in kcal mol^{-1}).

		P_4		P		Contribution to Atomisation Energy	
Correction	Level of Theory	Absolute correction	Deviation from QCISD(T) [a]	Absolute correction	Deviation from QCISD(T) [a]	Absolute correction	Deviation from QCISD(T) [a]
+	MP4	–4.3	–0.2	–0.6	0.0	2.0	0.2
	QCISD(T)	–4.1		–0.6		1.8	
2*df*,*p*	MP4	–118.8	–3.6	–16.3	0.1	53.5	3.8
	QCISD(T)	–115.2		–16.4		49.7	
G3Large	MP2(Full)	–797.6	3.6	–198.3	0.7	4.4	–0.7
	MP4(Full)	–803.3	–2.1	–199.1	0.0	7.0	1.9
	QCISD(T,Full)	–801.2		–199.0		5.1	
G3XLarge	SCF	–0.8	18.4	0.0	1.3	0.8	–13.2
	MP2(Full)	–20.8	–1.6	–1.8	–0.5	13.7	–0.4
	MP4(Full)	–20.0	–0.8	–1.3	0.0	14.9	0.9
	QCISD(T,Full)	–19.2		–1.3		14.0	
G3X2	MP2(Full)	–818.4	2.0	–200.1	0.2	18.1	–1.1
	MP4(Full)	–823.3	–2.9	–200.3	0.0	21.9	2.8
	QCISD(T,Full)	–820.5		–200.3		19.2	

[a] QCISD(T,Full) for G3Large, G3XLarge and G3X2.

5.3.2.1.2 P_2O, P_2, P_2H_2

Analysis of G3X and G3X2 results, as applied to P_4, was also carried out for P_2O, P_2, P_2H_2 and HOPO. The various corrections to the atomisation energies and their deviation from the QCI values for these four molecules, as well as P_4 for ready comparison, are listed in **Table 5.6**. We recall that for P_4 and PPO significant discrepancy in the G3X2 atomisation energy has been noted in comparison with QCISD(T,Full)/G3XLarge while in the case of P_2 and P_2H_2 there were no major discrepancies however the results were in poor agreement with the benchmark calculations. In contrast to these species, good agreement was found between the G3X2, QCISD(T) and CCSD(T)/CBS results for HOPO. For this set of molecules, the (+) correction is found to be consistently the smallest (less than 5 kcal mol^{-1} but becoming larger as oxygen atoms are added); deviations of MP4 from QCI are found to be small (< 1 kcal mol^{-1}) and positive. The (2*df,p*) correction, on the other hand, is by far the largest (up to about 50 kcal mol^{-1} for P_4). The deviations between the MP4 and QCI corrections are again found to be small and positive for P_2, P_2H_2 and HOPO; for PPO the deviation is also small although negative, but for P_4, as mentioned earlier, it is significantly larger at +3.8 kcal mol^{-1}. The G3Large, G3XLarge and G3X2 corrections are of intermediate magnitude (4 - 10 kcal mol^{-1} for G3Large, 3 - 15 kcal mol^{-1} for correlated G3XLarge corrections and 10 - 20 kcal mol^{-1} for G3X2). We note that in general the MP2 results show slightly better agreement with QCISD(T) (0.5 - 1.5 kcal mol^{-1} deviation for G3X2) than MP4 (1.0 - 2.8 kcal mol^{-1}). In addition, the correction terms obtained by MP2 are slightly lower than at the QCI level (giving a negative deviation), whereas the MP4 differences are all positive. This leads to significant cancellation of errors when the (+) and (2*df,p*) (obtained by MP4) and G3X2 (by MP2) corrections are added, resulting in good agreement between the final QCISD(T) and G3X2 atomisation energies for P_2, P_2H_2 and HOPO. As noted above, in the case of P_4, the (2*df,p*) correction is too large to be compensated for by the G3X2 correction, while for PPO all errors, with the exception of that in the (+) term, tend to reinforce each other, leading to the observed lack of agreement between G3X2 and QCISD(T,Full)/G3XLarge.

Table 5.6 Basis set enlargement corrections to the atomisation energies of P_4, P_2O, P_2, P_2H_2 and HOPO evaluated at various levels of theory (in kcal mol^{-1}).

		P_4		P_2O		P_2	
Correction	Level of Theory	Correction	Deviation from QCISD(T) [a]	Correction	Deviation from QCISD(T) [a]	Correction	Deviation from QCISD(T) [a]
+	MP4	2.0	0.2	3.2	0.1	0.6	0.1
	QCISD(T)	1.8		3.1		0.5	
2*df*,*p*	MP4	53.5	3.8	29.9	–0.5	13.0	0.3
	QCISD(T)	49.7		30.3		12.7	
G3Large	MP2(Full)	4.4	–0.7	6.9	–1.1	4.4	–0.4
	MP4(Full)	7.0	1.9	9.4	1.4	5.7	0.9
	QCISD(T,Full)	5.1		8.0		4.8	
G3XLarge	SCF	0.8	–13.2	0.6	–5.8	0.2	–4.3
	MP2(Full)	13.7	–0.4	6.0	–0.4	4.5	–0.1
	MP4(Full)	14.9	0.9	6.8	0.4	4.8	0.3
	QCISD(T,Full)	14.0		6.4		4.5	
G3X2	MP2(Full)	18.1	–1.1	12.9	–1.4	8.9	–0.5
	MP4(Full)	21.9	2.8	16.2	1.9	10.5	1.2
	QCISD(T,Full)	19.2		14.3		9.4	

Table 5.6. continued

		P_2H_2		HOPO	
Correction	Level of Theory	Correction	Deviation from QCISD(T) [a]	Correction	Deviation from QCISD(T) [a]
+	MP4	0.8	0.1	4.3	0.9
	QCISD(T)	0.8		3.4	
2*df*,*p*	MP4	28.6	0.6	32.7	0.6
	QCISD(T)	27.9		32.1	
G3Large	MP2(Full)	5.0	–0.9	8.5	–0.8
	MP4(Full)	6.5	0.6	10.3	1.0
	QCISD(T,Full)	5.9		9.3	
G3XLarge	SCF	0.3	–5.3	0.8	–2.4
	MP2(Full)	5.2	–0.4	2.8	–0.4
	MP4(Full)	5.8	0.3	3.4	0.2
	QCISD(T,Full)	5.6		3.2	
G3X2	MP2(Full)	10.2	–1.3	11.3	–1.2
	MP4(Full)	12.4	0.9	13.7	1.1
	QCISD(T,Full)	11.5		12.5	

[a] QCISD(T,Full) for G3Large, G3XLarge and G3X2.

5.3.3 Enthalpies of Formation

The heats of formation (at 0 and 298 K) of the molecules studied in this work, generated from the computed atomisation energies (**Table 5.3**), are listed **Table 5.7**, along with experimental and theoretical values from the chemical literature for comparison. For a number of molecules there has been an absence of experimental and/or theoretical values; for these the current calculations provide reliable heats of formation. For several others, where the imprecision in the literature values is quite large, we are able to offer improved data. It is gratifying, however, that in all cases the benchmark results agree with the accepted literature values within the respective error margins, even for P_4.

The information in **Table 5.7** also allows one to assess the performance of the G3, G3X and G3X2 methods in the context of thermochemistry. For most molecules, given the large experimental errors, there appears to be reasonable agreement between the available experimental heats of formation and those from any of the G3, G3X or G3X2 calculations, with the obvious exception of P_4. The differences are more evident if the comparisons are made with the benchmark values, in which case the G3X and G3X2 results are clearly superior to those of G3. As discussed already in the context of *AE*'s, in general G3X2 appears to be more accurate than G3X, especially if corrections for BSSE in the CV contributions are included in the calculations.

Table 5.7 Enthalpies of formation at 0 and 298K (in kcal mol^{-1}).

	Heat of Formation (0K)						Heat of Formation (298K)						
	CCSD(T) CBS [a]	G3	G3X	G3X2	G3X2 + CP(CV)	QCI [b]	CCSD(T) CBS [a]	G3	G3X	G3X2	G3X2 + CP(CV)	QCI [b]	Literature [c]
P_2	34.8	35.9	34.7	30.5	31.6	30.4	34.4 ± 1.0	35.5	34.3	30.0	31.2	29.9	34.3 ± 0.5 [d]
P_4	13.9	20.0	18.0	5.1	8.9	8.1	12.1 ± 2.5	18.2	16.2	3.4	7.2	6.4	14.1 ± 0.05 [d]
PH	56.8	56.2	55.9	55.1	55.2		56.6 ± 1.0	56.0	55.7	54.9	55.0		*60.6 ± 8.0* [e]
													57.4 ± 0.6 [f]
PH_2	32.4	33.5	33.1	31.5	31.8		31.5 ± 1.0	32.6	32.2	30.6	30.8		*26 ± 23* [g]
													33.1 ± 0.6 [f]
PH_3	2.8	5.0	4.3	2.1	2.5		0.9 ± 1.0	3.1	2.4	0.2	0.6		1.3 ± 0.4 [d]
P_2H_2	30.0	32.6	31.4	26.5	27.7	25.9	28.1 ± 1.5	30.6	29.4	24.6	25.8	23.9	
P_2H_4	8.2	13.1	11.6	6.4	7.7		4.9 ± 2.0	9.8	8.3	3.1	4.4		5.0 ± 1.0 [h]
PO [i]	–7.4	–6.9	–7.5	–8.8	–8.0		–7.6 ± 1.0	–7.1	–7.7	–9.0	–8.2		–5.6 ± 1.0 [d]
													–6.8 ± 1.9 [j]
													–7.8 [k]
PO_2	–69.0	–66.8	–68.5	–70.7	–69.1		–69.7 ± 1.5	–67.5	–69.2	–71.5	–69.9		–66.2 ± 3 [j]
													–70.3 [k]
PO_3	–106.7	–100.2	–105.3	–108.5	–106.2		–107.7 ± 2.0	–101.7	–106.3	–109.5	–107.2		*–107.5* [k]
P_2O	2.4	6.2	4.0	–1.4	0.9	–3.1	1.6 ± 1.5	5.5	3.3	–2.1	0.1	–3.9	
P_2O_2	–63.4	–58.5	–61.7	–66.0	–63.8		–65.1 ± 2.5	–59.8	–63.4	–67.7	–65.5		

Table 5.7 continued

	Heat of Formation (0K)						Heat of Formation (298K)						
	CCSD(T) CBS [a]	G3	G3X	G3X2	G3X2 + CP(CV)	QCI [b]	CCSD(T) CBS [a]	G3	G3X	G3X2	G3X2 + CP(CV)	QCI [b]	Literature [c]
HPO	–21.5	–19.6	–21.1	–23.1	–22.2		–22.4 ± 1.0	–20.5	–22.0	–24.0	–23.1		*–22.6* [k]
HPOH	–22.7	–20.9	–21.7	–23.4	–22.7		–24.4 ± 1.5	–22.5	–23.4	–25.1	–24.4		
H_2POH	–47.7	–44.3	–45.4	–47.8	–46.9		–50.2 ± 1.5	–46.8	–48.0	–50.3	–49.5		
H_3PO	–48.6	–44.1	–45.7	–48.5	–47.4		–51.5 ± 1.5	–46.9	–48.6	–51.4	–50.2		
HOPO	–110.4	–106.7	–108.7	–110.7	–109.7	–110.4	–112.0 ± 1.5	–108.3	–110.3	–112.3	–111.3	–112.0	–110.6 ± 3 [l]
													–112.4 [k]
$HOPO_2$	–168.3	–162.5	–165.1	–168.2	–165.9		–170.6 ± 2.0	–164.8	–167.4	–170.5	–168.1		–168.8 ± 4 [l]
													–171.4 [k]

[a] Including scalar relativistic corrections.

[b] QCISD(T,Full)/G3XLarge calculation including G3X higher level correction.

[c] Experimental values unless otherwise indicated by italics and footnotes.

[d] Ref. 63.

[e] Semiempirical estimate, Ref. 63.

[f] Ref. 64.

[g] Estimate, Ref. 63.

[h] Ref. 65.

[i] Calculated by G3*n*(RAD) methods.

[j] Ref. 66.

[k] RCCSD(T)/CBS computations, Ref. 15.

[l] Ref. 67.

5.4 Conclusion

Using the (R)CCSD(T) quantum chemical method in conjunction with correlation consistent basis sets, accurate heats of formation have been obtained for a series of small phosphorus containing molecules. These are regarded as convenient and useful benchmark values, especially in light of the paucity of accurate experimental values. The computed atomisation energies and hence heats of formation include complete basis estimates of valence correlation contributions, core-valence contributions which are corrected for basis set superposition and scalar relativistic corrections. The equilibrium geometries and vibrational frequencies were obtained by density functional theory. The resulting benchmark heats of formation are in good agreement with the available experimental and other high level quantum chemical data. Utilising the calculated benchmark values, we were able to carry out a critical study of the accuracy and reliability of three G3*n* type procedures, G3, G3X and G3X2, for phosphorus containing molecules. We have found that in general the G3X and G3X2 results are of comparable accuracy, both reproducing the benchmark heats of formation, on the average, to within ± 2 kcal mol^{-1}. The relative accuracy of G3X2 improves, however, on the introduction of BSSE corrections to the core-valence correlation contributions. The problem cases for the G3*n* methods appear to be molecules with unusual P-P bonding, such as P_2 and P_4.

5.5 References

1. A. Twarowski, *Combustion and Flame*, **1993**, *94*, 91.
2. A. Twarowski, *Combustion and Flame*, **1993**, *94*, 341.
3. A. Twarowski, *Combustion and Flame*, **1995**, *102*, 41.
4. A. Twarowski, *Combustion and Flame*, **1996**, *105*, 407.
5. O. P. Korobeinichev, S. B. Ilyin, T. A. Bolshova, V. M. Shvartsberg and A. A. Chernov, *Combustion and Flame*, **2000**, *121*, 593.
6. O. P. Korobeinichev, T. A. Bolshova, V. M. Shvartsberg and A. A. Chernov, *Combustion and Flame*, **2001**, *125*, 744.
7. M. A. MacDonald, F. C. Gouldin and E. M. Fisher, *Combustion and Flame*, **2001**, *124*, 668.
8. K. Sendt and G. B. Bacskay, *J. Chem. Phys.*, **2000**, *112*, 2227.
9. D. A. Dixon and D. Feller, *J. Phys. Chem. A*, **1998**, *102*, 8209.
10. D. A. Dixon, D. Feller and G. Sandrone, *J. Phys. Chem. A*, **1999**, *103*, 4744.
11. J. M. L. Martin, *Chem. Phys. Lett.*, **1996**, *259*, 669.
12. J. M. L. Martin and P. R. Taylor, *J. Chem. Phys.*, **1997**, *106*, 8620.
13. J. M. L. Martin, *Chem. Phys. Lett.*, **1999**, *310*, 271.
14. C. W. Bauschlicher, Jr. and A. Ricca, *J. Phys. Chem. A*, **1998**, *102*, 8044.
15. C. W. Bauschlicher, Jr., *J. Phys. Chem. A*, **1999**, *103*, 11126.
16. T. Helgaker, W. Klopper, H. Koch and J. Noga, *J. Chem. Phys.*, **1997**, *106*, 9639.
17. T. Helgaker, P. Jørgensen and J. Olsen, *Molecular Electronic-Structure Theory*; John Wiley & Sons, Ltd.: Chichester, **2000**, 322.
18. L. A. Curtiss, K. Raghavachari, P. C. Redfern, V. Rassolov and J. A. Pople, *J. Chem. Phys.*, **1998**, *109*, 7764.
19. L. A. Curtiss, P. C. Redfern, K. Raghavachari and J. A. Pople, *J. Chem. Phys.*, **2001**, *114*, 108.
20. N. L. Haworth, G. B. Bacskay and J. C. Mackie, *J. Phys. Chem. A*, **2002**, *106*, 1533.
21. A. D. Becke, *J. Chem. Phys.*, **1993**, *98*, 5648.
22. P. J. Stephens, F. J. Devlin, C. F. Chabalowski and M. J. Frisch, *J. Phys. Chem.*, **1994**, *98*, 11623.
23. A. D. Becke, *Phys. Rev. A*, **1988**, *38*, 3098.
24. C. Lee, W. Yang and R. G. Parr, *Phys. Rev. B*, **1988**, *37*, 785.

25. K. Raghavachari, G. W. Trucks, J. A. Pople and M. Head-Gordon, *Chem. Phys. Lett.*, **1989**, *157*, 479.
26. C. Hampel, K. A. Peterson and H.-J. Werner, *Chem. Phys. Lett.*, **1992**, *190*, 1.
27. T. H. Dunning, Jr., *J. Chem. Phys.*, **1989**, *90*, 1007.
28. R. A. Kendall, T. H. Dunning, Jr. and R. J. Harrison, *J. Chem. Phys.*, **1992**, *96*, 6796.
29. D. E. Woon and T. H. Dunning, Jr., *J. Chem. Phys.*, **1993**, *98*, 1358.
30. D. Feller, *J. Chem. Phys.*, **1992**, *96*, 6104.
31. C. Schwartz, *Methods in Computational Physics*; Vol. 2; Academic Press: New York, **1963**, 241.
32. K. A. Peterson and T. H. Dunning, Jr., *J. Chem. Phys.*, **2002**, *117*, 10548.
33. S. F. Boys and F. Bernardi, *Molec. Phys.*, **1970**, *19*, 553.
34. R. D. Cowan and M. Griffin, *J. Opt. Soc. Am.*, **1976**, *66*, 1010.
35. R. L. Martin, *J. Phys. Chem.*, **1983**, *87*, 750.
36. K. Andersson, P.-Å. Malmqvist, B. O. Roos, A. J. Sadlej and K. Wolinski, *J. Phys. Chem.*, **1990**, *94*, 5483.
37. K. Andersson, P.-Å. Malmqvist and B. O. Roos, *J. Chem. Phys.*, **1992**, *96*, 1218.
38. B. O. Roos, P. R. Taylor and P. E. M. Siegbahn, *Chem. Phys.*, **1980**, *48*, 157.
39. B. O. Roos, in *Ab initio Methods in Quantum Chemistry II*, K. P. Lawley, Ed.; *Advances in Chemical Physics*, I. Pigogine and S. A. Rice, Eds.; Vol. LXIX; J. Wiley & Sons Ltd.: Chichester, UK, **1987**, p. 399.
40. J. A. Pople, M. Head-Gordon, D. J. Fox, K. Raghavachari and L. A. Curtiss, *J. Chem. Phys.*, **1989**, *90*, 5622.
41. L. A. Curtiss, K. Raghavachari, G. W. Trucks and J. A. Pople, *J. Chem. Phys.*, **1991**, *94*, 7221.
42. L. A. Curtiss, P. C. Redfern, K. Raghavachari, V. Rassolov and J. A. Pople, *J. Chem. Phys.*, **1999**, *110*, 4703.
43. A. G. Baboul, L. A. Curtiss, P. C. Redfern and K. Raghavachari, *J. Chem. Phys.*, **1999**, *110*, 7650.
44. L. A. Curtiss, K. Raghavachari, P. C. Redfern and J. A. Pople, *J. Chem. Phys.*, **2000**, *112*, 1125.
45. L. A. Curtiss, K. Raghavachari, P. C. Redfern, A. G. Baboul and J. A. Pople, *Chem. Phys. Lett.*, **1999**, *314*, 101.
46. L. A. Curtiss, P. C. Redfern, K. Raghavachari and J. A. Pople, *Chem. Phys. Lett.*, **1999**, *313*, 600.

47. D. J. Henry and L. Radom, in *Theoretical Thermochemistry*, J. Cioslowski, Ed.; Kluwer: Dordrecht, **2001**.

48. P. M. Mayer, C. J. Parkinson, D. M. Smith and L. Radom, *J. Chem. Phys.*, **1998**, *108*, 604.

49. C. J. Parkinson, P. M. Mayer and L. Radom, *J. Chem. Soc., Perkin Trans. 2*, **1999**, *11*, 2305.

50. M. J. Frisch, G. W. Trucks, H. B. Schlegel, G. E. Scuseria, M. A. Robb, J. R. Cheeseman, V. G. Zakrzewski, J. A. Montgomery, R. E. Stratmann, J. C. Burant, S. Dapprich, J. M. Millam, A. D. Daniels, K. N. Kudin, M. C. Strain, O. Farkas, J. Tomasi, V. Barone, M. Cossi, R. Cammi, B. Mennucci, C. Pomelli, C. Adamo, S. Clifford, J. Ochterski, G. A. Petersson, P. Y. Ayala, Q. Cui, K. Morokuma, D. K. Malik, A. D. Rabuk, K. Raghavachari, J. B. Foresman, J. Cioslowski, J. V. Ortiz, B. B. Stefanov, G. Lui, A. Liashenko, P. Piskorz, I. Komaromi, R. Gomperts, R. L. Martin, D. J. Fox, T. Keith, M. A. Al-Laham, C. Y. Peng, A. Nanayakkara, C. Gonzalez, M. Challacombe, P. M. W. Gill, B. G. Johnson, W. Chen, M. W. Wong, J. L. Andres, M. Head-Gordon, E. S. Replogle and J. A. Pople, Gaussian 98 Revision A.7, Gaussian, Inc.: Pittsburgh, PA, **1998**,

51. P. J. Knowles, C. Hampel and H.-J. Werner, *J. Chem. Phys.*, **1993**, *99*, 5219.

52. MOLPRO 96.3 is a package of ab initio programs written by H.-J. Werner and P. J. Knowles with contributions from J. Almlöf, R. D. Amos, M. J. O. Degan, S. T. Elbert, C. Hampel, W. Meyer, K. Peterson, R. Pitzer, A. J. Stone, P. R. Taylor, R. Lindh, M. E. Mura, T. Thorsteinsson.

53. ACES II is a program product of the Quantum Theory Project, University of Florida. Authors: J. F. Stanton, J. Gauss, J. D. Watts, M. Nooijen, N. Oliphant, S. A. Perera, P. G. Szalay, W. J. Lauderdale, S. R. Gwaltney, S. Beck, A. Balková, D. E. Bernholdt, K.-K. Baeck, P. Rozyczko, H. Sekino, C. Hober, R. J. Bartlett. Integral packages included are VMOL (J. Almlöf, P. R. Taylor); VPROPS (P. Taylor); ABACUS (T. Helgekar, H. J. Aa. Jensen, P. Jørgensen, J. Olsen, P. R. Taylor).

54. K. Andersson, M. R. A. Blomberg, M. P. Fülscher, G. Karlström, R. Lindh, P.-Å. Malmqvist, P. Neogrády, J. Olsen, B. O. Roos, A. J. Sadlej, M. Schültz, L. Seijo, L. Serrano-Andrés, P. E. M. Siegbahn and P.-O. Widmark, MOLCAS Version 4, Lund University: Lund, Sweden, **1997**,

55. W. Klopper and L. Radom, *Private communication*.

56. T. H. Dunning, Jr., K. A. Peterson and A. K. Wilson, *J. Chem. Phys.*, **2001**, *114*, 9244.

57. B. J. Persson, P. R. Taylor and T. J. Lee, *J. Chem. Phys.*, **1997**, *107*, 5051.
58. B. J. Persson and P. R. Taylor, **to be published**.
59. G. S. Kedziora, J. A. Pople, M. A. Ratner, P. C. Redfern and L. A. Curtiss, *J. Chem. Phys.*, **2001**, *115*, 718.
60. E. R. Davidson, *J. Chem. Phys.*, **1967**, *46*, 3320.
61. K. R. Roby, *Mol. Phys.*, **1974**, *27*, 81.
62. R. Heinzmann and R. Ahlrichs, *Theor. Chim. Acta*, **1976**, *42*, 33.
63. M. W. Chase, Jr., *J. Phys. Chem. Ref. Data*, **1998**, *Monograph 9*, 1.
64. J. Berkowitz and H. Cho, *J. Chem. Phys.*, **1989**, *90*, 1.
65. S. R. Gunn and L. G. Green, *J. Phys. Chem.*, **1961**, *65*, 779.
66. J. Drowart, C. E. Myers, R. Szwarc, A. Vander Auwera-Mahieu and O. M. Uy, *J. Chem. Soc., Faraday Trans. 2*, **1972**, *68*, 1749.
67. D. L. Hildenbrand and K. H. Lau, *J. Chem. Phys.*, **1994**, *100*, 8373.

Chapter 6

The Role of the NNH + O Reaction in the Production of NO in Flames

The work described in this chapter involves a thermochemical and kinetic study of the importance of the NNH + O reaction in the production of NO in flames. This work comprises of two halves: the quantum chemical investigation of the potential energy surface (including the characterisation of all stationary points) followed by the calculation of the rates of all possible reactions and the kinetic modelling of various flame systems. The latter half of the work was performed by Associate Professor John Mackie.

6.1 Introduction

The presence of nitric oxide in the atmosphere is largely the consequence of combustion processes. As a result, many governments have recently placed stringent limits on the levels of emission of NO from combustion facilities. It is important in the development of new combustion technology that accurate chemical kinetic models of the combustion process be developed to predict the concentrations of NO produced.

Nitric oxide is produced in combustion via four main pathways.[1] The first of these is the well known Zel'dovich or thermal route, initiated by the reaction

$$N_2 + O \rightleftharpoons N + NO \qquad (6.1)$$

The prompt-NO route is initiated by

$$CH + N_2 \rightleftharpoons HCN + N \qquad (6.2)$$

A third route involves the formation of the intermediate, N_2O, and, for fuels containing fuel-bound nitrogen, there is a fuel-NO route.

Recently, Bozzelli and Dean[2] have discovered an additional pathway involving the intermediate NNH radical, formed by the reaction of H with molecular nitrogen:

$$N_2 + H \rightleftharpoons NNH \qquad (6.3)$$

The subsequent reaction of NNH with atomic oxygen then yields the products NO and NH:

$$\text{NNH + O} \rightarrow \text{NO + NH} \qquad (6.4)$$

Using the QRRK technique, Bozzelli and Dean[2] estimated the rate coefficient for this reaction to be $k_4 = 7\times10^{13}$ cm^3 mol^{-1} s^{-1} at 2000 K. This reaction and its rate coefficient have been subsequently incorporated into detailed chemical kinetic reaction models such as GRIMech 2.11[3] and its successor, GRIMech 3.0[4], developed to predict species profiles in the combustion of C_1 and C_2 hydrocarbons.

There have been no direct experimental studies of the reactions of NNH + O $\rightarrow$ products. In a study of NO profiles in laminar premixed flames of H_2 / O_2 / N_2, however, Hayhurst and Hutchinson[5] observed enhanced production rates of NO in the burnt gases that could not be explained on the basis of the Zel'dovich mechanism alone. They attributed their faster observed rates to the operation of the NNH + O pathway and, from a steady state analysis of their experimental NO profiles, arrived at a value of $k_4K_{P,3} = 1.4\times10^9 \exp(-2760/T)$ cm^3 mol^{-1} s^{-1} over the temperature range of 1800 – 2500 K; here k_4 is the rate coefficient of Reaction (6.4) and $K_{P,3}$ is the equilibrium constant of Reaction (6.3). From estimates of the NNH thermochemistry, they evaluated the equilibrium constant and arrived at a value of $k_4 = 1\times10^{14}$ cm^3 mol^{-1} s^{-1}, constant within a factor of 2.5, over the temperature range of 1800 – 2500 K. This result is comparable with the rate coefficient originally estimated by Bozzelli and Dean[2].

Recently, experimental and modelling studies of NO profiles in premixed flames[6] and in completely stirred reactors[7] have concluded, however, that in circumstances where the NNH + O route is likely to be important (that is, where the thermal and prompt NO routes are unimportant), models which employ the above rate coefficient for Reaction (6.4) lead to overprediction of NO production.

The current study is therefore motivated to make a detailed investigation of the NNH + O reaction potential energy surface using current techniques of computational quantum chemistry. Such a study will allow the calculation of reliable thermochemical and kinetic data

which can subsequently be applied to the modelling of combustion reactions in the presence of nitrogen.

Following Bozzelli and Dean, we have included

$$NNH + O \rightarrow N_2O + H \qquad (6.5)$$

and

$$NNH + O \rightarrow N_2 + OH \qquad (6.6)$$

in our system of reactions (in addition to Reactions (6.3) and (6.4)) as potentially competing channels to the production of NO in Reaction (6.4).

Reactions (6.4) to (6.6) are expected to take place via a common ONNH intermediate, which decomposes to yield NO + NH, N_2O + H or N_2 + OH. While no studies of the O + NNH association have previously been reported, the three decomposition reactions have been extensively investigated in the chemical literature over the past 18 years[8-17]. It has been found that ONNH, a planar molecule, is stable in both *cis* and *trans* forms. Although the latter is generally predicted to be the more stable[10-13], it has been concluded that decomposition to N_2O + H and N_2 + OH actually occurs via the *cis* isomer.[12,13]

Several other reactions are also considered in this work, in particular

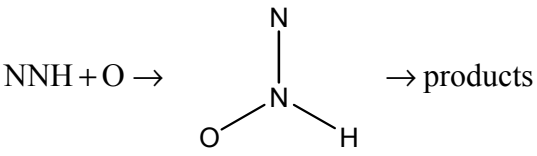

(6.7)

where the intermediate, ONHN, is an isomer of ONNH which can yield HNO + N, N_2O + H and N_2 + OH as decomposition products.

The isomerisation reactions between *cis*- and *trans*-ONNH and between *trans*-ONNH and ONHN are alternative channels which have also been studied, along with the direct abstraction reaction

$$NNH + O \rightarrow N_2 + OH \qquad (6.8)$$

The stability of the NNH intermediate plays a crucial role in determining the relative importance of channels (6.4), (6.5) and (6.6) in the chemistry of nitrogen in flames, in particular the reaction flux which passes through channel (6.4) to generate NO. High level quantum chemical calculations by Walch and Partridge[18] and by Gu et al.[19] have predicted the exothermicity of Reaction (6.3) to be between 3.8 and 4.3 kcal mol^{-1}, with a barrier height of 10.0 - 11.3 kcal mol^{-1}. As modelling studies are extremely sensitive to the stability of NNH, in the present work we have also undertaken the computation of the heats of formation of both NNH and the transition state leading to its formation (NN-H) at the highest currently achievable level of theory available to us, viz. complete basis estimates of the CCSD(T) (coupled cluster theory with single, double and perturbative triple excitations) energetics based on extrapolation of aug-cc-pV*x*Z results with $x = 5, 6$.

This work therefore involves an extensive investigation of the N_2OH potential energy surface using high level quantum chemical methods followed by the computation of the rate parameters for all NNH + O → products channels. Finally, in conjunction with the data set of the GRIMech 3.0 model, we use our revised thermochemistry and rate data to model the lean combustion of CO / H_2 / air and CH_4 / air in completely stirred reactors.

6.2 Theory and Computational Methods

6.2.1 Quantum Chemical Calculations of Thermochemistry

Heats of formation and other thermochemical data were computed via two different approaches: the Gaussian-3X (G3X) method of Curtiss et al.[20] and a CCSD(T)/CBS type scheme, utilising coupled cluster theory with single, double and (perturbative) triple excitations (CCSD(T)[21,22]) in conjunction with the correlation consistent basis sets[23-25], aug-

cc-pVQZ and aug-cc-pV5Z, and extrapolation to the hypothetical complete basis set (CBS) limit.

In both schemes molecular geometries and vibrational frequencies for equilibrium structures and transition states were determined by Density Functional Theory (DFT), using the B3LYP hybrid density functional[26-28] with the 6-31G(2*df*,*p*) basis set (frequencies scaled by 0.9854). Single point energy calculations were then performed at these geometries as required for the two different methodologies, viz. G3X and CCSD(T)/CBS. Open shell systems were treated by unrestricted calculations in the DFT geometry optimisations (UB3LYP) and the subsequent implementation of G3X but by restricted, RCCSD(T), methods in the CCSD(T)/CBS computations.

In the case of the CCSD(T)/CBS{Q,5} scheme, the single point energies were extrapolated to the complete basis limit using the x^{-3} extrapolation[29]

$$E(x) = A + Bx^{-3} \tag{6.9}$$

where x = 4, 5. In the case of a few species, e.g. NNH, more extensive calculations were performed where the sequence of basis sets include aug-cc-pV6Z, viz. x = 6. Core-core and core-valence correlation (CV) corrections were evaluated at the CCSD(T)/aug-cc-pCVQZ level of theory. Scalar relativistic effects (Darwin and mass-velocity terms)[30,31] were determined by complete active space SCF (CASSCF)[32,33] theory using cc-pVTZ basis sets. Spin-orbit corrections were also included for atomic species.[34]

As several important reactions, including the formation of ONNH and its decomposition to NO + NH, are barrierless, Variational Transition State Theory (VTST)[35-37] was utilised to locate and characterise the transition states at a range of temperatures between 1000 and 2500 K. As in previous work of ours[38], density functional theory (B3LYP/6-31G(2*df*,*p*)) was used to map the minimum energy path (MEP) along the potential energy surface (PES) as a function of the reaction coordinate. The latter was approximated as the critical bond forming or bond breaking distance; thus this critical bond distance was systematically varied while all other geometric parameters were allowed to relax. At each such point along the reaction coordinate the rate coefficient was calculated by the application of the canonical transition

state formula[39] at the given temperature, thus allowing the geometry which yielded the minimum rate to be identified as the variational transition state.

The Gaussian 98 programs[40] were used to perform all DFT calculations (geometry optimisations and PES scans) as well as the G3X calculations, while MOLPRO[21,41,42] was utilised for all (R)CCSD(T) computations. The CASSCF calculations of scalar relativistic corrections were carried out using DALTON[43] for all molecules and MOLCAS[44] for atomic species. The computations were performed on DEC alpha 600/5/333 and COMPAQ XP100/500 workstations of the Theoretical Chemistry group at the University of Sydney and on the COMPAQ AlphaServer SC system of the Australian Partnership for Advanced Computing National Facility at the National Supercomputing Centre, ANU, Canberra.

6.2.2 Derivation of Rate Coefficients for Individual Reaction Channels

As discussed above, addition of O to NNH produces three intermediates via chemical activation. These intermediates, which represent local minima on the potential energy surface, are *trans*-ONNH, *cis*-ONNH and ONHN. Further reaction leads to four product channels, that is, to NO + NH, N_2O + H, N_2 + OH and HNO + N. All but the last of these are exothermic processes. To derive rate coefficients for the overall reaction to the four product channels we have separately considered the three reaction surfaces for

$$\mathrm{NNH + O} \rightleftharpoons \mathit{trans}\text{-}\mathrm{ONNH} \rightarrow \text{products} \tag{6.10}$$

$$\mathrm{NNH + O} \rightleftharpoons \mathit{cis}\text{-}\mathrm{ONNH} \rightarrow \text{products} \tag{6.11}$$

and

$$\mathrm{NNH + O} \rightleftharpoons \mathrm{ONHN} \rightarrow \text{products} \tag{6.12}$$

We then assume that the vibrationally excited adduct (*trans*-ONNH, *cis*-ONNH or ONHN), is formed from NNH and O at an energy, *E*, and will undergo the reverse reaction at an energy-

specific rate coefficient, $k(E)$. The limiting high-pressure rate coefficient for this reverse (dissociation) reaction, $k_{uni,\infty}$, is given by

$$k_{uni,\infty} = \frac{1}{q(T)} \int_{E_0}^{\infty} k(E)\rho(E)\exp(-E/k_B T)dE \tag{6.13}$$

where $q(T)$ is the internal partition function of the adduct calculated at the translational temperature, T; $\rho(E)$ is the density of states and k_B is Boltzmann's constant. The lower limit for integration is the critical energy of reaction, E_0. The recombination rate coefficient in the high pressure limit, $k_{rec,\infty}$, is obtained from $k_{uni,\infty}$ by detailed balance using the equilibrium constant $K_c(T)$ as given by

$$k_{rec,\infty} = \frac{k_{uni,\infty}}{K_c(T)} \tag{6.14}$$

The overall pressure-dependent rate coefficient via each adduct to each of the product channels is obtained from

$$k_{overall} = f_{products} \times k_{rec,\infty} \tag{6.15}$$

where f_{prods} is the fraction of reaction flux to each product channel. We have carried out an RRKM analysis using the MultiWell suite of programs developed by Barker[45] to solve the internal master equation with densities of states calculated by an exact count method. Collisional energy transfer parameters were taken from the work of Barker.[46] Lennard-Jones parameters have been taken from the Chemkin Collection.[47] As all three adducts lead to the four reaction channels (but with different values of $f_{products}$), the final overall rate coefficients for NNH + O $\rightarrow$ products were obtained by summing the contributions from the three surfaces.

6.3 Results and Discussion

6.3.1 Quantum Chemistry

All potential stationary points on the NNH + O PES were investigated using B3LYP/ 6-31G(2*df*,*p*) on both the A′ and A″ surfaces. The A′ species were found to be consistently lower in energy (as found by other workers), so in general only results for this surface are presented.

The electronic energies of the stationary points on the PES as calculated at the (valence correlated) CCSD(T)/aug-cc-pVQZ and CCSD(T)/aug-cc-pV5Z levels of theory, along with the extrapolated results, are presented in **Table 6.1**. This Table also provides details of the CCSD(T)/aug-cc-pCVQZ core-valence correlation corrections, the scalar relativistic corrections and the zero point energies for each molecule, and thus the total CCSD(T)/CBS energy at 0K together with the corresponding G3X result. The thermal corrections between 0 and 298K for each molecule are also reported here. Unfortunately, it was not possible to perform such CCSD(T)/CBS calculation on the *cis* to *trans* transition state of ONNH (ONNH *c*-*t* TS), as the lack of symmetry in this molecule made the aug-cc-pV5Z and aug-cc-pCVQZ calculations too large. The geometries, rotational constants and vibrational frequencies for all equilibrium structures, transition states and variational transition states are summarised in **Appendix 3** (schematic structures for these species can also be found in **Figures 6.1** to **6.3**).

Table 6.2, in turn, contains the atomisation energies for each species as calculated using both the CCSD(T)/CBS and G3X approaches, as well as the resulting heats of formation at 0 and 298 K and literature values for the latter where available. Core-valence correlation and relativistic contributions to the atomisation energies are also included in this Table. Examination of the latter reveals that both effects are relatively small in magnitude and that their respective contributions cancel out to a large extent, resulting in a net contribution of ~ 0.5 kcal mol^{-1} or less.

According to Curtiss et al.[20], the heats of formation obtained from the G3X method are expected to have a *mean* absolute deviation of 1.0 kcal mol^{-1} from experiment. The CCSD(T)/CBS results are expected to have a higher degree of accuracy; our conservative

Table 6.1 Total CCSD(T) and G3X energies, core-valence (CV) correlation corrections, scalar relativistic corrections (in E_h) along with zero point energies and thermal corrections to enthalpies (in kcal mol^{-1}).

		Valence correlated energy			CV corr	ΔE_{rel}	ZPE	Total Energy[b]		$H^0_{298} - H^0_0$
		CCSD(T) aug-cc-pVQZ	CCSD(T) aug-cc-pV5Z	CCSD(T) CBS{Q,5}[a]	CCSD(T) aug-cc-pCVQZ	CASSCF cc-pVTZ	B3LYP 6-31G(2*df*,*p*)	CCSD(T) CBS{Q,5}	G3X	B3LYP 6-31G(2*df*,*p*)
N	^{4}S	–54.52506	–54.52780	–54.53068	–0.05613	–0.02921		–54.61601	–54.56490	1.04
O	^{3}P	–74.99493	–75.00041	–75.00615	–0.05907	–0.05237		–75.11795	–75.03224	1.04
H	^{2}S	–0.49995	–0.49999	–0.50004	0.00000	0.00000		–0.50004	–0.50097	1.01
N_2	$^1\Sigma_g$	–109.40724	–109.41551	–109.42418	–0.11344	–0.05818	3.42	–109.59034	–109.48808	2.07
NH	$^3\Sigma$	–55.15574	–55.15913	–55.16269	–0.05628	–0.02906	4.57	–55.24075	–55.19350	2.07
NO	$^2\Pi$	–129.75792	–129.76818	–129.77893	–0.11585	–0.08085	2.80	–129.97117	–129.83624	2.07
OH	$^2\Pi$	–75.66426	–75.67038	–75.67680	–0.05929	–0.05187	5.21	–75.77967	–75.69607	2.07
NNH	^{2}A′	–109.90091	–109.90907	–109.91763	–0.11344	–0.05790	8.18	–110.07595	–109.97501	2.39
NNO	$^1\Sigma$	–184.46683	–184.48141	–184.49671	–0.17313	–0.10956	6.98	–184.76828	–184.58323	2.27
HNO	^{1}A′	–130.34240	–130.35288	–130.36388	–0.11587	–0.08067	8.54	–130.54681	–130.41227	2.37
trans-ONNH	^{2}A′	–185.00994	–185.02643	–185.04373	–0.17290	–0.10949	13.04	–185.30534	–185.11715	2.52
cis-ONNH	^{2}A′	–185.00041	–185.01644	–185.03325	–0.17297	–0.10948	12.56	–185.29569	–185.10725	2.56
ONHN	^{2}A′	–184.97089	–184.98820	–185.00636	–0.17270	–0.10952	12.52	–185.26863	–185.07844	2.53
NN-H	^{2}A′	–109.88513	–109.89336	–109.90200	–0.11332	–0.05813	4.05	–110.06699	–109.96623	2.46
ONN-H	^{2}A′	–184.95143	–184.96843	–184.98626	–0.17301	–0.10955	7.38	–185.25707	–185.06898	2.76
ON_2-H	^{2}A′	–184.92953	–184.94647	–184.96424	–0.17276	–0.10957	7.77	–185.23418	–185.04605	2.57
NNOHsq	^{2}A′	–184.94179	–184.95694	–184.97283	–0.17210	–0.10985	8.91	–185.24059	–185.05381	2.50
NNOHtr	^{2}A′	–184.92091	–184.93646	–184.95278	–0.17257	–0.10976	8.20	–185.22205	–185.03713	2.71
ONNH *c-t* TS	^{2}A								–185.08082	
ONHN-ONNH*t*	^{2}A′	–184.91787	–184.93264	–184.94813	–0.17260	–0.10956	9.02	–185.21592	–185.03186	2.63

[a] Extrapolated CCSD(T) energy to CBS ($x = \infty$) limit using $x = 4, 5$ data.

[b] Including CV, ΔE_{rel} and ZPE corrections in CCSD(T)/CBS energies.

Table 6.2 CCSD(T)/CBS{Q,5} and G3X atomisation energies (along with CV correlation and scalar relativistic contributions to CBS) and heats of formation (at 0 and 298K) of reactants, products, intermediates and first order saddle points on the N_2OH surface (in kcal mol^{-1}).

	Atomisation Energy[a]				$\Delta_f H_0^0$		$\Delta_f H_{298}^0$		
	CV corr	ΔE_{rel}	CCSD(T)[b] CBS	G3X	CCSD(T)[b] CBS	G3X	CCSD(T)[b] CBS	G3X	Experiment
N_2	0.74	–0.15	224.9	224.8	0.2	0.2	0.2	0.2	0.00
NH	0.09	–0.09	78.3	80.1	85.9	84.1	85.9	84.1	85.32 ± 0.02[c]
NO	0.41	–0.46	148.9	150.0	22.7	21.5	22.7	21.5	21.82 ± 0.04[d]
OH	0.14	–0.31	101.5	102.2	9.2	8.4	9.2	8.5	8.83 ± 0.09[e]
NNH	0.74	–0.33	215.8	216.0	60.9	60.7	60.2	60.0	
NNO	1.13	–0.77	262.5	264.3	21.6	19.8	20.7	18.9	19.6 ± 0.1[f]
HNO	0.42	–0.57	196.3	197.1	26.9	26.0	26.2	25.3	$25.6^{+0.6}_{-0.1}$[g]
trans-ONNH	0.99	–0.82	285.7	285.0	50.0	50.7	48.4	49.1	
cis-ONNH	1.03	–0.82	279.7	278.8	56.0	56.9	54.5	55.4	
ONHN	0.86	–0.80	262.7	260.7	73.0	75.0	71.4	73.4	
NN-H	0.67	–0.18	210.2	210.5	66.5	66.2	65.9	65.6	
ONN-H	1.05	–0.78	255.4	254.8	80.3	80.9	78.9	79.6	
ON_2-H	0.90	–0.77	241.1	240.4	94.6	95.3	93.1	93.8	
NNOHsq	0.48	–0.59	245.1	245.2	90.6	90.5	89.0	88.8	
NNOHtr	0.78	–0.65	233.5	234.8	102.2	100.9	100.8	99.5	
ONNH *c-t* TS				262.2		73.5		71.9	
ONHN-ONNH*t*	0.80	–0.77	229.6	231.5	106.1	104.2	104.6	102.7	

[a] Including zero-point corrections.

[b] Including CV correlation and scalar relativistic corrections.

[c] $\Delta_f H_0^0$ from Ref. 48 with thermal corrections from this work.

[d] Ref. 49.

[e] Ref. 50.

[f] Ref. 49.

[g] Ref. 51.

estimate for the maximum uncertainty in *any* of the CBS heats of formation computed in this work is ± 1.0 kcal mol^{-1}. Comparison of the CCSD(T)/CBS and G3X heats of formation indicates the two sets of results agree with each other and with the available experimental data within their respective error margins.

In light of the sensitivity of the kinetic models to the stability of NNH, as noted above, a more extensive investigation was carried out for NNH, N_2 and the transition state, NN-H. The geometries and harmonic frequencies were redetermined at the CCSD(T)/aug-cc-pVQZ level of theory using numerical differentiation to obtain the appropriate force constants. The CCSD(T) valence correlated energies were calculated at the revised geometries using the aug-cc-pV5Z and aug-cc-pV6Z basis sets[52,53] and extrapolated as before. CCSD(T)/aug-cc-pCVQZ CV corrections, CASSCF/cc-pVTZ scalar relativistic corrections and atomic spin orbit corrections were again applied. In order to account, at least in part, for the effects of anharmonicity in the calculation of the zero-point energies and thermal corrections, the NNH bending frequencies were scaled by a factor of 0.97, the N-N stretching frequencies by 0.988 and the N-H stretching frequencies by 0.95. (These scaling factors were chosen by comparison of experimental harmonic and anharmonic frequencies of N_2, NH_3 and H_2O.) The results of these high level calculations are summarised in **Table 6.3**. As can be seen by comparison with the results in **Table 6.2**, the application of a substantially higher level of theoretical treatment leaves the heats of formation for N_2 and NNH largely unchanged; it does, however, reduce the barrier for the dissociation of NNH by ~ 1 kcal mol^{-1}.

Comparison of the CCSD(T)/aug-cc-pV5Z energies at the revised CCSD(T) geometries (in **Table 6.3**) with those at B3LYP geometries (in **Table 6.1**) demonstrates that for N_2 and NNH the small geometric changes (less than 0.01 Å in bond lengths and 0.6° in the NNH bond angle) have a negligible effect on the energies. For the NN-H transition state, however, the energy has been lowered by ~ 1 kcal mol^{-1}; this is accompanied by a decrease of 0.12 Å in the N-H bond length. The zero-point energies are effectively unchanged (differences of ~ 0.1 kcal mol^{-1} or less). For N, N_2 and NNH the CCSD(T)/CBS{5,6} energies are 0.54, 1.16 and 1.54 kcal mol^{-1} higher than the corresponding {Q,5} results. Thus, the effects of the extra degree of theoretical complexity implicit in the aug-cc-pV6Z calculations largely cancel in the atomisation energy computations of N_2 while the value for NNH is reduced by ~ 0.4 kcal mol^{-1}. Interestingly, for the NN-H transition state the combined effects of geometry changes

Table 6.3 Summary of the energetic contributions to the CCSD(T)/CBS{5,6} extrapolated atomisation energies (*AE*) and heats of formation for N_2, NNH and the NN-H transition state (in E_h unless otherwise noted).

	N	H	N_2	NNH	NN-H
CCSD(T)/aug-cc-pV5Z	–54.52780	–0.49999	–109.41550	–109.90913	–109.89164
CCSD(T)/aug-cc-pV6Z	–54.52865	–0.50000	–109.41838	–109.91167	–109.89596
CCSD(T)/CBS{5,6}	–54.52982	–0.50001	–109.42233	–109.91517	–109.90200
CCSD(T)/aug-cc-pCVQZ (core + valence)	–54.58205		–109.52248	–110.01611	–109.99847
CCSD(T)/aug-cc-pCVQZ (valence only)	–54.52592		–109.40906	–109.90267	–109.88515
CV correction	–0.05613		–0.11342	–0.11343	–0.11332
ΔE_{rel}	–0.02921		–0.05818	–0.05790	–0.05811
ZPE			0.00526	0.01287	0.00644
CCSD(T)/CBS {5,6} [a]	–54.61516	–0.50001	–109.58867	–110.07363	–110.06698
CCSD(T)/CBS {5,6} *AE* [a] /kcal mol^{-1}			224.87	215.43	211.26
CCSD(T)/CBS {5,6} $\Delta_f H_0^0$ [a] /kcal mol^{-1}			0.19	61.26	65.43
$H_{298}^0 - H_0^0$ /kcal mol^{-1}	1.04	1.01	2.07	2.39	2.44
CCSD(T)/CBS {5,6} $\Delta_f H_{298}^0$ [a] /kcal mol^{-1}			0.18	60.56	64.78

[a] Including CV, ΔE_{rel} and ZPE corrections.

and larger basis set have resulted in a CCSD(T)/CBS{5,6} energy that is essentially the same as that obtained via CCSD(T)/CBS{Q,5}. The net results is therefore a lower atomisation energy for NN-H; that is, the barrier to dissociation is reduced, by ~ 1 kcal mol^{-1}. These results are in support of our proposed uncertainty of ± 1 kcal mol^{-1} in our CCSD(T)/CBS heats of formation.

In **Table 6.4**, the G3X and CCSD(T)/CBS energetics are compared with the earlier theoretical work of Walch[12,18], Gu[19] and Durant[13]. As these workers reported their results as energies relative to N_2 + H (for NNH and NN-H) and NO + NH for all other species, we also present

Table 6.4 Energies[a] of NNH and N_2OH species relative to N_2 + H and NO + NH respectively computed at different levels of theory (in kcal mol^{-1}).

	CCSD(T) CBS {Q,5}	CCSD(T) CBS {5,6}	G3X	G2[b]	MR-CI[c]	CCSD(T)/ aug-cc-pVQZ[d]	MR-CI + Dav.[e]
NNH	9.1	9.4	8.8			8.6 ± 0.5	9.1
NN-H	14.7	13.6	14.3			14.4 ± 1.0	16.3
trans-ONNH	–58.6		–54.9	–56.0	–51.5		
cis-ONNH	–52.6		–48.6	–48.9	–46.2		
ONHN	–35.6		–30.6				
O + NNH	11.3		14.1				
NNO + H	–35.4		–34.2	–34.5	–31.7		
N_2 + OH	–99.2		–96.9	–96.9			
ONNH *c-t* TS			–32.1	–30.8			
ONN-H	–28.3		–24.6	–25.3	–21.4		
ON_2-H	–14.0		–10.2				
NNOHsq	–18.0		–15.1	–17.9	–15.4		
NNOHtr	–6.4		–4.6				
ONHN-ONNH*t*	–2.5		–1.3				

[a] Including zero-point corrections.

[b] Ref. 13.

[c] Ref. 12.

[d] Ref. 19 + B3LYP/6-31G(2*df*,*p*) zero point energy.

[e] MR-CI values, including Davidson's correction, from Ref. 18 + B3LYP/6-31G(2*df*,*p*) zero point energy.

our results in this form for easy comparison. Note also that the previous calculations on NNH and NN-H by Walch and Partridge[18] and by Gu, Xie and Schaefer[19] reported only electronic energy differences; we have therefore added our B3LYP/6-31G(2*df*,*p*) zero-point energies to their values for consistency. The results of Gu et al.[19] were obtained via CCSD(T)/ aug-cc-pVQZ calculations while Walch and Partridge utilised multireference CI (MRCI) (including Davidson's correction) in conjunction with the cc-pV*x*Z, *x* = D, T, Q, 5 basis sets and extrapolation via the exponential formula:

$$E(x) = A + B\exp(-Cx) \tag{6.16}$$

While there is broad agreement with respect to the stability of NNH, our best estimate of the barrier height for its dissociation is lower that those obtained by either of the other groups. Thus our results indicate that NNH is significantly less stable to dissociation and has a shorter lifetime than previously predicted.

The energies of the N_2OH species are compared in **Table 6.4** with the G2 values of Durant[13] and the MRCI results of Walch[12]. As may be expected, the G2 and G3X results are, in most cases, in good agreement. Walch's MRCI results, however, are found to be consistently higher than those obtained by either G2, G3X or CCSD(T)/CBS. We believe that this discrepancy is due to size extensivity problems in the MRCI approach, which in this case did not include Davidson's correction. Such problems are expected to be most serious in the calculation of dissociation energies. Consequently, as noted by Durant[13], in Walch's calculations the stabilities of the N_2OH species (as well as of N_2O + H) relative to NO + NH are underestimated by ~ 3 kcal mol^{-1}; when a correction of this size is applied to the MRCI results the agreement with the G2 and G3X results is much improved. It is seen, however, that the CCSD(T)/CBS{Q,5} results are generally significantly lower than their G3X counterparts, by up to 3.7 kcal mol^{-1}.

We believe that for the systems studied here the CCSD(T)/CBS approach, as outlined in this work, represents potentially the highest level of size consistent treatment of electron correlation that is currently available. Consequently, we expect our CCSD(T)/CBS results to be more accurate than those obtained previously.

6.3.2 Potential Energy Surfaces and Reaction Paths

Schematic potential energy diagrams showing the major stationary points on the N_2OH potential energy surface corresponding to the three main reaction channels (Equations (6.10) to (6.12)) are shown in **Figures 6.1** to **6.3**. The relative enthalpies (at 298K) shown in these diagrams are CCSD(T)/CBS{Q,5} values, except for ONNH *c-t* TS where the G3X result has been used. Clearly, the reaction channels producing N_2O + H and N_2 + OH are thermodynamically favoured over the formation of NO + NH. On the other hand, the reaction to form N + HNO is calculated to be endothermic by 19.4 kcal mol^{-1} and thus unlikely to compete with the other more favourable channels.

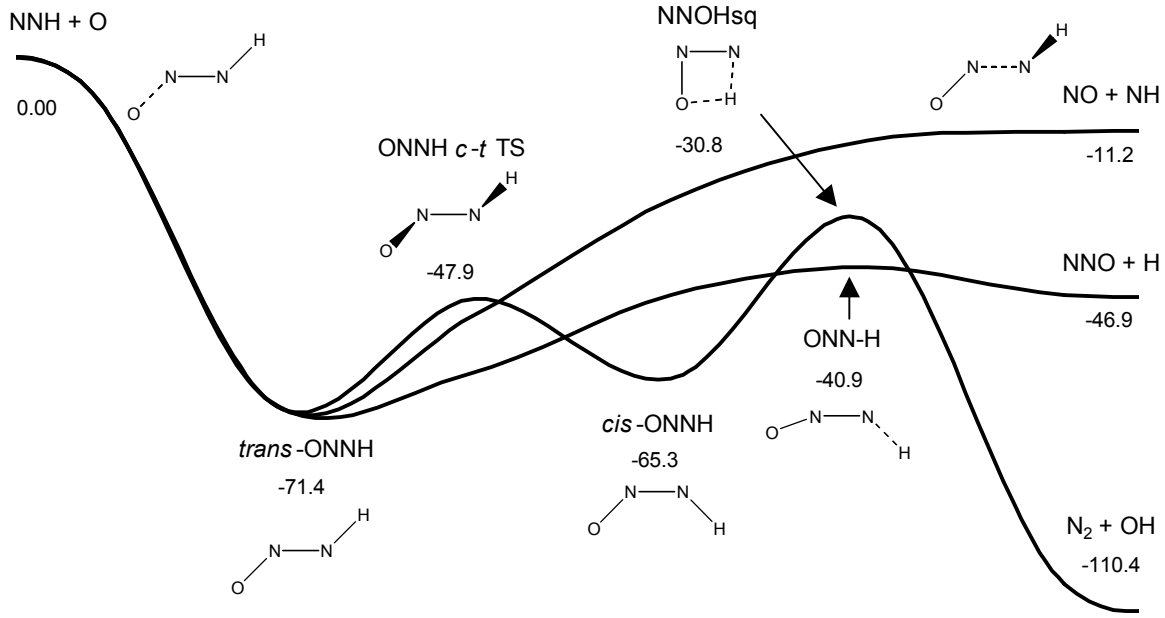

Figure 6.1 Schematic of potential energy surfaces for the reactions of *trans*-ONNH. Relative enthalpies at 298 K (in kcal mol^{-1}) from CCSD(T)/CBS{Q,5} calculations.

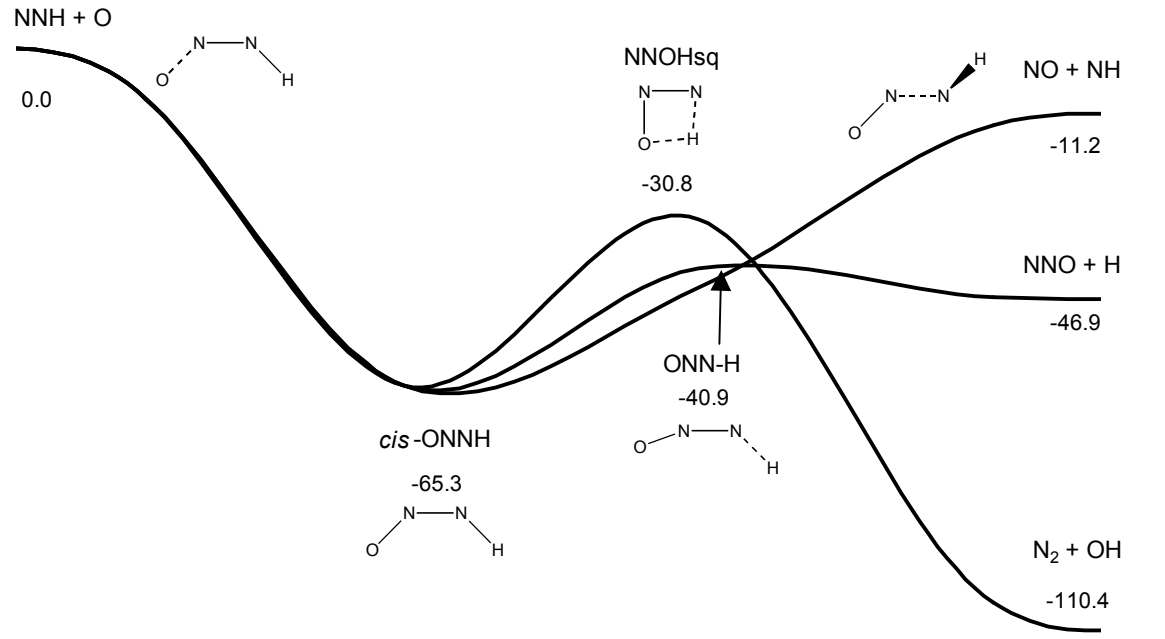

Figure 6.2 Schematic of potential energy surfaces for the reactions of *cis*-ONNH. Relative enthalpies at 298 K (in kcal mol^{-1}) from CCSD(T)/CBS{Q,5} calculations.

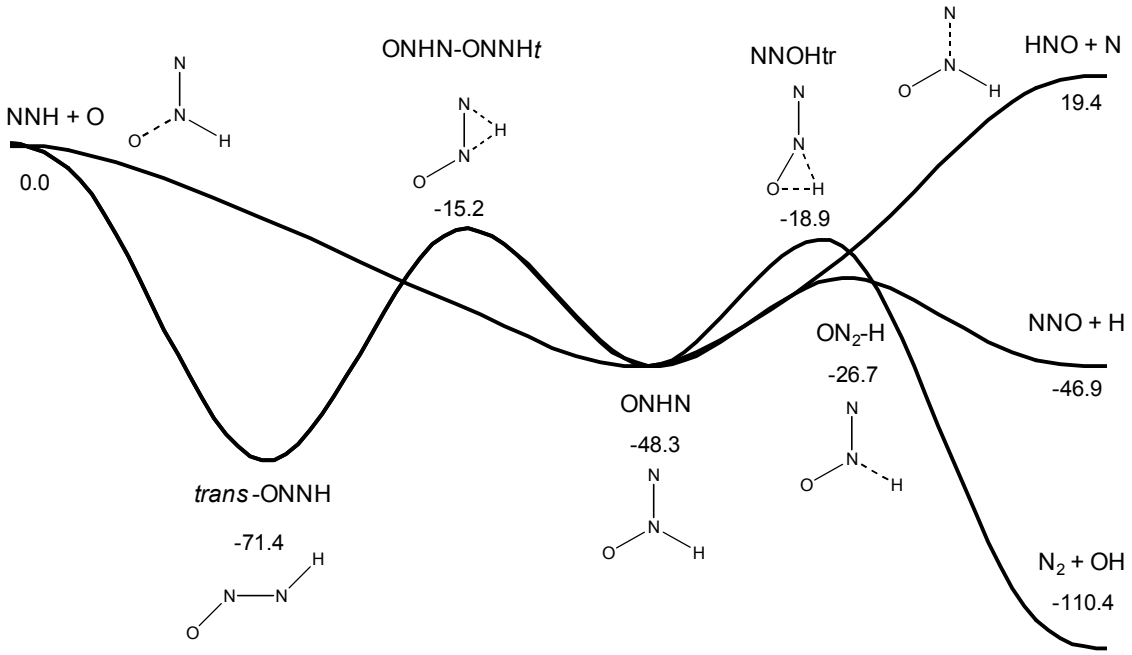

Figure 6.3 Schematic of potential energy surfaces for the reactions of ONHN. Relative enthalpies at 298 K (in kcal mol^{-1}) from CCSD(T)/CBS{Q,5} calculations.

As several of the reactions on this PES involve barrierless recombinations or dissociations, variational transitions state theory was applied in order to locate and characterise the (temperature dependent) transition states, as described in the **Section 6.2.1**. Energies, and thus heats of formation, at the CCSD(T)/CBS level of theory were estimated by utilising the B3LYP/6-31G(2*df*,*p*) estimate of the energy difference between the TS and the dissociated adducts along with the CCSD(T)/CBS energies for the dissociated species. The resulting heats of formation are listed in **Table 6.5**. Geometries, rotational constants and vibrational frequencies for these species are given in **Appendices 3.3** and **3.4**.

Table 6.5 G3X and CCSD(T)/CBS{Q,5} total energies, atomisation energies (at 0K) and heats of formation (at 0 and 298K) of variational transitions states (in kcal mol^{-1}).

Reaction	Temp. /K	$\Delta_f H_0^0$		$\Delta_f H_{298}^0$	
		G3X	CBS	G3X	CBS
trans-ONNH → NNH + O	1000	116.1	116.3	115.1	115.3
	1500	114.2	114.5	113.1	113.4
	2000	112.1	112.3	110.9	111.1
	2500	109.6	109.8	108.3	108.5
cis-ONNH → NNH + O	1000	116.8	117.1	115.9	116.1
	1500	116.2	116.4	115.2	115.4
	2000	114.9	115.1	113.9	114.1
	2500	112.7	112.9	111.5	111.8
ONHN → NNH + O	1000	117.0	117.2	116.1	116.3
	1500	115.5	115.7	114.5	114.8
	2000	111.4	111.7	110.3	110.5
	2200	107.0	107.2	105.7	105.9
trans-ONNH → NO + NH	1000	99.8	102.9	98.9	102.0
	1500	98.6	101.6	97.6	100.6
	2000	97.1	100.1	96.1	99.1
	2400	96.7	99.7	95.6	98.6
cis-ONNH → NO + NH	1000	99.6	102.6	98.7	101.7
	1500	98.2	101.3	97.3	100.3
	2000	96.7	99.7	95.6	98.6
	2500	96.2	99.2	95.1	98.1
ONHN → N + HNO	1000	135.5	136.4	134.2	135.0
	1500	135.1	135.9	133.7	134.6
	2000	134.5	135.3	133.1	133.9
	2500	134.1	135.0	132.7	133.5
NNH + O → N_2 + OH	1000	117.8	118.0	116.8	117.0
	1500	116.9	117.2	115.8	116.1
	2000	115.7	116.0	114.6	114.8
	2500	115.3	115.5	114.1	114.3

As noted in **Section 6.2.1**, the MEP's for all potential reaction channels were mapped using B3LYP/6-31G(2*df*,*p*). The important features of each surface are discussed here:

NNH (^{2}A′) + O (^{3}P) → *cis*- and *trans*-ONNH (^{2}A′). Both reactions, as indicated in **Figures 6.1** and **6.2**, are simple barrierless recombinations leading to the *cis*- and *trans*-ONNH adducts. Variational transition states were determined for both reactions, as described in **Section 6.2.1**. **Figure 6.4** shows the plots of the minimum energy paths along the PES for all three possible NNH + O recombination reactions (giving *cis*- and *trans*-ONNH as well as ONHN). It is interesting to note that, although the *cis*- isomer is higher in energy than the *trans*- at their respective equilibrium geometries, the *cis*- form is more stable over most of the PES. In the vicinity of the minima for *cis*- and *trans*-ONNH, the *cis*-*trans* interconversion takes place via torsion. The ONNH dihedral angle in the isomerisation transition state structure, ONNH *c*-*t* TS, was found to be 90.9°.

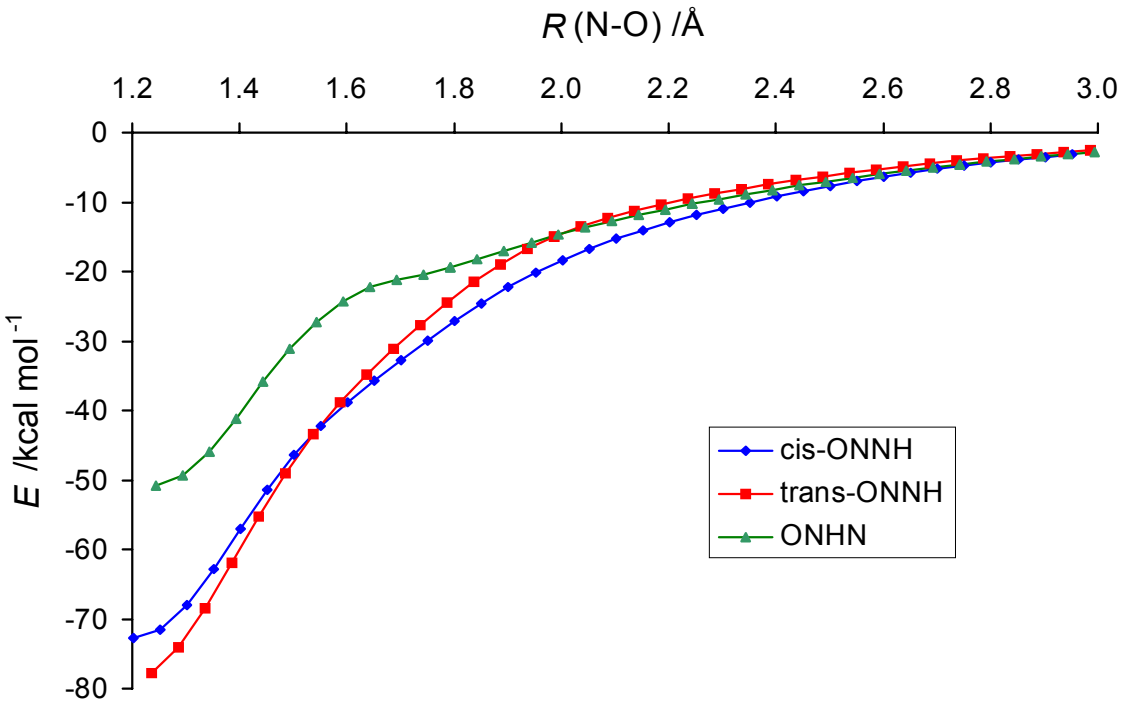

Figure 6.4 B3LYP/6-31G(2*df*,*p*) potential energy surfaces for NNH + O recombination reactions. Energy relative to NNH + O.

NNH (^{2}A′) + O (^{3}P) → ONHN (^{2}A′). This is also a barrierless recombination reaction as shown in **Figures 6.3** and **6.4**. The ONHN adduct and the variational transition states leading to it are all planar ^{2}A′ states. As shown in **Figure 6.5**, however, application of the time dependent density functional approach, viz. TD-B3LYP, at the ground state geometries reveals that the first two excited states (^{2}A″ and ^{2}A′ respectively) are quite close in energy to the ground state. **Figure 6.5** also suggests that there are two avoided crossings on this PES, one at ~ 1.45 Å (between the two excited states) and one at ~ 1.65 Å (between all three states). This indicates that, although the ground state is planar, the equilibrium geometries of the excited state molecules are likely to be non-planar, thus raising the symmetry constraints and allowing direct interaction between the states. In the context of the current work, however, these unusual features are of purely academic interest, the important point being the existence of a direct pathway leading to ONHN on the ^{2}A′ surface.

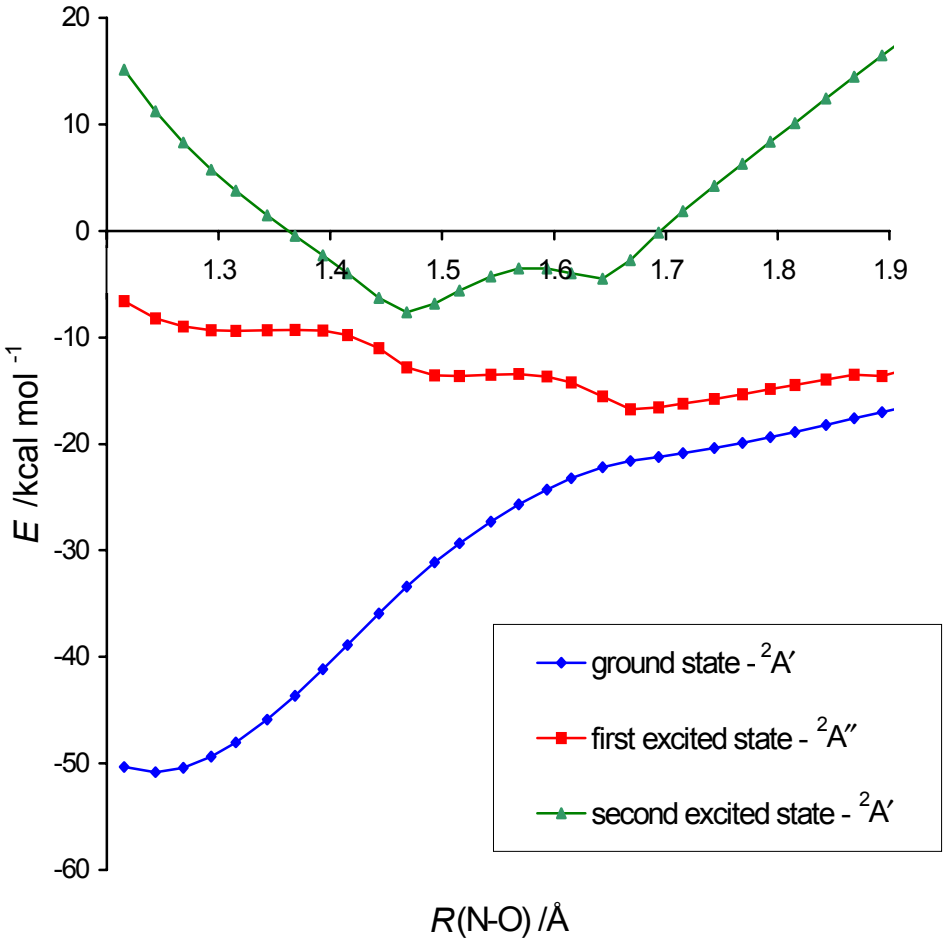

Figure 6.5 Ground and excited state B3LYP/6-31G(2*df*,*p*) potential energy surfaces for the NNH + O → ONHN recombination. Energy relative to NNH + O.

***cis*- and *trans*-ONNH (^{2}A′) → NO ($^2\Pi$) + NH ($^3\Sigma$).** The dissociation of both isomers was found to occur via a common, barrierless, non-planar surface, as shown in **Figures 6.1** and **6.2**. The MRCI studies of Walch[12] have previously established that dissociations of both *cis*- and *trans*-ONNH on the ^{2}A′ surface must pass over activation barriers while the analogous ^{2}A″ surfaces are barrierless. The same features are also observed on our B3LYP/6-31G(2*df*,*p*) PES, shown in **Figure 6.6**, with the surface crossings from ^{2}A′ to ^{2}A″ occurring at *R*(N-N) ≈ 1.67 Å for the *trans* isomer and *R*(N-N) ≈ 1.58 Å for *cis*-ONNH. When the minimum energy path for the dissociation of the *trans* isomer was mapped with no symmetry constraints applied, the *trans* ^{2}A′ surface was followed until the neighbourhood of the surface crossing from which point the molecule became non-planar and the dissociation followed a surface very similar to that of ^{2}A″ *trans*-ONNH; it therefore appears that the ^{2}A states of the non-planar variational transition states correlate with the ^{2}A″ surfaces of ONNH. Such states are accessible via torsion of the molecule, as shown in **Figure 6.7**. Here the potential energy surfaces for torsion of ONNH are shown for various N-N bond lengths. At low N-N separations there is a high barrier between ^{2}A′ *cis*- and *trans*-ONNH; as the bond stretches, however, the *cis* ^{2}A″ surface falls below the ^{2}A′ surface so that at *R*(N-N) = 1.6 Å the torsion of ^{2}A′ *trans*-ONNH actually results in the *cis* isomer on the ^{2}A″ surface. As the N-N bond is stretched beyond 1.65 Å, a minimum appears on the torsional PES at a dihedral angle of ~ 130°; this is consistent with the observed non-planar variational transition states. Further stretching of *R*(N-N) results in the ^{2}A″ state of *trans*-ONNH falling below the ^{2}A′ state. Although at 1.75 Å ^{2}A″ *trans*-ONNH is higher in energy than the non-planar structure, the energy difference is only ~ 0.6 kcal mol^{-1}; this barrier reduces further as the molecule dissociates (as seen in **Figure 6.6**) such that the non-planar MEP for the dissociation is effectively on the *trans* ^{2}A″ surface. In summary, therefore, we are proposing that the dissociation reaction of ONNH occurs via ^{2}A′ → ^{2}A″ surface crossing which can be achieved by the out-of-plane distortion, viz. torsion of the molecules. This is reasonable for the sort of systems we are modelling, where the ONNH adducts are generated in highly vibrationally excited states as a result of chemical and/or collisional activation. Surface crossing, via vibronic coupling, predominantly involving torsion, is expected to occur readily. Note, however, that even though there is a common MEP for both *cis* and *trans* dissociations, their respective variational transition states differ slightly because of the differences in the ground state energies and partition functions of the two ONNH isomers.

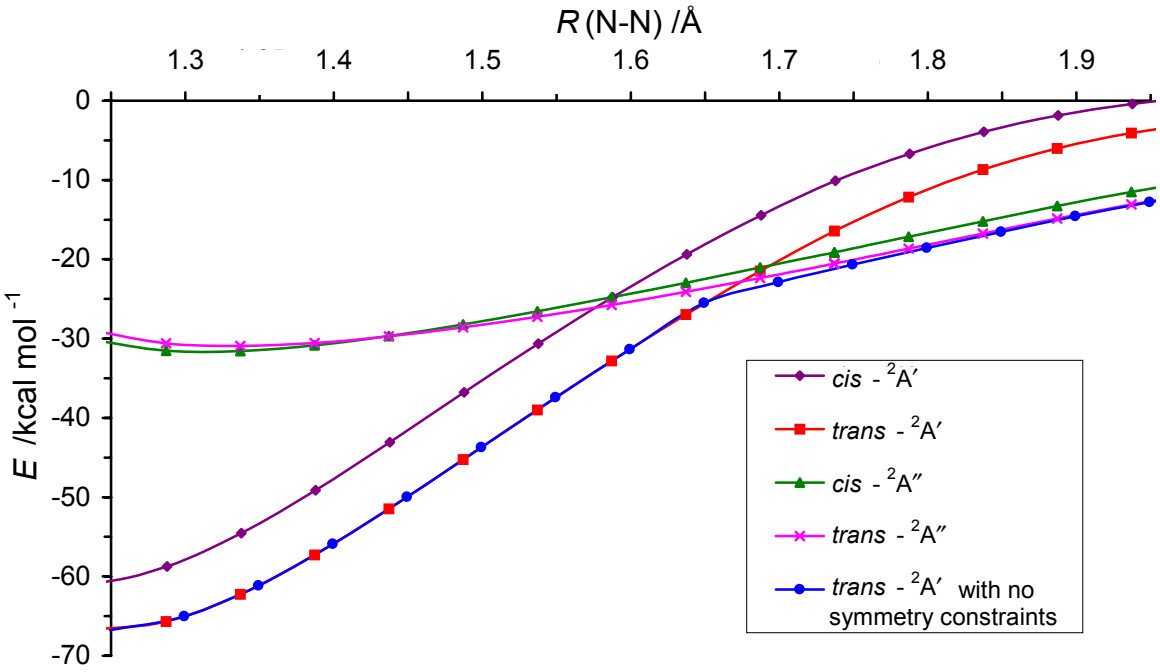

Figure 6.6 B3LYP/6-31G(2*df*,*p*) ^{2}A′ and ^{2}A″ PES's for ONNH → NO + NH showing the stretching of the N-N bond in the *cis*- and *trans*-isomers and in the non-planar reaction path for ^{2}A′ *trans*-ONNH with no symmetry constraints. (Energy relative to NO + NH.)

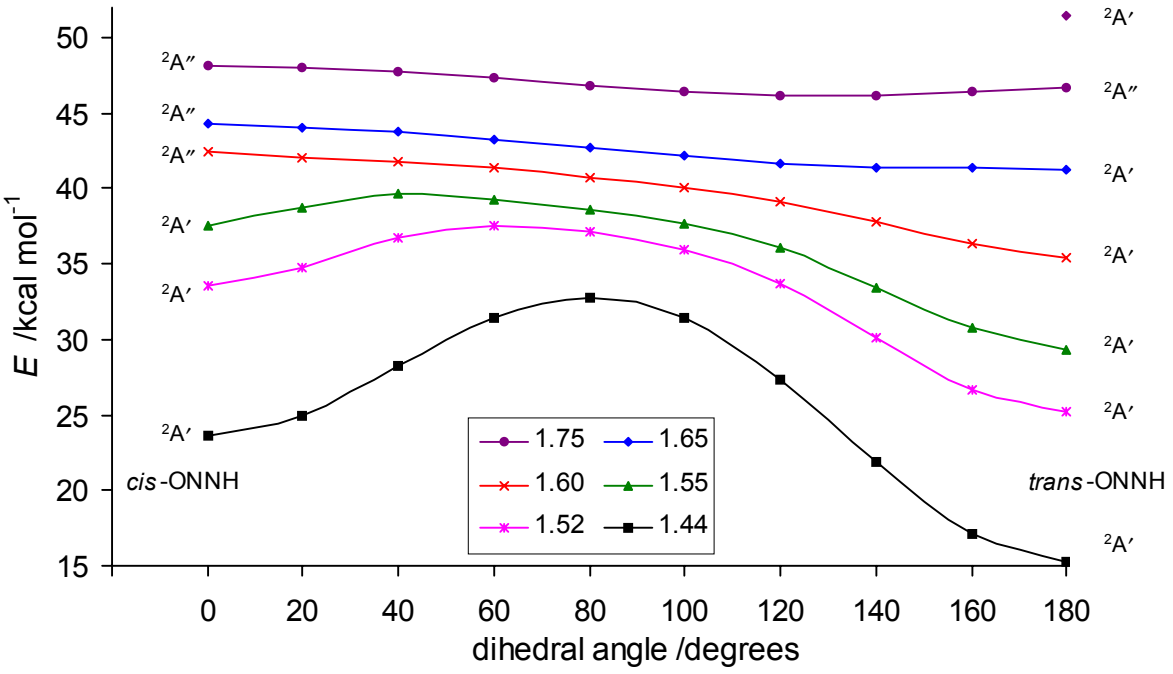

Figure 6.7 B3LYP/6-31G(2*df*,*p*) torsional potentials for ONNH at various *R*(N-N) (in Å) distances. (Energy relative to ^{2}A′ *trans*-ONNH.)

ONHN (^{2}A′) → HNO (^{1}A′) + N (^{4}S). This reaction (**Figure 6.3**) is complicated by a change in spin multiplicity from doublet to quartet as the N-N bond breaks. By mapping the minimum energy paths on both the doublet and quartet surfaces as a function of N-N distance, it was found that the intersection occurs at a distance of approximately 1.94 Å (**Figure 6.8**). The variational transition states for the dissociation at all temperatures are found to occur on the (barrierless) quartet surface at N-N distances of ~ 2.1 Å. We expect that the intersystem crossing will be substantially faster than the classical dissociation, hence the rate of this reaction was calculated using variational transition state and RRKM theory, utilising the transition state structures identified on the quartet surface.

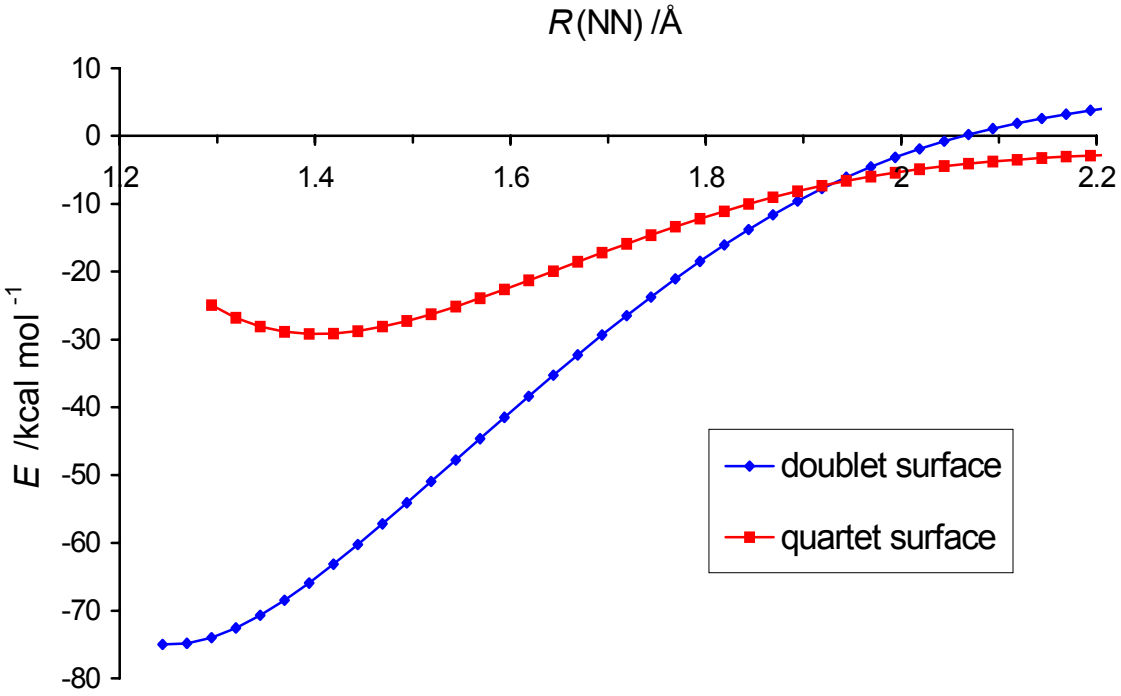

Figure 6.8 B3LYP/6-31G(2*df*,*p*) PES for ONHN → HNO + N showing the doublet and quartet surfaces. (Energy relative to HNO + N.)

***cis*- and *trans*-ONNH (^{2}A′) → N_2O ($^1\Sigma$) + H (^{2}S).** The dissociation of the *cis* isomer takes place over a barrier of 24.4 kcal mol^{-1} (6.1 kcal mol^{-1} above products) as shown in **Figure 6.2**. The B3LYP calculations reveal that in this transition state, labelled ONN-H, the ONN moiety is near-linear (*A*(NNO) = 173°) and the N-H separation is 1.66 Å. Attempts to find an analogous transition state on the *trans* surface were, however, unsuccessful as calculations

converged either to the *cis* transition state or to a second order saddle point. Mapping the minimum energy path as a function of N-H distance for *trans*-ONNH revealed a monotonic increase in the energy, significantly exceeding the barrier height to ONN-H in the region of *R*(N-H) ≈ 1.50 Å; at this point, however, the NNO angle of 156° is only 24° larger than at equilibrium. Stretching the N-H bond further results in a rapid increase in the NNO angle and collapse onto the *cis* surface (**Figure 6.9**). Further exploration of the potential energy surface revealed that there is a family of low energy (~ 5 – 10 kcal mol^{-1}) *trans* to *cis* isomerisation pathways that occur via the linearisation of the NNO moiety such that the maximum energy is below the energy of ONN-H. In summary, therefore, both *cis*- and *trans*-ONNH dissociate to N_2O + H via a common transition state as shown in **Figures 6.1** and **6.2**, with the understanding that the *trans* to *cis* isomerisation is part of the overall mechanism.

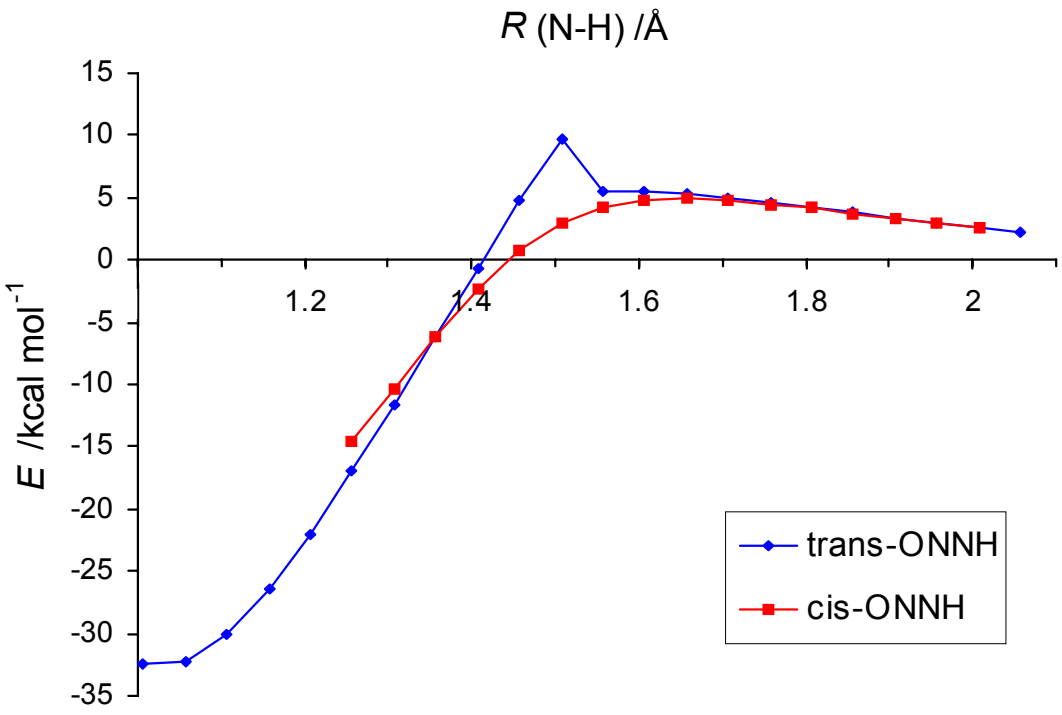

Figure 6.9 B3LYP/6-31G(2*df*,*p*) PES for ONNH → N_2O + H. (Energy relative to N_2O + H.)

ONHN ($^2A'$) → N_2O ($^1\Sigma$) + H (^2S). As shown in **Figure 6.3**, this reaction proceeds via a transition state (denoted ON_2-H) with a critical enthalpy of 21.7 kcal mol^{-1} and an exothermicity of 1.4 kcal mol^{-1} at 298 K.

***cis*-ONNH (^{2}A′) → N_2 ($^1\Sigma_g$) + OH ($^2\Pi$).** This reaction (**Figure 6.1** and **6.2**) occurs via a cyclic NNOH transition state (designated NNOHsq) followed by dissociation to N_2 + OH. Given the geometry of this transition state, the reaction can only proceed from the *cis* form of ONNH. The computed reaction barrier is 34.5 kcal mol^{-1}, that is, ~ 10 kcal mol^{-1} higher than for the N_2O + H channel. However, while ONNH → N_2O + H is endothermic, the ONNH → N_2 + OH reaction is highly exothermic (by 45.1 kcal mol^{-1}).

ONHN (^{2}A′) → N_2 ($^1\Sigma_g$) + OH ($^2\Pi$). This reaction proceeds by a 1,2 hydrogen shift from the central nitrogen to the oxygen, yielding a cyclic transition state, followed by decomposition into N_2 + OH (**Figure 6.3**). The transition state has been labelled NNOHtr; it is 29.4 kcal mol^{-1} higher in energy than ONHN and 91.4 kcal mol^{-1} higher than the dissociated products.

NNH (^{2}A′) + O (^{3}P) → N_2 ($^1\Sigma_g$) + OH ($^2\Pi$). This reaction represents the direct abstraction of the hydrogen of NNH by an oxygen atom. Somewhat surprisingly, no barrier was found for this reaction. This is likely to be a consequence of the very weak (breaking) N-H bond and the very strong interaction between the hydrogen and oxygen atoms, which is attractive at all O-H separations.

***trans*-ONNH (^{2}A′) → ONHN (^{2}A′).** These two intermediates can interconvert via a 1,2 hydrogen shift, although the barrier is rather high at 53.6 kcal mol^{-1} above *trans*-ONNH and 29.3 kcal mol^{-1} above ONHN (**Figure 6.3**). We also considered the possibility that this isomerisation could occur via a 1,2 oxygen shift. Although a transition state was found for this process using B3LYP/6-31G(2*df*,*p*), the subsequent RCCSD(T) calculations using this geometry showed large values of the τ_1 diagnostic and are therefore judged to be unreliable. Similarly, the corresponding higher level calculations which make up G3X were also not accepted as reliable due to the presence of significant spin contamination. As the energy of this transition state is ~ 28 kcal mol^{-1} higher than the analogous H transfer transition state at the B3LYP level of theory, this process was not investigated any further.

6.3.3 Kinetic Parameters

For the three reaction potential energy surfaces (viz. those shown in **Figures 6.1** to **6.3**) chemical activation simulations were carried out over the temperature range of 1000 – 2600 K and at pressures ranging from 1 to 10000 Torr using the MultiWell code. This temperature range spans the temperatures of relevance in flame studies. For each potential energy surface there are four barrierless reactions. These are the reverse fission reactions, adduct → NNH + O together with *cis*-ONNH → NO + NH, *trans*-ONNH → NO + NH and ONHN → HNO + N. For each of these reactions a variational transition state (VTS) was located at temperatures of 1000 K, 1500 K, 2000 K and at a higher temperature (2500 K except for *trans*-ONNH → NO + NH and ONHN→ O + NNH which were evaluated at 2400 K and 2200 K respectively). The VTS evaluated at 1000 K was used in the MultiWell modelling for temperatures 1000 and 1200 K, the VTS at 1500 K used for temperatures 1400 and 1600 K, the VTS at 2000 K for temperatures 1800, 2000 and 2200 K and the high temperature VTS for 2400 and 2600 K. Pressure-dependent overall rate coefficients to the four product channels were calculated using Equations (6.14) and (6.15).

No stabilisation of adducts or intermediates was found at any temperature or pressure in the studied range. Rate coefficients derived for individual reaction channels for a pressure of 1 atm are shown in **Table 6.6**. The rate coefficients did not show any significant pressure dependence between 1 and 10000 Torr and were not strongly dependent on temperature. The summed contribution to each channel from the two surfaces can be fitted by a modified Arrhenius expression and these rate coefficients are given in **Table 6.7**. From **Tables 6.6** and **6.7** we see that the major product channel is to N_2O + H, with all three surfaces contributing an approximately equal amount of reaction flux. The main contribution to the N_2 + OH channel is through the intermediate ONHN, with a somewhat smaller contribution arising from the *cis*-ONNH. Nearly all flux to NO + NH is through the *cis*- and *trans*- adducts. The endothermic reaction to HNO + N is only a very minor pathway and nearly all reaction flux is via the ONHN intermediate. A significant additional contribution to the production of N_2 + OH can also arise from the barrierless direct abstraction reaction for NNH + O.

Table 6.6 Rate coefficients ($cm^3\ mol^{-1}\ s^{-1}$) for NNH + O → product channels shown via adducts *cis*-ONNH, *trans*-ONNH and ONHN at 1 atm pressure.

	via adduct							
	cis-ONNH				*trans*-ONNH			
T/K	NO + NH	N_2O + H	N_2 + OH	HNO + N	NO + NH	N_2O + H	N_2 + OH	HNO + N
1000	6.51×10^{12}	1.64×10^{13}	3.19×10^{12}		9.45×10^{12}	2.17×10^{13}	8.36×10^{11}	
1200	7.23×10^{12}	1.56×10^{13}	3.09×10^{12}		9.35×10^{12}	1.82×10^{13}	6.33×10^{11}	
1400	7.07×10^{12}	1.56×10^{13}	3.18×10^{12}		7.65×10^{12}	1.90×10^{13}	8.13×10^{11}	
1600	7.88×10^{12}	1.52×10^{13}	3.19×10^{12}		7.60×10^{12}	1.66×10^{13}	6.44×10^{11}	
1800	7.62×10^{12}	1.69×10^{13}	3.55×10^{12}		7.55×10^{12}	1.69×10^{13}	6.07×10^{11}	
2000	8.16×10^{12}	1.65×10^{13}	3.50×10^{12}		8.09×10^{12}	1.64×10^{13}	5.59×10^{11}	
2200	8.84×10^{12}	1.60×10^{13}	3.50×10^{12}		7.45×10^{12}	1.35×10^{13}	4.62×10^{11}	
2400	9.40×10^{12}	1.63×10^{13}	3.58×10^{12}		7.15×10^{12}	1.32×10^{13}	4.89×10^{11}	
2600	9.77×10^{12}	1.57×10^{13}	3.50×10^{12}		7.05×10^{12}	1.19×10^{13}	4.50×10^{11}	2×10^{9}

Table 6.6. continued

	via adduct			
	ONHN			
T/K	NO + NH	N_2O + H	N_2 + OH	HNO + N
1000	3.61×10^{11}	1.94×10^{13}	6.55×10^{12}	
1200	2.52×10^{11}	1.99×10^{13}	6.13×10^{12}	
1400	3.00×10^{11}	1.86×10^{13}	5.88×10^{12}	
1600	5.07×10^{11}	1.70×10^{13}	5.89×10^{12}	3×10^{9}
1800	5.06×10^{11}	2.10×10^{13}	7.22×10^{12}	7×10^{9}
2000	5.40×10^{11}	1.83×10^{13}	6.41×10^{12}	6×10^{9}
2200	5.84×10^{11}	1.60×10^{13}	6.12×10^{12}	12×10^{9}
2400	5.52×10^{11}	1.63×10^{13}	6.10×10^{12}	20×10^{9}
2600	5.27×10^{11}	1.43×10^{13}	5.48×10^{12}	16×10^{9}

Table 6.7 Modified Arrhenius parameters for NNH + O → products via adducts *cis*-ONNH, *trans*-ONNH and ONHN ($k = AT^n \exp(-E_a/RT)$).

Reactions	A/cm^3 mol^{-1} s^{-1}	n	E_a/cal mol^{-1}
NNH + O → NO + NH	7.80×10^{10}	0.642	–1830.
NNH + O → N_2O + H	2.40×10^{16}	–0.765	1540.
NNH + O → N_2 + OH	2.57×10^{10}	0.702	–2320.
NNH + O → HNO + N	6.2×10^{-7}	4.84	0.
NNH + O → N_2 + OH [a]	3.00×10^{13}	0	0.

[a] Direct abstraction reaction via abstraction transition state.

Our branching ratios into the three principal reaction channels are very different from those estimated by Bozzelli and Dean.[2] In their QRRK analysis they only considered a single ONNH adduct. They also did not consider the ONHN adduct which we have discovered in the present work. The ONHN well is considerably shallower than that for *cis*- or *trans*-ONNH and significant flux flows through the ONHN adduct both to N_2O + H and to N_2 + OH (but *not* to NO + NH).

6.3.4 Comparison with Experiment

As mentioned in the Introduction (**Section 6.1**), Hayhurst and Hutchinson[5] reported a value for $k_4K_{P,3}$ from which they then estimated a rate coefficient, k_4, for reaction to NO + NH. Their method involved the assumption that every NH radical produced by Reaction (6.4) rapidly reacts to yield a second NO molecule. For fuel-rich flames of CH_4 / O_2 / N_2 and of H_2 / O_2 / N_2 the above assumption leads to the equation

$$k_4K_{P,3} = \left(\frac{d[\mathrm{NO}]}{dt} \cdot \frac{1}{2[\mathrm{N_2}][\mathrm{O}]} - k_4 \right) \cdot \frac{1}{x_{\mathrm{H}}} \tag{6.17}$$

where x_H is the mole fraction of H in the burnt gas. To obtain x_H, Hayhurst and Hutchinson measured OH and temperature profiles in the burnt gas. There are, however, very significant

random errors in their data, ranging from nearly 3 orders of magnitude at 2500 K to nearly an order of magnitude at 1800 K. If we fit our computed values of k_4 from the MultiWell simulations and $K_{P,3}$ derived from our thermochemical calculations we obtain $k_4 K_{P,3} = 3.7\times10^{7} \exp(-2800/T)$ cm^3 mol^{-1} s^{-1}. Comparing with Hayhurst and Hutchinson's value of $k_4 K_{P,3} = 1.4\times10^{9} \exp(-2760/T)$ cm^3 mol^{-1} s^{-1} shows that our value at 2000 K is over an order of magnitude lower than theirs but probably still within the considerable random error in their data.

6.3.5 Kinetic Modelling

As discussed earlier, detailed chemical reaction models, such as the two formulations of GRIMech[3,4] (containing the rate coefficient for k_4 estimated by Bozzelli and Dean[2]), have recently been found to overestimate the level of NO produced by combustion systems. We have chosen to use the GRIMech 3.0 model with our new NNH thermochemistry and kinetics. The value of k_4 in this model was altered to the value given in **Table 6.7** and the other three addition and decomposition reaction channels also included together with the direct abstraction of H by O atoms. This modified mechanism has been used to model two series of data[54] from a completely stirred reactor – a fuel lean methane / air combustion and a lean combustion of CO / H_2 / air at residence times, τ, between about 3 to 4 ms and equivalence ratios, ϕ, between 0.5 and 0.6 approximately. The first of these cases has been used to benchmark the performance of GRIMech.[4] **Figure 6.10** compares the performance of our modified kinetic model with that of the original GRIMech 3.0 formulation and experimental NO profiles.

As can be seen from **Figure 6.10(a)** both the original formulation of GRIMech 3.0 and our modified version with new NNH thermochemistry and kinetics reproduce the experimental NO data from CH_4 / air satisfactorily although our model gives a closer fit to experiment. With the runs in CO / H_2 / air (**Figure 6.10(b)**), however, significantly poorer performance occurs when using the original GRIMech 3.0 model. Whereas our present model gives a good fit to experiment, GRIMech 3.0 overestimates the level of NO by nearly a factor of two. To

ascertain the reason for this difference in performance we have carried out reaction path analyses on both kinetic models.

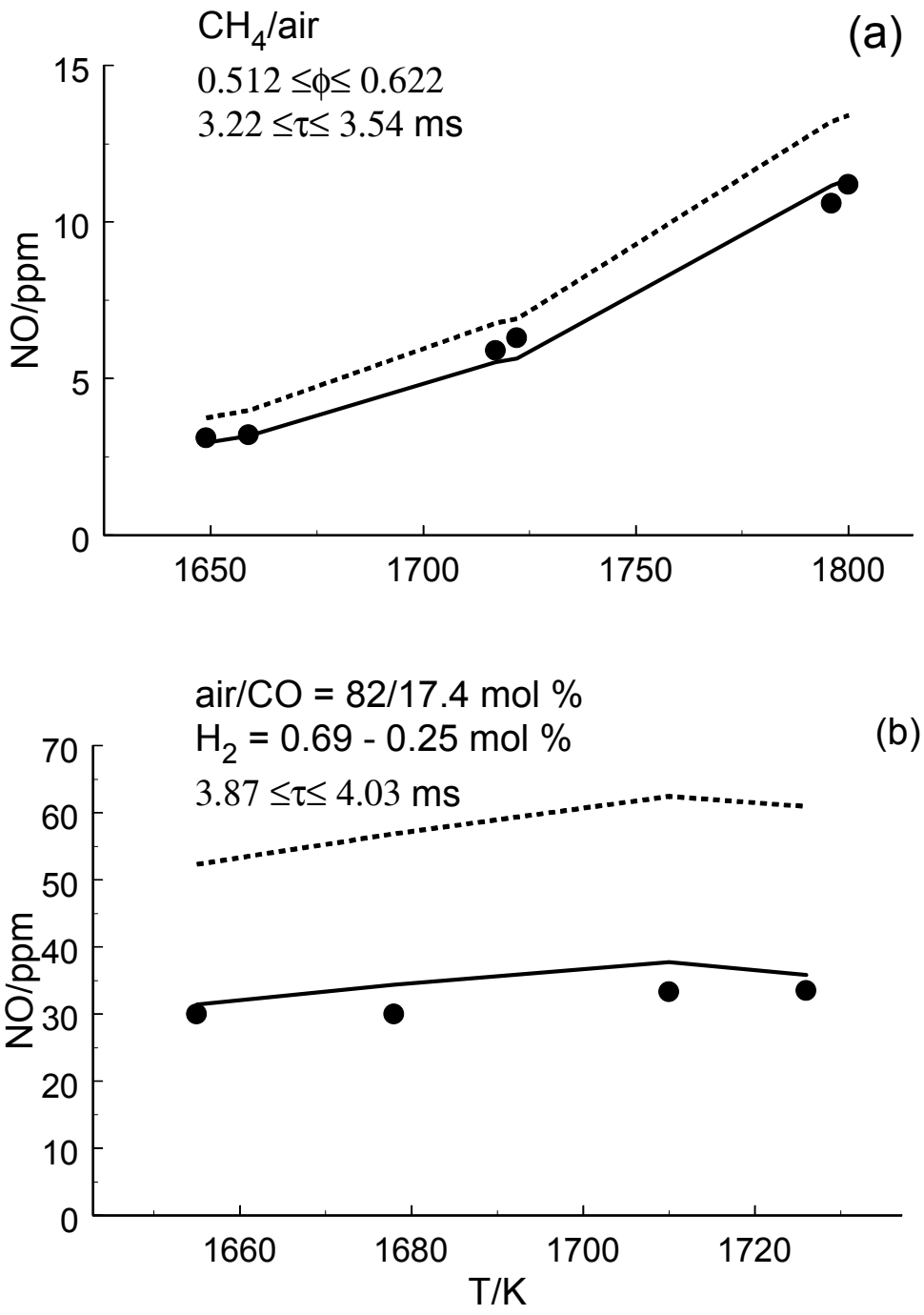

Figure 6.10 Comparison of NO profiles of combustion in a completely stirred flame reactor. **(a)** CH_4 / air, **(b)** H_2 / CO / air. Filled circles: Experimental data from Ref. 54. Dashed lines: predictions using GRIMech 3.0. Full lines: prediction using GRIMech 3.0 with NNH thermochemistry and kinetics from the present study.

We have sought to quantify the contribution that each of the four reaction pathways (Zel'dovich, Prompt-NO, N_2O and NNH + O) makes to NO production by using the following simplified procedure. In order to determine the contribution of a particular pathway, that pathway is eliminated from the kinetic model and the modified mechanism is then run to ascertain the effect of its omission. This is repeated in turn for each pathway. The basic assumption in this method is that there are no cross correlations between the pathways. It has been shown, however, that the error resulting form such neglect of cross correlation is of 5% or less in the total contribution of all pathways when applied to NO profiles in atmospheric opposed flow methane-air flames.[55] In our present path analysis the summation error is significantly less than 3%.

The contribution of the thermal pathway is assessed by eliminating its initiation reaction, (6.1). The prompt-NO pathway contribution was also determined by elimination of its initiation reaction, (6.2). To assess the contribution of the N_2O intermediate pathway, it was necessary to eliminate all reactions involving N_2O from the reaction model while the NNH + O route was quantified by elimination of its initiation reaction, (6.4). This procedure is similar to that used previously.[6, 55]

Figures 6.11(a) and **(b)** compare the contribution of each reaction pathway for our present model and for the original formulation of GRIMech 3.0 to methane-air studies in a completely stirred reactor.[54] The computed contributions of the N_2O intermediate, thermal and prompt-NO pathways are similar for both models. A larger contribution of the NNH + O pathway is calculated using GRIMech 3.0. Nevertheless, because the first three pathways all make significant contributions to the NO profile, the two models both give reasonable reproductions of the experimental data, although GRIMech 3.0 does somewhat overestimate the NO levels. It is with the runs in CO / H_2 / air (**Figure 6.11(c)** and **(d)**), however, that the computed contributions of the two models radically differ. The prompt-NO pathway makes no contribution in these runs. Again, the calculated contributions of the N_2O and thermal pathways are quite similar for both models, however GRIMech 3.0 predicts that the NNH + O pathway will make the greatest contribution to the NO profiles whereas our model, with new NNH thermochemistry and kinetics, predicts that this pathway makes only a very small contribution to the total. It is apparent, therefore, that by overestimating the contribution of the NNH + O pathway GRIMech 3.0 predicts too high a level of NO in this system. In methane-air combustion, where there are significant contributions from the prompt and

thermal routes, the overestimation of the NNH + O pathway is masked. Where the prompt and thermal pathways are minimised this overestimation becomes obvious. A detailed testing of our new thermochemistry and kinetics in modelling premixed and opposed flow flames will be presented elsewhere.[56]

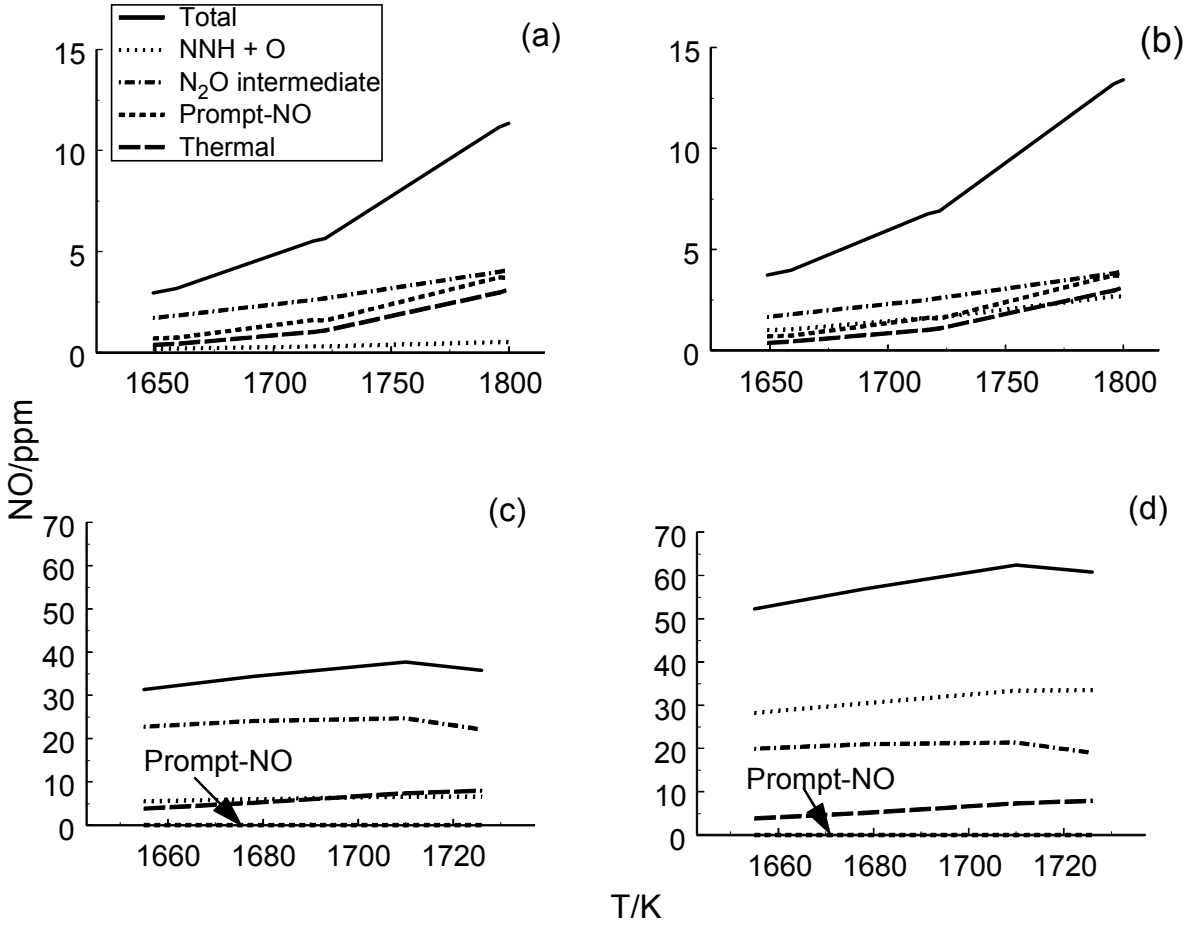

Figure 6.11 Predictions of the contribution of individual pathways to NO formation.

(a) Present model predictions for the CH_4 / air data of **Figure 6.10(a)**.

(b) GRIMECH 3.0 predictions for the CH_4 / air data of **Figure 6.10(a)**.

(c) Present model predictions for the H_2 / CO / air data of **Figure 6.10(b)**.

(d) GRIMECH 3.0 predictions for the H_2 / CO / air data of **Figure 6.10(b)**.

6.4 Conclusions

Three reaction potential energy surfaces for NNH + O → products have been investigated by ab initio quantum chemical calculations. Three adducts, namely *trans*-ONNH, *cis*-ONNH and ONHN, have been identified through which reaction to three exothermic product channels, NO + NH, N_2 + OH, N_2O + H, and one endothermic channel, HNO + N, takes place. Rate coefficients to each reaction channel have been obtained by RRKM analysis. The rate coefficient at 2000 K to the NO + NH channel is predicted to be approximately a factor of four lower than had been previously estimated[2] (and included in detailed reaction models such as GRIMech 3.0)[4]. A new value of $\Delta_f H^0_{298}$ (NNH) = 60.6 ± 0.5 kcal mol^{-1} has been obtained by CCSD(T) calculations which include extrapolation to the complete basis limit. This value, together with the rate coefficients we have derived for the NNH + O → products reactions, have been used to modify the GRIMech 3.0 reaction model. Using this new formulation we could satisfactorily model NO profiles produced in a completely stirred reactor[54] from both methane / air and CO / H_2 / air mixtures. Overestimation of NO profiles from the latter mixtures by GRIMech 3.0 has been shown, by reaction path analysis, to result from too high a rate coefficient for initiation of the NNH + O pathway. On the basis of the present work we conclude that this pathway represents a very minor route to NO in most combustion systems.

6.5 References

1. J. A. Miller and C. T. Bowman, *Prog. Energy Combust. Sci.*, **1989**, *15*, 287.
2. J. W. Bozzelli and A. M. Dean, *Int. J. Chem. Kinet.*, **1995**, *27*, 1097.
3. C. T. Bowman, R. K. Hanson, D. F. Davidson, W. P. Gardiner, Jr, V. Lissianski, G. P. Smith, D. M. Golden, M. Frenklach and M. Goldenberg, GRIMech 2.11, http://www.me.berkeley.edu/gri_mech.
4. G. P. Smith, D. M. Golden, M. Frenklach, N. W. Moriaty, B. Eiteneer, M. Goldenberg, C. T. Bowman, R. K. Hanson, S. Song, W. C. J. Gardiner, V. V. Lissianski and Z. Qin, GRIMech 3.0, http://www.me.berkeley.edu/gri_mech/.
5. A. N. Hayhurst and E. M. Hutchinson, *Combust. Flame*, **1998**, *114*, 274.
6. D. Charlston-Goch, B. L. Chadwick, R. J. S. Morrison, A. Campisi, D. D. Thomsen and N. M. Laurendeau, *Combust. Flame*, **2001**, *125*, 729.
7. A. A. Konnov and J. De Ruyck, *Combust. Flame*, **2001**, *125*, 1258.
8. C. F. Melius and J. S. Binkley, in *Twentieth Symp. (Int.) on Combustion*; The Combustion Institute: Pittsburgh, Pennysylvania, **1984**, p. 575.
9. P. Marshall, A. Fontijn and C. F. Melius, *J. Chem. Phys.*, **1987**, *86*, 5540.
10. T. Fueno, M. Fukuda and K. Yokoyama, *Chem. Phys.*, **1988**, *124*, 265.
11. J. A. Harrison and R. G. A. R. MacIagan, *J. Chem. Soc. Faraday Trans.*, **1990**, *86*, 3519.
12. S. P. Walch, *J. Chem. Phys.*, **1993**, *98*, 1170.
13. J. L. Durant, Jr., *J. Phys. Chem.*, **1994**, *98*, 518.
14. K. S. Bradley, P. McCabe, G. C. Schatz and S. P. Walch, *J. Chem. Phys.*, **1995**, *102*, 6696.
15. M. Simonson, K. S. Bradley and G. C. Schatz, *Chem. Phys. Lett.*, **1995**, *244*, 19.
16. S. Kristyan and M. C. Lin, *Chem. Phys. Lett.*, **1998**, *297*, 200.
17. M. C. van Beek and J. J. ter Meulen, *J. Chem. Phys.*, **2001**, *115*, 1843.
18. S. P. Walch and H. Partridge, *Chem. Phys. Lett.*, **1995**, *233*, 331.
19. J. Gu, Y. Xie and H. F. Schaefer, III, *J. Chem. Phys.*, **1998**, *108*, 8029.
20. L. A. Curtiss, P. C. Redfern, K. Raghavachari and J. A. Pople, *J. Chem. Phys.*, **2001**, *114*, 108.
21. C. Hampel, K. A. Peterson and H.-J. Werner, *Chem. Phys. Lett.*, **1992**, *190*, 1.

22. K. Raghavachari, G. W. Trucks, J. A. Pople and M. Head-Gordon, *Chem. Phys. Lett.*, **1989**, *157*, 479.
23. T. H. Dunning, Jr., *J. Chem. Phys.*, **1989**, *90*, 1007.
24. R. A. Kendall, T. H. Dunning, Jr. and R. J. Harrison, *J. Chem. Phys.*, **1992**, *96*, 6796.
25. D. E. Woon and T. H. Dunning, Jr., *J. Chem. Phys.*, **1993**, *98*, 1358.
26. A. D. Becke, *J. Chem. Phys.*, **1993**, *98*, 5648.
27. A. D. Becke, *Phys. Rev. A*, **1988**, *38*, 3098.
28. C. Lee, W. Yang and R. G. Parr, *Phys. Rev. B*, **1988**, *37*, 785.
29. T. Helgaker, W. Klopper, H. Koch and J. Noga, *J. Chem. Phys.*, **1997**, *106*, 9639.
30. R. D. Cowan and D. C. Griffin, *J. Opt. Soc. Am.*, **1976**, *66*, 1010.
31. R. L. Martin, *J. Phys. Chem.*, **1983**, *87*, 750.
32. B. O. Roos, P. R. Taylor and P. E. M. Siegbahn, *Chem. Phys.*, **1980**, *48*, 157.
33. B. O. Roos, in *Ab initio Methods in Quantum Chemistry II*, K. P. Lawley, Ed.; *Advances in Chemical Physics*, I. Prigogine and S. A. Rice, Eds.; Vol. LXIX; J. Wiley & Sons Ltd.: Chichester, UK, **1987**, p. 399.
34. L. A. Curtiss, K. Raghavachari, P. C. Redfern, V. Rassolov and J. A. Pople, *J. Chem. Phys.*, **1998**, *109*, 7764.
35. E. Pollack, in *Theory of Chemical Reaction Dynamics*, M. Baer, Ed.; Vol. 3; CRC Press, Inc.: Boca Raton, Florida, **1985**, p. 128.
36. W. L. Hase, S. L. Mondro, R. J. Duchovic and D. M. Hirst, *J. Am. Chem. Soc.*, **1987**, *109*, 2916.
37. D. G. Truhlar and B. C. Garrett, *Acc. Chem. Res.*, **1980**, *13*, 440.
38. J. C. Mackie, G. B. Bacskay and N. L. Haworth, *J. Phys. Chem. A*, **2002**, *106*, 10825.
39. J. I. Steinfeld, J. S. Francisco and W. L. Hase, *Chemical Kinetics and Dynamics*; Prentice Hall: Engelwood Cliffs, NJ, **1989**, 308.
40. M. J. Frisch, G. W. Trucks, H. B. Schlegel, G. E. Scuseria, M. A. Robb, J. R. Cheeseman, V. G. Zakrzewski, J. A. Montgomery, R. E. Stratmann, J. C. Burant, S. Dapprich, J. M. Millam, A. D. Daniels, K. N. Kudin, M. C. Strain, O. Farkas, J. Tomasi, V. Barone, M. Cossi, R. Cammi, B. Mennucci, C. Pomelli, C. Adamo, S. Clifford, J. Ochterski, G. A. Petersson, P. Y. Ayala, Q. Cui, K. Morokuma, D. K. Malick, A. D. Rabuck, K. Raghavachari, J. B. Foresman, J. Cioslowski, J. V. Ortiz, B. B. Stefanov, G. Lui, A. Liashenko, P. Piskorz, I. Komaromi, R. Gomperts, R. L. Martin, D. J. Fox, T. Keith, M. A. Al-Laham, C. Y. Peng, A. Nanayakkara, C. Gonzalez, M. Challacombe, P. M. W. Gill, B. G. Johnson, W. Chen, M. W. Wong, J.

L. Andres, M. Head-Gordon, E. S. Replogle and J. A. Pople, Gaussian 98 Revision A.7, Gaussian, Inc.: Pittsburgh, PA, **1998**,

41. P. J. Knowles, C. Hampel and H.-J. Werner, *J. Chem. Phys.*, **1993**, *99*, 5219.
42. MOLPRO 96.3 is a package of ab initio programs written by H.-J. Werner and P. J. Knowles with contributions from J. Almlöf, R. D. Amos, M. J. O. Degan, S. T. Elbert, C. Hampel, W. Meyer, K. Peterson, R. Pitzer, A. J. Stone, P. R. Taylor, R. Lindh, M. E. Mura, T. Thorsteinsson.
43. "DALTON, an ab initio electronic structure program, Release 1.0 (1997)" written by T. Helgaker, H. J. Aa. Jensen, P. Joergensen, J. Olsen, K. Ruud, H. Aagren, T. Andersen, K. L. Bak, V. Bakken, O. Christiansen, P. Dahle, E. K. Dalskov, T. Enevoldsen, B. Fernandez, H. Heiberg, H. Hettema, D. Jonsson, S. Kirpekar, R. Kobayashi, H. Koch, K. V. Mikkelsen, P. Norman, M. J. Packer, T. Saue, P. R. Taylor and O. Vahtras.
44. K. Andersson, M. R. A. Blomberg, M. P. Fülscher, G. Karlström, R. Lindh, P.-Å. Malmqvist, P. Neogrády, J. Olsen, B. O. Roos, A. J. Sadlej, M. Schültz, L. Seijo, L. Serrano-Andrés, P. E. M. Siegbahn and P.-O. Widmark, MOLCAS Version 4, Lund University: Lund, Sweden, **1997**,
45. J. R. Barker, Multiwell Software Version 1.2.0, Ann Arbor, MI, **2002**, http://aoss.engin.mumich.edu/multiwell/.
46. J. R. Barker, *Int. J. Chem. Kin.*, **2001**, *33*, 232.
47. R. J. Kee, F. M. Rupley, J. A. Miller, M. E. Coltrin, J. F. Grcar, E. Meeks, H. K. Moffat, A. E. Lutz., G. Dixon-Lewis, M. D. Smooke, J. Warnatz, G. H. Evans, R. S. Larson, R. E. Mitchell, L. R. Petzold, W. C. Reynolds, M. Caracotsios, W. E. Stewart, P. Glarborg, C. Wang and O. Adigun, CHEMKIN Collection Release 3.6, Reaction Design, Inc.: San Diego, CA, **2000**,
48. R. Tarroni, P. Palmieri, A. Mitrushenkov, P. Tosi and D. Barsi, *J. Chem. Phys.*, **1997**, *106*, 10265.
49. M. W. Chase, Jr., *J. Phys. Chem. Ref. Data*, **1998**, *Monograph 9*, 1.
50. B. Rusic, D. Feller, D. A. Dixon, K. A. Peterson, L. B. Harding, R. L. Asher and A. F. Wagner, *J. Phys. Chem. A*, **2001**, *105*, 1.
51. W. R. Anderson, *Combustion and Flame*, **1999**, *117*, 394.
52. A. K. Wilson, T. van Mourik and T. H. Dunning, Jr., *J. Molec. Struct. (Theochem)*, **1996**, *388*, 339.
53. T. van Mourik, A. K. Wilson and T. H. Dunning, Jr., *Mol. Phys.*, **1999**, *96*, 529.

54. R. C. Steele, P. C. Malte, D. G. Nicol and J. C. Kramlich, *Combust. Flame*, **1995**, *100*, 440.

55. D. D. Thomsen and N. M. Laurendeau, *Combust. Flame*, **2001**, *124*, 350.

56. J. C. Mackie, N. L. Haworth and G. B. Bacskay, *2003 Australian Symposium on Combustion & The 8th Australian Flames Days, Melbourne, December 8-9,* **2003**.

Chapter 7

The Enthalpy and Mechanism of the Photolysis of $CFClBr_2$

The work described in this chapter represents a combined experimental and theoretical investigation into the thermochemistry of the bromomethane $CFClBr_2$. It is being jointly published in *Chemical Physics Letters*.[1] The experimental work (**Section 7.2**) was performed by N. L. Owens, K. Nauta and S. H. Kable and has also been reported in the Honours thesis of Owens[2]. The theoretical and experimental aspects of this work are heavily interreliant and thus the work has been reported here in its entirety.

7.1 Introduction

The role of halons and CFC's in the chemistry of the atmosphere has been well documented for many decades. As a general class of molecules, halomethanes absorb ultraviolet light via a $\sigma^* \leftarrow \sigma$ transition, which results in the cleavage of the weakest C–X bond (where X is halogen or hydrogen). The fate of the atom is very well understood and central to the depletion of stratospheric ozone. The fate of the halomethyl radical is less well understood, but the primary reaction is probably O_2 addition leading to the formation of halogen-substituted aldehydes and slow transport back to the troposphere.

Over the past couple of decades, several reports of UV or vacuum-UV excitation of halomethanes, resulting in cleavage of two C–X bonds, have appeared. Bromo- and iodomethane species seem to exhibit triple fragmentation pathways when the wavelength is shorter than 200 nm.[3-10] For wavelengths longer than 200 nm, however, only the difluoro-species, CF_2I_2, CF_2Br_2 and CF_2BrI have been reported to undergo triple fragmentation. CF_2I_2 undergoes a single C–I cleavage at longer wavelengths, which is believed to become two sequential C–I cleavages and finally concerted loss of two I-atoms as the energy of the dissociating photon is increased.[10] Triple fragmentation of CF_2Br_2 and CF_2BrI are also thought to be stepwise processes.[5-9]

In a series of papers on carbene spectroscopy, Kable and co-workers have created carbenes by photolysis of suitable halon precursors, for example CFCl from $CFClBr_2$,[11] and both CHF and CFBr from $CHFBr_2$.[12] At the time, no attempt was made to elucidate the mechanism of carbene formation. In this paper we investigate the mechanism by which CFCl is formed from $CFClBr_2$ (halon-1112).

Interpretation of the results is made more difficult by the absence of thermochemical data concerning halon-1112. In fact, we could locate thermochemical data for only two dibromomethane compounds: CF_2Br_2 [13] and CH_2Br_2 [14]. The literature thermodynamic data for carbenes, including CFCl, are also highly varying. The most reliable current values are probably theoretical values obtained by Dixon et al. for CF_2,[15,16] CHBr and CBr_2 [17] and by Sendt and Bacskay[18] for CFCl. Both groups utilised the coupled cluster method with extrapolation to the complete basis limit and expect their results to be accurate to within ± 4 kJ mol^{-1}. The Gaussian-3 (G3) calculations of Sendt and Bacskay[18] for CF_2 and CFCl and the Gaussian-2 results of Cameron and Bacskay[19] for CHBr and CBr_2 are in good agreement with these coupled cluster results. More recently, the G3 procedure has been extended to be able to describe molecules containing atoms from the third row.[20] We have therefore calculated bond energies and heats of formation for a number of molecules containing bromine atoms using the G3 methodology. In addition to facilitating the interpretation of the experimental data, the calculations also permit us to test the accuracy of the G3 method for larger bromine containing molecules, especially since the largest in the G3 test set is CH_3Br.

The objectives of the current work are threefold. Firstly we seek to establish whether there is a triple fragmentation pathway for $CFClBr_2$ following absorption of a single photon at stratospherically relevant wavelengths. Secondly, we use these data to determine thermochemical properties for the various species involved, including heats of formation and bond energies. Finally, we calculate those same thermochemical properties using the new formulation of G3 theory for third row atoms to verify both the experimental data and the validity of the theoretical method for larger bromine-containing compounds.

7.2 Experimental Methods and Results

7.2.1 Methodology

Details of the experiment can be found in the previous work on CFCl of Guss et al.[11] Very briefly, helium (2 bar) was bubbled through $CFClBr_2$ (*l,* 0°C) and expanded via a pulsed nozzle into a vacuum chamber. $CFClBr_2$ was photolysed at the nozzle orifice by a Nd:YAG pumped OPO laser (Coherent Infinity 40-100 and OPASCAN). The output of the OPO was varied from 480 to 560 nm and frequency doubled to yield light from 240 to 280 nm. The ensuing CFCl fragments were probed about 10 mm downstream, approx. 6 μs after the photolysis pulse, by an excimer pumped dye laser (Lambda Physik Lextra 200 and LPD 3001E, Exalite 398 dye). By allowing the CFCl to cool in the expansion, any effect of different CFCl product state distributions as a function of photolysis energy is negated. The trade-off in doing this is that the parent $CFClBr_2$ is fairly warm (we estimate 100-200 K).

Fluorescence from CFCl was imaged onto the slits of a Spex Minimate monochromator with 5 mm slits, which acts like a 20 nm triangular bandpass filter. This filter provides no real rotational or vibrational resolution for the CFCl fluorescence. The broadband fluorescence was detected by an EMI 9789QB photomultiplier, the signal passed to an SRS-250 boxcar averager and finally to an SRS-245 A/D board and a personal computer. The experiment was timed using the internal variable delays provided by the Infinity laser.

7.2.2 Results

An absorption spectrum of $CFClBr_2$, diluted in air, measured on a Cary 4E spectrometer, is shown in **Figure 7.1** (top). The spectrum shows negligible absorption in the actinic range ($\lambda >$ 295 nm) and no sharp features, which is typical of halon and CFC species. At least two broad overlapping features are evident, the one to the red (around 240 nm) forming a pronounced shoulder on the stronger feature to the blue, which peaks further to the blue than the range of the spectrometer. By analogy with other CFC's and halons, these features are likely to be $\sigma^* \leftarrow \sigma$ transitions involving a C–Br bond.

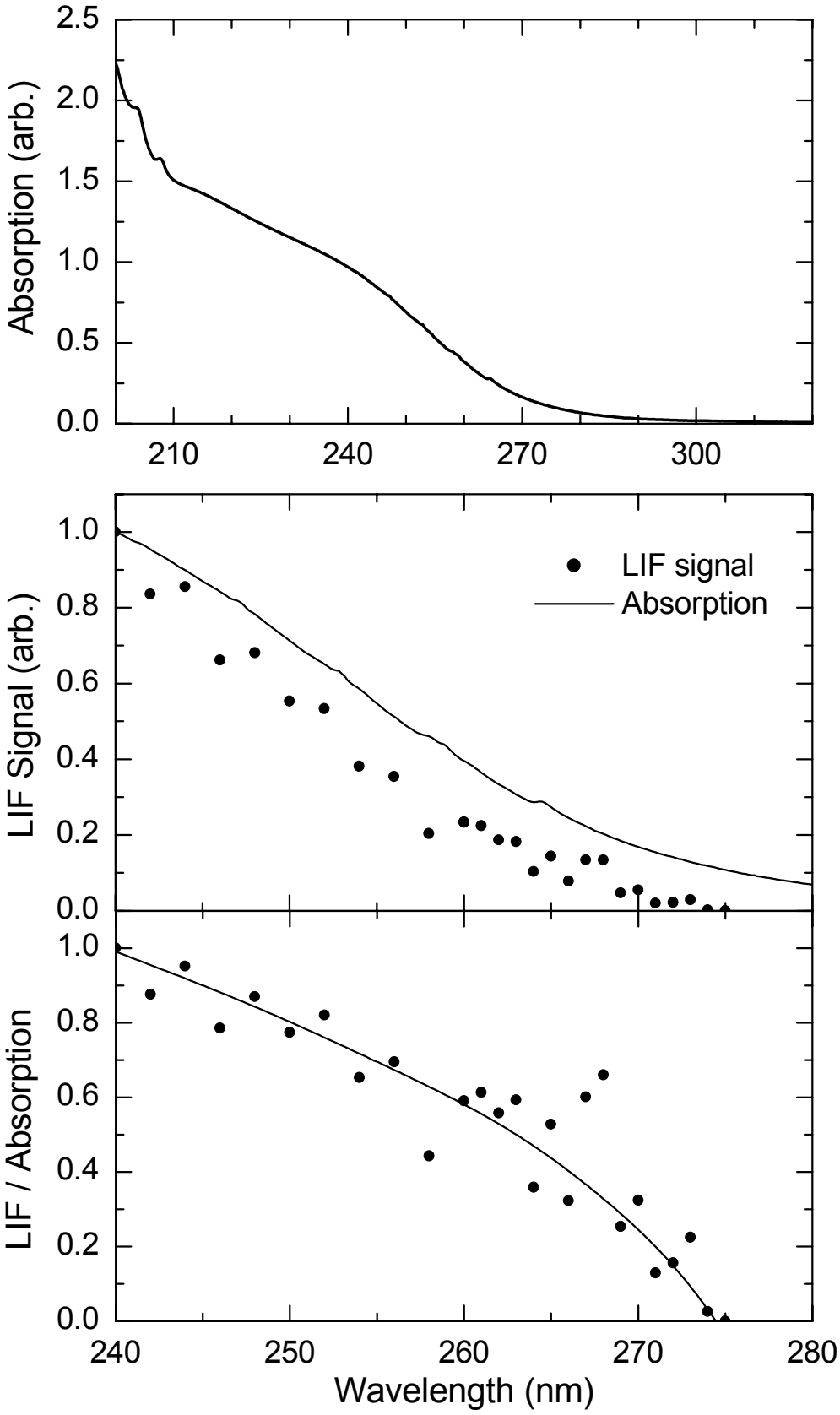

Figure 7.1 (top) $CFClBr_2$ absorption spectrum; (centre) fluorescence excitation spectrum of $CFClBr_2$; (bottom) ratio of fluorescence signal to absorption signal.

The photolysis of $CFClBr_2$ is known to result in the formation of CFCl.[11] Several LIF spectra of CFCl produced in this way are shown in **Figure 7.2**. The origin region is shown, which is quite weak due to poor Franck-Condon overlap with the ground state. However, it is relatively uncongested, least affected by chlorine isotopic features, and also has well-assigned hot bands and so we have concentrated on this region. The spectral features pertinent to this work are the origin transition and a variety of hot-band transitions emanating from the $\upsilon_2 = 1$ and $\upsilon_3 = 1$ levels (ν_2 = bend, ν_3 = C–Cl stretch). The main rotational sub-branches are indicated by a comb. The main feature is the strong $^{r}Q_0$ sub-branch, flanked by the $^{r}Q_1$ to shorter wavelength and the $^{p}Q_1$ to longer wavelength. The reader is referred to previous work on CFCl spectroscopy[11] for any further details.

The mechanism of CFCl production from $CFClBr_2$ was not explored previously. The first test that was performed was to establish the dependence of the CFCl signal on pump laser power. The LIF signal from the central peak of the 0_0^0 transition was monitored as the pump power was varied randomly. The resulting dependence is shown in **Figure 7.3** and indicates that the observed signal varies linearly with laser power.

The LIF intensity from 0_0^0 transition was also monitored as the pump wavelength was changed randomly between 240 and 275 nm as shown in **Figure 7.1** (centre). The data points in the figure arise from about 1000 laser shots and were take taken every 2 nm below 260 nm and then every 1 nm above 260 nm. For comparison, the absorption spectrum is also plotted on the same axes, arbitrarily normalised to the value at 240 nm. The shapes of the two spectra are similar, but the excitation spectrum rises more rapidly towards 240 nm than does the absorption spectrum. Additionally, the excitation spectrum has reached zero (no CFCl observed) at 275 nm while the absorption spectrum is still about 10% of the 240 nm value and, as shown in the top panel, continues well beyond 280 nm. The actual wavelength at which the excitation spectrum reaches zero is rather difficult to determine in this spectrum as the data converge asymptotically to zero over about 5 nm.

The difference between the excitation and absorption spectrum is accentuated in **Figure 7.1** (bottom) by plotting the ratio of the excitation to absorption intensity. Quite clearly, relative to the absorption spectrum, the intensity of the excitation spectrum drops consistently from 240 to 260 nm and then drops quite sharply towards 275 nm. The line is a heavily smoothed

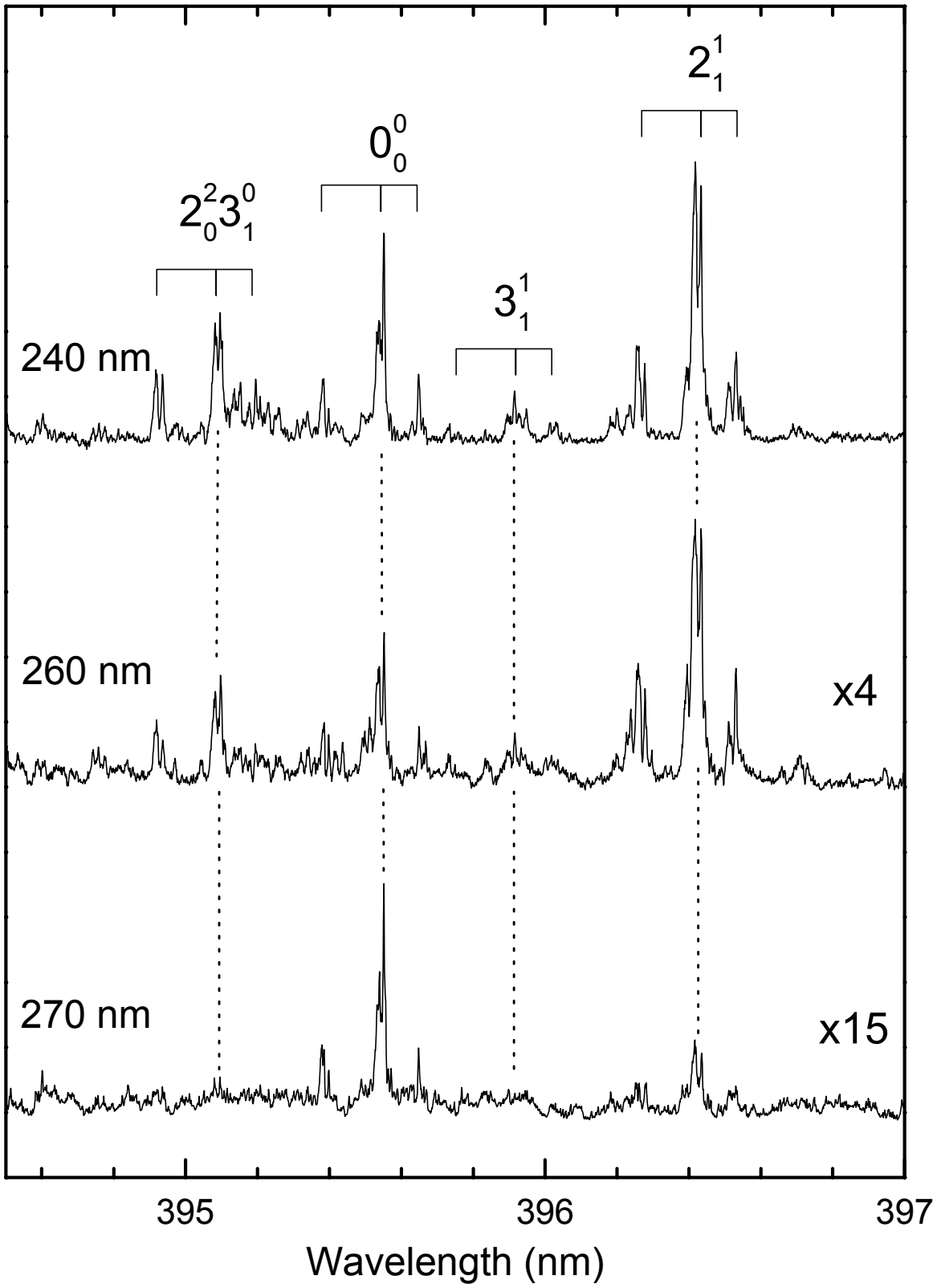

Figure 7.2 CFCl fluorescence excitation spectra in the origin region following dissociation in $CFClBr_2$ at 240, 260 and 270 nm.

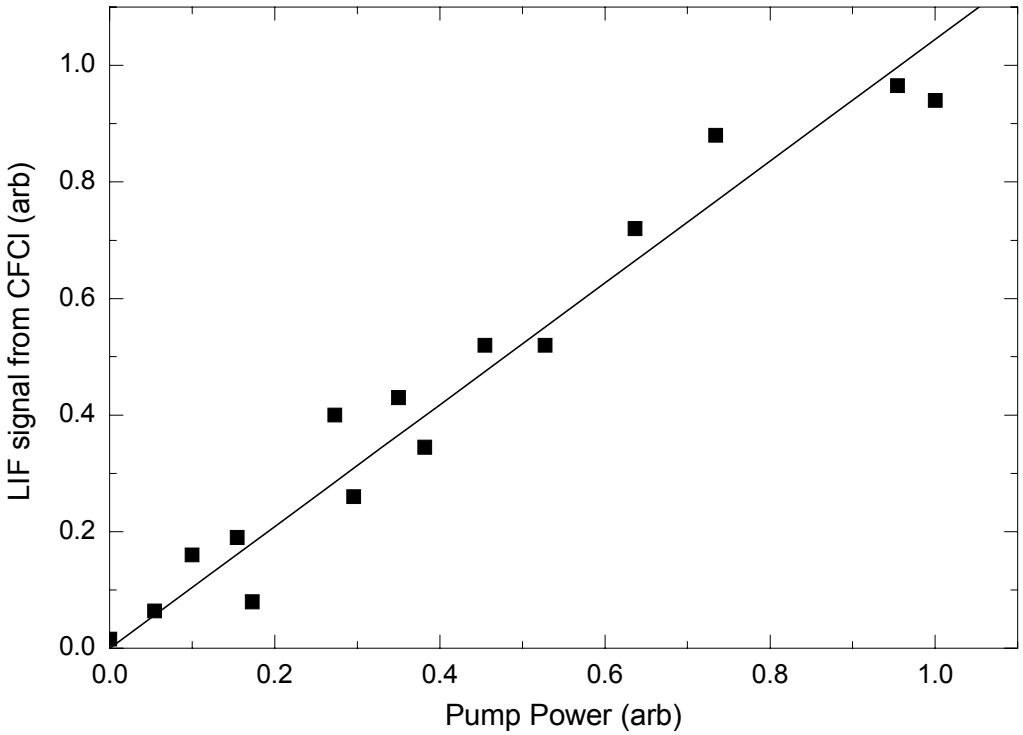

Figure 7.3 Power dependence of the CFCl signal following dissociation of $CFClBr_2$ at 240 nm.

spline fit, which cuts the abscissa at 274 nm and we estimate the threshold for production of CFCl from $CFClBr_2$ to be 274 ± 2 nm, which corresponds to a photon energy of 36,500 ± 280 cm^{-1}.

More information about the threshold can be obtained by examining the CFCl spectrum as a function of wavelength. Three such spectra are shown in **Figure 7.2**, obtained following excitation of $CFClBr_2$ at 240, 260 and 270 nm. The 240 nm spectrum was discussed earlier and shows features arising from population in $\upsilon = 0$, $\upsilon_2 = 1$ and $\upsilon_3 = 1$, which have vibrational energies of 0, 447 and 753 cm^{-1} respectively.[11] Although the 2_1^1 transition is strongest, the Franck-Condon factor for the 2_1^1 transition is about 15× larger than the 0_0^0 transition[11] so the population in the $\upsilon_2 = 1$ level is actually about an order of magnitude less than $\upsilon = 0$. The 3_1^1 Franck-Condon factor is similar to 0_0^0 [11] and therefore the $\upsilon_3 = 1$ population is also much less than $\upsilon = 0$.

At 260 nm the relative population in these vibrational levels has not changed much, although the overall signal is reduced by a factor of about four. The 270 nm spectrum, however, shows CFCl population only in the $\upsilon = 0$ and $\upsilon_2 = 1$ levels, with the 0_0^0 transition dominant. The overall signal is now about 15 times reduced in comparison with the 240 nm spectrum.

The data above are summarised in **Figure 7.4**. A photon energy of 36,360 cm^{-1} (275 nm) does not lead to detectable CFCl. At 37,037 cm^{-1} (270 nm) CFCl in the $\upsilon = 0$ and $\upsilon_2 = 1$ states are produced and at 38,460 cm^{-1} (260 nm), $\upsilon = 0$, $\upsilon_2 = 1$ and $\upsilon_3 = 1$ levels are populated. The energy level diagram shows that all three observations are satisfied if the combined dissociation energy for both C–Br bonds is 36,475 ± 120 cm^{-1}. This is in good agreement with the threshold from the excitation spectrum of **Figure 7.1**, which was 36,500 ± 280 cm^{-1}.

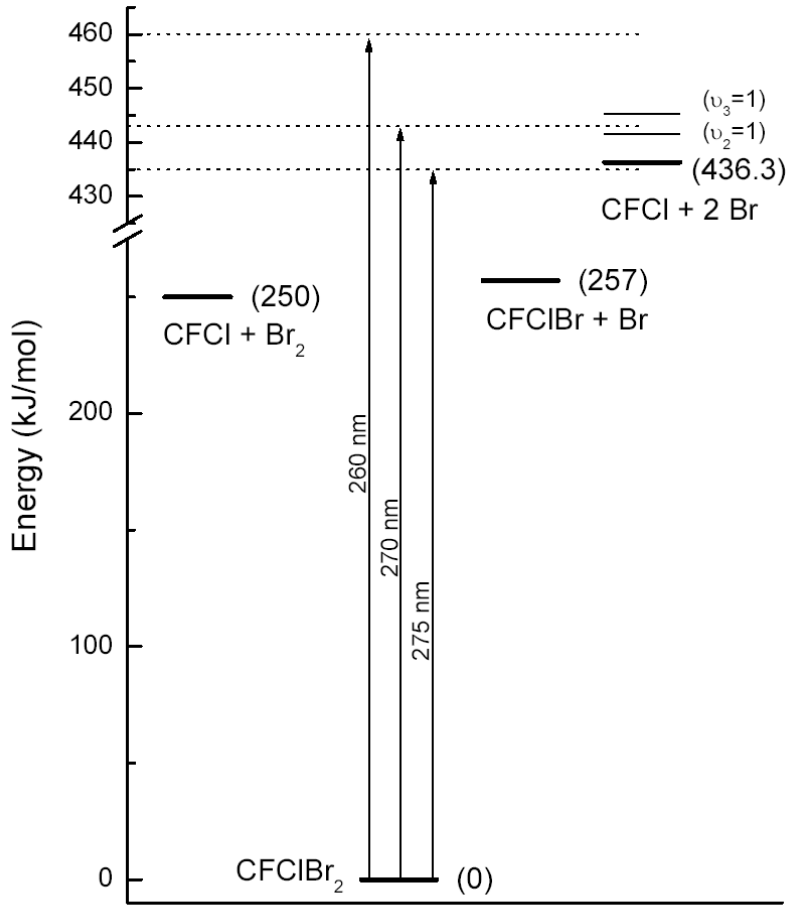

Figure 7.4 Energy level diagram of $CFClBr_2$ and various reaction products calculated in this work.

There are two concerns at this stage about proclaiming this to be an unambiguous experimental measurement of the threshold to triple fragmentation of $CFClBr_2$: i) the observation of a linear power dependence for CFCl production is a necessary but not sufficient condition for the process to be single photon, and ii) we have not addressed the possibility that CFCl is produced in concert with the Br_2 molecule, rather than two Br atoms. These issues could be resolved by detailed consideration of the thermochemistry of the appropriate processes. In the absence of reliable heats of formation for $CFClBr_2$ or CFClBr we have carried out high level ab initio calculations of these properties, which are presented in the next section. The theoretical and experimental data are tied together to resolve these issues in the Discussion.

7.3 Theoretical Methods and Results

7.3.1 Methodology

The G3 procedure for molecules with third row atoms has only been developed very recently.[20] The method is essentially the same as that initially proposed for first and second row atoms[21], where the energy of a hypothetical QCISD(T) calculation with a large basis set is approximated by performing such a calculation with a significantly smaller basis set, followed by corrections for enlargement of the basis set, which are computed at lower levels of theory, namely MP2 and MP4. The G3 energy can be summarised as

$$
\begin{aligned}
E_0[\mathrm{G3}] = {} & E[\mathrm{QCISD(T)/6\text{-}31G}(d)] \\
& + \{E[\mathrm{MP4/6\text{-}31+G}(d)] - E[\mathrm{MP4/6\text{-}31G}(d)]\} && (+\text{ correction}) \\
& + \{E[\mathrm{MP4/6\text{-}31G}(2df,p)] - E[\mathrm{MP4/6\text{-}31G}(d)]\} && (2df,\,p\text{ correction}) \\
& + \left\{ \begin{array}{l} E[\mathrm{MP2(Full)/GTLarge}] - E[\mathrm{MP2/6\text{-}31G}(2df,p)] \\ \quad - E[\mathrm{MP2/6\text{-}31+G}(d)] + E[\mathrm{MP2/6\text{-}31G}(d)] \end{array} \right\} && (\mathrm{G3Large\ correction}) \\
& + \Delta E_{\mathrm{ZPE}} + \Delta E_{\mathrm{SO}} + \Delta E_{\mathrm{hlc}}
\end{aligned}
\qquad (7.1)
$$

where the appropriate corrections due to successive basis set enlargement are evaluated at the MP4 and MP2 levels of theory. ΔE_{ZPE} is the zero point vibrational energy, ΔE_{SO} denotes spin-orbit coupling corrections and ΔE_{hlc} is an (empirical) higher level correction.

The geometry and zero point vibrational energy are determined at the MP2(Full)/6-31G(*d*) and HF/6-31G(*d*) levels of theory respectively. Note that the G3 formulation for third row atoms recommends the use of a new set of basis functions[20] which are based on the 6-31G basis of Rassolov et al.[22] As for first and second row atoms, the G3 calculations on molecules containing third row atoms are performed with six *d* and seven *f* functions, except in the case of G3Large calculations which utilise the spherical harmonic representation for all orbitals, viz. (5*d*, 7*f*). Furthermore, following the work of Duke and Radom[23], who noted an improvement in the accuracy of the G2 procedure when the 3*d* electrons of third row atoms were unfrozen to correlation, the G3 procedure also prescribes the inclusion of the 3*d* orbitals of third row atoms in the valence space.

Once G3 absolute energies have been calculated, atomisation energies and thus heats of formation can be evaluated using the relevant (experimental) atomic data. Heats of formation can also be determined on the basis of reaction enthalpies, preferably those of isodesmic reactions where the number of bonds of each type are conserved in the reaction. Errors in the theoretical description of a particular atom or bond are then expected to cancel, resulting potentially in a relatively accurate estimate of the heat of the reaction. Application of Hess' Law then allows the determination of the heat of formation of a given species, provided accurate (experimental) heats of formation are available for all other species in the reaction. Isodesmic reaction schemes have been used in this work to confirm the reliability of the heats of formation obtained from G3 atomisation energies.

The quantum chemical computations were carried out using the Gaussian98 suite of programs[24] on DEC alpha 600/5/333 and COMPAQ XP100/500 workstations of the Theoretical Chemistry group at the University of Sydney and on the COMPAQ AlphaServer SC system of the Australian Partnership for Advanced Computing National Facility at the National Supercomputing Centre, ANU, Canberra

7.3.2 Results

The computed G3 total energies, atomisation energies and heats of formation at 0 and 298K are reported in **Table 7.1**. The absolute energies of Br_2, Br and CH_3Br have been reported earlier by Curtiss et al.[20] As they did not report the atomisation energies or heats of formation of Br and CH_3Br, we have generated these additional data and include them here for completeness. The G3 results for CFCl, CH_4, CH_2F_2, CH_3Cl, CH_2Cl_2 and CF_4 have also been published previously[18,21] but are quoted here because of their importance in the decomposition reactions of $CFClBr_2$ and in the isodesmic reaction schemes.

Table 7.1 Energies, atomisation energies and heats of formation (at 0 and 298K) (kJ mol^{-1} unless otherwise noted).

Species	E_0 /E_h	*AE*	$\Delta_f H_0^{0\,a}$	$\Delta_f H_{298}^0$		
	G3	G3	G3	G3/*AE* [a]	G3/*ID* [b]	Experimental
$CFClBr_2$	−5745.04026	1319.2	−187.4	−188.2	−190.6	−184 ± 5
CFClBr	−3171.42502	1062.5	−42.5	−42.9		
CFCl	−597.83777	879.2	28.9	29.8		31 ± 13 [c]
Br_2	−5147.10746	190.4	33.3	34.6		30.91 ± 0.11 [d]
Br	−2573.51747					111.87 ± 0.12 [d]
CH_3Br	−2613.41950	1500.0	−28.9	−36.1		−34.2 ± 0.8 [e]
						−36 ± 1 [f]
CH_4	−40.45762	1643.3	−68.0	−75.9		−74.87 [d]
CH_2F_2	−238.86226	1743.6	−445.8	−453.4		−450.66 [d]
CH_3Cl	−499.91301	1552.5	−73.6	−81.5		−83.68 [d]
CH_2Cl_2	−959.37121	1469.2	−86.7	−93.5		−95.52 [d]
CF_4	−437.30780	1951.4	−931.1	−936.8		−933.04 ± 0.7 [g]

[a] Heat of formation calculated from atomisation energies.

[b] Heat of formation calculated by isodesmic schemes.

[c] Ref. 24.

[d] Ref. 25.

[e] Ref. 26.

[f] Ref. 27.

[g] Ref. 28.

Table 7.2 lists the various isodesmic reactions which were employed to determine the heat of formation of $CFClBr_2$ from the G3 reaction energies, along with the resulting enthalpies of formation. The spread of values about the mean is less than 4 kJ mol^{-1}, suggesting chemical accuracy in the results. The average value obtained by this approach differs by only 2.4 kJ mol^{-1} from the heats of formation obtained from the G3 atomisation energies, which is well within the expected uncertainties of the G3 calculations. This suggests that the G3 procedure is indeed capable of producing accurate heats of formation from atomisation energies for larger third row containing molecules and therefore the use of isodesmic schemes is not warranted.

Table 7.2 Isodesmic reaction schemes and resulting G3 enthalpies of formation for $CFClBr_2$ (kJ mol^{-1}).

Reaction	$\Delta_f H^0_{298}$
$2CFClBr_2 + 4CH_4 \rightarrow CH_2F_2 + CH_2Cl_2 + 4CH_3Br$	−190.5
$2CFClBr_2 + 5CH_4 \rightarrow CH_2F_2 + 2CH_3Cl + 4CH_3Br$	−192.2
$2CFClBr_2 + 3CH_4 + CH_2F_2 \rightarrow CH_2Cl_2 + 4CH_3Br + CF_4$	−190.9
$2CFClBr_2 + 3CH_4 + 2CH_3Cl \rightarrow 2CH_2Cl_2 + 4CH_3Br + CH_2F_2$	−188.9
Average for $CFClBr_2$	−190.6

7.4 Discussion

The experimental data demonstrate conclusively that CFCl is a by-product of $CFClBr_2$ photolysis and that the process is likely to involve the absorption of only one photon. The threshold for CFCl production was found to be 436 ± 2 kJ mol^{-1} or 36,460 ± 150 cm^{-1}. CFCl can be formed from $CFClBr_2$ by two different reactions:

$$CFClBr_2 \xrightarrow{h\nu} CFCl + Br_2 \qquad \text{Reaction 7.1}$$

$$CFClBr_2 \xrightarrow{h\nu} CFCl + 2\,Br \qquad \text{Reaction 7.2}$$

The observed appearance threshold for CFCl could correspond to either of these reactions. A schematic of the chemical energies involved in each process in shown in **Figure 7.4**. The left side of the figure shows the Br_2 production, while the right hand side shows sequential or concerted elimination of two Br atoms. To help distinguish between these two reactions we turn to the ab initio results from above.

The G3 method has provided estimates of the heats of formation ($\Delta_f H^0$) for all species involved in this work, see **Table 7.1**. (The heats of formation of Br and Br_2 are well known.[26]) These thermochemical data were used to evaluate the reaction energies for various reactions, as shown in **Table 7.3**. The calculated energy required for Reaction 7.1 is 250 ± 5 kJ mol^{-1} and for Reaction 7.2 is 440 ± 5 kJ mol^{-1}. The value for Reaction 7.2 is comfortably within the mutual error limits for the theoretical and experimental estimates. This does not absolutely discount Reaction 7.1 because as a three-centre elimination it would probably require a barrier. However it would seem fortuitous that the barrier height is exactly the same as the thermochemical threshold for the other channel. Therefore we have rejected the three-centre elimination pathway as much less likely than the triple fragmentation pathway. These conclusions are also in accord with the analogous findings for the CF_2Br_2 [8] and CF_2BrI [5] molecules.

Table 7.3 Reaction energies for possible decomposition pathways for $CFClBr_2$ (kJ mol^{-1}).

Reaction	$\Delta_r E$ (0K) G3	$\Delta_r H^0_{298}$ G3
$CFClBr_2 \rightarrow CFCl + 2Br$	439.9	441.7
$CFClBr_2 \rightarrow CFClBr + Br$	256.7	257.2
$CFClBr \rightarrow CFCl + Br$	183.2	184.5
$CFClBr_2 \rightarrow CFCl + Br_2$	249.5	252.6

Since $\Delta_f H^0$ is known for CFCl and Br we can use the threshold energy to determine an experimental $\Delta_f H^0_0$ for $CFClBr_2$. The value so determined is −183.4 ± 5 kJ mol^{-1} (using the G3 value for CFCl as the experimental value is quite uncertain). The G3 method also provides heat capacity correction factors between 0 K and 298 K. For $CFClBr_2$ this difference is 0.8 kJ

mol^{-1}, which provides an estimate for $CFClBr_2$ of $\Delta_f H^0_{298} = -184.2 \pm 5$ kJ mol^{-1}. The G3 values are in excellent agreement with this experimental heat of formation.

The triple fragmentation reactions of several halomethane species containing Br and I have been reported previously. Most of the experiments have been carried out in the far or vacuum ultraviolet region ($\lambda < 200$ nm), which typically excites the second absorption band (see **Figure 7.1** for this band in $CFClBr_2$). For example CF_2BrCl [3], CF_2BrI [5], CH_2BrI [4], CF_2Br_2 [4-9] and CF_2I_2 [10] have all been reported to exhibit competing chemical channels, cleaving one or other of the C–Br or C–I bonds (if different), and for cleavage of both bonds. Chloro- and fluoromethane species (containing no Br or I), conversely, do not show triple fragmentation (involving C-Cl cleavage), at least down to 193 nm.

The mechanism for the triple fragmentation of halomethanes is not assured with some studies favouring a concerted triple whammy, while others favour the formation of a hot halomethyl radical intermediate, followed by spontaneous dissociation into the carbene. The problem is that, although the spectra of these species appear simple, there are actually several electronic transitions that contribute to each "peak" in the spectrum. To our knowledge, there has been no definitive theoretical study of a bromo- or iodomethane species where one of these states has been shown to correlate with concerted triple fragmentation. In the absence of theoretical assistance experimentalists rely on the nuances of the atom recoil energy distributions to try and decide between concerted and stepwise mechanisms.

In the first electronic absorption band of bromomethane species there is fairly uniform agreement that a $\sigma^* \leftarrow \sigma$ transition localised on a C-Br bond is excited, which leads to formation of Br plus a halomethyl radical with quantum yields approaching unity. Only two other bromomethanes have been reported to undergo triple fragmentation within this band, namely CF_2BrI [4] and CF_2Br_2 [7,9]. The work on CF_2Br_2 has been quite extensive over a couple of decades and the consensus now seems to be that CF_2Br_2 undergoes triple fragmentation for $\lambda < 260$ nm. At these wavelengths the primary process is still the breaking of one C–Br bond. The resultant CF_2Br radicals are born with a wide range of internal energy, some having sufficient energy for spontaneous decomposition into CF_2 + Br. The experimental data for $CFClBr_2$ bear a striking similarity to CF_2Br_2, which leads us to suspect that the mechanism of triple fragmentation is probably the same; that is, direct loss of one Br atom, followed by spontaneous loss of the second Br atom from a hot intermediate CFClBr radical.

7.5 Conclusion

In this work we have established that CFCl is formed from single photon dissociation of $CFClBr_2$ for wavelengths shorter than 274 nm. We attribute this to a thermochemical threshold, and hence determine the energy required to break both C-Br bonds to be 436 ± 2 kJ mol^{-1}. Ab initio calculations using the G3 method confirm that two bromine atoms are the partners in this reaction. The heat of formation of $CFClBr_2$ is inferred from these experiments to be $\Delta_f H^0_{298} = -184 \pm 5$ kJ mol^{-1}, in excellent agreement with the computed G3 value of -188 ± 5 kJ mol^{-1}. These ab initio calculations are the first reports of dibromo species at the G3 level. Comparison of the heat of formation by G3 calculation with that calculated as the average value from a set of isodesmic reactions shows agreement to within 2.4 kJ mol^{-1}, thereby confirming the reliability of the G3 method for these species.

7.6 References

1. N. L. Owens, K. Nauta, S. H. Kable, N. L. Haworth and G. B. Bacskay, *Chem. Phys. Lett.*, **2003**, *370*, 469.
2. N. L. Owens, *Honours Thesis*, School of Chemistry, University of Sydney, **2001**.
3. G. Baum and J. R. Huber, *Chem. Phys. Lett.*, **1993**, *213*, 427.
4. L. J. Butler, E. J. Hintsa, S. F. Shane and Y. T. Lee, *J. Chem. Phys.*, **1987**, *86*, 2051.
5. P. Felder, X. Yang, G. Baum and J. R. Huber, *Israel J. Chem.*, **1993**, *34*, 33.
6. T. R. Gosnell, A. J. Taylor and J. L. Lyman, *J. Chem. Phys.*, **1991**, *94*, 5949.
7. J. van Hoeymissen, W. Uten and J. Peeters, *Chem. Phys. Lett.*, **1994**, *226*, 159.
8. M. R. Cameron, S. A. Johns and S. H. Kable, *Phys. Chem. Chem. Phys.*, **2000**, *2*, 2539.
9. M. S. Park, T. K. Kim, S.-H. Lee, K.-H. Jung, H.-R. Volpp and J. Wolfrum, *J. Phys. Chem. A*, **2001**, *105*, 5606.
10. G. Baum, P. Felder and J. R. Huber, *J. Chem. Phys.*, **1993**, *98*, 1999.
11. J. S. Guss, O. Votava and S. H. Kable, *J. Chem. Phys.*, **2001**, *115*, 11118.
12. T. W. Schmidt, G. B. Bacskay and S. H. Kable, *J. Chem. Phys.*, **1999**, *110*, 11277.
13. M. R. Cameron and G. B. Bacskay, *J. Phys. Chem. A*, **2000**, *104*, 11212.
14. S. J. Paddison and E. Tschuikow-Roux, *J. Phys. Chem. A*, **1998**, *102*, 6191.
15. D. A. Dixon and D. Feller, *J. Phys. Chem. A*, **1998**, *102*, 8209.
16. D. A. Dixon, D. Feller and G. Sandrone, *J. Phys. Chem. A*, **1999**, *103*, 4744.
17. D. A. Dixon, W. A. de Jong, K. A. Peterson and J. S. Francisco, *J. Phys. Chem. A*, **2002**, *106*, 4725.
18. K. Sendt and G. B. Bacskay, *J. Chem. Phys.*, **2000**, *112*, 2227.
19. M. R. Cameron and G. B. Bacskay, *Chem. Phys.*, **2000**, *104*, 11202.
20. L. A. Curtiss, P. C. Redfern, V. Rassolov, G. Kedziora and J. A. Pople, *J. Chem. Phys.*, **2001**, *114*, 9287.
21. L. A. Curtiss, K. Raghavachari, P. C. Redfern, V. Rassolov and J. A. Pople, *J. Chem. Phys.*, **1998**, *109*, 7764.
22. V. A. Rassolov, M. A. Ratner, J. A. Pople, P. C. Redfern and L. A. Curtiss, *J. Comput. Chem.*, **2001**, *22*, 976.
23. B. J. Duke and L. Radom, *J. Chem. Phys.*, **1998**, *109*, 3352.
24. M. J. Frisch, G. W. Trucks, H. B. Schlegel, G. E. Scuseria, M. A. Robb, J. R. Cheeseman, V. G. Zakrzewski, J. A. Montgomery, R. E. Stratmann, J. C. Burant, S.

Dapprich, J. M. Millam, A. D. Daniels, K. N. Kudin, M. C. Strain, O. Farkas, J. Tomasi, V. Barone, M. Cossi, R. Cammi, B. Mennucci, C. Pomelli, C. Adamo, S. Clifford, J. Ochterski, G. A. Petersson, P. Y. Ayala, Q. Cui, K. Morokuma, D. K. Malik, A. D. Rabuk, K. Raghavachari, J. B. Foresman, J. Cioslowski, J. V. Ortiz, B. B. Stefanov, G. Lui, A. Liashenko, P. Piskorz, I. Komaromi, R. Gomperts, R. L. Martin, D. J. Fox, T. Keith, M. A. Al-Laham, C. Y. Peng, A. Nanayakkara, C. Gonzalez, M. Challacombe, P. M. W. Gill, B. G. Johnson, W. Chen, M. W. Wong, J. L. Andres, M. Head-Gordon, E. S. Replogle and J. A. Pople, Gaussian 98 Revision A.7, Gaussian, Inc.: Pittsburgh, PA, **1998**,

25. J. C. Poutsma, J. A. Paulino and R. R. Squires, *J. Phys. Chem.*, **1997**, *101*, 5327.
26. M. W. Chase, Jr., *J. Phys. Chem. Ref. Data*, **1998**, *Monograph 9*, 1.
27. K. C. Ferguson and E. Whittle, *J. Chem. Soc., Faraday Trans. 1*, **1972**, *68*, 295.
28. G. P. Adams, A. S. Carson and P. G. Laye, *Trans. Faraday Soc.*, **1966**, *62*, 1447.
29. L. V. Gurvich, I. V. Veyts and C. B. Alcock, *Thermodynamic Properties of Individual Substances*; CRC Press: Boca Raton, Florida, **1994**.

Chapter 8

The Molecular Structure and Intra- and Inter-Molecular Bonding of PSOrn

8.1 Introduction

N^{δ}-(*N*′-Sulfodiaminophosphinyl)-L-ornithine (PSOrn) is the active component of phaseolotoxin, which in turn is derived from a toxin produced by *Pseudomonas syringae* pv. *phaseolicola*. PSOrn has been found to bind to the *E. coli* enzyme ornithine transcarbamoylase (OTCase) with a dissociation constant of 1.6×10^{-12} M at 37°C, pH = 8.[1] OTCase catalyses the reaction of carbamoyl phosphate with L-ornithine, forming L-citrulline and phosphate and forms part of the urea cycle for mammals. It is also involved in the synthesis of arginine by plants and bacteria. The binding of PSOrn to OTCase irreversibly halts this catalysis, resulting in cell death.

The X-ray crystal structure of PSOrn within the enzyme has been determined at 1.8 Å resolution by Langley et al.[1] The resulting heavy atom backbone of this molecule is shown in **Figure 8.1**. Since crystal structures refined at this resolution define only the positions of non-hydrogen atoms, the chirality, tautomeric form and the ionisation state of the bound inhibitor could at best be inferred from the structural data using chemical considerations. This study aims to investigate, using the methods of computational quantum chemistry, the chemical identity of PSOrn in both free and bound states, determine their relative stabilities and clarify the nature of bonding both within the inhibitor and between the enzyme and inhibitor.

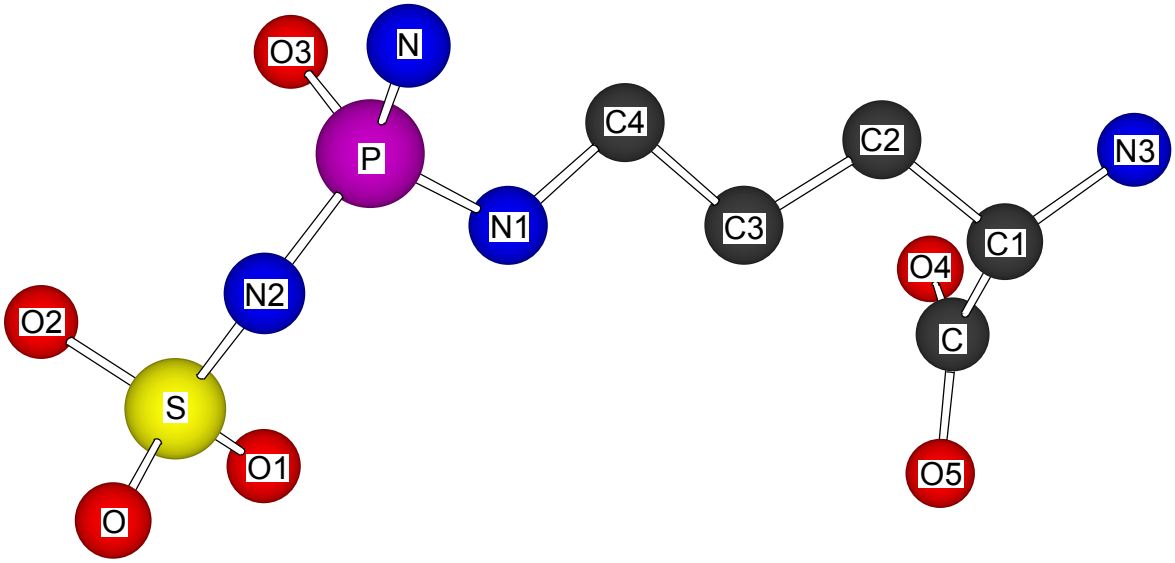

Figure 8.1 Structure of PSOrn within OTC as determined by X-ray diffraction.[1]

Langley et al.[1] proposed that PSOrn acts as a transition state analogue within the enzyme; that is, it adopts the same conformation and forms the same type of hydrogen bonds with the enzyme as in the suggested carbamoyl phosphate + L-ornithine transition state. They examined the self-consistency of possible hydrogen bonding networks at the enzyme active site and concluded that the most likely chemical form of the bound inhibitor is a doubly ionised "imino" tautomer and that the phosphotriamide is the R enantiomer as shown in **Figure 8.2** (along with the substrates, proposed transition states and a more conventional amino form of the inhibitor). The observed potent inhibitory activity of PSOrn could thus be rationalised because this species is a structural mimic of the substrates in a proposed transition state.

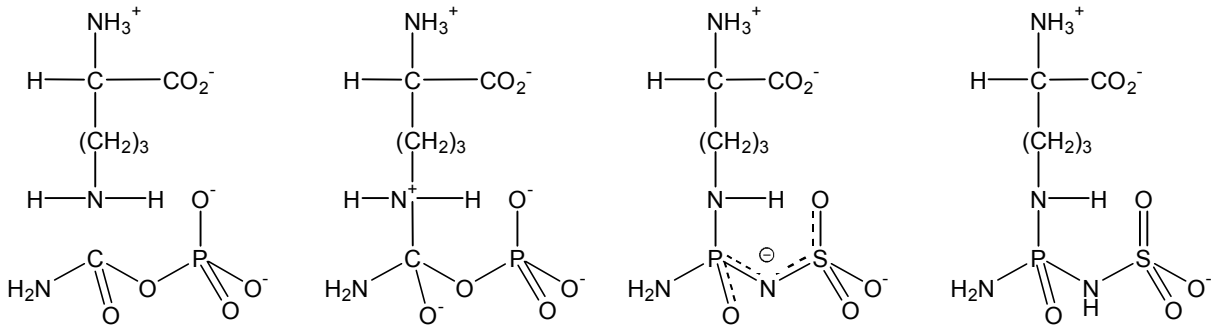

Figure 8.2 Imino and amino tautomers of PSOrn as transition state analogues for the OTC catalysed reaction, as proposed by Langley et al.[1]

Conventional chemical wisdom suggests that free PSOrn would be more stable in the amino form, that is, with the P-N-S nitrogen protonated. Moreover, such protonation would not necessarily preclude hydrogen bond donation to this nitrogen, given the presence of a lone pair on N. The current investigations were undertaken with the primary aim of elucidating the nature of the interaction between PSOrn and some of the important enzyme residues, in particular the hydrogen bonding of an arginine to the P-N-S nitrogen of the inhibitor. To reduce computational costs the $(CH_2)_3CH(NH_3^+)(CO_2^-)$ side-chain of PSOrn has been replaced by a methyl group. The relative stabilities of several tautomeric amino and imino forms of the resulting neutral model compound are investigated by density functional theory,

followed by similar studies on adducts of these with one and two (model) arginine molecules. In addition to providing information on the relative stabilities of the amino and imino forms of the inhibitor in both free and bound forms, these studies also yield charge distribution data and thus some insight into the nature of bonding within the inhibitor as well as between inhibitor and enzyme.

8.2 Methods

In the work reported in this chapter neutral PSOrn is represented by model compound, denoted PSO, obtained by the replacement of the $(CH_2)_3CH(NH_3^+)(CO_2^-)$ side-chain of PSOrn by a methyl group. The structure of an amino form of PSO is shown schematically in **Figure 8.3**. As indicated by the X-ray data, the side-chain is not directly involved in the binding of PSOrn to the arginine residues. Therefore, the above simplification of the inhibitor is not expected to significantly affect the inhibitor/arginine interactions, especially since the $CH(NH_3^+)(CO_2^-)$ group, being at the end of a fully extended saturated alkyl chain, would only marginally affect the covalent bonding pattern (and hence electron density) within the "active" PSO moiety (either via through-space or through-bond interactions).

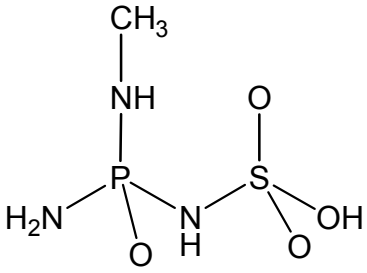

Figure 8.3 The structure (connectivity) of PSO, the model compound for PSOrn.

The quantum chemical calculations on PSO and the PSO/arginine adducts were carried out using density functional theory (see **Section 2.3**), utilising the B3LYP exchange-correlation hybrid functional[2-4] and the 6-31G(*d*) basis set. Full geometry optimisations were performed as well as constrained optimisations, where only the hydrogen coordinates were allowed to relax while the heavy atom coordinates were constrained at the X-ray values. For a number of

species the energies were recalculated using the fully polarised 6-31G(*d*,*p*) basis. The inclusion of polarisation functions on the hydrogens resulted in effectively negligible changes in the relative energies. Due to computer resource limitations vibrational frequencies and hence zero point energy (ZPE) corrections were not, in general, computed. On the basis of ZPE computations on the Zw1 and Zw2 dimers and their constituent PSO and arginine monomers, the dissociation energy of a dimer would be reduced by ~ 5 - 10 kJ mol^{-1}, viz. up to ~ 15%, by the inclusion of ZPE. As this work does not aim to produce energies of chemical accuracy, the omission of ZPE is justifiable.

All calculations were carried out using the Gaussian98 programs[5] on DEC alpha 600/5/333 and COMPAQ XP1000/500 workstations of the Theoretical Chemistry group at the University of Sydney and the 64 processor SGI Origin 2400 of the Australian Centre for Advanced Computing and Communications (ac3).

8.3 Results and Discussion

8.3.1 Free (Model) Inhibitor

All chemically reasonable tautomers of the model inhibitor PSO were considered in an effort to locate the most stable tautomer and to quantify their relative stabilities. Free PSO, and thus PSOrn, has the potential to form intramolecular hydrogen bonds which, in all probability, will have a considerable effect on these stabilities. The optimised structures of five amino and three imino tautomers of neutral PSO are shown in **Figure 8.4** and **Figure 8.5**, along with their relative energies. Although it may not be immediately obvious from these figures, the geometries of the heavy atom backbones of the various tautomers are quite different, especially in the angles. The variation is attributed, in part at least, to the effects of intramolecular hydrogen bonding which, of course, are tautomer dependent. Constraining the heavy atom coordinates to their X-ray values effectively eliminates most of the intramolecular hydrogen bonds at an energy cost of ~ 400 kJ mol^{-1}. As only part of this energy could be reasonably attributed to the hydrogen bonds, the relaxation energy associated with optimisation of the (covalent) bond distances and bond angles is obviously substantial. In light of such demonstrated sensitivity of the energy to relatively small variations in the

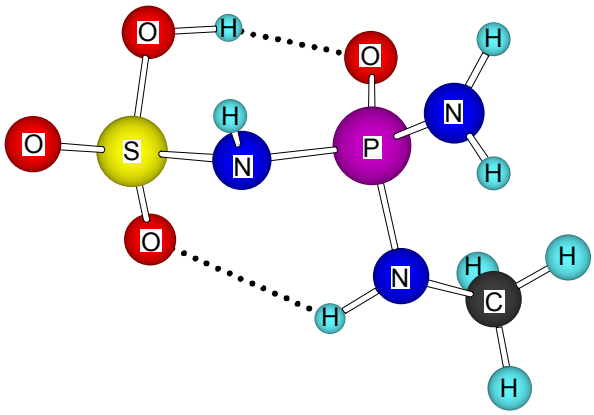

Amino1: E = 0.0 kJ mol^{-1}

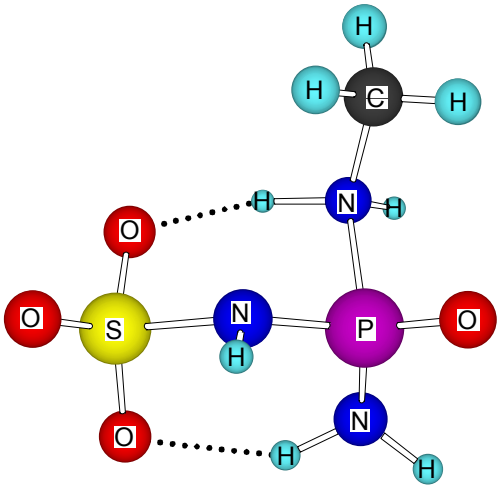

Amino2: E = 8.9 kJ mol^{-1}

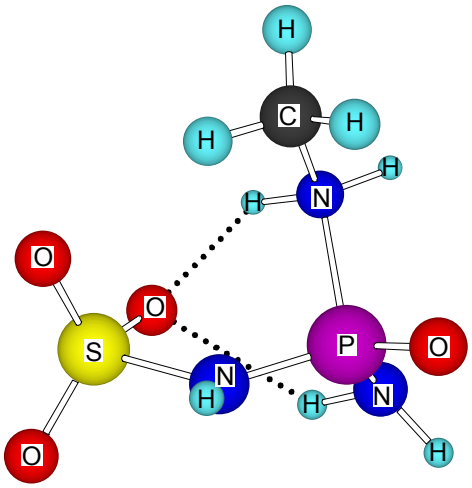

Amino3: E = 19.1 kJ mol^{-1}

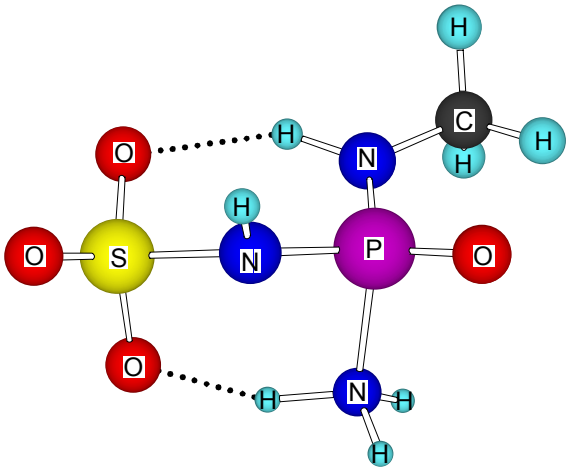

Amino4: E = 22.8 kJ mol^{-1}

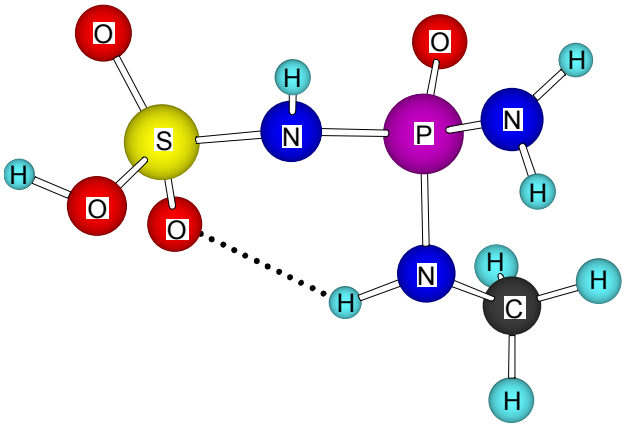

Amino5: E = 37.5 kJ mol^{-1}

Figure 8.4 Amino tautomers of PSO. (Energies relative to amino1.)

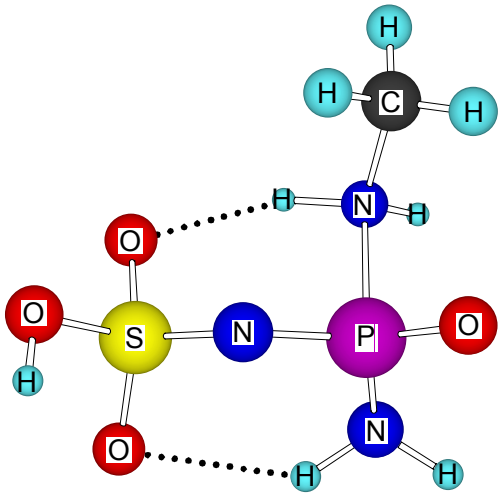

Imino1: E = 52.3 kJ mol^{-1}

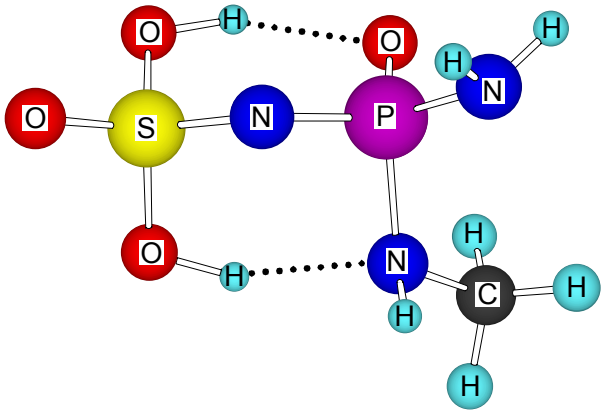

Imino2: E = 75.4 kJ mol^{-1}

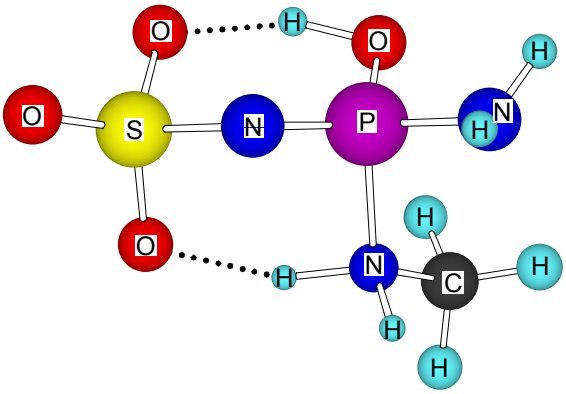

Imino3: E = 125.6 kJ mol^{-1}

Figure 8.5 Imino tautomers of PSO. (Energies relative to amino1.)

geometry, there is clearly a need for fully relaxed calculations; i.e., we cannot rely entirely on the results of constrained computations.

According to the computed equilibrium energies listed in **Figure 8.4** and **8.5** the imino tautomers are substantially less stable than the amino forms. This was expected, as in the former the S–N–P nitrogen would have two lone pairs of electrons and a formal negative charge; to stabilise such a structure considerable charge delocalisation would be needed. As will be shown later (**Section 8.3.3**), the sulfur and phosphorus atoms in their respective

environments in PSO cannot participate in π bonding to any appreciable degree; that is, no significant π charge delocalisation occurs. This is contrary to the implications of the Lewis structure of the imino form of PSOrn in **Figure 8.2**. Hence the marked difference in stabilities between amino and imino tautomers.

8.3.2 Bound (Model) Inhibitor

The crystal structure of PSOrn in OTCase indicates that the inhibitor is hydrogen bonded to an arginine residue (Arg57), as shown in **Figure 8.6**. In particular, the distance of 2.79 Å between the S–N–P nitrogen (N2) and the C–N–C nitrogen (N_{Arg}) of the arginine residue suggests a strong hydrogen bond mediated N···N interaction, as noted by Langley et al.[1] However, the N2···N_{Arg} interaction may be expected to be destabilising in the case of an amino tautomer, since the near-planar arrangement of the S–N2–P and C–N_{Arg}–C groups would imply that the N2–H and N_{Arg}–H groups would be pointing towards each other, which would result in strong repulsion between the hydrogens.

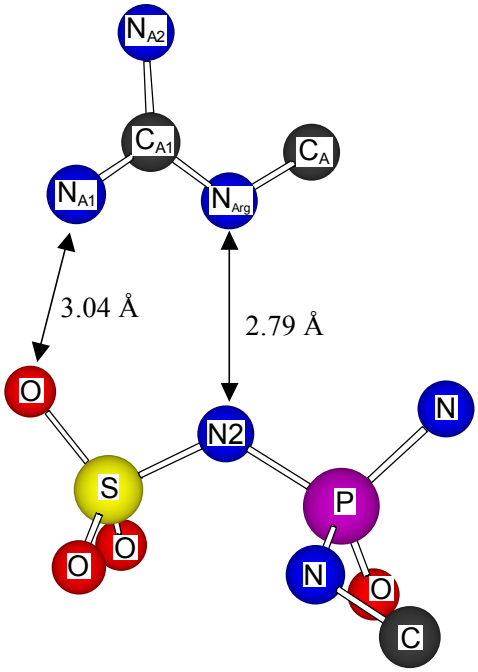

Figure 8.6 X-ray structure of PSOrn fragment with Arg57 residue.

As this interaction is expected to have the most significant effect on the relative stabilities of the tautomers, it was studied in some detail. Two approaches were used: (a) full optimisation of the geometry (relaxed calculation) and (b) partial optimisation, where the heavy atom backbone is constrained at the X-ray geometry and only the hydrogen positions are optimised (unrelaxed calculation). The first approach has the advantage of yielding optimal geometries, including hydrogen bond distances, and interaction energies. However, the strong intramolecular hydrogen bonds in the inhibitor, as discussed in the previous section, could considerably deform the structure, thus making comparisons between the computed equilibrium geometries and the X-ray values effectively meaningless. (In reality the enzyme bound PSOrn forms intermolecular hydrogen bonds to the various residues around it in preference to intramolecular hydrogen bonds.) To simplify the calculations only the interaction between PSO and a truncated form of the arginine residue ($C_2N_3H_7$), as shown in **Figure 8.6**, was studied.

Initially the range of PSO-arginine adducts that were studied were hydrogen bonded complexes of the various (amino and imino) tautomers of PSO (as shown in **Figure 8.4** and **8.5**) and neutral arginine, i.e., dimers. The lowest energy dimer in this group is a complex involving the amino1 tautomer, with binding energies computed as 27.5 and 11.3 kJ mol^{-1} from the relaxed and unrelaxed calculations respectively. This suggests that the N2$\cdots N_{Arg}$ interaction is stabilising, although the N2$\cdots N_{Arg}$ distance is considerably longer than in the X-ray structure. As can be seen from the structure in **Figure 8.7**, in the complex the arginine moiety is distorted, with the N_{Arg}–H bond rotated out of the molecular plane. The interaction of the imino1 tautomer with arginine gives rise to considerably larger binding energies: 50.9 and 26.8 kJ mol^{-1} from the relaxed and unrelaxed calculations respectively. Nevertheless, in absolute terms the amino1-arginine complex is more stable by ~ 29 kJ mol^{-1}, as indicated by the relaxed calculations.

On extending the calculations to zwitterionic dimers, that is, complexes of deprotonated PSO (denoted PSO^-) and protonated arginine, it was found that two of these are more stable, even in gas phase, than the dimers between neutral partners. The structures of these complexes (denoted Zw1 and Zw2) are also shown in **Figure 8.7**. The PSO^- moieties in both of these dimers are imino tautomers. As can be seen from the tabulated distances in **Table 8.1**, the

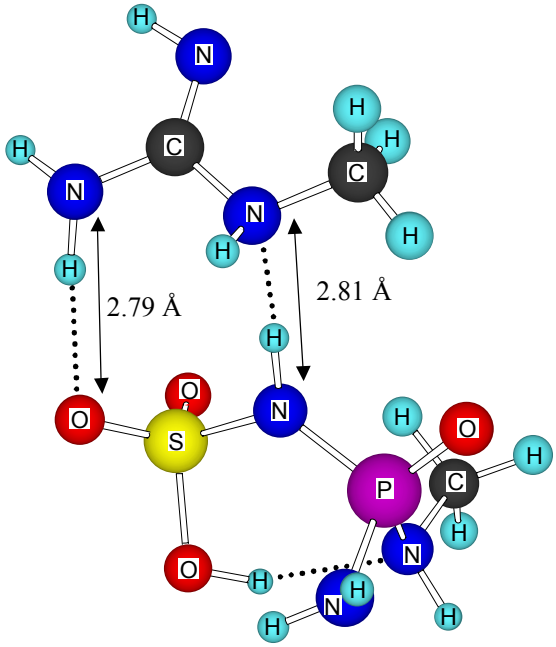

PSO(Amino1)···Arg Dimer

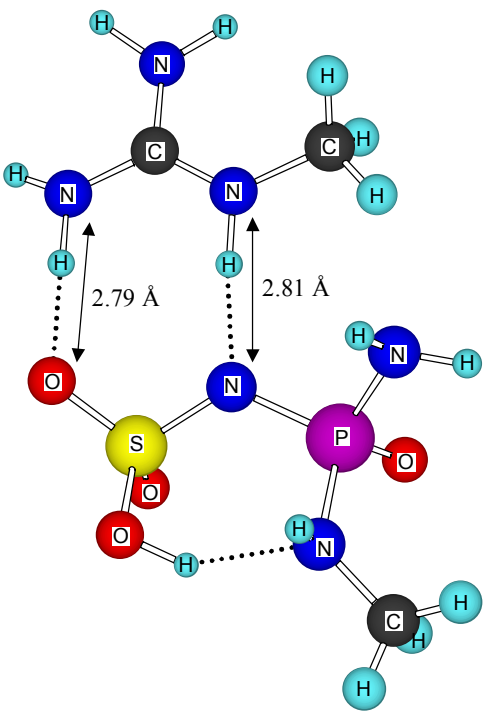

PSO^{-}(Imino)···$ArgH^{+}$ (Zw1) Dimer

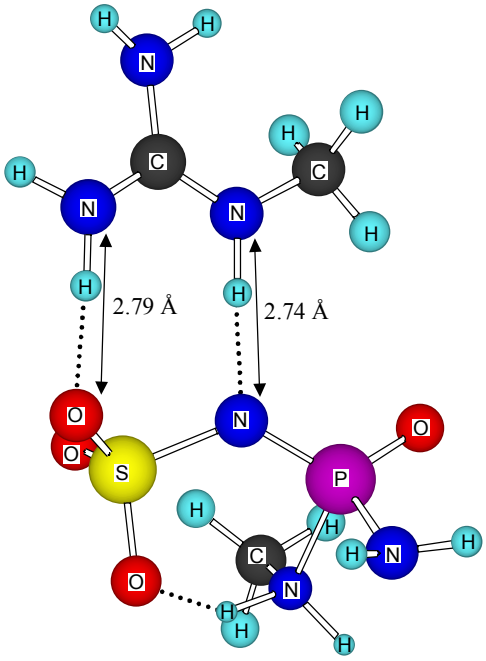

PSO^{-}(Imino)···$ArgH^{+}$ (Zw2) Dimer

Figure 8.7 Structures of the three most stable PSO···Arg dimers.

Table 8.1. Selected X-ray distances for enzyme bound PSOrn and corresponding computed distances in PSO···Arg dimers and PSO···$(Arg)_2$ trimer.[a]

	Atom-Atom Distance /Å			
	Bound PSOrn X-ray	PSO···Arg (Zw1)	PSO···Arg (Zw2)	PSO···$(Arg)_2$ Trimer
S–O	1.51	1.48	1.49	1.50
S–O1	1.34	1.63	1.50	1.52
S–O2	1.58	1.46	1.48	1.49
S–N2	1.60	1.62	1.69	1.65
N2–P	1.66	1.65	1.59	1.63
P–O3	1.48	1.49	1.49	1.52
P–N	1.72	1.71	1.69	1.71
P–N1	1.61	1.74	1.89	1.70
N1–C	1.48	1.47	1.49	1.47
N2–N_{Arg}	2.79	2.81	2.74	2.72
O–N_{A1}	3.04	2.76	2.76	2.70
C_A–N_{Arg}	1.46	1.46	1.45	1.45
N_{Arg}–C_{A1}	1.33	1.32	1.32	1.32
C_{A1}–N_{A2}	1.33	1.36	1.37	1.37
C_{A1}–N_{A1}	1.33	1.34	1.34	1.34
O1–N_{a1}	2.76			2.72
O3–N_{a2}	2.73			2.69
C_a–N_a	1.45			1.47
N_a–C_{a1}	1.33			1.36
C_{a1}–N_{a1}	1.32			1.34
C_{a1}–N_{a2}	1.32			1.34

[a] Labelling of atoms as indicated in **Figure 8.1**.
Subscripts Arg, A, A1, A2 refer to atoms of Arg57 (See **Figure 8.6**).
Subscripts a, a1, a2 refer to atoms of Arg106.

fully optimised geometry of Zw1 matches the X-ray data reasonably well. Agreement between theory and experiment is less convincing in the case of Zw2, where the P–N1 bond distance of 1.89 Å is clearly at variance with the X-ray value of 1.61 Å. Zw2, however, appears to be the more stable (by 13.2 kJ mol^{-1}) of the two dimers. Compared with the lowest energy amino1-arginine complex, Zw1 and Zw2 were computed to be 24.0 and 37.2 kJ mol^{-1} more stable respectively, corresponding to binding energies of 51.5 and 64.7 kJ mol^{-1} with

respect to neutral arginine and the amino1 form of PSO. The stabilities of the various dimers, as well as of a trimer (as discussed below), are summarised in **Table 8.2** as dissociation energies to a range of neutral and charged moieties.

Table 8.2 Computed dissociation energies of PSO···Arg dimers and trimers.

			ΔE /kJ mol^{-1}
PSO(Amino1) ··· Arg Dimer	→	PSO(Amino1) + Arg	27.5
PSO(Imino1) ··· Arg Dimer	→	PSO(Amino1) + Arg	–1.3
PSO(Imino1) ··· Arg Dimer	→	PSO(Imino1) + Arg	50.9
PSO^-(Imino) ··· $ArgH^+$ Dimer (Zw1)	→	PSO(Amino1) + Arg	51.5
PSO^-(Imino) ··· $ArgH^+$ Dimer (Zw1)	→	PSO^-(Imino) + $ArgH^+$	332.8
PSO^-(Imino) ··· $ArgH^+$ Dimer (Zw2)	→	PSO(Amino1) + Arg	64.7
PSO^-(Amino) ··· $ArgH^+$ Dimer (Zw3)	→	PSO(Amino1) + Arg	126.5
PSO^{2-}(Imino) ··· $(ArgH^+)_2$ Trimer	→	PSO(Amino1) + 2 Arg	170.8
PSO^{2-}(Imino) ··· $(ArgH^+)_2$ Trimer	→	PSO^- ··· $ArgH^+$ Dimer (Zw1) + Arg	119.3
PSO^{2-}(Imino) ··· $(ArgH^+)_2$ Trimer	→	PSO^{2-} + 2 $ArgH^+$	1284.2

The relative stabilities of PSO and PSO···Arg dimers, as obtained in constrained and relaxed calculations are shown in **Figure 8.8**. The trends in the stabilities appear to be qualitatively reproduced by the constrained optimisations, but clearly the energy differences, especially between the PSO(Amino1)…Arg dimer and Zw1, are predicted to be considerably larger by the constrained calculations. As remarked in the previous section, in light of the large energy differences between the unrelaxed and relaxed structures, we regard the latter as the more reliable.

Interactions between amino tautomers of PSO^- and protonated arginine (denoted $ArgH^+$) were found to be repulsive, as expected. Although in the latter complexes $ArgH^+$ did bind to PSO^-, this did not occur via N2, as would be required for a valid description of the binding of PSOrn in the enzyme.

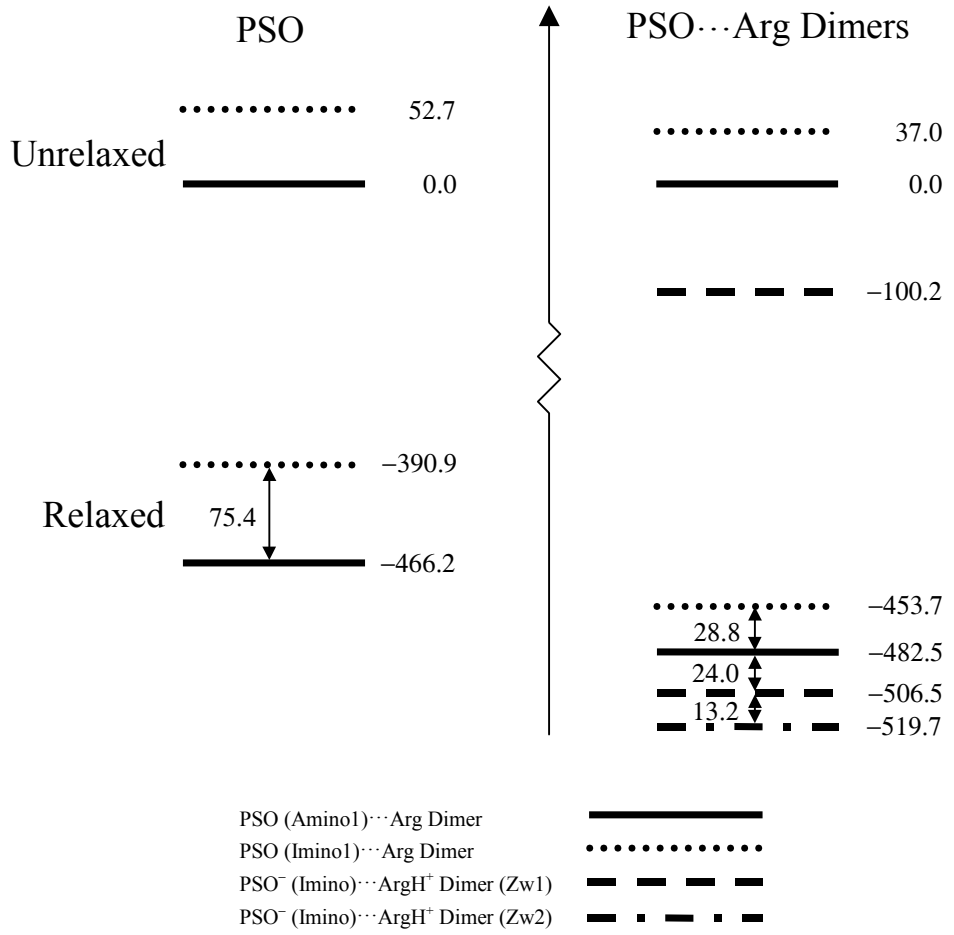

Figure 8.8 Relative energies (in kJ mol^{-1}) of PSO tautomers and PSO···Arg dimers from constrained and relaxed calculations.

According to the X-ray data, PSOrn interacts with two arginine residues, the second (Arg106) effectively bridging the O1 and O3 atoms of PSOrn (see **Figure 8.1**). A trimer of PSO with two arginines is clearly a more realistic model for the binding of PSOrn to the enzyme. Given the apparent propensity of arginine to exist in protonated form, our trimer calculations were restricted to a complex of a (doubly deprotonated) dinegative PSO (denoted PSO^{2-}) and two $ArgH^+$ subunits. The computed structure of this trimer is shown in **Figure 8.9**. The key interatomic distances are listed in **Table 8.1**. The agreement with the X-ray data is good, given the relatively high estimated errors of ± 0.2 Å in the X-ray distances. The large binding energy of 170.8 kJ mol^{-1}, relative to neutral PSO and two arginines, is consistent with the action of PSOrn as an effective inhibitor that binds irreversibly to the enzyme.

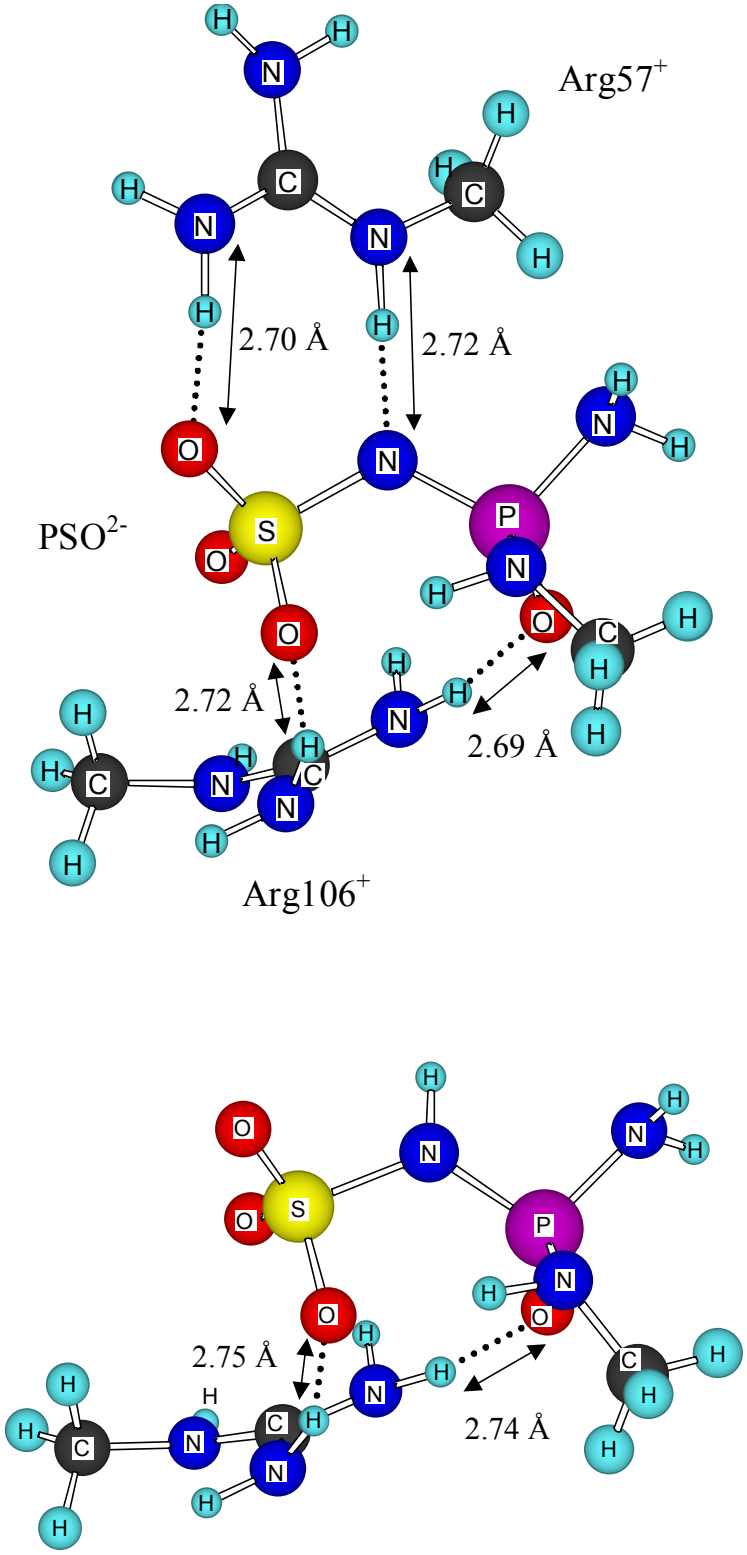

Figure 8.9 Structures of PSO···$(Arg)_2$ trimer and PSO···Arg (Zw3) dimer.

The very much higher stability of the trimer (to dissociation) than of the dimers Zw1 and Zw2 suggests that the interaction between a PSO^- ion and $ArgH^+$ (representing the Arg106 residue) is actually the dominant contribution to the overall stability, rather than the interaction with the (protonated) Arg57 residue. To test this hypothesis the structure of a third zwitterionic dimer (Zw3) was optimised. This derives from the trimer by the removal of neutral Arg57 (See **Figure 8.9**). PSO^- in Zw3 was chosen to be an amino tautomer. According to the calculations Zw3 is more than twice as stable as Zw1, its dissociation energy to PSO and Arg having been computed to be 126.0 kJ mol^{-1}. Thus the overall binding energy of the trimer is, to a good approximation, the sum of the individual binding energies to the two arginine residues.

In the zwitterionic dimers, as well as in the trimer discussed above, the overall binding between the negatively charged PSO^- and $ArgH^+$ moieties, in addition to the hydrogen bonding, has a substantial ionic (electrostatic) contribution. This can be quantified through the analysis of the binding energies of Zw1, Zw2 and the trimer, relative to neutral PSO and Arg as well as relative to the ions PSO^-, PSO^{2-} and $ArgH^+$. These results are included in **Table 8.2**. Thus Zw1 and Zw2 are bound by nearly 350 kJ mol^{-1} relative to the ions, but because of the very different proton affinities of PSO^- and Arg, the binding energies relative to the most stable amino tautomer of PSO and Arg are nearly an order of magnitude smaller. Furthermore, the $PSO^{2-}\cdots(ArgH^+)_2$ trimer is bound by 1284 kJ mol^{-1} relative to the ions.

8.3.3 Charge Distribution and Bonding

In **Figure 8.2**, following the usual convention, the Lewis structures of amino and imino tautomers of PSOrn were drawn with several PO and SO double bonds, with the implication that P and S are hypervalent; that is, they accommodate more than eight electrons in their valence shells. In the case of the P=O and S=O bonds this implies utilisation of the 3*d* atomic orbitals of P and S in the formation of the appropriate P-O and S-O π molecular orbitals. The validity of such "expansion of the octet" has been strongly debated in the literature over the past 20 years.[6-9] On the basis of careful quantum chemical studies several authors have concluded that the electronic structures of molecules with apparently hypervalent multiply bonded second row atoms are best described by invoking semipolar bonds, where, for

example, the P and S atoms acquire formal charges of up to +2, which then allows these atoms to form up to four covalent bonds with O^- (or other atoms or ions)[6,7,9,10]. The semipolar bonds thus have both covalent and ionic components and are comparable in strength with double bonds, with bond lengths to match.

In light of the above observations, the amino structure of PSOrn in **Figure 8.2** would be more correctly drawn by replacing each P=O and S=O with $P^+ – O^-$ and $S^+ – O^-$ semipolar bonds (which would result in S with a formal 2+ charge), as shown in **Figure 8.10**. The imino tautomer, however, as drawn in **Figure 8.2**, relies on π resonance to partially delocalise the negative charge on the PNS nitrogen due to the two lone pairs. Thus, if P and S cannot participate in π bonding, the above mechanism for charge delocalisation cannot be invoked. Hence our initial suspicion that amino forms of PSO would be considerably more stable than any imino tautomer. In the case of isolated PSO these suspicions proved well-founded as the computations located five amino type tautomers which were more stable than the lowest energy imino tautomer (**Figures 8.4** and **8.5**).

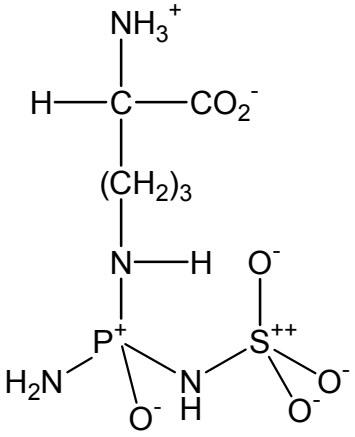

Figure 8.10 Lewis structure of an amino tautomer of PSOrn with semipolar bonds.

8.3.3.1 Population Analysis

As in previous studies which have addressed the problem of hypervalency, we have used the Roby-Davidson (RD) method[11-14] (with the B3LYP/6-31G(*d*) density matrix) to carry out population analyses on free as well as bound PSO, yielding atomic charges and shared electron numbers (σ) for pairs of atoms. The latter is interpreted as a direct measure of the covalent character of a given bond. It must be noted, however, that shared electron numbers are not bond orders and thus their interpretation requires calibration. This was carried out by analysing the shared electron numbers of a range of small molecules (H_2PNH_2, $PO(NH_2)_3$, H_3PNH, HPNH, HPO, HOPO, H_3PO, $HSNH_2$, H_2SNH, SNH, HSOH, H_2SO_4, H_3SO, SO) and correlating the shared electron numbers with bond lengths and bond orders, provided the latter could be reasonably assigned, for example double bonds in S=O and HP=O, and single bonds in $H_2P–NH_2$ and $HS–NH_2$. Thus, as shown in **Table 8.3**, for PN and PO: σ = 1.0 - 1.22 are consistent with single bonds, σ = 1.76 - 1.83 describe double bonds, while σ = 1.40 - 1.50 apply to semipolar bonds. Lower σ values describe such bonds in the case of SN and SO linkages. Atomic charges can also be calibrated, with q_N or q_O values of ~ –0.25 to ~ –0.5 being consistent with single or double bonds and ~ –0.6 to ~ –0.75 consistent with semipolar bonding. q_P and q_S show greater variation with the nature of their bonding partners, in general, however, q = 0.1 to 0.5 indicate single or double bonds whereas q > 0.6 (with only one N or O partner) indicate the presence of a semipolar bond. Bonding to additional N or O atoms increases q_P or q_S such that S in H_2SO_4 (with two single and two semipolar SO bonds) has a charge of 1.87. As noted earlier, this calibration shows that it is not possible to distinguish between double and semipolar bonds on the basis of bond lengths (which may have led to the original assumption that semipolar bonds were π bonds); semipolar bonds can be identified, however, by the lower values of σ and the higher atomic charges.

The computed shared electron numbers and atomic charges for the amino1 and imino1 tautomers of PSO, along with those of the zwitterionic dimer Zw1 are listed in **Table 8.4** and **Table 8.5**. Almost all the bonds between the heavy atoms of PSO are described as single or semipolar bonds. A partial double bond character has been assigned to the P–N2 bond in the imino1 tautomer of PSO. In this molecule, due to the protonation of N1, the P–N1 bond is long and weak and therefore a degree of bonding π interaction between the P and N2 atoms is possible. The high positive charges on the S and P atoms along with the high negative charges

Table 8.3 Calibration of Roby-Davidson population analysis results (shared electron populations and atomic charges) along with bond lengths for P-N, P-O, S-N and S-O single, double and semipolar bonds.

	P–N					P–O				
	Molecule	R_{PN} /Å	σ	q_P	q_N	Molecule	R_{PO} /Å	σ	q_P	q_O
Single Bond	H_2PNH_2	1.73	1.22	0.24	–0.44	H_2POH	1.68	1.04	0.33	–0.44
	$PO(NH_2)_3$	1.69	1.01	1.30	–0.53	HOPO	1.64	1.00	0.64	–0.45
Semipolar Bond	H_3PNH	1.57	1.50	0.79	–0.66	H_3PO	1.49	1.41	0.87	–0.60
						$PO(NH_2)_3$	1.50	1.39	1.30	–0.66
Double Bond	HPNH	1.59	1.83	0.30	–0.37	HOPO	1.48	1.75	0.64	–0.41
						HPO	1.50	1.75	0.50	–0.37

	S–N					S–O				
	Molecule	R_{SN} /Å	σ	q_S	q_N	Molecule	R_{SO} /Å	σ	q_S	q_O
Single Bond	$HSNH_2$	1.72	0.85	0.13	–0.41	HSOH	1.70	0.91	0.20	–0.41
						H_2SO_4	1.63	0.76	1.87	–0.51
Semipolar Bond	H_2SNH	1.61	1.25	0.64	–0.70	H_3SO	1.49	1.19	1.06	–0.72
						H_2SO_4	1.45	1.21	1.87	–0.65
Double Bond	SNH	1.58	1.64	0.13	–0.26	SO	1.52	1.47	0.31	–0.31

274

Table 8.4 Selected bond lengths (R in Å), Roby-Davidson shared electron numbers (σ in e) and assigned bond types of amino and imino tautomers of PSO and of the PSO···Arg dimer (Zw1)[a]

	PSO (Amino1)			PSO (Imino1)			PSO···Arg Dimer (Zw1)		
	R	σ	Bond Type	R	σ	Bond Type	R	σ	Bond Type
S–O	1.45	1.3	Semipolar	1.63 [b]	0.8	Semipolar	1.48	1.1	Semipolar
S–O1	1.46	1.2	Semipolar	1.47	1.2	Semipolar	1.63 [b]	0.8	Semipolar
S–O2	1.61 [b]	0.8	Single	1.48	1.1	Single	1.46	1.2	Single
S–N2	1.70	0.9	Single	1.61	1.1	Part. Double	1.62	1.1	Single
P–N2	1.72	1.0	Single	1.60	1.3	Single	1.65	1.1	Single
P–O3	1.50	1.3	Semipolar	1.48	1.5	Semipolar	1.49	1.4	Semipolar
P–N	1.66	1.1	Single	1.67	1.1	Single	1.71	1.0	Single
P–N1	1.67	1.1	Single	1.92	0.6	Weak Single	1.74	0.9	Single

[a] Labelling of atoms as indicated in **Figure 8.1**.

[b] Part of SOH group.

Table 8.5 Atomic charges (in e) on heavy atoms for PSO in amino and imino tautomers of PSO and of the PSO···Arg dimer (Zw1) from Roby-Davidson analysis.[a]

	PSO (Amino1)	PSO (Imino1)	PSO…Arg Dimer (Zw1)
S	1.79	1.77	1.84
O	–0.72	–0.46 [b]	–0.82
O1	–0.59	–0.81	–0.59 [b]
O2	–0.53 [b]	–0.64	–0.74
N2	–0.82	–1.08	–1.19
P	1.32	1.27	1.05
O3	–0.89	–0.78	–0.76
N	–0.56	–0.62	–0.46
N1	–0.54	–0.28	–0.33

[a] Labelling of atoms as indicated in **Figure 8.1**.

[b] Part of SOH group.

on the oxygens of PSO are consistent with semipolar S-O and P-O bonds. The high negative charge on N2 is according to expectations in the case of imino tautomers, although it is quite high in the amino1 form as well, due to the polar N-S, N-P, and especially N-H bonds. Interestingly, there is an increased negative charge localisation on N2 in the case of the Zw1 dimer. This is probably due to the polarisation of PSO by the Arg^+ residue.

The population analyses for the amino1 and imino2 tautomers were repeated with basis sets containing two additional sets of *d* functions on the P and S atoms (with exponents chosen as 1/3 and 1/9 of those in the 6-31G(*d*) sets). This was done to ensure that the description of the atomic 3*d* orbitals on these atoms is sufficiently accurate and flexible to resolve any incipient π bonding. No significant changes in charges, shared electron numbers or relative energies occurred. We conclude therefore that no appreciable π bonding is present in the various tautomers of PSO and its complexes.

8.3.3.2 Hydrogen Bonding

A related issue is the hydrogen bonding potential of the various terminal oxygen and nitrogen atoms in PSO. The traditional explanation of hydrogen bonding is that the protonic hydrogen of the proton donor seeks out regions of high electron density, which are generally provided by the lone pairs of the proton acceptor. As hydrogen bonds are usually (near) linear, it is assumed that in general each lone pair is only capable of forming one hydrogen bond. It would therefore be expected that a doubly bound oxygen atom, formally having two lone pairs, would be able to form two hydrogen bonds. On the other hand, an oxygen atom involved in a semipolar bond formally has three lone pairs and would therefore have the potential to form three hydrogen bonds. The net effect of three lone pairs of electrons is an effectively uniform (directionless) charge distribution on the oxygen atom. It is therefore possible that this, coupled with the large negative charges, q_O, for oxygens involved in semipolar bonding (as shown in **Table 8.3**) may allow the formation of more than three hydrogen bonds.

The validity, or otherwise, of this view of hydrogen bonding is particularly important when attempting to postulate and interpret which enzyme-inhibitor interactions in the crystal

structure of Langley et al.[1] involve hydrogen bonds. Careful analysis of the crystal structure data indicates that for each of the oxygen atoms attached to S (O, O1 and O2 as defined in **Figure 8.1**) there are three potential proton donors with appropriate distances and relative orientations for the formation of three hydrogen bonds. In addition there are four potential proton donor residues which are appropriately placed to form hydrogen bonds to O3.

It is therefore important to determine whether it is realistic to assign such a large number of hydrogen bonds to oxygen atoms in these environments. This section thus presents an investigation of the stabilisation or destabilisation which is obtained for various model compounds with a range of hydrogen bonding interactions. These model compounds include H_2CO (as the simplest and best understood example of a doubly bound oxygen atom), HPO (in order to determine the effect of phosphorus on the hydrogen bonding), H_3PO (as a simple example of an oxygen in a semipolar bond) and $PO(NH_2)_3$ (as a model for the O3 oxygen in PSOrn). Water molecules were used as proton donors where the orientation of these moieties was fixed so there could be no additional stabilisation due to hydrogen bonds between adjacent water molecules or to other parts of the model compound (see **Figure 8.11**). The hydrogen bonds were also constrained to be linear. All other inter- and intramolecular parameters were then optimised using MP2/cc-pVDZ, thus allowing the stabilisation energy, E_{stab}, to be calculated relative to the non-interacting monomers. It was, of course, particularly important to estimate the possible contribution of basis set superposition error to this stabilisation energy. This was done using the Boys-Bernardi method (described in **Section 2.4.5**) for each of the interacting molecules. The sum of the individual counterpoise corrections was subtracted from E_{stab} to give the counterpoise corrected estimate of the hydrogen bonding energy, E_{HB}. The successive hydrogen bond energies corresponding to the introduction of 1, 2, 3 and 4 hydrogen bonding water molecules are presented in **Table 8.6**.

H_2CO and HPO, as typical doubly bonded systems, were expected to have two lone pairs and form two hydrogen bonds; this expectation is clearly confirmed by the results in **Table 8.6**. In the case of H_2CO a minimum energy structure was also found with the addition of a third H_2O, however two of the water molecules were within only 70° of each other (rather than 120°) indicating that they were binding to the same lone pair on the H_2CO oxygen. Although this structure was found to be stable by 1.7 kcal mol^{-1} before the application of counterpoise

Table 8.6 Successive stabilisation energies corresponding to the addition of water molecules as proton donors to H_2CO, HPO, H_3PO and $PO(NH_2)_3$.

Hydrogen Bonds	E_{HB} /kcal mol^{-1}			
(H_2O molecules)	H_2CO	HPO	H_3PO	$PO(NH_2)_3$
1	–3.0	–3.0	–4.7	–6.6
2	–2.3	–2.3	–4.1	–6.4
3	0.9	–	–2.7	–6.2
4	–	–	0.0	–2.7

corrections, once superposition errors had been accounted for the tetramer was found to be unstable by 0.9 kcal mol^{-1}, suggesting that the structure is simply an artefact of the relatively small cc-pVDZ basis set. In terms of its hydrogen bonding propensity, HPO is very similar to H_2CO, although for HPO no local minimum structure with three waters could be found. Thus it appears that doubly bonded oxygen atoms will only form two hydrogen bonds and that these align with the expected orientations of two equivalent localised lone pairs (See **Figure 8.11**).

H_3PO formally has a semipolar P-O bond and, as expected, it can form up to three hydrogen bonds. Local minima were also found on the PES with four and even five water molecules apparently hydrogen bonded to the oxygen of H_3PO. In both these structures the water molecules appear evenly distributed around the oxygen atom suggesting that the lone pair charge distribution is fairly directionless (that is, the lone pairs are not spatially discrete). The stability of these structures could again be a BSSE artefact, however, as suggested by the counterpoise corrected energies. For the structure with four water molecules the possibility of attractive interaction between the water molecules was also investigated, however it was found that the water-water interactions were, in fact, repulsive by 3.7 kcal mol^{-1}.

Finally, binding to the oxygen atom in the hypothetical molecule $PO(NH_2)_3$ was investigated as a model for the O3 atom (bound to P) in PSOrn. Even with the inclusion of the counterpoise correction, this model compound is capable of forming four hydrogen bonds with water molecules. The first three interactions are of comparable strength (and much stronger than those in H_2CO, HPO or H_3PO) while the fourth seems significantly weaker although still binding.

We therefore conclude that up to four hydrogen bonds can be attached to an oxygen atom which is bound by a semipolar bond; it is therefore reasonable to interpret the crystal structure of PSOrn as showing up to three hydrogen bonds to O, O1 and O2 and up to four hydrogen bonds to O3.

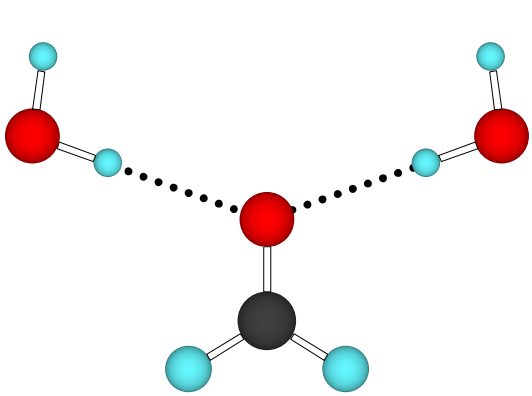

$H_2CO.(H_2O)_2$

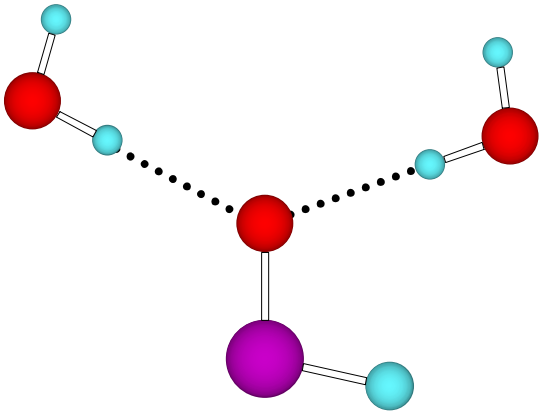

$HPO.(H_2O)_2$

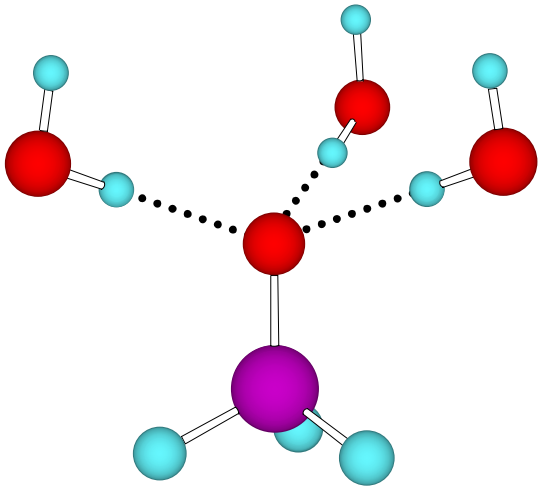

$H_3PO.(H_2O)_3$

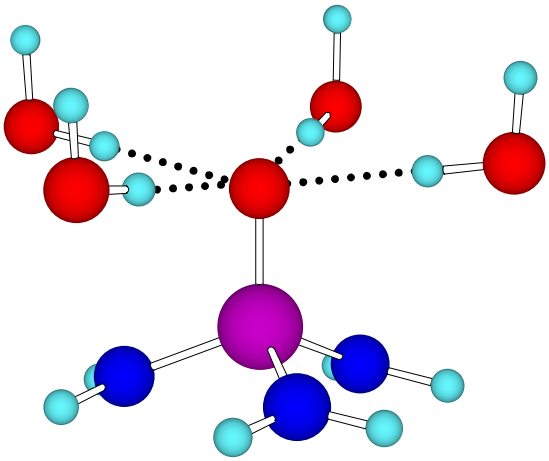

$PO(NH_2)_3.(H_2O)_4$

Figure 8.11 Most stable hydrogen bonded structures for H_2CO, HPO, H_3PO and $PO(NH_2)_3$.

8.4 Conclusion

With the aid of quantum chemistry, viz. density functional theory, the binding of PSOrn to the enzyme OTCase was investigated and modelled through a study of PSO, a simplified model for PSOrn, and its interaction with one and two arginine molecules. The PSO···$(Arg)_2$ trimer was found to be bound by ~ 171 kJ mol^{-1}. Such high stability, due to the presence of four hydrogen bonds as well as a large ionic interaction between the dinegative PSO^{2-} and protonated arginines, is consistent with the experimental observation that PSOrn is a powerful enzyme inhibitor. The calculations confirm the proposals of Langley et al.[1], inasmuch as bound PSOrn is a dinegative imino tautomer. While in the case of free (neutral) PSO the most stable tautomers were calculated to be amino types, when bound to one or two (protonated) arginines PSO (as PSO^{-} or PSO^{2-}) is predicted to prefer an imino form. However, as in other phosphorous and sulfur containing molecules, according to the population analyses that were carried out the P-N, P-O, S-N and S-O bonds in PSO are generally best described as single or semipolar bonds.

8.5 References

1. D. B. Langley, M. D. Templeton, B. A. Fields, R. E. Mitchell and C. A. Collyer, *J. Biol. Chem.*, **2000**, *275*, 20012.
2. A. D. Becke, *Phys. Rev. A*, **1988**, *38*, 3098.
3. C. Lee, W. Yang and R. G. Parr, *Phys. Rev. B*, **1988**, *37*, 785.
4. A. D. Becke, *J. Chem. Phys.*, **1993**, *98*, 5648.
5. M. J. Frisch, G. W. Trucks, H. B. Schlegel, G. E. Scuseria, M. A. Robb, J. R. Cheeseman, V. G. Zakrzewski, J. A. Montgomery, R. E. Stratmann, J. C. Burant, S. Dapprich, J. M. Millam, A. D. Daniels, K. N. Kudin, M. C. Strain, O. Farkas, J. Tomasi, V. Barone, M. Cossi, R. Cammi, B. Mennucci, C. Pomelli, C. Adamo, S. Clifford, J. Ochterski, G. A. Petersson, P. Y. Ayala, Q. Cui, K. Morokuma, D. K. Malik, A. D. Rabuk, K. Raghavachari, J. B. Foresman, J. Cioslowski, J. V. Ortiz, B. B. Stefanov, G. Lui, A. Liashenko, P. Piskorz, I. Komaromi, R. Gomperts, R. L. Martin, D. J. Fox, T. Keith, M. A. Al-Laham, C. Y. Peng, A. Nanayakkara, C. Gonzalez, M. Challacombe, P. M. W. Gill, B. G. Johnson, W. Chen, M. W. Wong, J. L. Andres, M. Head-Gordon, E. S. Replogle and J. A. Pople, Gaussian 98 Revision A.7, Gaussian, Inc.: Pittsburgh, PA, **1998**,
6. A. E. Reed and P. v. R. Schleyer, *J. Am. Chem. Soc.*, **1990**, *112*, 1434.
7. J. A. Dobado, H. Martínez-García, J. M. Molina and M. R. Sundberg, *J. Am. Chem. Soc.*, **1999**, *121*, 3156.
8. K. Jug and E. Fasold, *Int. J. Quantum Chem.*, **1992**, *41*, 687.
9. W. Kutzelnigg, *Angew. Chem. Int. Ed. Engl.*, **1984**, *23*, 272.
10. A. P. L. Rendell, G. B. Bacskay and N. S. Hush, *J. Am. Chem. Soc.*, **1988**, *110*, 8343.
11. E. R. Davidson, *J. Chem. Phys.*, **1967**, *46*, 3320.
12. K. R. Roby, *Mol. Phys.*, **1974**, *27*, 81.
13. R. Heinzmann and R. Ahlrichs, *Theor. Chim. Acta*, **1976**, *42*, 33.
14. C. Ehrhardt and R. Ahlrichs, *Theor. Chim. Acta*, **1985**, *68*, 231.

Chapter 9

Conclusion

The major focus of the research work presented in this thesis is the calculation of accurate thermochemical data, including atomisation energies and heats of formation. Gaussian-3 (G3) and related methodologies have been found to be particularly useful for this purpose, yielding chemically accurate heats of formation in most cases, with relatively modest computational cost. Thus the G3 heats of formation of approximately 120 C_1 and C_2 fluorocarbons and oxidised fluorocarbons (along with selected C_3 fluorocarbons) were calculated. For the most part, these showed good agreement with the best available theoretical and experimental literature data, particularly when G3 was used in conjunction with isodesmic reaction schemes. For molecules for which the G3 results were found to be in poor agreement with experiment or for which the experimental values had large uncertainties (e.g., HCCF, FCCF, CCH, CCF and HCOO), more extensive CCSD(T)/CBS calculations have confirmed the validity of the G3 results, indicating that the literature values may need to be revised. Two less computationally expensive approximations to G3 were also proposed: G3MP4(SDQ) and G3[MP2(Full)]. These methods were found to reliably reproduce the G3 results, with mean absolute deviations from G3 of ~ 0.4 and ~ 0.5 kcal mol^{-1} respectively for heats of formation from atomisation energies. These deviations could be further reduced by the application of isodesmic reaction schemes.

The G3 method was also successfully applied to the calculation of the heats of formation of molecules containing third row atoms, in particular $CFClBr_2$, and by extension to the thermochemistry of its dissociation reactions. As G3 results for bromine containing species had been previously only reported for very small molecules such as HBr, Br_2 and CH_3Br, it was gratifying to find excellent agreement between the experimentally determined $\Delta_f H^0_{298}$ of 184 ± 5 kJ mol^{-1} and the G3 value of 188 ± 5 kJ mol^{-1}. This work therefore provided further evidence for the wide range of applicability of the G3 method. In addition, these results have also provided valuable aid in the determination of the photolysis mechanism for $CFClBr_2$ at 265 nm. Our calculations have predicted the dissociation energy for the two C-Br bonds to be equal to the (experimental) energy required to produce the CFCl carbene, thus supporting the hypothesis that the photolysis proceeds via a triple fragmentation pathway, releasing two Br atoms, rather than by the concerted elimination of a Br_2 molecule.

G3 type methods (including G2, G3, G3X and G3X2) as well as more extensive CCSD(T)/CBS type calculations were also employed in the calculation of the

thermochemistry of 18 small phosphorus containing compounds (P_2, P_4, PH, PH_2, PH_3, P_2H_2, P_2H_4, PO, PO_2, PO_3, P_2O, P_2O_2, HPO, HPOH, H_2POH, H_3PO, HOPO and $HOPO_2$). The CCSD(T)/CBS results are consistent with the available experimental values and, as the estimated uncertainties are quite small, they constitute the most accurate set of heats of formation available for these molecules. They are therefore regarded as an excellent benchmark for the testing of the more approximate G3*n* methods. The G3 and G3X methods were found to consistently underestimate the benchmark atomisation energies, on average by 3.6 and 1.8 kcal mol^{-1} and by up to 6.5 and 5.6 kcal mol^{-1} respectively for this set of molecules (excluding P_4); G2 is comparable in performance to G3. The G3X2 method was therefore proposed in an effort to improve the G3X results; G3X2 accounts for a higher degree of electron correlation in comparison with G3 and G3X and, with the inclusion of counterpoise corrections for BSSE on the phosphorus atoms in the core-valence correlation calculations, it does show a modest improvement (with a mean absolute deviation from the benchmark results of 1.5 kcal mol^{-1}). Further investigation has also revealed that the approximations underlying the Gaussian-*n* methods become unreliable for molecules which involve unusual P-P bonding, such as double bonds (in P_2 and P_2H_2), double and semipolar bonds (in PPO) or large structural strain (in P_4). We therefore recommend great care with the application of these methods to molecules with bonds between second row elements unless these are simple, unstrained single bonds.

Accurate thermochemical data, in particular those obtained by CCSD(T)/CBS calculations, along with similar calculations for transition state structures (with appropriate approximations for variational transition states) allowed us to reliably predict the kinetics of Twarowski's proposed catalytic schemes for H + OH recombination. The application of transition state and RRKM theory resulted in rate coefficients which are consistent with the results of experimental and modelling studies, although they are in most cases significantly lower than Twarowski's estimated values. At 2000K the rates of both catalytic schemes were found to be comparable and significantly higher than the uncatalysed recombination; both cycles are therefore expected to be catalytic at this temperature.

The potential energy surfaces for all possible reactions stemming from the NNH + O recombination were investigated in detail along the appropriate reaction coordinates at the B3LYP/6-31G(2*df*,*p*) level of theory. This study revealed the presence of several reaction

channels which had not been considered previously (including direct abstraction of H by O and three product channels via the intermediate ONHN) and yielded improved descriptions of channels which had hitherto been incompletely characterised (dissociation of *cis*- and *trans*-ONNH into NO + NH). The heats of formation were determined for each of the species corresponding to stationary points on the PES using both G3X theory and a CCSD(T)/CBS type scheme. A reasonable level of consistency, corresponding to agreement of ~ 2 kcal mol^{-1} or better between the two sets of results, was observed. This thermochemical and geometric data was further utilised to generate rate coefficients for the various reaction channels on the potential energy surface via (variational) transition state and RRKM theories, thus allowing the overall rate coefficients and the flux through each channel to be determined. We were therefore able to conclude that the NNH + O channel is considerably less important in combustion systems than had been previously believed. This was supported by modelling studies of two combustion systems in the presence of N_2 which yielded good agreement with experiment when our revised thermochemical and kinetic data was employed.

In a study aimed at modelling the binding of the inhibitor PSOrn to OTCase, the relative stabilities of various amino and imino tautomers of PSO, a model compound for PSOrn, were investigated both in the gas phase and when bound to (model) residues from the active site of OTCase. Gas phase calculations revealed that the amino tautomer is the most stable form of free (neutral) PSO; in the presence of arginine residues, however, the imino structure becomes lower in energy, the most stable structure being a doubly deprotonated PSO bound to two Arg^+ residues. Thus when bound to the active site of the enzyme, PSOrn would be expected to adopt a dinegative imino form. Population analysis and hydrogen bonding studies have revealed that the intramolecular bonds involving second row atoms are either single or semipolar in nature and that the terminal oxygen atoms are capable of accommodating up to four hydrogen bonds.